AIRFOIL RESPONSE TO PERIODIC DISTURBANCES--
THE UNSTEADY KUTTA CONDITION

by

David R. Poling

Dissertation submitted to the Faculty of the
Virginia Polytechnic Institute and State University
in partial fulfillment of the requirements for the degree of
DOCTOR OF PHILOSOPHY
in
Engineering Mechanics

APPROVED:

Dr. D. P. Telionis, Chairman

Dr. D. T. Mook

Dr. T. Herbert

Dr. S. L. Hendricks

Dr. M. Williams

August, 1985

Blacksburg, Virginia

AIRFOIL RESPONSE TO PERIODIC DISTURBANCES--
THE UNSTEADY KUTTA CONDITION

by

David R. Poling

(ABSTRACT)

Unsteady flow fields over a NACA 0012 at an angle of attack are investigated. The first is the classical pitching motion about the airfoil's quarter chord. The second is the flow over a fixed airfoil immersed in the wake of the pitching airfoil. Large reduced frequencies are considered. Measurements were obtained in a water tunnel by Laser-Doppler velocimetry. Ensemble-averaged velocity measurements were obtained in the vicinity of the trailing edges of both the pitching and the fixed airfoils. The flowfields in the wake and at the trailing edges of both airfoils were studied visually. The validity of the quasi-steady and an extension to an unsteady Kutta condition are examined. A new dynamic similarity parameter is proposed. An analytical method based on the dynamics of discrete vortices is employed. Numerical calculations of the flow over the fixed airfoil are compared with experimental results.

I dedicate this dissertation

to

my family

ACKNOWLEDGEMENTS

I wish to express my sincere appreciation to my committee chairman and advisor, Dr. Demetri P. Telionis for his support and encouragement throughout my program of study. It has been a rewarding and gratifying experience to have had the opportunity to engage in this level of education with Dr. Telionis.

My thanks and appreciation are also extended to Dr. Dean T. Mook for his help and constructive evaluation throughout the progress of my work. Thanks are also extended to Drs. Hendricks, Herbert, Saric and Williams for their help in reviewing the dissertation and their guidance as members of my graduate committee. Thanks is also extended to Dr. Frederick for his help and consideration in my work as an instructor.

I am most appreciative for the help of the personnel in the machine shop. Special thanks are extended to , , and for their help in the technical phases of the experimental work. Thanks is also extended to for his expertise in the use of the photographic equipment. Also, I am grateful to for his work on some of the figures.

Thanks are extended to , , , and for their clerical support. My appreciation is also expressed to and and their staff for their patience and expertise in typing this dissertation.

My deepest gratitude is expressed to the late
for his interest and technical support in the experimental work. It was with his technical ability and expertise that several difficult obstacles were crossed throughout the series of experiments. I am grateful to him for his support and friendship.

Thanks are also extended to all of the members of the Blue Ridge Soaring Society for their fellowship and moral support.

Special thanks is expressed to for his help and guidance throughout my academic career as a student.

Finally, I would like to express my appreciation to my family, whose love and support helped me to finish this work.

This research was supported by NASA, Project Number 47-004-801. The monitors of this grant, and later , have contributed substantially by their support and criticism. Thanks is expressed to and of NASA-Ames who made many helpful suggestions.

TABLE OF CONTENTS

LIST OF FIGURES

LIST OF TABLES

CHAPTER ONE

INTRODUCTION

Unsteady flows about airfoils involve length scales that differ by many oders of magnitude. Solving the full Navier-Stokes equations for such problems with the computers of today and perhaps the next generation is often not practical. Methods based on interacting boundary layers will remain useful for some time to come. The trailing edge of the airfoil plays a crucial role in controlling the entire structure of the flow field for unseparated flows. The results of this research offer some experimental evidence on the physical characteristics of unsteady flow in the neighborhood of a sharp trailing edge. Methods based on potential flow theory can predict quite accurately attached unsteady flows if a proper Kutta condition is provided. This dissertation also discusses the numerical results of such a method and the validity of an unsteady Kutta condition. The results presented here may therefore assist in the development of interacting codes as well as purely inviscid methods.

The classical Kutta condition for sharp-edged airfoils requires that the stagnation streamline in the aft of the airfoil is attached to the trailing edge. This condition is sufficient to render the solution unique and in fact it can be easily proved that then, at least for steady flow, a number of other conditions are met at the trailing edge:

(i) the pressure is continuous, or equivalently, the loading tends to zero,

(ii) the velocity is zero or at most finite,

(iii) the shedding of vorticity vanishes,

(iv) the stagnation streamline bisects the wedge angle of the airfoil.

In fact, any of these conditions can be used to solve the problem and then all other conditions are automatically satisfied.

It has slipped the attention of many investigators that such solutions are unique only if formulated in an analytical way. If a typical panel method is used, then requiring that the rear stagnation point be located at the trailing edge is not enough to render the solution unique. There is an infinity of solutions that satisfy conditions (i), (ii) and (iii) and are therefore physically acceptable. All these solutions are quite realistic if the trailing edge is somewhat rounded. In this case the classical Kutta condition is in principle inapplicable. What is interesting about the Kutta condition is that in real life, a small curvature of the trailing edge does not influence the flow and the stagnation streamline leaves the airfoil in a direction that bisects the airfoil wedge. The wedge corresponds to what would be the extension of the trailing edge if the edge were not rounded. In finite-panel methods, therefore, it should also be required that condition (iv) is met as well.

This idea can be illustrated more clearly by virtue of the schematic representations of Fig. 1.1. In Fig. 1.1a the classical

situation of a sharp edge is depicted. Standard conformal mapping concepts are convincing from the standpoint that the stagnation streamline bisects the wedge angle. This is simply because (a) the image point of the wedge corner is a point where the velocity in the physical plane is singular, (b) the stagnation streamlines are always perpendicular to the surface of the cylinder (except for the case when the two stagnation points coalesce), and (c) angles there are magnified by the same factor. Any real airfoil edge is not perfectly sharp. If the edge is rounded, then any direction is acceptable as shown in Fig. 1.1(b). Nevertheless, experimental evidence indicates that the standard analytical solution predicts the flow with remarkable accuracy, which implies that the trailing-edge streamline leaves the airfoil in the direction of the wedge bisector, as shown in Fig. 1.1(c).

These arguments should not be totally reassuring. The logic is exposed to the serious question: How small should the radius of curvature be to permit application of the classical Kutta condition? Certainly, for well rounded trailing edges, viscous effects cannot be neglected (see Vatsa, Werle, and Verdon, 1982). It is argued very correctly by Basu and Hancock (1978) that there is no definite statement of the "Kutta condition" and each mathematical formulation requires its own "consistent" Kutta condition to ensure a unique solution; "the relevant and appropriate Kutta condition needs to be formulated separately for each mathematical model".

In unsteady flow the situation changes drastically. If there is no separation upstream of the trailing edge, then the rear stagnation point

coincides again with the trailing edge. However, any changes of bound vorticity require shedding of equal and opposite vorticity. Thus, condition (iii) is therefore violated. In this case the direction of the flow in the neighborhood of the trailing edge coincides with one of the two sides of the wedge as shown schematically in Fig. 1.2 and argued convincingly by Giesing (1969) and Maskell (1971). The basic idea is that any stagnation streamline contained in the extended wedge corresponds to zero velocity on both sides of the airfoil; namely, for $|\phi| < \frac{\theta}{2}$ (see Fig. 1.2(c)), $U_u = U_l = 0$, whereas any streamline outside of the extended wedge (see Fig. 1.2(d)) leads to an infinite value of the velocity on one side of the airfoil. The first case (see Fig. 1.2(c)) does not allow shedding of vorticity, whereas the second (see Fig. 1.2(d)) should be discarded because of the singularity. This leaves only the situations of Fig. 1.2(a) and (b) as the only other alternatives. These arguments would be meaningless if the interaction between the viscous and inviscid regions in the vicinity of the trailing edge is strong.

Sears (1956 and 1976) has extended the classical Howarth condition to unsteady flow. By calculating the vorticity flux shed by the boundary layers at the points of separation of a two-dimensional body, he arrived at the relationship

$$-\frac{d\Gamma}{dt} = \left[\frac{1}{2} U_e^2 - U_{sep} U_e\right]_l^u \tag{1.1}$$

where $[\quad]_l^u$ denotes the difference between the values at the upper and lower surface respectively, U_e is the boundary-layer-edge velocity at separation and U_{sep} is the speed of the point of separation. In the case presented here, the flow stays attached until the trailing edge and therefore $U_{sep} = 0$. Equation (1.1) therefore reduces to

$$\frac{d\Gamma}{dt} = \frac{1}{2}\left(U_l^2 - U_u^2\right) \tag{1.2}$$

Where either U_l or U_u is zero as depicted schematically in Fig. 1.2. Basu and Hancock have arrived at Eq. (1.2) following purely inviscid arguments of vortex shedding. Moreover, they have proved that Eq. (1.2) is compatible with condition (i), namely that the pressure is continuous at the trailing edge.

These arguments are a natural extension of the steady flow theory and are mathematically unambiguous and consistent. However, there is a serious flaw in the logic described. The unsteady solutions do not tend asymptotically to the steady solution. For any time rate of change of bound circulation, no matter how small, the trailing edge streamline forms an angle $\theta/2$ with the wedge bisector. In other words, ϕ does not tend to zero as $d\Gamma/dt$ tends to zero. What actually happens during the time interval around the vanishing of $d\Gamma/dt$ is not very well understood. Perhaps the most reliable approach is to require condition (i), namely zero loading across the trailing edge. Basu and Hancock present some very encouraging numerical results using this particular condition. The aims of the present work are to (i) experimentally study the flow field

in the neighborhood of a trailing edge for a range of frequencies extending well into the unsteady regime, (ii) examine whether the quasi-steady or a truly unsteady Kutta condition is valid. To the knowledge of the author this has not been attempted so far. Moreover, a numerical method based on discrete-vortex dynamics is presented as an example of how a numerical solution can be obtained based on the proposed criterion. Indeed, the experimental data provide support for the Giesing-Maskell model as well as the details of how the flow changes from the $d\Gamma/dt > 0$ to the $d\Gamma/dt < 0$ trailing edge flow pattern.

The experiments were conducted in a water tunnel. Laser Doppler Velocimetry was used to obtain the measurements which were stored on a laboratory computer. Measurements were obtained around the trailing edge of a pitching airfoil as well as around the edge of a fixed airfoil encountering a street of vortices. The details of all of the laboratory equipment including those of the water tunnel are described in Chapter Two. In Chapter Three the experimental results of the flow in the aft regions of both trailing edges, the wake effects, vortex and boundary layer measurements over the fixed airfoil and flow visualizations are presented. The theory behind the analytical scheme is presented in Chapter Four and the numerical results along with comparisons with the experiments are given in Chapter Five. The conclusions and recommendations are presented in Chapter Six. The beginning of each chapter includes a discussion of similar work performed in the past along with comparisons of the results of the present work with earlier findings.

CHAPTER TWO

FACILITIES AND EQUIPMENT

2.1 Introduction

Experiments were conducted in the VPI and SU closed circuit water tunnel (See Fig. 2.1). For unsteady flows, tests in water offer significant advantages over tests in air. Realistic Reynolds numbers can be achieved in water with speeds and frequencies of unsteadiness 15 times smaller than corresponding speeds in wind tunnels. Laser-Doppler velocimetry is much more convenient in water, since it generates a continuous signal. Moreover, methods involving flow visualization are much more effective in water than in air.

The water tunnel was constructed in 1976 by the Engineering Science and Mechanics Department at VPI and SU with the support of the Army Research Office. The basic design is described by Koromilas (1978) and Mezaris (1979). Since the construction of the tunnel several modifications were made. The modifications involved the installation of a by-pass system, side-walls and flaps mounted in the test section. Screens and honeycombs were added to improve the quality of the flow.

The data obtained in the earlier stages of the present work involved the use of a DISA two-channel LDV system in the forward-scatter mode. Due to the complexity of the work as the research progressed, it was necessary to purchase a single channel TSI optical system and counter. The purchase of this type of equipment also required updating

the data acquisition system. The LDV and data acquisition systems are described in more detail in sections 2.5 and 2.6 respectively.

Previous work in the VPI and SU water tunnel involved unsteady flow fields generated by the dynamic control of a flapping or rotating mechanism in a steady stream environment (Koromilas and Telionis, 1980; Mezaris and Telionis, 1980; Jones, Barbi and Telionis, 1981; Kim, 1985 and Mathioulakis, 1985). In some situations the flapping mechanism was the model and other cases involved a flap or rotating vane mounted near the model, or at another location in the tunnel. The work described here required a periodic wake generated by the model.

2.2 Water Tunnel

The 570 gallon water tunnel is constructed of poly-vinyl chloride (PVC) and plexiglass. Plexiglass was used primarily to allow flow visualization in the test section and other areas along the lower half of the tunnel.

2.2.1 Water Tunnel Components

The components of the tunnel that contributed to the flow conditions in this work, are explained in the following three sub-sections: a) speed control, b) temperature control, c) the test section.

a. Speed Control

A variable speed electric DC motor connected to a centrifugal pump controls the free stream velocity in the range from 0 to 5 m/s. A

variable-flow control by-pass section, consisting of PVC material, was installed recently downstream of the test section to reduce the speed of the flow. It was observed that for tests at very low speeds (10 cm/s) the belt turning the pump would slip around the shaft of the DC motor causing the free stream velocity to fluctuate. It was then considered to install a by-pass system as a way of achieving low speed flow without belt slippage. Thus, for this work, low speeds have been successfully maintained for by-pass butterfly valve openings not greater than two full turns. Valve openings beyond this results in a higher turbulence level than normally desired. Further information on the turbulence level can be found in section 2.2.2.

b. Temperature Control

A temperature control unit is employed as a source for maintaining essentially a constant viscosity in the flow field. The temperature of the water can be kept fairly constant, to within ±0.5°C. The heating system has the ability to increase the water temperature at the rate of about 3°C per hour.

c. The Test Section

The two-dimensional 6:1 contraction at the end of the settling chamber carries the flow through the 25 cm x 30 cm test section. The total length of the test section is 183 cm with two sections on both ends consisting of 61 cm and 91.5 cm, thus having three interchangeable sections.

To eliminate the end effects in the work described here, a special test section was designed and constructed (See Fig. 2.2.1). The main

idea was to provide a set of false inner side walls and allow the wall boundary layers to be directed behind the false walls. A set of flaps were mounted at the trailing edges of the walls to control the amount of flow through the narrow passages and avoid separation at the leading edges. An alternate method consists of a suction system which was designed and constructed. However, only the first method was tested. Mean boundary-layer velocity and RMS of fluctuation profiles were measured on the inside of both false walls at several flap positions. These profiles are shown in Fig. 2.2.2 and Fig. 2.2.3 respectively. The flow rate through the narrow passage is zero when the flaps are fully closed. The side wall boundary-layer and the percent level of turbulence increase with the flap in this position. It was therefore advantageous to keep the flaps at an angle greater than zero degrees. Further testing was obtained as a means of determining the optimum flap angle on the side-walls. Results indicated that the boundary-layer was minimum when the flap was positioned at 10 degrees (Kim, 1985). Thus, the corresponding thickness of the boundary-layer was 4% of the airfoil span.

2.2.2 Turbulence Level and Calibration

Earlier tunnel calibration (Koromilas, 1978 and Mezaris, 1979) indicated that the free-stream turbulence level ranged from 0.5% to 1% (in some cases greater than 1%). This work employed the use of two honeycomb sections (aluminum hexagonal with 3 cm^2 area of each element) located in the settling chamber. Later work (Jones, 1980) indicated

that this range of turbulence in the free-stream was undesirable. It was determined that the turbulence level was well on the order of 1% and in some cases larger. As a method to further reduce the turbulence level from 1%, a small honeycomb section (1/4" cell size, 2" length) was installed at the end of the converging section. Thus, the turbulence level was reduced to 0.5% but changed with the speed of the tunnel to 0.8%.

Favorable turbulence levels (at or less than 0.5%) were achieved several years later (Mathioulakis, 1985) with the addition of standard mesh window screens. The screens essentially reduced the axial turbulent eddies (Scheiman and Brooks, 1980). Three of these screens were located downstream of the honeycombs. One was attached exactly behind the last honeycomb and the other two were positioned at 5 and 20 inches further downstream in the settling chamber. With respect to the screen diameter, vortex shedding will occur through the screen at a critical Reynolds number of 50 ($R_d = U_\infty d/\nu$). Thus, the screen diameter, d, was chosen so that R_d would be greater than 50 (Tan-Atichat et al. 1982). It was necessary to remove the screens when using pliolite particles for flow visualization. This enabled the particles to pass through the test section without blockage.

Another improvement in decreasing the free-stream turbulence level resulted in accurately positioning guide vanes in the diffuser section of the tunnel (Mathioulakis, 1985). This work involved observing the flow pattern of the water after it turned the 90° bend and prior to entering the settling chamber. Dyes and pliolite particles were used in

order to position the guide vanes so the water would flow into the settling chamber uniformly. Further details of the calibration of the water tunnel can be found in Telionis, Mathioulakis, Kim and Jones (1984).

2.3 Models

Two symmetrical airfoils with a 4" chord (101.6 mm) and 8" span (203.2 mm) were mounted in the test section as shown in Fig. 2.3.1. These models were cast from 5309-MOS fiber resin with a stainless steel spar passing through the quarter-chord axis. The profile of these airfoils was that of a NACA 0012. The airfoils were designed and constructed at Ames Research Center and Aeromechanics Laboratory, U.S. Army Aviation R & D Command. The NACA 0012 was chosen since the guidelines of the research were to simulate the wake generated by a helicopter rotor blade during the pitching mode. The 0012 is basically the general type of airfoil used for the rotor blade on a helicopter. The criteria under which these models were designed and constructed is described in detail by McAlister and Carr (1978).

Both airfoils were instrumented and constructed for two types of flow visualization; hydrogen bubbles and dyes. The first type was tested and proved to generate very weak hydrogen bubbles and was never used. The second employed two different color dyes which were injected in the spar independently and fed through two chordwise channels, being dispersed into the free stream at mid span and 80% chord on the top and

bottom of the airfoil. Further detail on the flow visualization will be discussed in the next section.

The airfoils were mounted in the test section between the side or "false" walls as shown in Fig. 2.2.1. The fixed airfoil was mounted 2 chord lengths downstream of the pitching airfoil. The pitching airfoil was used primarily to generate a disturbance field for the downstream fixed airfoil. A small rectangular fin was attached at the left end (See Fig. 2.3.2) of both airfoils which became an attachment point for an aluminum sleeve that held the airfoil in place while inside the test section. The 1/4" diameter spar protruded through the other end (right end) that was basically a pin support in the false wall. The aluminum supports were designed so the sleeve would fit inside the test section (when fastened to the airfoil) while a threaded extension (rod) fit through the outside wall. This threaded rod enabled, in one case, angle of attack adjustments for the fixed airfoil, and in the second case, facilitated continuous motion (at the quarter chord) for the upstream pitching airfoil.

The motion of the pitching airfoil was generated by a four-bar-linkage system (See Fig. 2.3.3) operated by a 3/4 hp Morse DC electric motor. The four-bar-linkage system was used primarily to eliminate vibrations in the flow during oscillation. The shaft of the DC motor was connected to a gear box with a 16:1 gear ratio. The output speed of the shaft on the gear box was one sixteenth of that of the motor. A 6" diameter aluminum flywheel-disk was attached to the output shaft of the gear box upon which the push rod of the four-bar-linkage system was

connected (See Fig. 2.3.3). The push rod was connected in a manner such that the amplitude of the pitching airfoil was 10° positive and 10° negative. This amplitude could be changed by positioning the push rod at various radial distances from the center of the flywheel. The frequency of oscillation was controlled by an electronic feed-back system to within 1% of the set value. A frequency counter was connected to the feed-back system for close monitoring of the frequency of oscillation. A Datel electronic shaft encoder, attached to the shaft of the DC motor provided pulses (600/rev) that were fed through the feed-back system to the frequency counter. A photo diode (optical transducer) was positioned on the flywheel as a means of triggering a pulse to the data acquisition system.

2.4 Flow Visualization

The flow visualization was made using two methods which enabled particle path lines and streaklines to be observed. The former method employed the use of PLIOLITE particles while the latter consisted of two different color dyes. The technique involving the use of PLIOLITE particles was developed in the laboratory by Koromilas and Telionis (1980).

2.4.1 Particles and Dyes

PLIOLITE particles with diameter of 0.2 to 0.8 mm are neutrally buoyant in water (ρ = 1.02 gm/cm^3). The particle paths nearly aligned themselves with the direction of the instantaneous velocity vectors.

The dyes were obtained from the Environmental Engineering Department at VPI and SU. The two colors consisted of #14352 Rhodamine B (red) and M-291 Methylene (blue). These two chemicals were chosen primarily because of the color intensity they possessed in water. The red color dye fluoresced under a high intensity source of light. In the early stages of the visualizations, it was necessary for at least one of the dyes to fluoresce when black and white-particle/dye visualizations were made in the wake of the pitching airfoil. The blue color dye did not fluoresce and it was later determined that the fluorescing capability was not indispensable when color-particle/dye visualizations were made.

2.4.2 Photographic Techniques

To record the history of the particle paths in the unsteady wake a NIKON 35 mm camera was used with a time exposure on the order of one fifteenth of a second. In order to illuminate the particles in the test section, two tungsten-halogen 1000 watt high pressure lamps were used. With one lamp positioned on top of the test section and one on the bottom, two sheets of light were directed in the test area using a thin slot 10 mm in width. This provided enough light to illuminate the particles passing over the airfoils. This method of recording the history of the particle paths in the wake of the pitching airfoil, as well as obtaining the pattern of particle paths over the fixed airfoil, was performed with the camera mounted on a tripod near the test section (i.e., in a fixed frame of reference). Pictures in this configuration were taken with both color and black and white film.

To record the flow with respect to a frame of reference attached on the model, the camera was mounted on one bar of the four-bar linkage. The field of view of the trailing edge was enlarged. Attention was focused on the last 30% of airfoil chord. The detail of such a view was obtained by the use of a NIKON f-3.5 macro (close-up) lens. In order to record the position of the trailing edge during the pitching motion, a marker was attached to the test section. The marker appeared in the field of view by the use of a mirror mounted on the camera (See Fig. 2.4.1). The trailing edge positions of the pitching airfoil were calibrated with an arrow attached to the camera that was also in the same field of view as the marker. This arrow would then point to a trailing edge position (angle of attack) on the marker during motion. The mirror was used because of the depth of field problems.

Many exposure/contrast related problems were encountered using this moving frame technique. In this configuration, to obtain the correct contrast and detail necessary to provide a clear recording of the particle paths, KODAK-#2475 High Speed Recording film (black and white) and KODAK-Kodachrome ASA 1600 (color) film were used. The 1600 color slide film could be processed either at 800 or 1600 ASA. This was the so-called "push processing" film. The 1600 level of sensitivity was chosen mainly to improve the depth of field at the trailing edge. The aperture setting must be increased (in this case) in order to improve the depth of field. Therefore, it was necessary to go to a higher film sensitivity level. The black and white moving-frame pictures were taken with a shutter speed of one fifteenth of a second and f-3.5 aperture

setting. The color pictures (slides) were taken with corresponding settings of one-sixtieth of a second and f-3.5. Color slides were taken mainly to see the interaction of the two-color dyes and particle paths. The interest was to see how the particle paths would compare with the streakline (i.e., vortex roll-up) generated by the dyes.

The same technique, superimposing both particle paths and streaklines, was performed in the fixed frame mode primarily to view the interaction of the particles and dyes in the wake of the pitching airfoil and fixed airfoil as well. These pictures were taken using the same camera, lens and ASA (push processing) 1600 slide film, with a shutter speed of one-thirtieth of a second and f-3.5. Black and white (ASA 400) film was used to record the array of the particle paths at the trailing edge of the fixed airfoil. These pictures were taken with camera settings of one-fifteenth of a second and f-3.5. The depth of field and contrast were not critical in this case, therefore the ASA 400 film was chosen over the ASA 1000 (#2475) film. As in the case of the pitching airfoil, an electronic digital clock was in the field of view with the use of a mirror mounted on the camera (See Fig. 2.4.2). The clock was then mounted at the same focal point as that of the trailing edge of the fixed airfoil. The clock was electronically designed to reset itself to zero when triggered at the end of one period of oscillation. This gave an indication of the position (phase) of the approaching vortices. The pictures taken over the fixed airfoil were obtained primarily to make comparisons with the numerical scheme, which will be discussed in later chapters.

A NIKON motor drive attached to the camera, capable of indexing 4.5 frames/sec, was used in situations when it was necessary to view (in time) the periodicity of the wake at and behind the trailing edge of the pitching and fixed airfoils. These cases utilized a shutter speed of one-sixtieth of a second for both particles and dyes and one-five hundredth or one-one thousandth of a second for dyes.

2.5 Laser-Doppler Velocimetry

All of the velocity data obtained in the VPI and SU water tunnel required the use of very sophisticated, high response flow-measuring equipment. Laser-Doppler velocimetry (LDV), or otherwise referred to as Laser-Doppler anemometry (LDA), was the type of flow-measuring equipment used for this research. The Laser-Doppler velocimeter measures the velocity of particles in a moving fluid environment based on the Doppler shifted frequency of scattered light. The scattered light pattern is obtained by neutrally buoyant particles moving in a fluid flow crossing a set of equally spaced, parallel, dark and bright regions of laser light. This pattern of light, or more commonly referred to as a fringe pattern, is established by projecting two equally spaced beams through a lens. The space where the beams interact is referred to as the measuring volume or control volume (See Fig. 2.5.1). This control volume (ellipsoid) establishes the fringe pattern necessary for flow measurement. The scattered light is received by a photodetector which is then converted to an electric current. The frequency of this

electric current is the Doppler frequency which is directly proportional to the particle velocity.

The laser system has many advantages over other flow measuring instruments. These advantages are briefly described as follows:

a) Placing probe-type instruments in the fluid distorts the flow and in some cases may cause a local disturbance. This is particularly important for measurements involving flow reversals. The Laser-Doppler velocimeter projects light beams in the flow that can be positioned anywhere.

b) There is no calibration required. The frequency output of the photodetector is linearly proportional to the particle velocity in the flow.

c) With the addition of frequency shifting, flow reversals can be detected.

d) The small control volume and high frequency response enable detailed flow measurements to be accurately obtained while maintaining a high signal-to-noise ratio.

e) Temperature changes in the fluid are usually problems encountered with hot-wire probes. The laser beams are not sensitive to changes in the fluid temperature.

The laser and optics of an LDV system can be arranged using either a forward-scatter or back-scatter mode. The forward-scatter is the mode in which the receiving optics are placed ahead or in front of the path of laser light through which the beams are directed. The advantage is in receiving the signal with low power levels. The disadvantage is in

traversing the control volume. The receiving optics are positioned in a manner that makes traversing somewhat difficult. The back-scatter is the mode in which the receiving optics are placed behind the path of laser light in which the beams are directed. The advantage is in the ability to traverse, since the receiving optics are mounted on the same platform (or base) as the laser and optics system and on the same side of the tunnel. The disadvantage is in the power requirements. The system requires a high power setting to achieve an acceptable signal. In some cases this is difficult to accomplish. The quality of the signal will be discussed in sections 2.5.1 and 2.5.2. As mentioned earlier, this research employed the use of DISA and TSI optical systems. The two systems utilized a 5 (DISA) and 15 (TSI) mw He-Ne laser respectively, both having a wavelength of 632.8 nm. The components of the two optical systems are described in sections 2.5.1 and 2.5.2. Both systems are comprised of two parts, a) sending optics, and b) receiving optics. The last section (2.5.3) discusses the traversing capabilities of both systems.

2.5.1 Optical Components - DISA System

In a forward-scatter mode the arrangement of the DISA system is shown in figure 2.5.2.

a) Sending Optics

The beam is directed through a DISA 55L01 beam splitter and is split into two beams, each having an equal intensity level. The two beams pass through a 150 mm focal length lens which forms the control

volume. The product of the fringe spacing d_f and the Doppler frequency f_D are related to the particle velocity via

$$U = f_D d_f \tag{2.5.1}$$

with

$$d_f = \frac{\lambda}{2\sin\theta} \tag{2.5.2}$$

where λ is the wavelength of the laser light and θ is the half angle of the beam intersection (Brayton, et al., 1973). From the laws of refraction, d_f remains the same through any medium but λ may change from one medium to another. A good signal, obtained by the receiving optics, requires a large number of particles in the measuring volume with basically the same velocity as that of the fluid. Thus, the particle needs to be small enough to move with the fluid yet large enough to scatter light within the control volume. The particles (seeding) used to accomplish this consisted of a polymer with a diameter between 1 to 2 microns. The polymer, #XP-143, was made by POLYMERICS INC. It should be pointed out, that in the forward-scatter mode, particles naturally found in water provide adequate distribution in the C.V. necessary to achieve a reasonable signal. However, seeding the fluid provides a signal of higher quality (i.e., higher data rate).

b. Receiving Optics

The light scattered by the particles in the control volume was received by the DISA 55L10 photomultiplier. The photomultiplier converts the scattered light signals into electrical signals that were sent to the DISA 55L20 signal processor. More information on the signal processor will be discussed in section 2.6. In the forward-scatter mode the photomultiplier is positioned along the same horizontal axis as the sending optics (See Fig. 2.5.2).

2.5.2 Optical Components - TSI System

In a backward-scatter mode the arrangement of the TSI system is shown in Fig. 2.5.3.

a. Sending Optics

The laser beam is split through the equal intensity beam splitter (TSI 9115-2). One of the beams, reflected by the beam splitter (TSI 9115-2) is directed through a polarization rotator (TSI 9103-2) which changes its polarity by 45°. The beams are now of equal polarity. The beam passing through the polarization rotator (TSI 9103-2) goes through the 40 MHZ frequency shifter known as the bragg-cell (TSI 9182-2). Shifting the frequency of one of the beams shifts the zero velocity indication and enables the system to determine positive or negative quantities in the flow field. Reducing the size of the control volume results in an increase of the signal to noise ratio. This is done by passing both beams through the beam displacing module (TSI 9114-22) and on through the beam expander (TSI 9188). This reduces the control

volume by a factor of 2. The diameter of each beam is enlarged inside the beam expander, but decreases once the beams are passed through the achromatic 250 mm focal length lens (TSI 9118).

The calculations for the control volume are given in the TSI manual (pg. 77). The diameter of the ellipsoid d_m and the length of the control volume l_m are expressed as

$$d_m = \frac{4\lambda f}{\pi D E} \text{ and } l_m = \frac{d_m}{\tan k} \qquad (2.5.3)$$

where k is the half angle of the intersection of the two beams, λ is the wavelength of the laser light, f is the focal length of the lens, D the diameter of the laser beam and E the expansion ratio of the beam expander. Each of these values that were used for this research were also used in the work by Kim (1985) and Mathioulakis (1985). The calculations result in the following dimensions for the control volume,

$$d_m = 0.088 \text{ mm}$$

$$l_m = 1.24 \text{ mm}$$

With respect to these variables, and via Eq. (2.5.2) the fringe spacing, d_f, is found to be

$$d_f = 4.47 \ \mu\text{m}$$

As mentioned previously, the light is scattered in the control volume by the particles in the flow. This light is scattered in all directions according to the Mie diagram and its power fluctuates with the Doppler Frequency which is given by Eq. (2.5.1).

The quality of the electronic signal (data rate) of the local velocity depends mainly on the distribution of particles in the flow.

As mentioned earlier, this is critical in the backscatter mode. Care must be taken to insure that all lenses and transmitting surfaces are kept clean. In this work the correct particle distribution (seeding) was achieved by using Silicon-Carbide seed with a particle diameter of 1.5 microns. With this and proper alignment of the laser system and optics, a signal of 250 to 500 bursts/sec was achieved with a noise level less than 50 mv.

b. Receiving Optics

The light scattered by the particles in the control volume is received by the receiving assembly (TSI 9162). As shown in Fig. 2.5.3, the receiving system is mounted in the back-scatter mode. The detected signal is sent to the TSI counter model 1990. Using two rotating mounts (TSI 9178-2 and TSI 9179) the entire optics train has the capability to rotate about an axis parallel to the beam axis. This feature of the system enables data to be obtained in the vicinity near a curved surface.

2.5.3 The Traversing Mechanisms

The mechanisms used to move the control volume from one point in the flow field to another are discussed in this section. The earlier stages of the work employed a scissors-jack that controlled the movement of the control volume in the vertical direction. This was used with the DISA optics system. In the later stages of the work, a traversing system with mirrors was designed, constructed and used with the TSI

system components. Both of these techniques for traversing will be described in two parts, a) DISA system and b) TSI system.

a. DISA System

The laser and optics system were mounted on a modified lathe mechanism that was attached to a movable cradle (See Fig. 2.5.2). The movable cradle, insulated from floor vibrations, supported the system and acted as a mobile unit during assembly and disassembly of the components of the flow measuring equipment. The detail and description of this system can be found in Mezaris (1979) and Jones (1980). Traversing with the scissors-jack was a crude approach, but facilitated movement in the vertical direction to within 1 mm accuracy. This accuracy was obtained manually with the use of an alignment card attached to the test section and calibrated prior to obtaining data. This card was used primarily as a reference marker when traversing to a new measuring point.

b. TSI System

As in part (a), the optical table (bench) containing the entire laser and optics train was also attached to the cradle. The scissors-jack was used for large movements in the vertical direction and smaller more exact vertical movements were obtained with a high-precision lead screw and mirrors (See Fig. 2.5.4). Vertical displacements of the measuring volume were obtained with the use of a sliding mechanism attached to the optical bench (See Fig. 2.5.4). Details of the mirror tower are shown in Fig. 2.5.5. The details involved in adjusting the mirrors to maintain proper beam alignment during vertical movement is

described in Mathioulakis (1985). Horizontal displacements were achieved by allowing the entire train of optics to slide on a linear high-precision table, controlled again by a lead screw.

The vertical, forward and aft movements were controlled by two SLO-SYN stepping motors that were interphased with the MINC-11 minicomputer. The rotation of the lead screws connected to the stepping motors was controlled by pulses sent from the "digital-out" module of the MINC. Each pulse or step corresponds to 1.8 degrees of rotation. In this way the accuracy obtained moving the control volume to any position in the flow field was to within 0.1 mm.

A technique developed by Koromilas and Telionis (1980), enables velocity measurements very close to a surface to be accurately obtained. This involves giving an inclination to the optical bench (See Fig. 2.5.2) such that the beams are directed into the test section at a small angle, with respect to the surface on which measurements are obtained. The angle of inclination is about 3 degrees.

2.6 Data Acquisition

The data obtained in the earlier stages of the work employed the use of a DISA 55L series tracker and a TSI 1990 counter. As mentioned earlier these two signal processors receive the output signal from the photomultiplier. The tracker calculates the Doppler frequency f_D and displays this indication on the DISA 55L40 meter unit. The calculation is made by measuring the fundamental component of a rectangular waveform. The counter measures the instantaneous velocity of each

particle passing through the control volume. This is performed by measuring the time for a predetermined number of Doppler cycles generated from the signal. Therefore by knowing the fringe spacing and the number of cycles, the velocity can be determined.

Both processors filtered as much noise as possible from the signal of the photomultiplier using high-and low-pass filters (i.e., a band-pass filter). The signal was then converted to a square wave by a Schmitt trigger. The Schmitt trigger converts the analog signal into a train of digital pulses. As previously mentioned, the noise level for the counter was about 50 mv and the level of noise for the tracker was adjustable. In most applications the counter was more advantageous than the tracker. The advantages are described as follows:

a) The ratio of the bandwidth frequency around which the Doppler frequency changed with the flow speed was much higher for the counter than the tracker.

b) Movement of the control volume did not require readjustment with the counter, as required for the tracker.

c) The tracker would not operate with high amplitude and high frequency response levels.

The main advantage of the tracker over the counter was its ability to operate at a lower signal quality than the counter.

The signal output from the counter or tracker was sent to a two-channel HP-5420A digital spectrum analyzer (FFT). The HP-5420A would ensemble average the data in the time domain (or frequency domain) given any number of specified averages. This would essentially smooth

any bad data, therefore giving an acceptable velocity waveform. The addition of the TSI optics system, with the same 1990 counter and 15 mw laser, proved to generate accurate data at a faster rate. Since the system was coupled with Bragg cells, flow reversals were indicated on the velocity waveform. Extensive data was obtained using the HP-5420A with the TSI system for most of the experimental work. The later stages of the experimental work employed the use of a MINC-11 minicomputer with a DEC VT-105 terminal and keyboard. This computer was interphased directly with the LDV counter. The computer controlled the shape and size of the contours traversed by the measuring volume. It also ensemble averaged the data and stored the complete velocity waveform. Due to the storage capacity of the computer, only a predetermined number of data points were selected from the waveform and then stored in the minicomputer. The Fortran program used to control the minicomputer is shown in Appendix I.

The majority of the basic program was written and tested by Mathioulakis (1985). Versions of this program were also used by Kim (1985). The program in Appendix I was modified for the present work, to perform traversing paths so that contour integrations of the velocity waveform could be performed. These paths were generated by a sub-program that controlled the stepping motors. This sub-program is also shown in Appendix I.

CHAPTER THREE

EXPERIMENTAL WORK

3.1 Introduction

In this chapter the experimental investigation of an unsteady periodic flow over a sharp trailing edge is discussed. Emphasis is placed at the flow field in the immediate vicinity aft of the trailing edge of a pitching and fixed airfoil. The effects of the flow field there were examined at very high frequencies of oscillation. In order to completely understand the periodicity of the flow, velocity data was obtained in the wake behind the pitching airfoil. This helped to describe the interaction of the unsteady flow field over the fixed airfoil.

Data in the potential region was obtained at four chordwise locations over the fixed airfoil, primarily to see what effect the unsteady pattern had on this region close to the surface of the airfoil. Velocity data was also obtained over the fixed airfoil to determine the position of the vortices as they were convected downstream. Results were obtained near the trailing edge of the fixed airfoil to study the streamline pattern of the flow in that region. Knowing the position of the vortices over the fixed airfoil enabled the pattern of streamlines to be analyzed. Flow visualizations were obtained at all locations mentioned, primarily to understand and verify the general patterns synthesized by the local velocity measurements. The following

subsection is a literature review of experimental work performed in the past which is similar to the work reported in this chapter.

3.1.1 Review of Previous Experimental Research

Experimental work on unsteady airfoils has been reviewed carefully by McCroskey (1976) and (1982). He maintains for the trailing-edge and wake effects that, in the unsteady case, the flow at the trailing-edge "is poorly understood, both physically and mathematically".

The usual assumption made in inviscid analyses is that the change in pressure above and below the trailing edge and the wake must be zero. Thus, a finite pressure change is unacceptable. From the theory set forth by Giesing (1969) and Maskell (1971), as discussed by Basu and Hancock (1978), the streamlines next to the airfoil leave the trailing edge tangentially either to the upper, or lower surface, depending on the sign of $d\Gamma/dt$, where Γ is the bound circulation. Moreover, the shed vorticity is postulated to stay, initially at least, along the stagnation streamline. However, flow visualizations at the trailing edge indicate that the flow rolls into a series of vortices, in the form similar to a von Karman vortex street. With this in mind, McCroskey then indicates that experimental evidence shows that there could be a finite pressure loading and under certain conditions a streamline curvature can exist as well. The flow visualizations described in the present work agree with this concept of streamline curvature only for higher values of the reduced frequency parameter ($k > 2.4$). The

agreement is based primarily on the theory set forth by Giesing (1969) and Maskell (1971).

The specific question of whether the classical Kutta condition is actually violated in unsteady flows has been addressed by a number of experimentalists. Archibald (1975) discusses the unsteady Kutta condition on the basis of experimental pressure measurements at the trailing edge of a long flat plate and a 10C4 airfoil. It is determined that "the most severe violation of the unsteady Kutta condition is the case of acoustically correlated vortex shedding". Thus, the vortex shedding frequency "locks" with the acoustic frequency, with the shedding being distributed over the span. This results in a violation of the Kutta condition in the spanwise direction and the pressure loading at the trailing edge is twice the pressure on one side. In the same work he reported that the Kutta condition is violated for reduced frequencies of $k > 5.0$.

Satyanarayana and Davis (1978) obtained experimental pressure data over a pitching NACA 64A010 airfoil. Their findings indicated that at lower values of the reduced frequency ($k < 0.1$) the pressure difference approaches zero at the trailing edge. At higher reduced frequencies ($k > 5$) the pressure difference at the trailing edge was finite therefore violating the classical trailing edge condition of zero loading. In their theoretical analysis it was determined that the Kutta condition was valid for reduced frequencies of $k \leq 0.6$ in predicting the loading in the trailing edge region. At reduced frequencies of $k > 0.8$ the

results "underestimate" the loading near the trailing edge, and the "deviations" increase with the reduced frequency.

Fujita and Kovasznay (1974) discuss experimental results on the response of a fixed airfoil to the wake of a series of rotating rods positioned upstream. They measured the chordwise pressure distribution at four angles of attack and found that the response was in agreement with linear theory over 90% of the chord and the last 10% did not compare. They found poor agreement with the theoretical data due to the loading at the trailing edge.

Commerford and Carta (1974) measured unsteady pressure distributions at a high reduced frequency ($k = 3.9$). The experimental configuration involved a cylinder mounted upstream of a circular arc airfoil. The airfoil was instrumented to obtain fluctuations in pressure. They report that the unsteady pressure distributions tend to zero at the trailing edge, therefore satisfying the Kutta condition. The last chordwise pressure measurement was taken at 90% chord resulting in "good agreement". However, Satyanarayana and Davis (1978) indicate that the "good agreement" at 90% chord probably occurred by "accident" since the agreement with theory in the leading-edge was not good. Also, the measured phase gave very poor results.

Osdiek (1975) experimentally obtained the pressure distribution over an airfoil in a cascade with a very low reduced frequency ($k = 0.08$). The results he obtained compared nicely with the predicted results in the leading edge region but did not compare with the region

at the trailing edge. The unsteadiness was generated by oscillating an inlet section at an angle of attack variation between 6 and 12 degrees.

The conditions at the trailing edge of an oscillating flat plate, for a non-separating laminar boundary layer, are presented by Brown and Daniels (1975). They used the triple-deck structure of Stewartson (1974) for trailing edge flows and scaled the reduced frequency and amplitude in terms of powers of the Reynolds number based on chord. Thus, the magnitudes for the reduced frequency and the amplitude are respectively, $Re^{1/4}$ and $Re^{-9/16}$. They divided the flow over the plate into five regions for which asymptotic analytic solutions were determined in four of the regions, while in the fifth a correlation to the circulation due to viscous effects was obtained via a linear solution. In the inviscid potential case, the potential flow over the airfoil employed an arbitrary constant which was a function of the Reynolds number, and they satisfied the condition of zero loading at the trailing edge in the limit as $Re \to \infty$.

The unsteady flow leaving a jet nozzle was studied by Bechert and Pfizenmaier (1975). The wave-like manner of a smoke filament moving with the flow issued from the edge of a jet was detected by a laser-optical system. Through LDV techniques the deflection of the jet boundary was then measured. Mean velocity and fluctuation measurements were obtained by the use of hot wires. Their results indicate that the jet deflection region has nearly a parabolic shape at the edge of the nozzle. They also report that the parabolic deflection region decreases with decreasing Strouhal number. The experimental results confirmed

that at low fluctuation amplitudes, the unsteady motion of the "flow problem" was linear. Thus, for the results presented, they found the Kutta condition was not valid.

DeRuyck and Hirsch (1982) measured the instantaneous velocity and turbulence profiles in the wake of a pitching NACA 0012 airfoil. The values of the reduced frequencies considered, ranged from 0 to 1.23. The results are compared with the steady state case. They used a rotating slanted x-wire to measure the instantaneous velocity profiles at several chordwise positions downstream of the trailing edge. Their results for the steady state case show a velocity discontinuity at 0.7% chord which gradually disappears downstream at 20% chord. This is primarily due to the interaction of the viscous shear layer into the flow aft of the trailing edge. Even at 0.7% chord, this indicates that the steady Kutta condition may be violated. For each of the values of the reduced frequencies tested, the results for the unsteady case (only two were reported; $k = 0.36, 1.01$) show that the path of a line extending through the minimum of the chordwise velocity profiles is essentially a streamline. The curvature of this streamline is more pronounced further downstream than close to the trailing edge. Near the trailing edge it appears that the path of the streamline is a bisector of the trailing edge wedge angle. As mentioned earlier, this violates the Giesing-Maskell criterion, i.e., that the streamline right at the trailing edge should be parallel either to the upper or lower surface of the trailing edge. The results for both of the reduced frequencies show

this trend. It seems then that only the quasi-steady condition is satisfied.

Covert, et al. (1983), measured the mean velocity fluctuation in the wake of a NACA 0012 airfoil. The unsteadiness was generated by a rotating elliptic cylinder near the trailing edge. The normal and tangential velocity components were ensemble averaged for reduced frequencies up to 6.4 based on semichord. Their results were based on the mean flow velocity rather than the instantaneous velocity fluctuation as described in the present work and by Ho and Chen (1981).

Kovasznay and Fujita (1972) measured the position of the stagnation streamline aft of the trailing edge of a flat plate placed in the wake of a jet perturbed by a rotating rod. With the use of hot-wire anemometry, both u and v velocity components were sampled at predetermined times at and behind the trailing edge of the flat plate. Similar to the methods employed in the present work, they integrated the u and v velocity components around a rectangular measuring grid until they obtained the position of the stagnation streamline. From inviscid potential flow theory they calculated the stagnation streamline assuming violation of the Kutta condition, in which case the rear stagnation point is not located at the trailing edge. In this case the rear stagnation streamline is positioned outside of the trailing edge bisector. Their results show that the position of the streamline along the centerline of the bisection obtained from velocity measurements does not coincide with the streamline obtained from the calculations. It is from this comparison that they conclude that the Kutta condition, "even

in rapidly changing flow", is still satisfied for reduced frequencies up to k = 4.9. However, it seems again that their results are valid only for the quasi-steady case.

From the study of airfoil cascades, Fleeter (1980) points out that the Kutta condition is valid only for the cases when the reduced frequency is small and only data from the low reduced frequency spectrum exists. At high reduced frequencies Fleeter investigated the validity of the Kutta condition for isolated airfoils and airfoil cascades at various incidence angles. He essentially measured the pressure distribution on the surface at the trailing edge region of a flat plate, a flat plate cascade and a cambered airfoil cascade. This data was then compared with a theoretical flat plate model at zero incidence that employs the Kutta condition as well. The results indicate that the Kutta condition was valid for the flat plate and flat plate cascade up to k = 10 but failed for the cambered airfoils in a cascade.

In all of these investigations it appears that there are a wide range of reduced frequencies considered. This makes very difficult the task of determining what range of reduced frequencies bring consistent conclusions to the material available. It has been considered in the present work that the effect of amplitude may take an important role in arriving at a consistent conclusion. Therefore, it is proposed here that the reduced frequency is not a good dynamic similarity parameter and a more proper criterion should include the amplitude of the oscillation. It is suggested that a good parameter could be the ratio of the maximum velocity of the trailing edge to the velocity of the free

stream. For a pitching oscillation this works out to be $\ell = \frac{r\omega\alpha_o}{2U_\infty}$ with r the distance from the pivot to the trailing edge, while for the plunging airfoil, this becomes $\ell = \frac{h_o\omega}{2U_\infty}$ where h_o is the linear amplitude of the oscillation. The range of the number ℓ for the present experimental work is 0.1047 to 0.5139 whereas for the experiments of Ho and Chen (1981) it is 0.01631 to 0.3201. The experiments of DeRuyck and Hirsch (1982) fall in the same range as Ho and Chen. A value of about ℓ = 0.1 appears then to be in both references a limit above which the quasi-steady criterion is not valid. The experiments of Satyanarayana and Davis (1978) result in values of ℓ below 0.015705, therefore all experiments were conducted well below the limit of the validity of the quasi-steady criterion (See Table 3.1). Those investigations for which the value of K was very large were those in which the data for the calculation of ℓ was not available or the generation of the unsteadiness in the flow was created by a mechanism other than a pitching or plunging motion.

The flow behind an airfoil in the plunging motion was studied visually for reduced frequencies (based on full chord) ranging from 1 to 19 by Ohashi and Ishikawa (1972). Their visualization technique, configured in the exit section of a low speed wind tunnel (1 to 6 m/sec), employed the Schlieren method. Comparisons were made with two NACA 65-010 airfoils with one being modified with an increased trailing edge radius. Their work is primarily based on two assumptions; 1) the wake is assumed to be a straight line extension of the bisector of the trailing edge wedge parallel to the uniform stream, 2) the Kutta

condition for the steady case holds at the trailing edge independently of the plunging frequency. Both of these assumptions are valid for the quasi-steady case. Thus their results indicate that at reduced frequencies up to 3 (based on full chord) the first assumption is valid. As the reduced frequency increases, the pattern of the wake conforms to the shape of a Karman vortex street, and their two assumptions are then violated. For all cases presented, their results also indicate that as the reduced frequency decreases, the normalized amplitude of the fluctuation increases. Another test to check the validity of the Kutta condition, in which ammonia gas was injected into the free stream at the trailing edge upper surface and reacted with a reagent on the lower side, indicated that the flow may be turning around behind the trailing edge leaving a thin viscous shear-layer region for the case of the blunt trailing edge. The results for this case compared with the same test performed on a sharp trailing edge wedge angle. Thus, they concluded that the thin viscous shear-layer formed behind the blunt trailing edge is basically a stagnation zone and is considered to be an "extended part of the real airfoil." Here again, as with the other cases discussed, their results hold at the lower reduced frequency satisfying only the quasi-steady case and both of their assumptions are valid. However, at the higher reduced frequencies ($K > 2$, based on semichord) both assumptions were violated.

With only a few exceptions, in most of the investigations it is the unsteady pressure distribution which is examined, a quantity which can offer little insight into the actual flow situation in the trailing edge

region. Moreover, and perhaps more importantly, in all of these investigations no alternative condition is suggested. Thus, it is the validity of the quasi-steady condition that is investigated over the wide range of the parameters involved. Ho and Chen (1981) point out that the range of the reduced frequencies for the validity of the steady Kutta condition is a function of the general configuration. However, situations arise in practical engineering problems where the flow clearly departs from the quasi-steady case. Examples of some of these type of flows are those in which blades or wings encounter gusts, or when turbomachinery blades are immersed in the wake of an upstream cascade.

As previously mentioned, an extension of the Kutta condition to unsteady flow was suggested by Giesing (1969) and Maskell (1971). The most severe criticism of this extension to the Kutta condition centers around the fact that this unsteady condition does not reduce to the classical steady condition. Basu and Hancock (1978) offer as a possible explanation the fact that in the "unsteady problem, the curvature of the streamline emanating from the trailing edge tends to infinity as $d\Gamma/dt \to 0$", where Γ is the bound circulation. The problem is not academic in nature, because such situations are encountered twice within a single period of a periodic disturbance. It is therefore not just a limiting process for a weak unsteadiness in question but a significant phase of a dynamic phenomenon, whereby the time rate of the bound circulation changes sign.

At this point no experimental efforts have been undertaken to provide evidence for the validity of the Giesing-Maskell criterion. This was therefore the motivation behind the present work. Indeed, the experimental results presented here for flows over the pitching and fixed airfoils support the Giesing-Maskell criterion.

Our experimental approach is similar to the one employed by Kovaznay and Fujita (1972) and Ho and Chen (1981). However, both groups of investigators confined their attention to a single point in the period. In the present work Laser-Doppler velocimetry was used to provide data for similar integration paths. Our results pertain to a large number of phase angles covering the entire period of the oscillation as well as streamlines above and below the airfoils. Also, the experimental results presented here pertain to a pitching airfoil in a steady stream and a fixed airfoil in an oscillating stream. Ho and Chen (1981) took data no closer than 5% chordlength downstream of the airfoil edge. Their results tend to agree with the quasi-steady case. They have expressed the opinion (Ho, 1982) that the stagnation streamline may be turning sharply in the immediate vicinity of the sharp edge. Only such a behavior would compromise the data they obtained with the location of the airfoil edge. This is in agreement with the curvature argument presented by Basu and Hancock (1978). To shed more light on the structure of the flow in this region, in the present work measurements were obtained closer than 1% of the chordlength to the trailing edge.

3.2 Experimental Approach

In this section the experimental arrangement and procedure is described. In the next section we give an overview of the measuring locations used to obtain the velocity data. The procedure describes the way in which the data was manipulated to obtain the final results.

3.2.1 Arrangement

The general measuring grid and layout of the experimental arrangement for both of the airfoils is shown in Fig. 3.2.1. The measuring grid was separated in 5 groups designated with Roman numerals. Groups I and II were employed for contour integrations and the determination of instantaneous streamlines in the neighborhood of the trailing edges of the pitching and fixed airfoils respectively. Groups III and IV were used to track the vortices upstream and over the fixed airfoil respectively and Group V was used to provide a crude picture of the mean and fluctuating velocity field in the wake of the pitching airfoil. Group IV also contains data obtained close to the surface of the airfoil (potential region) at a zero degree angle of attack (See Fig. 3.2.5). This data was obtained in the preliminary stages of the work. In the later stages the same group also contains detailed data obtained at a five degree angle of attack (See Fig. 3.2.8) in the boundary layer at 98% chord.

Groups I and II consist of rectangular and diamond-shape measuring contours respectively. The rectangular grid of Group I (See Fig. 3.2.2) required horizontal and vertical ensemble-averaged velocity

components to facilitate contour integrations. Contour integrations of the quantity

$$\psi = \int (udy - vdx) \tag{3.2.1}$$

were then obtained along the upper and lower paths of the measuring grid. In this way data were obtained for 3 azimuthal trailing edge positions. The horizontal velocity component was measured along the vertical sides and the vertical component was measured along the top and bottom sides of the rectangular contour respectively. It was thus possible to perform the integration by collecting all the velocities in space at a particular phase. For each edge position, a bank of conditionally averaged data were obtained instantaneously for points along the 4 vertical lines as shown in Fig. 3.2.2. As shown in the figure, the path of the trailing edge due to pitching oscillations about the quarter-chord indicates that contour integrations can be performed at the points indicated by the asterisks. Starting at any point, as for example point A in Fig. 3.2.3, contour integrations were performed around a portion of the measuring grid until the streamfunction, ψ, became zero

$$\psi = 0 = \int_{A}^{y_1} (udy - vdx) \tag{3.2.2}$$

It must be emphasized at this point that the contour integration of Eq. (3.2.1) was derived for a fixed frame of reference. A more

appropriate representation of this integration involves an additional component which was obtained from a moving frame of reference attached to the airfoil. The additional components involved in the moving reference frame is discussed in more detail in section 3.3.1.

The "portion" of the grid involves either the upper or the lower part of the measuring contour depending on whether the direction of integration is clockwise or counterclockwise. This technique of using a second path of integration was suggested by Ho and Chen (1981). With reference to Fig. 3.2.3, integrations around the grid in the counterclockwise direction (Path I) were performed using the following equation

$$\psi\ (C) = \int_A^B udy - \int_B^C vdx \tag{3.2.3}$$

where $\psi(C)$ is the value of the streamfunction at point C on the grid. The value of the position on the grid where the stream function is zero is obtained by solving the following equation for y_1

$$\psi\ (y_1) = 0 = \psi(C) + \int_C^{y_1} udy \tag{3.2.4}$$

Eq. (3.2.4) completes the integration around Path I for the location of the position of the streamline. Referring again to Fig. 3.2.3, the second integration of Path II (clockwise direction) obtained in the same manner as the integration around Path I, employed the equations

$$\psi(y_2) = 0 = \psi(E) + \int_E^{y_2} u\,dy \tag{3.2.5}$$

where

$$\psi(E) = \int_A^D u\,dy - \int_D^E v\,dx \tag{3.2.6}$$

From Eqs. (3.2.4) and (3.2.5), the values, y_1 and y_2 were then averaged to obtain the final position. In all cases the second integration of Eq. (3.2.5) was performed primarily to check the position where the streamfunction was again zero. Theoretically, the two points, y_1 and y_2 should coincide. Thus, the difference in the positions of the streamline for both paths resulted in a discrepancy of 10%. It is interesting, however, that this discrepancy was consistent for each of the cases considered. This could be attributed to the boundary layers which follow the airfoil in its motion as it cuts through the rectangular mesh. Moreover, the discrepancy can also be attributed to the difficulty in obtaining the vertical velocity component of the flow at the points on the horizontal ends of the rectangular grid. The difficulty is that the mean of the vertical velocity fluctuation is only a few percent of the horizontal-streamwise velocity component. Due to the nature of the fluctuation, the component of the vertical velocity produced a weak signal from the LDV system. Ho and Chen (1981) discuss the same problem with their system.

As the research progressed, the data obtained behind the trailing edge of the fixed airfoil employed a diamond shaped measuring grid (Group II) to obtain the direction of the streamlines aft of the

trailing edge. The diamond shape grid of Fig. 3.2.4 did not require both the horizontal and vertical velocity components in the integration to obtain the directions of the streamlines. The advantage of this geometry over the rectangular grid was in obtaining the velocity fluctuation. The direction of the required velocity was perpendicular to the sides of the grid, therefore not deviating much from the local direction of the free stream velocity. This eliminated the necessity to obtain a vertical velocity component. The integration of the velocity perpendicular to the measuring grid was obtained in the same way as in the case of Group I. The details of the integration of the streamlines for Group II are described in the following way.

As shown in Fig. 3.2.4 ensemble averaged velocity data was obtained for all grid points. The integration for the path of the streamlines originated at each of 13 grid points indicated by the asterisks resulting in a set of 13 streamlines for each position of the approaching vortex. As in the case of Group I, two paths of integration (counterclockwise and clockwise) were performed around the grid until the position of the zero streamfunction was obtained. Here again, similar to Group I, the difference in the positions of the streamline (around both paths of integration) was about 5%, thus half the discrepancy in Group I. The smaller discrepancy is attributed to the poor quality of the distribution of particles in the flow in the immediate region aft of the trailing edge. This resulted in a low data rate for laser probe volume positions in a radius extending from the trailing edge of 4c/100. The two positions, obtained from both paths of

integration, were then averaged, giving the coordinate point through which the streamline was directed from the initial grid point under consideration.

Some measurements (Group IV) were obtained in the potential region over the fixed airfoil at a zero degree angle of attack at four chordwise stations as shown in Fig. 3.2.5. The size of the control volume formed by the laser beams (0.5 mm x 35 μm) enabled as many as ten ensemble averaged velocity fluctuations at all four locations to be obtained with 6% chord above the surface of the airfoil. This data was obtained on a very coarse experimental rig prior to the implementation of stepping motors which provided much more accuracy in traversing and obtaining more measuring points in the boundary layer. Thus, traversing could be performed to within one-one-hundredth of a millimeter. However, with only a few points mentioned here, enough information was available to obtain a crude picture of the velocity profile and the amplitude of the velocity fluctuation within the potential region of the fixed airfoil. It must be emphasized that this data does not in any way completely describe the flow in the boundary layer due to the unsteadiness.

The detail of the measuring grid used to track the vortices in Groups III and IV is shown in Fig. 3.2.6. At all points shown, the horizontal u-component of the velocity was measured and conditionally averaged. The corresponding waveform of the velocity fluctuation presented the information necessary to determine the sense of the approaching vortex. For points positioned above the vortex street

(Group III) a maximum in the waveform indicates the instant that a vortex with positive vorticity is immediately below the point of measurement. Similarly, a minimum in the waveform indicates the instant that a vortex with negative vorticity is immediately below the point of measurement. The measurement of the time elapsed between two maxima in the waveform, at two different measuring points, gave the vortex drift velocity. For points spaced a distance x_0 apart, the vortex drift velocity is x_0/t_0. The period T is the time between two consecutive peaks in the time record obtained from a point in space. This together with the vortex drift velocity gives the vortex spacing, a, (See Fig. 3.2.7) namely the product x_0T/t.

The propagation of the oncoming vortices was measured from the data obtained at the grid points in Group IV. The change in phase of the velocity waveform encountered at each point corresponded to the time required for the vortex to drift from one point to the next. Thus, the peak to peak change in phase of two neighboring waveforms is the time delay between these two points which is the vortex drift time.

Since the later stages of the work employed the use of stepping motors, detailed data in the boundary layer near the trailing edge of the fixed airfoil was obtained. The measuring grid is shown in Fig. 3.2.8. The data was obtained at 98% chord. Within a distance of 4% chord, 15 grid points perpendicular to the surface of the airfoil were used above and below the trailing edge to measure the thickness of the viscous shear-layer. This data was obtained primarily to compare the shear-layer thickness at 98% chord with the viscous shear-layer

thickness in the region of 1% to 5% chord downstream of the trailing edge. The viscous shear-layer was approximated from the pattern of streamlines obtained experimentally aft of the trailing edge.

3.2.2 Procedure

The basic procedure in which the velocity data was obtained and manipulated is described by the flow chart in Fig. 3.2.9. It required several years to obtain the level of sophistication of the arrangement shown in this figure. The flowchart describes the entire process in which the data was converted to concrete results. In each case 50 to 70 conditional averages were obtained and stored either on tape (via the HP-5420A) or on a floppy disk (via the MINC-11). The data was then manipulated either by a hand calculator, for small calculations, or in most cases by the IBM 370 mainframe computer system. The later manipulations required transfer of data from the MINC-11 minicomputer to the IBM 370. The steps involved in this process are outlined in Appendix II. In most cases, once the data was transferred to the IBM 370, a Fortran program was written either to plot the velocity data or to perform the contour integrations in order to obtain the paths of the streamlines behind the fixed airfoil.

3.3 Results

This section discusses the detail of the experimental results obtained at the trailing edge and in the wake of the oscillating

airfoil. Also, the results of the data obtained over the fixed airfoil and its wake are presented.

3.3.1 Oscillating Airfoil

The condition of the flow, for which the data was obtained in Group I (See Fig. 3.2.1), was set at a free stream velocity of U_∞ = 20 cm/sec and an oscillating frequency of f = 1.5 Herz. The corresponding Reynolds number and reduced frequency were Re = $U_\infty c/\nu$ = 20,000 and k = $\pi fc/U_\infty$ = 2.4, respectively. The amplitude of the (peak to peak) oscillation was $\Delta\alpha$ = 20°. Along the 4 vertical lines of the rectangular grid, contour integrations were performed. Around the grid velocity data was obtained for 3 azimuthal edge positions, namely x_1 = 0, y_1 = 0, x_2 = 0, y_2 = 0.03c, x_3 = -0.01c, y_3 = 0.09c. These coordinates correspond to angles of attack of α_1 = 0.00°, α_2 = 2.25°, α_3 = 6.82° respectively. A trigger was supplied externally by the oscillating mechanism. When the airfoil passed through a 0° angle of attack during its downward motion, a 5 volt triggering pulse was sent to the minicomputer. For each point on the data mesh, about 2 periods of the conditionally-averaged response were obtained. The results obtained from the contour integrations are plotted in Figs. 3.3.1 a and b. These Figures show only one extension of the path of the streamline behind the trailing edge. Both are plotted with downstroke motions as indicated. In these cases, the streamline is the stagnation streamline since the integration originated at the trailing edge. In order to gain more confidence in these results, contour integrations were also performed

starting at points higher and lower than the instantaneous position of the edge. These configurations are shown in Figs. 3.3.2 and 3.3.3. The slopes of all of these streamlines are essentially equal. For a reduced frequency of 2.4, it therefore appears that the trailing edge streamline is approximately tangent to the wedge formed at the trailing edge, therefore in agreement with the Giesing-Maskell criterion.

The results presented thus far, are calculated in a frame of reference fixed to the airfoil. It is in this frame that the Giesing-Maskell model should be observed. The necessary correction to account for the rotating coordinates was calculated analytically. In addition to the terms in Eq. (3.2.1), terms involving $\int \omega r\cos\theta dx$ and $\int \omega r\sin\theta dy$, where ω, r and θ are the angular velocity, polar radius and polar angle respectively, were the terms used to account for the correction. This resulted in a very basic evaluation of the integrals, since $r\cos\theta$ and $r\sin\theta$ are respectively equal to x and y. Therefore, with the additions of these terms and reference to Fig. 3.3.4, the following contour integrations for path I were then evaluated using the following equation

$$\psi(\text{path I}) = \int_A^B u\,dy - \int_B^C v\,dx - \int_C^D u\,dy +$$

$$- \int_A^B \omega r \sin\theta\, dy + \int_B^C \omega r \cos\theta\, dx +$$

$$+ \int_C^D \omega r \sin\theta\, dy \qquad (3.3.1)$$

The contribution from the quantities $\omega r \sin\theta dy$ were very small ($0.002U_\infty c$) and were neglected, leaving only one additional term to the basic form of Eq. (3.2.1). Thus

$$\psi(\text{path I}) = \int_A^B u\,dy - \int_B^C v\,dx - \int_C^D u\,dy + \int_B^C \omega\, x\,dx \qquad (3.3.2)$$

The corresponding contour integrations for path II were evaluated with the following equation

$$\psi(\text{path II}) = -\int_A^E u\,dy + \int_E^F v\,dx + \int_F^G u\,dy + \int_E^F \omega\, x\,dx \qquad (3.3.3)$$

Thus, the quantities $\int \omega x dx$ in Eqs. (3.3.2) and (3.3.3) are the necessary terms needed for the evaluation of the integration when reference is made with respect to the moving frame.

3.3.2 Wake of the Oscillating Airfoil

The flow field behind the trailing edge of the oscillating airfoil was examined primarily for comparison with basic earlier investigations. Moreover, data was obtained in the downstream region in order to document the properties of the flow which the fixed airfoil encountered. The general configuration of the measuring grid used to obtain the data in group V is shown in Fig. 3.3.5. The variation of the mean velocity and the amplitude of the velocity fluctuation are plotted in Figs. 3.3.6

and 3.3.7 respectively. As expected, the momentum of the flow increases at the center line. Basically the amount of work input to the four-bar oscillating mechanism is transformed into the energy which increases the momentum of the flow. Averaged wave patterns of the velocity response are shown in Figs. 3.3.8 and 3.3.9 for two points, one away from the axis of the airfoil and one along the x-axis, respectively. At the point away from the axis the velocity oscillates with the frequency of oscillation, while on the axis, the velocity is affected strongly by the passage of the trailing edge and results in a frequency twice as large as the pitching frequency. It is interesting in this case, that at points near the axis, both frequencies can be observed as shown in Fig. 3.3.10.

3.3.3 Vortex Tracking

The position and the path of the vortices shed by the oscillating airfoil were obtained along several grid points as designated by groups III and IV. The dimensions that were used for both of the measuring grids are shown in Fig. 3.2.6. At all points the u-component of the velocity was measured and conditionally averaged. Velocity waveforms, similar to those described in section 3.3.2, were obtained in order to determine the point where the velocity was a maximum or minimum. As discussed in section 3.2.1, the maximum or minimum indicates the sense of rotation of the vortex for points positioned either above or below the vortex street. Extensive data, obtained in this region by Mathioulakis (1985), indicates that the flow pattern of the vortices

differs from that of the wake behind a bluff body. The difference is that the sense or rotation of the vortices is in the opposite direction (Katz and Weihs, 1981).

The horizontal and vertical dimensions of the vortex spacing, a and b respectively (See Fig. 3.2.7) and the circulation of the vortices Γ, were calculated using a closed form solution, Milne-Thomson (1960). It was assumed that the velocity field induced by the vortices was approximately equal to the field generated by an infinite array of vortices with the same spacing. Thus, the maximum and minimum velocities, u_{max} and u_{min}, were measured at a height of c/2 from the axis of the system of vortices. The three equations used to solve for a, b and Γ, knowing the period T, u_{max} and u_{min}, are expressed in the following manner

$$\frac{a}{T} = U_{\infty} + \frac{\Gamma}{2a} \coth \frac{\pi b}{a} \tag{3.3.4}$$

$$u_{max} = \frac{\Gamma}{2a} \left\{ \coth \frac{\pi}{2a} (c-b) + \tanh \frac{\pi}{2a} (c+b) \right\} \tag{3.3.5}$$

$$u_{min} = \frac{\Gamma}{2a} \left\{ \coth \frac{\pi}{2a} (c+b) + \tanh \frac{\pi}{2a} (c-b) \right\} \tag{3.3.6}$$

For the case presented in these results, the horizontal distance a was measured and the quantities Γ and b were then determined. The results of the calculations gave a = 0.95 c and Γ = 0.40 c U_∞. A more elaborate computation scheme and further detail in the evaluation of this solution can be found in Mathioulakis (1985).

The propagation of the oncoming vortices was measured from velocity waveforms obtained from the data of group IV. At each point the u-component of the velocity was measured and conditionally averaged. Examples of this type of waveform are shown in Figs. 3.3.11 and 3.3.12. In both cases more than 50 conditional averages of the velocity waveform were obtained. Each waveform corresponds to a position of the control-volume of the laser on which the measurement was made. Thus, the delay in time measured from two neighboring peaks corresponds to the time required for the vortex to drift from one point to the next. In this way the position of the approaching vortex (above the fixed airfoil) could be matched in phase with the instantaneous position of the trailing edge of the oscillating airfoil. This was a necessary measurement prior to the investigation of the flow in the region of the trailing edge of the fixed airfoil.

3.3.4 The Fixed Airfoil and Its Wake

Measurements at the trailing edge and in the wake of the fixed airfoil (Group II) were obtained at a velocity of U_∞ = 10 cm/sec and an oscillation frequency of f = 1.2 Herz. The flow speed and frequency of oscillation correspond to a Reynolds number and reduced frequency of Re

= 10,000 and k = 3.9 respectively. The measurements obtained in this group are shown in Figs. 3.3.13-20. In the same figure the relative position of the oncoming vortices, as determined by the tracking of vortices (as in section 3.3.3), are shown. In these figures, it appears that the streamline structure in the immediate region of the trailing edge deviates greatly from the preferred direction of the flow around it (the Giesing-Maskell criterion). The thickness of the boundary-layer was found to be on the average approximately 2c/100 (See section 3.3.5) and this region is totally immersed in the viscous shear layers. This is clearly a region of viscous-inviscid interaction. This reasoning is due to the fact that within a distance of 3c/100 to 5c/100 from the trailing edge, the pattern of the streamlines display very large curvatures. This implies that there exist strong cross-flow pressure gradients.

The degree of roundedness of the trailing edge of the fixed airfoil was measured and reported to be on the order of 0.45c/100. Other findings (Ohashi and Ishikawa, 1972) report that usually the standard sharp edge radius is on the order of 1/10 the size indicated above. Thus, the pressure variation across the free shear layer is not negligible.

The jump in pressure was estimated to be 10% of the mean pressure coefficient over the airfoil. The calculation of the pressure jump coefficient was performed with the use of the velocity data obtained in the viscous shear region of the measuring grid. For very small distances, the effect of viscosity may be neglected and therefore the

Euler equation can be employed. The process in which these calculations were made is described in the following manner. The average of the data from the velocity waveform, obtained from the points on the measuring grid representing the viscous shear layer (See Fig. 3.3.21), were used for the transverse component of the velocity in the Euler equation. Euler's r-component equation in curvilinear coordinates (Fox and McDonald 1973) is expressed as

$$-\frac{1}{\rho}\frac{\partial P}{\partial r} = \frac{\partial V_r}{\partial r} + V_r\frac{\partial V_r}{\partial r} + \frac{V_\theta}{r}\frac{\partial V_r}{\partial \theta} + V_z\frac{\partial V_r}{\partial z} - \frac{V_\theta^2}{r} \qquad (3.3.7)$$

where V_r and V_θ are the radial and transverse components, respectively. With the θ coordinate aligned with the streamlines, the quantity V_r and its derivatives are negligible and therefore Eq. (3.3.7) reduces to

$$-\frac{1}{\rho}\frac{\partial P}{\partial r} = -\frac{V_\theta^2}{r} \qquad (3.3.8)$$

or approximately

$$\frac{\Delta P}{\Delta r} = \rho\frac{V_\theta^2}{r} \qquad (3.3.9)$$

where r is the radius of curvature of the streamlines in the viscous shear layer as shown in Fig. 3.3.21. For each position in phase of the approaching vortex $\Delta\phi$, the velocity was averaged and the radius of curvature of the streamlines was measured. From Eq. (3.3.9) the quantity ΔP was the pressure jump at the edge of the viscous shear-layer

and the inviscid field. This quantity was nondimensionalized by the dynamic pressure resulting in the following pressure coefficient at the edge

$$C_{P_e} = \frac{\Delta P_e}{\frac{1}{2}\rho U_\infty^2} \tag{3.3.10}$$

Values for each position in phase $\Delta\phi$, were obtained from Eq. (3.3.10) and averaged. The mean pressure coefficient over the airfoil was obtained from Abbott and Doenhoff (1959) for a NACA 0012 at a 5° angle of attack and approximately the same Reynolds number.

In the framework of the theory of inner and outer expansions, the experimental results indicate that a jump in the pressure could be acceptable at the trailing edge only for the inviscid outer solution. Therefore the condition of zero-loading is inapplicable in high-frequency unsteady flows. With reference to Figs. 3.3.13-20, the streamlines in the viscous shear layer align themselves approximately with the inviscid flow at a radial distance of 3c/100 to 5c/100 from the trailing edge. This is a clear indication that the pressure discontinuity across the trailing edge vortex sheet is eliminated quickly. Outside of the viscous region the potential flow appears to follow approximately the Giesing-Maskell criterion. However in some cases, the flow appears to form angles of $\phi > \theta/2$, as shown in Fig. 1.1. The flow visualizations using the two-color dyes indicate that the continuous vortex sheets released from the trailing edge of the pitching airfoil have not rolled up into discrete vortices by the time they

approach the fixed airfoil. The results from the flow visualizations will be presented in section 3.4. The discrepancies that were indicated earlier, whereby ϕ appeared to be greater than $\theta/2$, may be caused by concentrated vorticity being directed over the airfoil and maybe interacting with the attached boundary layers. Detailed measurements in the boundary layer, presented in section 3.3.5, indicate that because of the disturbances noted above the boundary layers near the edge are most likely turbulent.

3.3.5 Potential Region and Boundary Layer Over the Fixed Airfoil

This section presents the results obtained from the measurements in the potential region and boundary layer over the fixed airfoil at low separate angles of attack, namely angles of 0° and 5° respectively. The results will be presented in two sub-sections: a) potential region, b) boundary layer region.

a) Potential Region

These results are the preliminary measurements obtained in the earlier stages of the work on a very coarse experimental rig as discussed in section 3.2.1. Mean velocity profiles for a reduced frequency of $k = .4.7$ are plotted at chordwise stations of 0.1c, 0.4c, 0.6c and 0.9c in Figs. 3.3.22-25. The corresponding amplitude data of the velocity fluctuation is shown in Figs. 3.3.26-29. The results presented here include portions of the inviscid flow and the boundary layer. Again, as previously mentioned, this is only a crude representation of a portion of the boundary layer. In all cases of the

preliminary measurements of this section, the velocity data was obtained with the use of the DISA optics system and TSI counter. The data was obtained conditionally with 30-40 ensemble averages using the measuring grid shown in Fig. 3.2.5.

A defect in the velocity profiles of Figs. 3.3.22-25 is not an experimental error. This defect is a physical characteristic of the flow. The unsteadiness created by the passage of a vortex is the primary cause of this defect in the velocity profile. The velocity profiles clearly indicate that as the chordwise position increases the velocity at the edge of the boundary layer decreases which is what should be expected on the basis of potential flow. Moreover, as the position in the chordwise direction increases the boundary layer thickness also increases. At 0.9c the thickness is about 0.4c, whereas at 0.1c the thickness is about 0.005c.

Figs. 3.3.26-29 show the amplitude of the velocity fluctuation at the four chordwise stations. The amplitude decreases with increasing distance along the chord. Moreover, at a lower reduced frequency (data not displayed here) the amplitude of the fluctuation is smaller. This should be the case with a decreasing reduced frequency. However, at 0.9c the overall amplitude is larger for the lower reduced frequency. This could be attributed to the interaction of vorticity washing over the trailing edge in the viscous shear layer due to a higher flow velocity, therefore causing a larger amplitude of fluctuation. However, in all cases, with the exception of the 90% chordwise position, the amplitude decreases very close to the surface of the airfoil. This

indicates that the fluctuation is approaching zero closer to the airfoil surface. At 90% chord the amplitude increases close to the surface indicating a region where the flow may be turbulent near the trailing edge.

b) Boundary Layer Region

As the research progressed the interest in the viscous effects at the trailing edge due to the unsteady environment required more attention than the boundary layer upstream of the edge. It was therefore decided to focus all efforts of the measurements at the trailing edge of the fixed airfoil. The results presented here were obtained with the use of a more sophisticated experimental rig (See section 3.2.1) which provided the accuracy necessary to obtain detailed velocity data in the boundary layer, both on the top and bottom surfaces at 98% chord. The velocity data presented in Figs. 3.3.30-35 were conditionally averaged at 15 points along a measuring grid perpendicular to the two surfaces as shown in Fig. 3.2.8. In Figs. 3.3.30-35 the phase of the periodic motion is shown representing only those points obtained during one period. A total of 200 points were used to plot the entire waveform and only 10 (every 20 points in a period) of these points were actually stored in the minicomputer. On both the top and bottom of the trailing edge a shift in phase of the velocity profiles is evident. The phase shift is a result of the unsteady periodicity in the wake as it interacts with the trailing edge. This can be attributed to the passage of a vortex as the viscous shear layer washes over the trailing edge. Referring to Figs. 3.3.33-35, which represent the

profiles on the bottom, this effect is more predominant than the profiles of the top surface (See Figs. 3.3.30-32). This is most likely caused by the vortex on the bottom interacting closer with the viscous shear layer than the passage of the vortex on top, due to the angle of attack of 5°. In both cases (top and bottom) the passage of vortices doesn't appear to present the defect in the profiles as in the case of the potential region data because the center of the vortex is higher at the 0° angle of attack. The boundary layer thickness on the bottom surface is about 1.5%c and that on the top surface is about 3%c.

3.4 Flow Visualization

In this section results of the flow visualizations at the trailing edge and wake of the oscillating airfoil and fixed airfoil are presented. Special emphasis is placed on the flow field in the region of the trailing edge of the oscillating airfoil. It is in this region that the validity of the Giesing-Maskell criterion is tested. The flow is visualized by particles and dyes as well as both, particle and dyes together.

3.4.1 Oscillating Airfoil

The experimental results presented in this section were conducted at 4 reduced frequencies, namely k = 0.8, 1.2, 2.4 and 3.9. These results are in support of the Giesing-Maskell condition for the reduced frequencies between 0.8 and 1.2. The condition starts to break down between 1.2 to 2.4 and is strongly violated at 3.9. The lowest

frequency tested actually represents a moderate frequency for practical applications. The findings here indicate that at k = 0.8, the quasi-steady condition does not hold, in agreement with the measurements of Figs. 3.3.1-3 and in agreement with earlier findings of Ho and Chen (1981) and Satyanarayana and Davis (1978).

Typical flow visualization results are shown in Figs. 3.4.1-8 for all 4 values of the reduced frequency. In these figures only the aft 30% portion of the airfoil trailing edge is shown and the flow field is moving from left to right. At each reduced frequency, the instants at which the photograph was obtained corresponds to angles of attack of $\alpha = 0°$ and $10°$ with the direction of motion of the trailing edge being either an upstroke or downstroke as indicated below the figure. The instant when $\alpha = 0°$ corresponds to the time during the motion when the edge has a maximum angular velocity, and that of $10°$ corresponds to the time when the edge is changing direction. These two positions were chosen because the former was the point at which the unsteady Kutta condition should be tested and the latter was selected to view how fast the streamlines turn around when changing direction.

As shown, at the extreme angle of attack, the streamlines change direction very quickly, leaving no lag time. The boundary layer thickness near the edge is approximately equal to 4c/100. For each of the frames of Figs. 3.4.1-8, the slope of the streamline on the advancing side of the trailing edge was measured at a distance of approximately c/100 above the airfoil. This often required averaging over particle paths at a distance of $\pm$ 2c/100 upstream and downstream of

the edge. The data thus obtained is displayed in Figs. 3.4.9 and 3.4.10.

It should be noted that the quasi-steady Kutta condition should require that all such points collapse on the horizontal axis. Since the trailing edge wedge angle of the NACA 0012 is approximately 16°, the Giesing-Maskell criterion would require that the data fall on $\theta = 8°$ and $\theta = -8°$ for the upstroke and the downstroke motion, respectively. The deviation of the data beyond $\theta = \pm 8°$ implies that neither of the conditions is valid. The error in the calculation of the instantaneous angle of attack was estimated at $\pm 0.5°$ whereas the error in the inclination of the streamline was approximately $\pm 1°$.

3.4.2 Wake of the Oscillating Airfoil

Visualizations of the flow in the wake of the oscillating airfoil for a reduced frequency of 3.9 are displayed in Figs. 3.4.11-14. Figs. 3.4.11-12 were obtained using only the two-colored dyes, whereas Figs. 3.4.13-14 were obtained with both dyes and particles. The time difference between the two readings corresponding to Figs. 3.4.11-12 is 0.12 seconds.

Vortices consisting both of a large and small diameter core (large scale and small scale) are clearly visible in Figs. 3.4.11-12. Shedding of a vortex occurs when the trailing edge passes through a zero degree angle of attack. As shown, the blue color dye has "rolled" into a descrete vortex and is being shed aft of the edge during the downstroke

motion. A vortex draws into it some of the distributed vorticity and grows further downstream into a large-scale vortex.

The visualizations of Figs. 3.4.13-14 show the same wake with the addition of the PLIOLITE particles. The streamline configuration as detected by particles appears to have a wavy-like pattern and shows that the peak and valley of each wave passes through the center of each large scale vortex. These vortices strongly resemble potential vortices. It appears that the small-scale discrete vortices at the edge of the street do not actually contain vorticity. This is because the streamline pattern is not disturbed in their neighborhood. They are therefore either very weak or just represent a history of earlier events. In other words the presence of a second wave, that normally would be thought to be generated by the small scale vortices, is nonexistent.

3.4.3 Fixed Airfoil

As a result of the same unsteady periodic wake of Figs. 3.4.11-14, the visualizations of Figs. 3.4.15-17 show the pattern of particle paths at the trailing edge region of the fixed airfoil at $k = 3.9$. A digital clock zeroed by an LED sensor on the flywheel of the disturbing mechanism indicated the phase of the period of oscillation. Clearly the flow at the trailing edge is affected by the passage of a vortex either on top or on the bottom of the airfoil. The location of the vortex is evident from the peak and valley of the wave depicted in the streamline pattern. A peak adjacent to a valley in the wave indicates 1/2 of a cycle of motion. Therefore, a peak or valley close to the trailing edge

indicates that vortex is nearby. The passage of a vortex near the edge strongly affects the flow in that region. As displayed in the figure, a vortex traveling over the top of the trailing edge region turns the flow upward and that over the bottom turns the flow slightly downward. Thus, the effect is more pronounced over the top than the bottom.

3.5 Discussion

This section compares the results obtained in the present work with those obtained in the past by other investigators. Comparisons will be made with the data and flow visualizations obtained from Groups I, II and V of Fig. 3.2.1 which are the results behind the oscillating airfoil, fixed airfoil and wake of the pitching airfoil (vortex street) respectively.

3.5.1 Oscillating Airfoil

The direction of the paths of the streamlines of Figs. 3.3.1-3 confirm the validity of the Giesing-Maskell criterion. For a reduced frequency of 2.4, the path of the streamline is tangent to the upper or lower surface of the trailing edge depending on the upward or downward motion. Comparisons with the work of Ho and Chen (1981) are rather difficult to achieve. This is due primarily to the fact that their investigations resulted in obtaining the stagnation streamline aft of a plunging airfoil for reduced frequencies only up to $k = 1$. Moreover, the direction of the streamline follows a line extending as the bisector of the trailing edge-wedge angle. Thus, their results are not in

agreement with the Giesing-Maskell condition, and they satisfied only the quasi-steady case for k = 0.5. Comparisons with Figs. 3.3.1-3 are difficult to achieve since no experimental efforts have been undertaken to validate the Giesing-Maskell condition.

The flow visualizations of the present work in the region of the trailing edge of the pitching airfoil, Figs. 3.4.1-4, show that the Giesing-Maskell condition is satisfied for the reduced frequencies indicated. The visualizations of Figs. 3.4.5-8 show that the condition starts to break down at k = 2.4 and is strongly violated at k = 3.9. However, at k = 2.4 the pattern of the particle paths compare with the paths of the streamlines plotted in Figs. 3.3.1-3, only close to the trailing edge (within 2c/100) and beyond this distance, the particle paths turn even more than what the Giesing-Maskell model dictates.

3.5.2 Vortex Street

Preliminary results (See Figs. 3.3.6-10) in the wake of the pitching airfoil agree with other similar investigations. Ohashi and Ishikawa (1972) indicate that the mean of the velocity fluctuation behind a plunging airfoil increases close to the "center plane". This is the case shown in Fig. 3.3.6. DeRuyck and Hirsch (1982) present experimental evidence of this phenomenon for several locations in the wake of an oscillating NACA 0012 airfoil (See Fig. 3.5.1a). Measurements in the wake differ slightly from those of Fig. 3.3.6, since their data was obtained at downstream positions of 0.7, 2, 5, 10 and 20% chord. However the shape of their profiles slightly above the center of

the pitchwise coordinate axis indicates that the flow is accelerating and close to the axis it decelerates due to the effects of the viscous shear-layer. The results of the fluctuation in the time domain of the u and v velocity components (See Fig. 3.5.1b) in the wake of a cylinder (Commerford and Carta, 1974) show basically the same response as that of Figs. 3.3.8-10. The appearance of a second waveform for both the u and v velocity components of Fig. 3.5.1b is similar to Fig. 3.3.10.

Experimental results of Ho and Chen (1980) of the flow field downstream of a NACA 0012 airfoil in a plunging motion are shown in Fig. 3.5.1c. This figure shows the mean of the fluctuation of the streamwise and transverse velocity components. As shown, the streamwise velocity component increases close to the origin of the pitchwise coordinate axis indicating that the momentum there increases due to the plunging motion of the airfoil. This is the same situation as shown in Fig. 3.3.6 of the pitching airfoil of the present work.

3.5.3 Fixed Airfoil

Ohashi and Ishikawa (1972) indicate that for a rounded or blunt trailing edge of an airfoil in a plunging motion, there exists a stagnation zone consisting of a thin viscous shear-layer (See Fig. 3.5.2). Their findings show a pattern of streaklines turning around in the rear of the trailing edge caused by the shedding of vorticity. The streaklines turn with the viscous shear-layers on the top and bottom of the trailing edge due to the unsteadiness. Their pattern of the viscous shear-layer aft of the edge remains the same regardless of whether the

geometry of the trailing edge is sharp or blunt. The blunt edge used in one of their cases was increased from a standard 0.15c/100 to 2.5c/100 radius. The trailing edge radius of the fixed airfoil in the present work was measured and found to be 0.45c/100. As shown, (See Fig. 3.5.2) they indicate that the blunt edge forms its own sharp trailing edge with the small region of stagnant fluid that exists in the rear. The turning of the streamlines of Figs. 3.3.13-20 was caused by the viscous shear-layer formed on the top and bottom surfaces and was not caused by the degree of roundedness at the trailing edge. This same reasoning holds for the case of the oscillating airfoil as well.

CHAPTER FOUR

THEORY AND ANALYSIS

4.1 Introduction

This chapter presents an overview of previous analytical work used in the development of computer solutions for various unsteady aerodynamic flow cases. The details involved in the numerical analysis of the present work will also be discussed. The theoretical efforts were focused on the calculation of the unsteady field over a fixed airfoil. This is the flow over an airfoil which is immersed in the wake of alternate vortices shed by the oscillating airfoil. To simplify the problem, it was decided to work with a Joukowski airfoil that approximates a NACA 0012. The negative curvature of the Joukowski airfoil was eliminated by employing a slightly rounded trailing edge. This was done primarily to see if the trailing edge condition of Giesing and Maskell was valid under the influence of an unsteady periodic wake. Therefore it was necessary to use an airfoil with a finite trailing edge angle.

The study of the effects of unsteadiness required modeling of the wake of the upstream airfoil. It was assumed that the wake of the oscillating airfoil consisted of a vortex street very similar to a von Karman street, the difference being that the frequency and wavelength of this street were controlled independently of the free stream velocity. Also, from the interpretation of the experimental results, the sense of

the shed vorticity of the wake is of opposite sign to that of the von Karman street. Moreover, the vortices are well-organized and maintain their configuration for a much higher Reynolds number. The results of this analytical scheme are presented in Chapter 5 and comparisons are made with the experimental results of Chapter 3.

4.1.1 Previous Analytical Research

Work on unsteady flows has been conducted by many investigators and several analytical models have been developed. These models can be categorized as (i) the full Navier-Stokes, (ii) potential flow solutions and (iii) descrete vortex dynamics. The following review presents some of the previous work done for each of these three models.

Methods involving the solution of the Full Navier-Stokes equations for unsteady flows have been employed by several investigators with considerable success. Mehta and Lavan (1975) studied the stall characteristics of laminar unsteady flow at low Reynolds numbers over an airfoil. They employed an implicit finite-difference scheme and solved the vorticity and streamfunction equations. They found that laminar separation occurs during stall which is then followed by reattachment. Usually in the cases of laminar separation, the analysis of the flow field over the airfoil must be divided into regions and each region is then solved individually. This would then require an iteration procedure between boundary-layer flow and potential flow. However, flows for which separation is well defined cannot be or are not suitable for this type of approach. Thus, the Navier-Stokes equations were

solved numerically over the entire flow field of the airfoil. The numerical solution utilized the finite difference approach for the unsteady laminar flow. In their analysis the flow over three different bodies was considered, namely a Joukowski airfoil, a flat plate and an elliptical cylinder. The unsteady motion was governed by impulsively starting the body. Results indicated that the front and rear stagnation points start to move shortly after the motion has begun. As time increases a bubble is formed over the top surface of the airfoil. As indicated, "the lift increases when counterclockwise bubbles are swept away and when clockwise bubbles grow." The lift then decreases when the opposite occurs. It is indicated that this study is applicable in the problem of trailing edge flows of an oscillating airfoil.

The viscous incompressible two-dimensional flow over an airfoil with a finite thickness was investigated by Kinney and Cielak (1977). The analysis of the unsteady viscous flow past an airfoil was divided into two parts, namely a theoretical and a numerical development. The theoretical approach employs the technique in which the airfoil surface is represented by bound vorticity around the surface. Free vorticity is produced by imposing the no-slip condition on the surface of the airfoil. The unsteadiness is generated by impulsively starting the airfoil in a translational motion. At all times the total vorticity is conserved. The numerical results (Part II of Kinney and Cielak, 1978) present the solutions of the unsteady vorticity transport equation. The equation is solved using finite differences. The geometry of the airfoil is that of a symmetrical Joukowski airfoil with a 12% thickness

and a cusp at the trailing edge. The flow conditions were such that the Reynolds number was 400 with angles of attack of 0° and 30°. The results indicated that agreement with experimental data (i.e. velocity profiles, pressure distributions and vorticity contours) was good even in the vicinity of the cusped edge.

Yates (1977) considered the case of an oscillating semi-infinite airfoil in a subsonic parallel shear flow. Yates calculated the pressure distribution at the trailing edge using the full Kutta condition in one case and no Kutta condition as a second case. Using a small shear layer approach the Wiener-Hopf technique was applied and a solution was developed. The results indicate that the calculated lift is infinite with the application of the Kutta condition and is zero with no Kutta condition. It is left as a question as to which Kutta condition should actually be applied in the case of a parallel shear flow.

Usually the main concern with the solution of these problems using the full Navier-Stokes equations stems mainly from practical considerations. Solving the full Navier-Stokes for such problems is often not practical. However, methods employing interacting boundary layers will remain useful as well as practical for future applications. Methods based on potential flow theory can predict attached unsteady flows providing that the proper Kutta condition is used.

Methods for the solution of an unsteady potential flow employing arbitrary unsteady motions was developed by Giesing (1968) for a two-dimensional airfoil of arbitrary shape. A study involving nonlinear

effects was also presented. The wake aft of the airfoil is characterized by the shedding of a vortex-sheet which is convected with the fluid particles. The solution for the potential function is broken into two parts, namely one that neglects the circulation, the airfoil and the wake, which is essentially a quasi-steady phenomenon, and one that considers only the circulation and wake. Comparison of the potential flow solution with accurate experimental data indicate that there are substantial differences in the results. The discrepancies here are attributed to the effects of viscosity. Thus, they indicate that the viscous effects were considered in the calculated values of the quasi-steady lift. These results indicated that, for the high frequencies considered, the phase lag increased rather than decreased. The results of the calculations of the quasi-steady lift is too high and the large deviation in phase is still under question.

Basu & Hancock (1978) developed a numerical method that calculates the pressure distribution, forces and moments acting on a two-dimensional airfoil. They employed a panel method and solved the case of an airfoil experiencing an arbitrary unsteadiness in an incompressible inviscid flow field. A large portion of the discussion of the analysis is placed on the Kutta condition for an airfoil in a steady and unsteady environment. The condition appropriate to render the solution unique, in the case of an unsteady motion, is based on the analysis set forth by Giesing (1969) and Maskell (1972) as already mentioned in Chapter 3 and Section 4.1. Maskell's argument is based solely on the sense of the shed vorticity. Thus, depending on the sign

of the quantity $d\Gamma/dt$ vorticity is shed in a direction tangent to either the upper or lower surface of the trailing edge wedge angle as shown in Fig. 4.1.1. The figure shows that if the shed vorticity is counter-clockwise then the flow departs from the trailing edge in a direction tangent to the lower surface, and if the sense of the vorticity is clockwise the flow departs in a direction tangent to the upper surface. This analysis can be proved very elegantly by applying the unsteady Bernoulli equation at the trailing edge. Keeping in mind the condition of zero loading at the edge, the equation is easily manipulated to show the proper direction in which the flow leaves the trailing edge. The work of Giesing (1969) is somewhat different from that of Maskell but the conclusion is the same.

Analyses (van der Vooren and van der Vel, 1964) similar to the work of Basu and Hancock, Giesing and Maskell, have been performed with results indicating that smooth flow and zero loading at the trailing edge is achieved only for a cusped edge. No work has been done so far to provide an analytical solution for an airfoil in an unsteady motion which satisfies the trailing edge conditions of zero loading and finite velocities. Giesing's Kutta condition requires that the magnitude and the direction of the velocity vectors at the center of the last two elements (i.e. top and bottom elements) of the trailing edge are equal. This implies that there exists a finite loading at the edge and also a finite loading across the wake of the shed vorticity aft of the trailing edge. This procedure is based on the work of Hess and Smith (1967). As previously mentioned, conclusions to these various schemes indicates

that each mathematical procedure essentially requires its own Kutta condition to ensure that the solution is unique.

Using thin airfoil theory McCroskey (1973) developed equations that describe the flow fields of unsteady airfoils. The velocity potential was reduced into three components consisting of airfoil thickness, camber and angle of attack. The results indicated that there is good agreement with numerical calculations and experimental pressure measurements.

The method of discrete vortex dynamics has been employed with considerable success to solve problems of stalled airfoils. The work by Ham (1968) involved calculating the inviscid flow over a flat plate at an angle of attack via conformal mapping. He imposed the condition that the sum of the free and bound vortices is invariant in time. Vorticity was released from the leading and trailing edges of the flat plate. His approach is based on the assumption that the stagnation point at the trailing edge of an airfoil "persists" and is supported by interferograms that depict the flow situation at the trailing edge. Results indicate that the aerodynamic loading on a two-dimensional airfoil is strongly influenced by vorticity shedding from the leading edge during motions consisting of large amplitudes of oscillation. The theory shows that the shed vorticity from the leading edge rolls up into a discrete vortex having basically the same strength as the bound vorticity.

The work of Katz and Weihs (1981) utilized a modified linear airfoil theory to describe the wake roll up of an airfoil in either a

pitching or heaving motion. During a particular time step the strength of a shed vortex was equal in magnitude to the change of the bound circulation around the airfoil. The reduced frequencies tested ranged from 0.7 to 8.6. Results indicated that the shed vortices aft of the trailing edge formed a vortex sheet that usually broke up at reduced frequencies greater than k=2. The results of the wake patterns were basically the same for both the heaving and pitching cases. The wake of both cases resembled that obtained from a quasi-steady case for the reduced frequencies of 0.7 and 1.3, almost in agreement with the experimental results obtained by Ho and Chen (1981) as explained earlier.

The discrete vortex approach was also considered by Ono et al. (1981). They modeled the boundary layer of the airfoil and the separated shear layer using a layer of discrete vortices at low Reynolds numbers. The approach basically employed a panel method where each panel contained a vortex strength which was obtained from the no-slip condition on the surface of the body. At each time step, a panel of vorticity or vortex filament would convect to a new position. As the time increases vorticity was then generated and shed aft of the body representing a vortex shedding pattern often seen in flow visualizations. The results predict what is actually occurring in a dynamic stall situation. However, as indicated by McCroskey (1981), their method requires more work in order to be of any value in practice.

The method of discrete vortices was employed to study the lift and drag components over a Joukowski airfoil via conformal mapping by Chow

and Huang (1983). In an unsteady flow it is necessary that a vortex wake be shed aft of the airfoil trailing edge since the airfoil lift is changing with time. Their analysis was based on the fact that the total amount of circulation was conserved and the velocity at the trailing edge vanished therefore enabling the circulation of the shed vortex to be determined. Therefore at each time step vorticity was shed aft of the trailing edge thus forming a wake roll up. The Kutta condition that they chose to satisfy was the one proposed by Ham (1968). They considered the case when a vortex of known strength was released at several positions upstream and studied the effects this vortex had as it passed over the airfoil. The result of this particular approach indicated that under the influence of a strong vortex the airfoil generated a very high lift coefficient. They used basically the same technique to investigate the stability of a "captured" vortex over a symmetric airfoil. The results indicated that the vortex could not be captured around the airfoil. The discrete vortex model was also employed to simulate an airfoil in a stalled configuration. At a high angle of attack the placement of a discrete vortex upstream of the trailing edge simulates the flow pattern of a leading edge separated flow. The results of this consideration indicate that the lift produced by the airfoil would require a vortex of a strength much larger than the lift generated by a vortex of constant-strength with basically the same circulation.

Mathioulakis and Telionis (1983) modeled the flow through a cascade of turbine blades using conformal mapping and distribution of bound

vortices. Their approach was similar to the one outlined by Ham (1968). They employed two stagnation points, one at the front of a circular cylinder and one at the rear, both corresponding to the leading and trailing edge stagnation points respectively. The phenomenon of rotating stall was thus modeled by the shedding of vorticity from the leading and trailing edges at each time step and then adjusting the bound vorticity to ensure that the total amount of circulation was conserved. In order to completely describe the shape of each blade in the wake, Joukowski and Theodorsen transformations were used. This approach mapped a linear cascade of blades to that consisting of closed contours where one represents a circle. The predictions of the numerical scheme of their work indicated that the exact location of separation was very crucial. The shape of the wake from both the leading and trailing edges changed to a large degree if the stagnation points were repositioned. The authors indicated that calculations involving unsteady separation and boundary layers should be added to the theory.

Kim and Mook (1985) modelled the unsteady wake effects behind a pitching airfoil using continuous vorticity panels. They satisfied the no-penetration condition at the mid-point of each panel and the total amount of circulation around the airfoil and wake was conserved. At each time step the wake was generated aft of the trailing edge by placing a discrete vortex in the field and convecting it with the local velocity. The Kutta condition that they chose to satisfy is the same one used in the present analytical model. The distributed vorticity at

each panel around the airfoil is piecewise linear and goes to zero at the trailing edge. Thus, the velocity is zero there as well. A discrete vortex is then placed at a point very close to the edge and convected with the local velocity. The discrete vortex cores shed aft of the trailing edge form the unsteady wake and these results compare nicely with the flow visualizations of Chapter Three.

The present analytical work was modelled using discrete vortex dynamics. This approach was chosen primarily to simplify the problem and to investigate the condition of Giesing and Maskell. The analytical model provided accurate information of the oncoming wake and flow field aft of the trailing edge and comparisons with experimental results were easily obtained. Because of the periodic nature of the flow field and the initial placement of the vortices the results from the analytical model required a small number of time steps when comparisons were made with corresponding experimental results. Due to the simplicity of the program the computer execution time for large time steps was much smaller than those models involving the full Navier-Stokes equations and potential flow solutions. The earlier findings of the analytical model were compared with the work of Mathioulakis (1985). Comparisons indicated that the equations in the program were correct and all routines were executing properly.

4.2 Numerical Analysis

The analytical scheme is based on the circle theorem as outlined in Milne and Thomson (1960). Discrete vortices are thus placed in the flow

field of a circular cylinder and convected with the free stream velocity as shown in Fig. 4.2.1. A straightforward conformal mapping using the Joukowski transformation

$$\zeta(z) = z + \frac{a^2}{z} \tag{4.2.1}$$

generates the unsteady flow about a modified Joukowski airfoil under the influence of an oncoming vortex street. The result of this flow requires that vorticity must be shed aft of the airfoil trailing edge and convected downstream. The vortex street was placed in the flow field around the airfoil, and was then allowed to convect with the velocity field.

In order to render the solution unique at each time step, a condition at the trailing edge was specified. The trailing edge condition employed here was the one proposed by Giesing and Maskell as discussed earlier. This is similar to the one proposed by Ham (1968) and Mathioulakis and Telionis (1983). Due to the roundedness of the trailing edge a stagnation point was placed at what would be the trailing edge if the edge were not rounded. This corresponded to a point slightly downstream of the trailing edge. This point was chosen since the flow in that neighboring region essentially forms its own sharp trailing edge as indicated by Ohashi and Ishikawa (1972). The tip of the edge formed by the flow coincides with the intersection of the trailing edge bisector. Thus, the vanishing of the velocity at the

trailing edge provided the arbitrary Kutta condition which was used to determine the strength of the nascent vortex.

At every time step a vortex was shed and the bound vorticity was adjusted to insure that the total amount of circulation was conserved. The shed vortex was placed an arbitrary distance slightly downstream of the trailing edge near the point of stagnation.

In the results presented in Chapter 5, the calculations were made using a vortex street consisting of 20 vortices alternately spaced according to the experimental findings, namely a=0.95c and b=0.5c. It was determined that 20 vortices was sufficient to adequately describe the unsteadiness of the periodic wake upstream and in the vicinity of the fixed airfoil. This technique resulted in less computation time and was found to be more advantageous than bringing the vortices into the plane of the airfoil one by one from an imaginary window upstream. The earlier stages of the numerical efforts utilized this imaginary window technique and it was found that after several time steps too many shedding vortices were scattered in the flow field aft of the trailing edge. The idea of pairing the vortices into discrete clusters was considered as a viable alternative, however estimating their corresponding centroidal positions and strengths for later time steps became cumbersome. The 20 vortices, placed in the flow field at the first time step, with their position as well as the shed vorticity are allowed to drift with the flow. The results of this scheme are presented in chapter 5 and the details of the mathematics are discussed in the sections that follow.

4.2.1 Conformal Mapping

A transformation $\zeta = \zeta(z)$, is conformal if the angle between any two curves at any point in the z plane is preserved locally. A necessary and sufficient condition for conformal mapping is the analyticity of $\zeta(z)$ and $\frac{d}{dz}\zeta(z)$. Moreover, the function $\zeta(z)$ must be analytic or the derivative $\frac{d}{dz}\ \zeta(z)$ will have a different value in various directions and the angle between any two curves at a point in the z plane will no longer be preserved. Thus, geometric shapes are preserved locally through the transformation.

4.2.2 The Unsteady Inviscid Flow Field Over the Circular Cylinder

The mapping of an inviscid irrotational two-dimensional flow over a circular cylinder in the z plane to the flow over a Joukowski airfoil in the ζ plane requires the use of the transformation of Eq. (4.2.1). Depending on the position and radius of the circle in the z plane a variety of shapes in the ζ plane may be obtained. In the initial stages of the work it was necessary to adjust the radius of the circle and its position in the z plane until the shape in the ζ plane represented very nearly that of a NACA 0012 airfoil. The Joukowski airfoil thus employed has a trailing edge radius of curvature equal to that of a NACA 0012, namely 0.5% of the chord length and coordinates no different than 1% chord when compared to a NACA 0012. The corresponding quantities of the circular cylinder in the z plane, namely the radius of the circle and its x and y coordinate positions, are respectively 1.111, 0.079 and 0.00. Fig. 4.2.2 shows the position of a circle in the z plane with

radius extending outside of the singular points of the transformation. The same figure also shows a corresponding Joukowski airfoil superimposed with a NACA 0012. It was intended to present in this figure a crude illustration of the NACA 0012 with an arbitrary modified Joukowski airfoil. The correct version of the Joukowski airfoil coincided very well when superimposed with the NACA 0012 to the point that it was too difficult to distinguish between them.

The classical inviscid irrotational two-dimensional flow over a circular cylinder is described by superimposing a uniform stream, a doublet and a vortex resulting in the following complex potential function

$$F(z^*) = - z^* U_\infty e^{i\alpha} + \frac{R^2 U_\infty}{z^*} e^{i\alpha} + \frac{i\Gamma}{2\pi} \ell n\, z^* \qquad (4.2.2)$$

where R is the radius of the circular cylinder and Γ is the circulation of the vortex. The terms with asterisks and overbars in Eq. (4.2.2) denote quantities that are dimensional and complex conjugates respectively. The corresponding flow field in the image plane is shown in Fig. 4.2.3. The addition of discrete vortices in the flow (See Fig. 4.2.1) requires additional terms in Eq. (4.2.2). These involve terms that represent N discrete vortices with their conjugates which preserve the shape of the circular cylinder. The condition of no penetration on the surface of the cylinder is satisfied by placing two image vortices inside the circle corresponding to each vortex placed in the flow field. One image vortex is placed at the center of the circular cylinder

and another at the conjugate point, namely the point at $1/\bar{Z}_q$, where q is the order of the discrete vortex. Eq. (4.2.2) thus becomes

$$F(z^*) = - z^* U_\infty e^{i\alpha} - \frac{R^2 U_\infty}{z^*} e^{-i\alpha} + \frac{i\Gamma^*}{2\pi} \ell n z^*$$

$$+ \frac{i}{2\pi} \sum_{q=1}^{N} \Gamma_q^* \left[\ell n (z^* - z_q^*) - \ell n \left(z^* - \frac{R}{z_q^*}\right) \right.$$

$$\left. + \ell n z^* - \ell n \left(-\bar{z}_q^*\right) \right] \qquad (4.2.3)$$

The quantities of (4.2.4) listed below render the above equations dimensionless

$$Z = \frac{Z^*}{R} \quad , \quad W = \frac{W^*}{U_\infty} \quad , \quad \Gamma = \frac{\Gamma^*}{2\pi R U_\infty}$$

$$\Gamma_q = \frac{\Gamma_q^*}{2\pi R U_\infty} \quad , \quad Z_q = \frac{Z_q^*}{R} \qquad (4.2.4)$$

Substitution into Eq. (4.2.3) of expression (4.2.4) results in the following potential function

$$F(z) = - ze^{i\alpha} - \frac{e^{-i\alpha}}{z} + i\Gamma \ell nz$$

$$+ i \sum_{q=1}^{N} \Gamma_q \left[\ell n(z-z_q) - \ell n(z-\frac{1}{\bar{z}_q}) + \ell nz - \ell n(-\bar{z}_q) \right] \qquad (4.2.5)$$

The dimensional terms in the parameters of (4.2.4) are; Γ^* which is the bound circulation of the cylinder, Γ_q^* is the strength of the qth vortex, and Z_q^* is its position, R is the radius of the circle, W* is the magnitude and direction of the complex velocity vector at any point Z* and α is the angle of attack of the flow over the circular cylinder. The complex velocity W(z) in the z plane can be expressed in terms of a real and imaginary part, such as

$$W(z) = u - iv \qquad (4.2.6)$$

and in terms of the complex potential function

$$W(z) = \frac{d}{dz} F(z) = -e^{i\alpha} + \frac{i\Gamma}{z} + \frac{e^{-i\alpha}}{z^2}$$

$$+ i \sum_{q=1}^{N} \Gamma_q \left\{ \frac{1}{z-z_q} - \frac{1}{z-\frac{1}{\bar{z}_q}} + \frac{1}{z} \right\} \qquad (4.2.7)$$

There are two quantities that are unknown at each time step. These are the circulation of the shed nascent vortex and the bound circulation. Therefore the two conditions necessary to determine these quantities employs the vanishing of the trailing edge complex velocity and the total amount of circulation of vorticity around the cylinder and wake. The latter of these two conditions is Kelvin's theorem, indicating that the net vorticity in a closed contour must be zero at all times. The contour here contains the circular cylinder with its wake of shed vorticity and the N discrete vortices. Therefore at each time step the two conditions are expressed by

$$-e^{i\alpha} + \frac{i\Gamma}{Z_{te}} + \frac{e^{-i\alpha}}{z_{te}^2} + i \sum_{q=1}^{N} \Gamma_q \left\{ \frac{1}{z_{te}-z_q} - \frac{1}{\bar{z}_{te}-\frac{1}{\bar{z}_q}} + \frac{1}{Z_{te}} \right\} = 0 \qquad (4.2.8(a))$$

and

$$\Gamma + \sum_{q=1}^{N} \Gamma_q = 0 \qquad (4.2.8(b))$$

At each time step Eqs. (4.2.8(a)) and (b) are solved simultaneously for the bound circulation around the cylinder and the circulation or strength of the shed vorticity. The circulation of each vortex comprising the vortex street was determined from the laboratory measurements (See section 3.3.3), namely $\Gamma=0.4cU_\infty$, where c is the airfoil chord.

The velocity of the qth vortex at any point z in the z plane can be obtained from the equation

$$W_q = W - \frac{i\Gamma_q}{z-z_q} \tag{4.2.9}$$

where W is given by Eq. (4.2.7). At the position of the qth vortex the denominator of the term on the far right of (4.2.9) goes to zero resulting in an infinity in the velocity. The velocity w at this point is also very large. Thus, the two cancel and at such points the position of the qth vortex is not included. This is essentially the condition for a free-force vortex. This type of vortex is convected only with the local velocity. In the computer program a "cutoff" statement was used when two or more vortices approached one another. If the positions of two vortices were within a small radius ε near each other,

$$\left| Z_q - Z \right| \leq \varepsilon$$

the computer program would skip that calculation and continue until the difference of any two neighboring positions were outside of this limit. The parameter ε was chosen to be 0.1. This scheme was employed

because artificially high velocities would occur in the neighborhood where vortices gather. Several schemes have been developed in the past to avoid this particular problem. As outlined by Mathioulakis (1982), techniques of rediscretization of vortex sheets considered by Sarpkaya (1979) and the work of Ham (1968) using a single equivalent vortex to replace several vortices were used with results not always satisfactory.

The convection of the vortices at each time step was performed via the equation

$$Z_q(t+\Delta t) = Z_q(t) + W_q(Z_q,t) \cdot \Delta t \qquad (4.2.10)$$

where Δt is the time increment and $Z_q(t+\Delta t)$ is the new position of the corresponding vortex. The value of the parameter Δt ranged from 0.05 to 0.30. The results of the program were valid in this range.

4.2.3 The Unsteady Inviscid Flow Field Over The Modified Joukowski Airfoil

With ζ the physical plane and z the plane of the circle, the transformation reads

$$\zeta(z^*) = Rz^* + \frac{a^2}{Rz^*} \qquad (4.2.11)$$

Where a is the distance between the two points of singularity which is 1 and * denotes the dimensional form of the transformation as described in

section 4.2.2. Using the parameters of (4.2.4) the nondimensional form of the transformation of Eq. (4.2.11) is expressed as

$$\zeta\ (z) = z + \frac{1}{z} \tag{4.2.12}$$

The initial positions of the vortices in the z plane, $Z_q(t)$, correspond directly to positions in the ζ plane $\zeta_q(t)$ through the conformal transformation. However, positions at the 2nd time step and time steps thereafter, namely $Z_q(t+\Delta t)$ and $\zeta_q(t+\Delta t)$, are not image points of each other. However, Routh's theorem dictates that the path of a vortex in the z plane does not follow the same path of the corresponding vortex in the ζ plane. The strength of the vortex remains the same in both planes. According to Routh's theorem the vortices in the ζ plane are convected by the equation

$$\zeta_q(t+\Delta t) = \zeta_q(t) + \left[\frac{W_q(z_q,t)}{\left.\frac{d\zeta}{dz}\right|_{z=z_q}} + i\Gamma_q \frac{d}{d\zeta} \ln \frac{1}{\left.\frac{d\zeta}{dz}\right|_{z=z_q}} \right] \cdot \Delta t \tag{4.2.13}$$

where

$$\frac{d\zeta}{dz} = 1 - \frac{1}{z^2}$$

which is the derivative of the transformation.

Using the transformation function $\zeta(z)$ the complex potential function $F(z)$ can be mapped into the physical plane thus giving the relationship that

$$F(z) = \tilde{F}(\zeta) = \tilde{F}[\zeta(z)]$$

and the derivative with respect to z is then expressed as

$$\frac{dF(z)}{dz} = \frac{d\tilde{F}(\zeta)}{d\zeta}\frac{d\zeta}{dz}$$

and rearranging gives

$$\frac{d}{d\zeta}\tilde{F}(\zeta) = \frac{dF(z)}{dz}\frac{1}{\frac{d\zeta}{dz}} \qquad (4.2.14)$$

where the left hand side is the complex velocity in the physical plane. Rewriting (4.2.14) gives

$$W(\zeta) = W(z)\left\{\frac{1}{1-\frac{1}{z^2}}\right\} \qquad (4.2.15)$$

At the critical points of the transformation ($z=\pm 1$) the physical plane velocity $W(\zeta)$ goes to infinity. Therefore it is important that $W(z)$ be made zero at one of the critical points or the critical points lie away from the region of interest. The velocity at any point in the

unsteady flow field in the physical plane can then be determined from Eqs. (4.2.7) and (4.2.15).

4.2.4 Calculation of the Streamfunction and the Pressure Distribution

The real and the imaginary parts of the complex potential are the potential function and the streamfunction respectively. Thus

$$F(z) = \Phi + i\psi \tag{4.2.16}$$

Knowing the streamfunction of the unsteady flowfield enables streamlines to be plotted at any point in either plane. Knowing the potential function, the pressure distribution may be plotted over the airfoil in the physical plane. The potential-function Φ and the streamfunction ψ have the same value for corresponding points in both planes.

In the earlier stages of the numerical development a scheme was devised to plot streamlines around the airfoil. The function ψ in the plane of the cylinder is given by

$$\psi = \text{Imag } [F(z)] \tag{4.2.17}$$

where Imag denotes the imaginary part of the complex potential F(z). The scheme employed here, referred to as the "Pac-Man" scheme, generated streamlines at any point or points in the plane of the cylinder, and using the transformation function of Eq. (4.2.12) these points were then obtained in the plane of the airfoil (See Fig. 4.2.3). The basic idea

of the "Pac-Man" approach was to generate the value of the streamfunction in the flowfield at an initial point and then march forward to an arbitrary position projecting at an angle of ±30° an arc that would search the local sector until the value of the streamline was equal to that obtained at the initial point. The location of the streamline was then determined at the point on the arc where the streamfunction was within a difference of ±0.0001 with respect to the initial point. The scheme required excessive computation time and for this reason streamlines only in vicinities around the airfoil of prime interest were plotted. These areas consisted of small regions like the immediate aft portion of the trailing edge. In the later stages of the work it was decided instead to plot at several points velocity vectors. This approach required less computation time and resulted in a much more efficient computational scheme. A copy of the fortran computer program used for these computations and the necessary details involved in running the program can be found in Appendix III.

The pressure distribution on the surface of the airfoil was calculated using the unsteady Bernoulli equation for incompressible, inviscid, irrotational flow. This equation employs the potential function and is expressed as

$$\frac{p^*}{\frac{\rho}{2} U_\infty^2} = -\frac{2}{U_\infty^2} \frac{\partial \Phi^*}{\partial t^*} - \left| \frac{W_s^*}{U_\infty} \right|^2 + \frac{c(t)}{\frac{\rho}{2} U_\infty^2} \qquad (4.2.18)$$

where, as before, the * terms denote dimensional quantities with p* and W_s* representing the pressure and the complex velocity on the surface of the airfoil respectively, Φ the potential function and c(t) is an arbitrary constant which depends on time. In terms of the nondimensional form, Eq. (4.2.18) is expressed as

$$p = -\frac{2}{R}\frac{\partial \Phi}{\partial t} - \left| W_s \right|^2 + c_1(t) \tag{4.2.19}$$

where

$$p = \frac{p^*}{\frac{\rho}{2} U_\infty^2}$$

The potential function Φ is obtained in a similar manner as the streamfunction ψ. Thus

$$\Phi = \text{Real } [F(z)] \tag{4.2.20}$$

where F(z) is given by Eq. (4.2.5). The partial derivative $\frac{\partial \Phi}{\partial t}$ at a time t is approximated by the following equation

$$\left.\frac{\partial \Phi}{\partial t}\right|_t = \frac{\Phi|_t - \Phi|_{t-\Delta t}}{\Delta t} \tag{4.2.21}$$

The pressure distribution is determined using 180 points located around the surface of the airfoil. At each of these points the pressure p of Eq. (4.2.19) is determined and can then be plotted with respect to the airfoil chord.

CHAPTER FIVE

NUMERICAL RESULTS

5.1 Wake Behind the Pitching Airfoil

In this section the numerical results of the wake of the approaching vortex street are compared with the flow visualization of the present work and the work of Mathioulakis, et al. (1985). Their work involved making comparisons with the experimental work of the wake behind an oscillating NACA 0012 (see Mathiouiakis, 1985) and the analytical work of a vortex pannel method of an oscillating airfoil (see Kim and Mook, 1985).

Using the measured spacing and strength of the oncoming vortices (see section 3.3.3), the velocity field in the wake of the vortex street ahead of the fixed airfoil was calculated and plotted as shown in Fig. 5.1.1. This is the field obtained by 20 ideal vortices arranged in a street. A critical streamline is a streamline which emanates from a singularity point (see Fig. 5.1.2). In the experimental results there are no singularities. However, a critical streamline may be approximately identified as the streamline with the sharpest kink (see Fig. 5.1.1). A good comparison of the vortex street of the experimental and analytical efforts is the ratio of the vortex spacing a and the depth of the critical streamline wave e. The ratio e/a (see Fig. 5.1.2) for the calculation shown in Fig. 5.1.1 was found to be e/a=0.1915. The same ratio was calculated from the flow visualizations of Figs.

3.4.13-14 and was found to be e/a=0.2019. This comparison is based on a reduced frequency of k=3.9.

Mathioulakis (1985) measured the u-component of the velocity with a Laser-Doppler Velocimeter for a different value of k and calculated the v-component via the continuity equation. The vector field thus obtained is shown in Fig. 5.1.3. From this figure we estimated again the ratio e/a to be equal to 0.1613 (See Table 5.1). The reduced frequency used in their experimental investigation was k=2.77. The experimental findings of their work, namely $\Gamma = 0.58cU_{\infty}$, a=1.3c and b=0.2c, were used again as input in the numerical scheme of the present work. The results indicate that e/a=0.17460 (See Table 5.1). The corresponding velocity field is shown in Fig. 5.1.4.

Using the same conditions of the experiments of the present work, those for which k=3.9, the numerical results of Mathioulakis, et al. (1985) (See Fig. 5.1.5) yield a value of e/a=0.21739 (See Table 5.1). This yields a difference of about 12% more the value obtained by the numerical analysis of the present work.

The experimental and analytical results seem to be consistent when reference is made with respect to the vortex spacing a and the wave depth e. This is a good indication that the analytical scheme of the present work is valid in the wake of the pitching airfoil. These results indicate that as the value of k increases the ratio of e/a decreases as well and the vortex spacing a increases.

5.2 Interaction of Vortices

This section discusses the results of the interaction of the vortices with the fixed airfoil, using the same values of the vortex spacing and strength of section 3.3.3. The numerical results of the velocity field aft of the trailing edge at an angle of attack of 5° are compared with the experimental results of the fixed airfoil of section 3.3.4.

The paths traced by the oncoming vortices and the vortices shed aft of the trailing edge are shown in Figs. 5.2.1-6 for time steps corresponding to t=5, 10, 15, 20, 25 and 30, respectively. These results are presented primarily to show the wake roll-up and the way in which the vortices are convected over the airfoil at each time step. The vortex street consists of 20 vortices that are initially placed behind and in front of the airfoil. Due to the limitation of the size of the figure only the convection of those vortices around the airfoil are shown. The position of the vortex (passing over the top surface) of the experimental results of Figs. 3.3.14-19 is compared with the position of the eleventh vortex in the numerical scheme. Fig. 5.2.7 compares the relative position in phase of the vortex passing over the top of the airfoil in both the experimental and analytical results. Slight deviations in slope toward the rear of the airfoil indicate that the vortex in the experiment may be moving faster than the eleventh vortex in the analysis. The earlier stages of the analytical work employed only four vortices convected over the airfoil starting from an imaginary window upstream. Comparisons with the position of the third

vortex of that previous analysis are shown in Fig. 5.2.8 with those obtained from the experimental results and the field consisting of twenty vortices. Clearly it is evident that more vortices placed in the flow approximate quite accurately the actual flow over the fixed airfoil. This was the main reason for adding more vortices in the flow.

A detail of the velocity field aft of the trailing edge is shown in Figs. 5.2.9-14. The approximate position of the eleventh vortex in each of these figures corresponds to 0.095c, 0.24c, 0.48c, 0.65c, 0.80c and 0.98c, respectively. Comparisons of the velocity field aft of the trailing edge of Figs. 5.2.9-14 are made with Figs. 3.3.14-19 of the experimental results. The velocity field aft of the trailing edge of both sets of figures is shown in the diamond-shaped measuring grid. This grid was plotted in the analytical scheme only to facilitate comparisons with corresponding experimental results. In order to preserve the detail of the velocity field, the shedding of vorticity aft of the trailing edge is not shown.

The curvature of the streamlines in the viscous shear layer just aft of the trailing edge in Figs. 3.3.14-19 is not evident in the analytical results of Figs. 5.2.9-14. This should be the case due to the nature of the potential flow analysis and the fact that in the experiment, there exists a strong viscous shear layer in the aft region of the trailing edge. However, near the top and bottom ends of the diamond-shape grid the analytical and experimental directions of the flow are in qualitative agreement. It is necessary to notice in the results of the analytical scheme (see Figs. 5.2.9-14) that the

Giesing-Maskell condition is satisfied. The velocity vectors just aft of the trailing edge are tangent to either the upper or lower surface, depending on the sign of the shed nascent vortex.

From the analytical results presented here the condition of tangency at the trailing edge for unsteady flows is satisfied automatically when a stagnation point is placed at what would be the location of the trailing edge if the edge were not slightly rounded.

5.3 Analytical Experiments

Special flow cases generated by the analytical scheme of the present work are presented in this section. These include increasing the angle of attack to 10° and comparing the effects of the flow over the airfoil with the results of section 5.2. Also, the effects of increasing the width of the vortex street will be considered as well.

The paths of the oncoming vortices and those shed aft of the trailing edge are shown in Figs. 5.3.1-5 for time steps corresponding to t=5, 10, 15, 20 and 30 respectively. Comparisons of these figures with those of Figs. 5.2.1-6 show little change in the position of both the approaching vortices and the shed vortices. Slight deviations in the wake roll up aft of the trailing edge are evident but this is due to the increase in the angle of attack.

The velocity field in front of the airfoil was calculated and plotted using two different values for the width b of the vortex street. Referring to Fig. 5.1.2, the value b was 0.5 c and the second value was b=c. These results are shown in Figs. 5.3.6 and 7 for the two

respective values. The ratio of the wave depth e to the vortex spacing a for the two corresponding figures is e/a = 0.1333 and 0.1600, respectively. These results, when compared with the analytical results of section 5.1 using the same spacing a in the previous calculations, gives evidence to the fact that the ratio e/a decreases when the value of b increases.

In these results the value of a remained constant. Thus, the value of a should actually change as b changes. It therefore remains as future work to consider the effects of changes in the spacings a, b and e as the reduced frequency changes.

CHAPTER SIX

CONCLUSIONS AND RECOMMENDATIONS

Extensive work has been done in the past with emphasis placed on the condition at the trailing edge for a broad range of reduced frequencies, most of which possessed very small amplitudes. Moreover, most investigators examined the condition of zero loading near the trailing edge by measuring static pressure. These results left considerable question as to whether the condition of zero loading was actually satisfied for unsteady flows. What appears at first to be an obvious requirement, soon turns out to be an ambiguous condition. For an inviscid theory there can be no pressure jump across two neighboring streamlines unless a solid body is interfering. Within the approximation of this theory, boundary layers are infinitely thin vortex sheets and free vortex sheets cannot sustain forces. In other words, the edge cannot be loaded. All of these arguments are valid, if the interaction between the viscous and inviscid regions is weak.

In the present analysis it was determined that more reliable information could be obtained by measuring the velocity vectors at the trailing edge region. The condition employed here would then be the alignment of the streamline with one of the two sides of the trailing edge. The controlling parameter is the sign of the time derivative of the airfoil circulation. This condition, adopted in the present work as the unsteady Kutta condition, was the condition proposed by Giesing (1969)

and Maskell (1971) for high frequency unsteady flows. From the results of the present investigation and previous studies, this condition has proved to be more reliable in determining the limits of the reduced frequency parameter for which numerical solutions for high frequency flows are valid.

The only case of airfoil flows which can be conveniently treated with inviscid theories is the case of an airfoil with a cusped trailing edge. For finite trailing edge angles, the classical solution of steady potential flow equations is unique, if the stagnation point is positioned at the trailing edge. For inviscid flows then, the trailing stagnation streamline is tangent to the bisector of the wedge at the trailing edge. Thus, flows with such characteristics satisfy the "classical Kutta condition".

The present experimental data indicate that for periodic flows with reduced frequencies larger than k=2 and not very small amplitudes, the classical Kutta condition is never satisfied. The reduced frequency has usually been employed as a parameter controlling the extent of the validity of the Kutta condition. As suggested in the present work, a more proper criterion should include the amplitude of the oscillaton. It was thus suggested that a good parameter could be the ratio of the maximum velocity of the trailing edge to the velocity of the free stream. For a pitching motion this would be $\ell=r\omega\alpha_0/2U_\infty$ with r the distance from the pivot to the trailing edge.

In both cases, which include the pitching and fixed airfoils corresponding to reduced frequencies of k=2.4 (ℓ=0.3159) and k=3.9

(ℓ=0.5139), respectively, the classical Kutta condition is clearly violated. The case of the fixed airfoil provides data on a much finer measuring grid which penetrates the viscous region. In this region there is evidence of finite normal pressure gradients and therefore nonzero trailing edge loadings. However, outside the viscous regions, it appears that for both cases, the Giesing-Maskell criterion approximately holds, as long as $d\Gamma/dt$ is far from its zero. During time intervals centered about the zero of $d\Gamma/dt$, the trailing edge streamline changes direction smoothly with time.

The measurements (aft of the fixed airfoil) extend well within the viscous region and reveal the true character of the flow in the vicinity of the trailing edge. They also indicate that the violation of the condition of zero loading does not extend further than 3 percent of the chordlength downstream of the trailing edge. It remains for the numerical analyst to examine the influence of imposing zero loading at the trailing edge or a short distance downstream. This may not be an appropriate remedy, because for unsteady flow the loading near the trailing edge varies very sharply with distance from the trailing edge. Even a few percent of chordlength may have a significant effect on global characteristics like instantaneous or averaged lift and drag.

The present visual data indicate that for the range of $0.8 \leq k \leq 2.4$ and $0.1047 \leq \ell \leq 0.31590$, the Giesing-Maskell criterion is valid for the entire period of the oscillation. It can be assumed with very good accuracy, that the trailing-edge streamline instantly adjusts itself to become tangent to the side of the airfoil which leads the pitching

motion. This observation therefore makes this criterion a useful practical tool for calculating unsteady airfoil flows at high frequencies. It was determined from the experimental data and the visual data that the Giesing-Maskell criterion breaks down for reduced frequencies larger than k=2.4 (ℓ=0.3159).

The Kutta condition employed in the analytical efforts of this research was the vanishing of the velocity at the trailing edge while simultaneously a nascent vortex was positioned very near the edge. At every time step the trailing-edge vortex was shed aft of the edge, the bound vorticity was adjusted to insure that the total amount of circulation was conserved and a new nascent vortex was added. Using this condition, results of the velocity field aft of the trailing edge indicated that the Giesing-Maskell criterion was satisfied automatically. Results of the velocity field in the vortex street obtained from the analysis and the flow visualization data of the present work compare very nicely and also compare well with the work of Mathioulakis, et al. (1983). These results indicate that the ratio of the wave depth e to the vortex spacing a is increasing when the reduced frequency decreases. This indicates that as the reduced frequency decreases the vortex spacing increases and the street of vortices essentially spreads itself out.

In order to enhance the validity of the experimental results, tests involving a wider range of reduced frequencies should be performed. Also, the experiments in the region aft of the trailing edge of the fixed airfoil should be extended further downstream and the tracking of

the vortices around the airfoil should be performed on the bottom side in addition to those obtained on the top. Data involving lift and drag over both airfoils should be performed to study the aeroelastic effects at these high reduced frequencies. The condition of zero loading at the trailing edges of both airfoils should also be investigated and comparisons made with other work. Much of the follow-on work may require the use of a small wind tunnel as far as the investigation of surface pressure and zero trailing edge loading conditions are concerned.

Further tests with the analytical model should be performed with emphasis placed on the pressure distribution over the fixed airfoil. Also, the condition of zero loading at the edge could be investigated. These analytical experiments should be performed at various angles of attack and results should be compared with the pressure data from experiments.

The analysis presented in this work complemented nicely the guidelines of the experimental work and provided a mechanism by which several comparisons were drawn and evaluated. These evaluations expanded the scope of recent work in the area of unsteady aerodynamics.

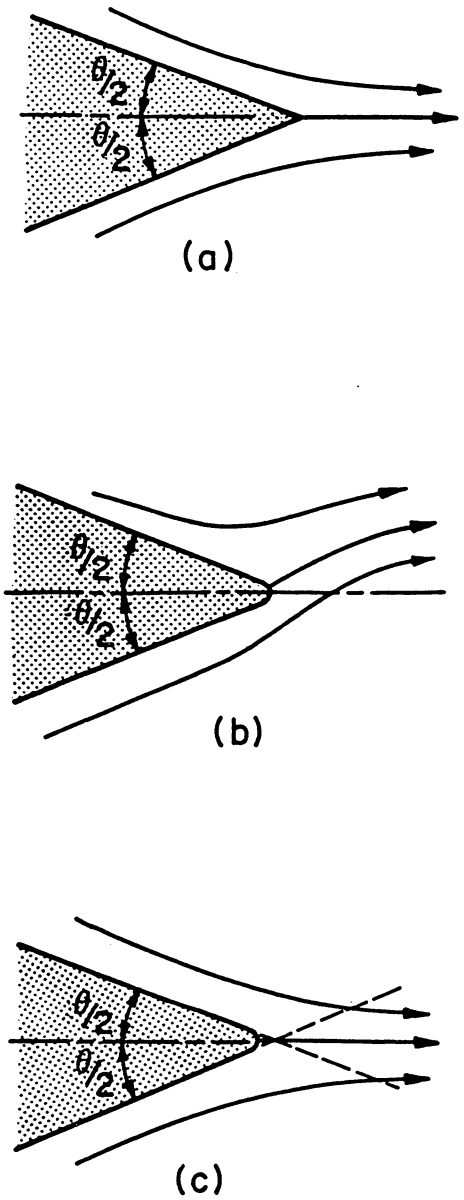

Fig. 1.1 Schematic representation of trailing edge streamlines for steady flow (a) sharp edge; (b,c) rounded edge.

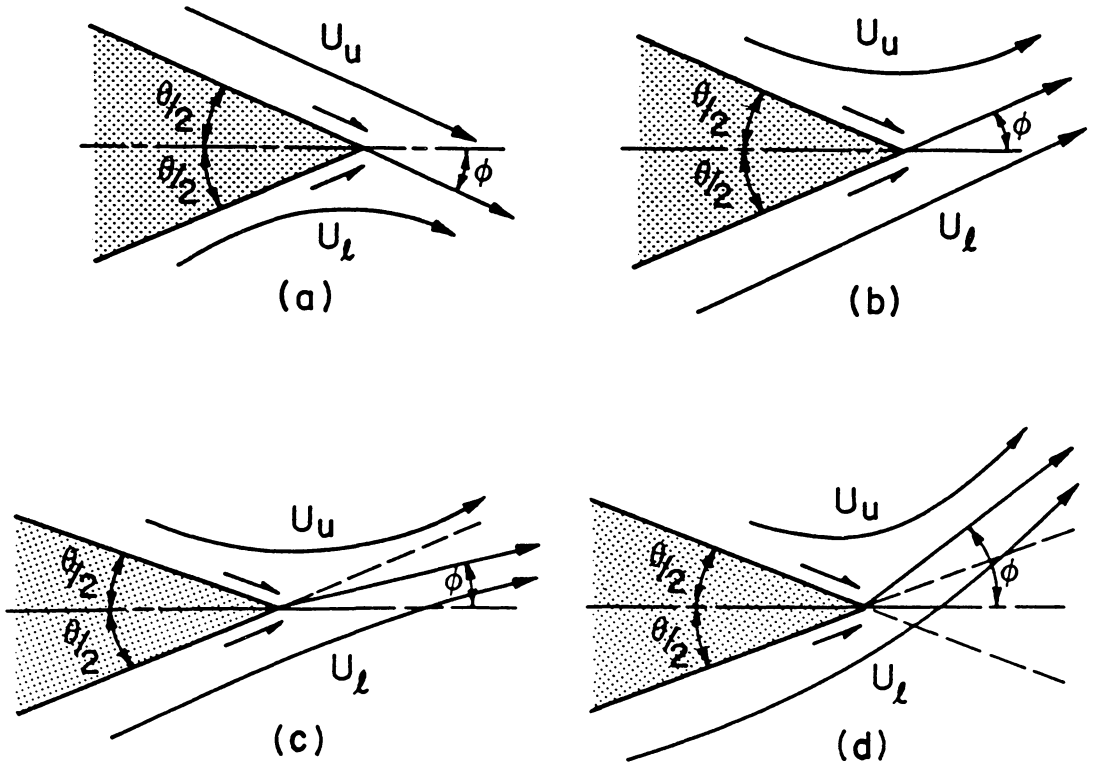

Fig. 1.2 Schematic representation of trailing edge streamlines for unsteady flow. (a) for $d\Gamma/dt<0$, shed vortices are in clockwise direction, (b) for $d\Gamma/dt>0$, shed vortices are in counterclockwise direction, (c) if $\phi<\theta/2$, then $U_\ell=U_u=0$, (d) if $\phi>\theta/2$, then one of U_ℓ and U_u is singular.

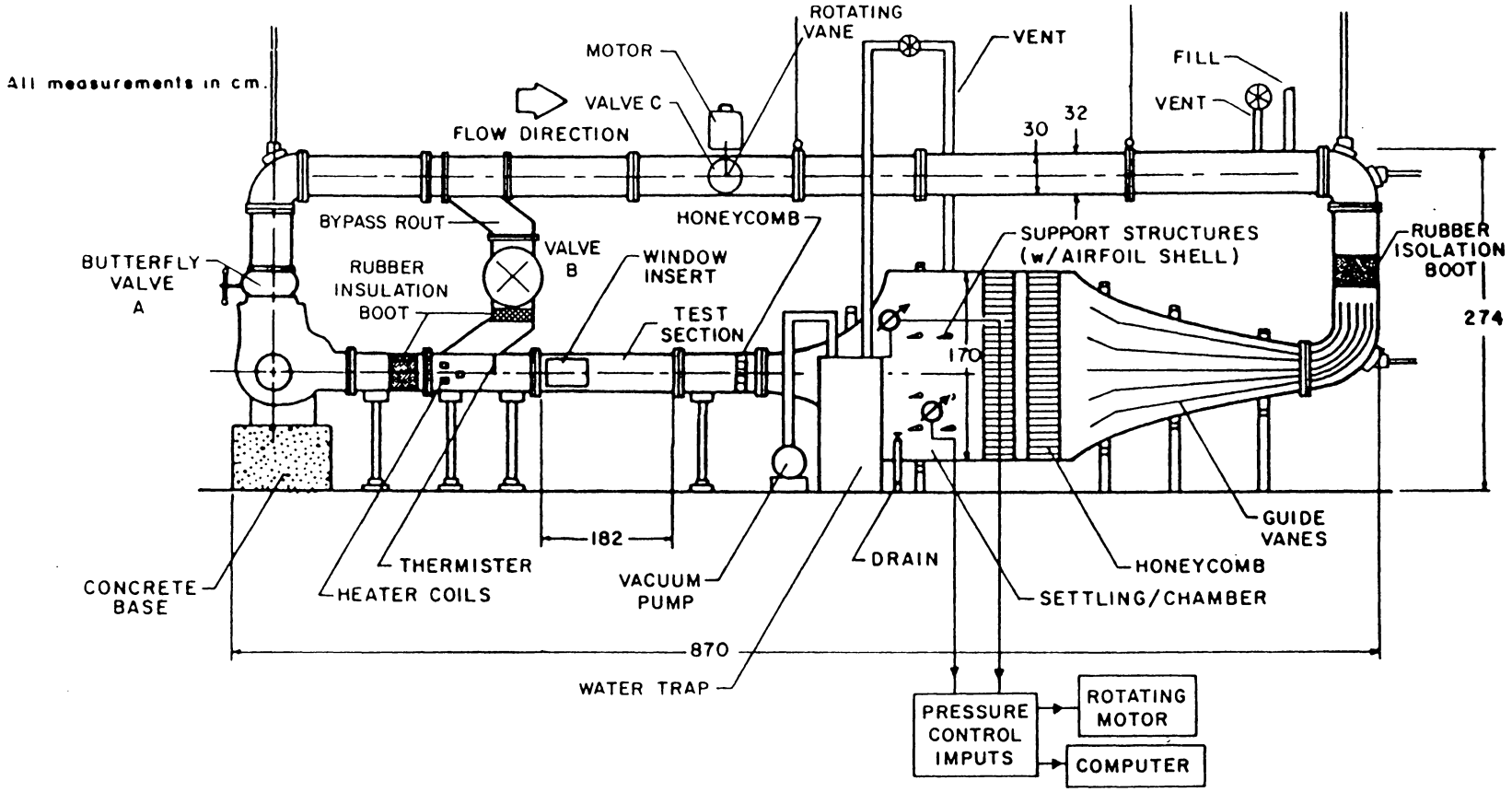

Fig. 2.1 The ESM water tunnel.

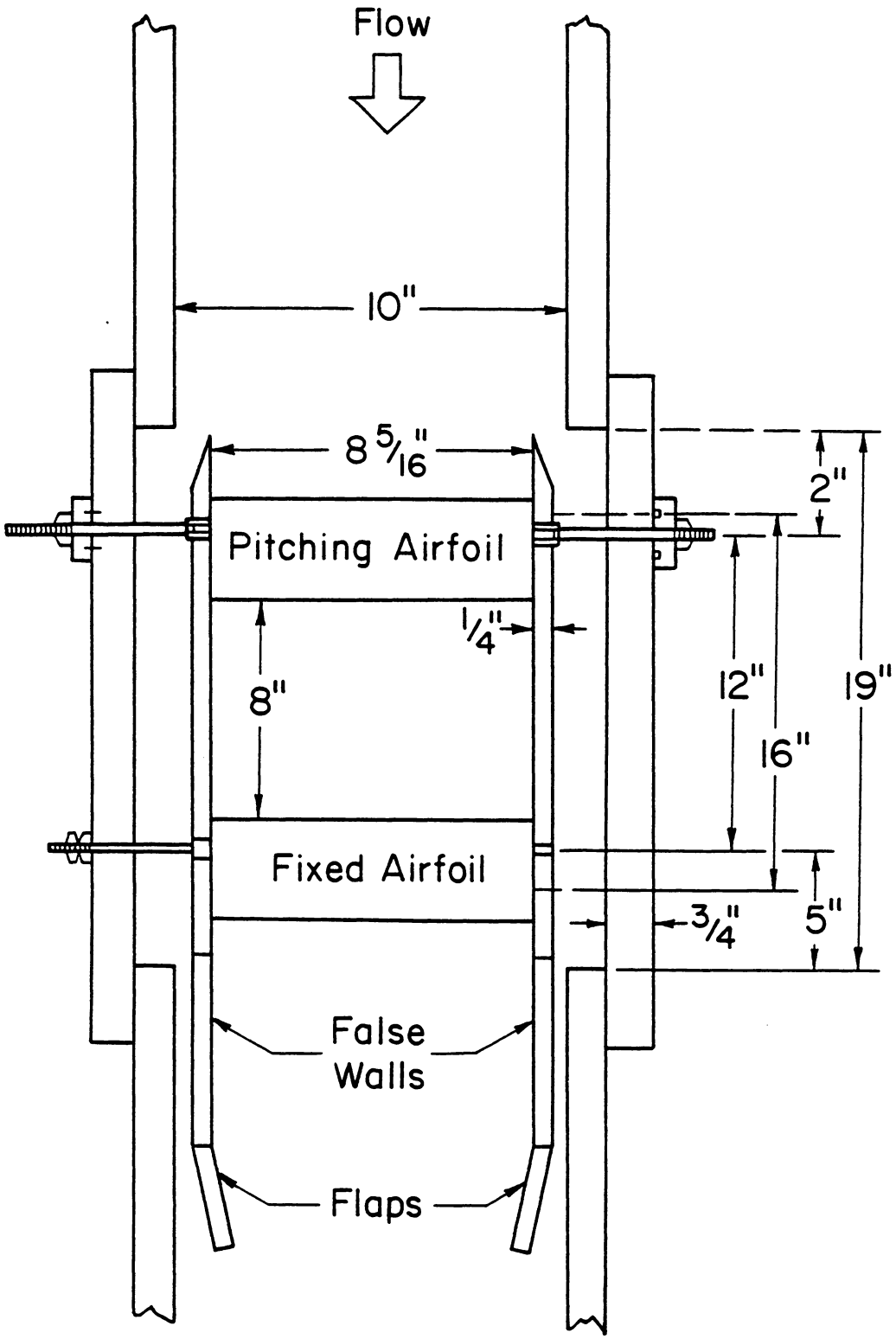

Fig. 2.2.1 Top view of test section showing the airfoils attached to the false walls.

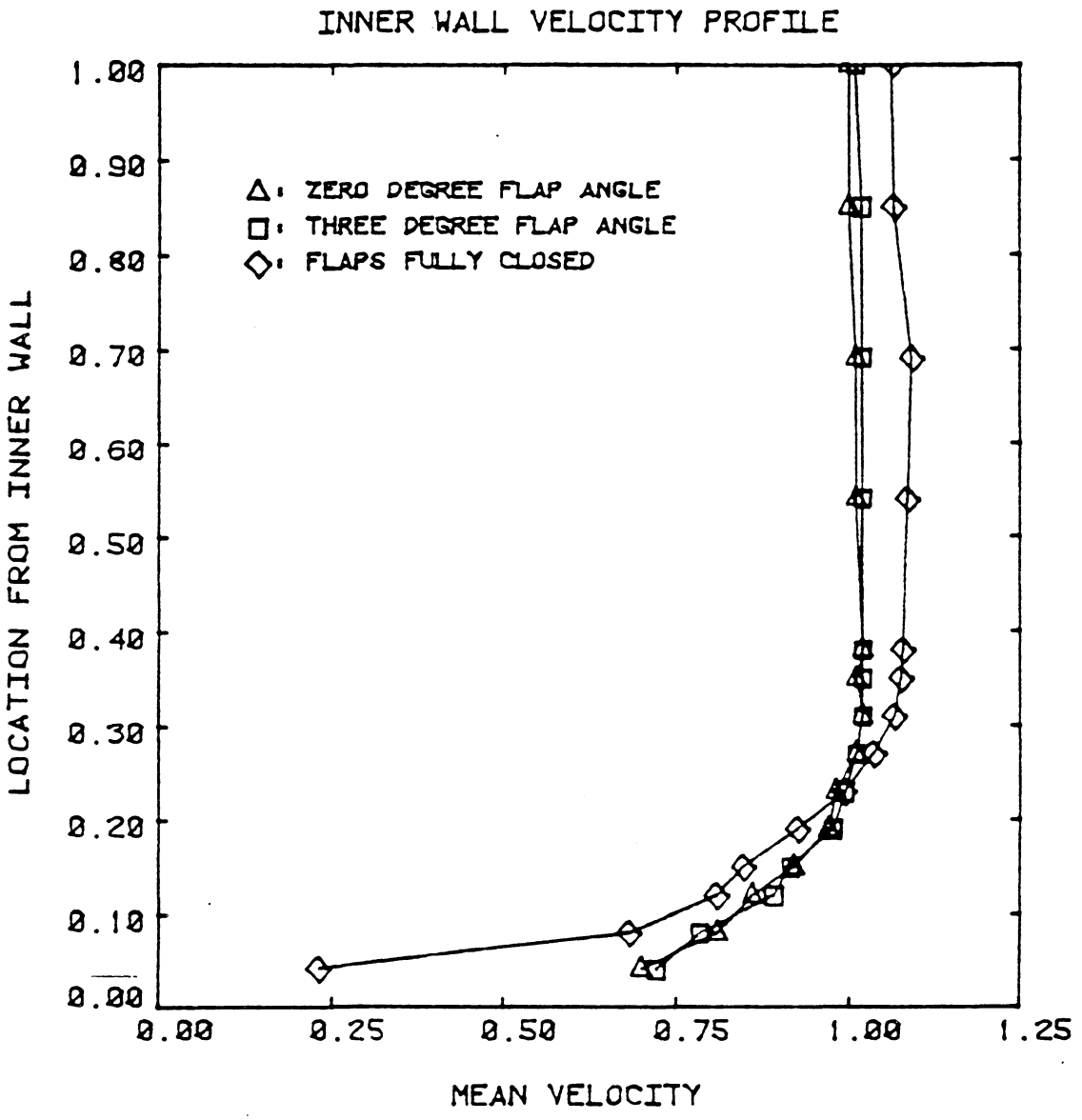

Fig. 2.2.2 Velocity profile on the inside of the false wall with a free stream velocity of 20 cm/sec. (The vertical scale is a percentage of one-third the airfoil span)

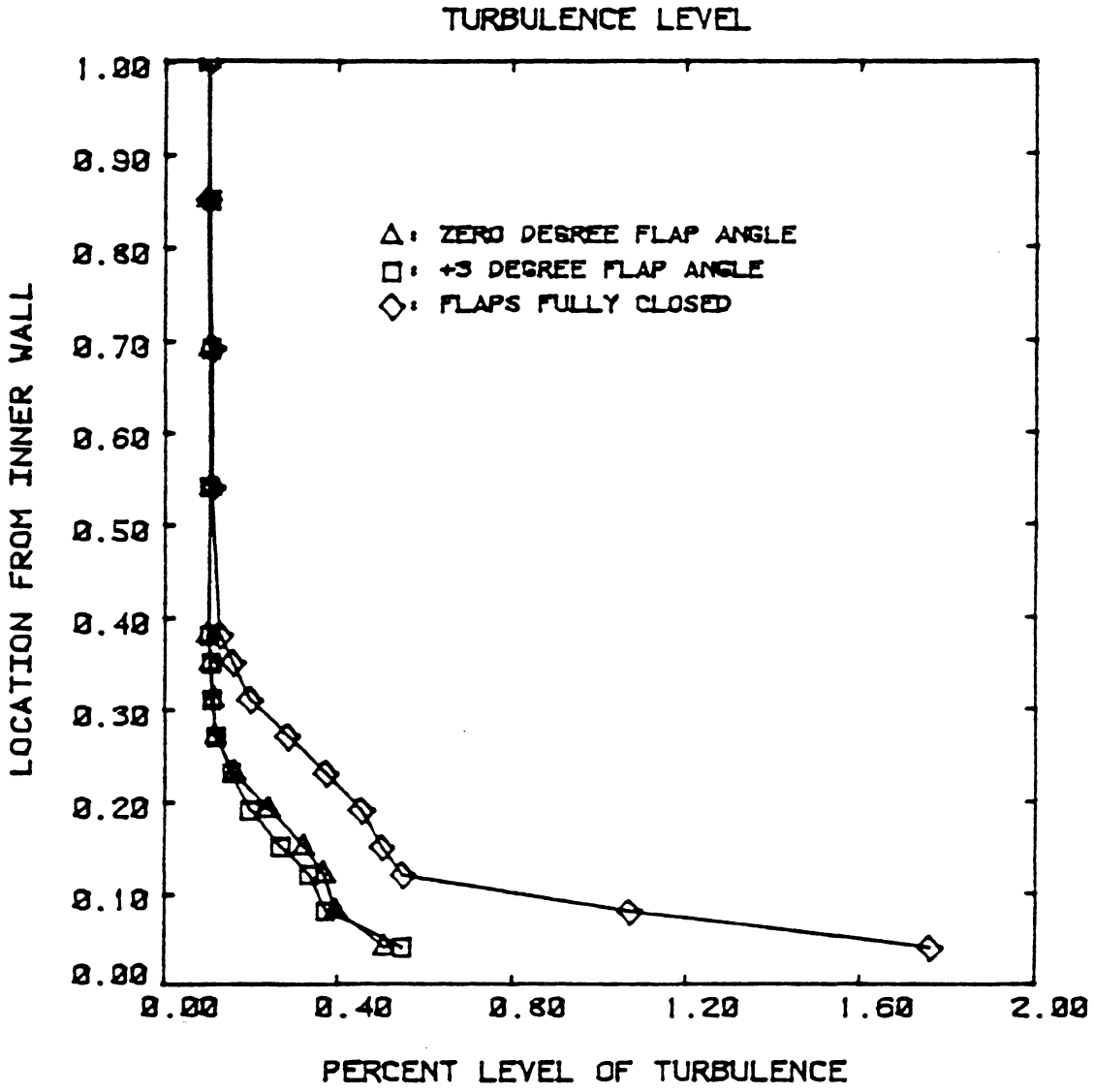

Fig. 2.2.3 Turbulence level on the inside of the false wall with a free stream velocity of 20 cm/sec. (The vertical scale is a percentage of one-third the airfoil span)

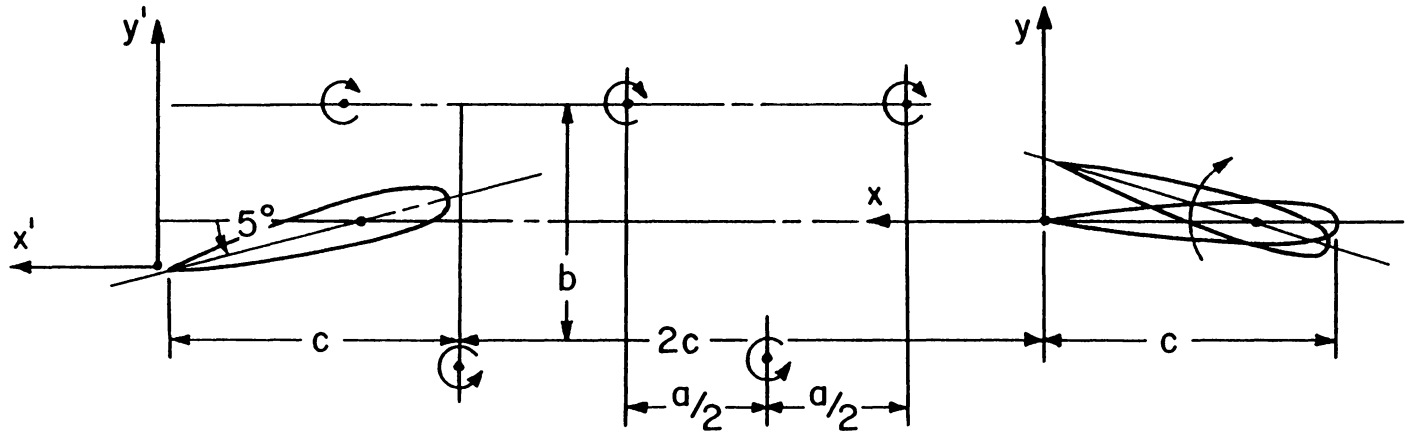

Fig. 2.3.1 Basic experimental configuration.

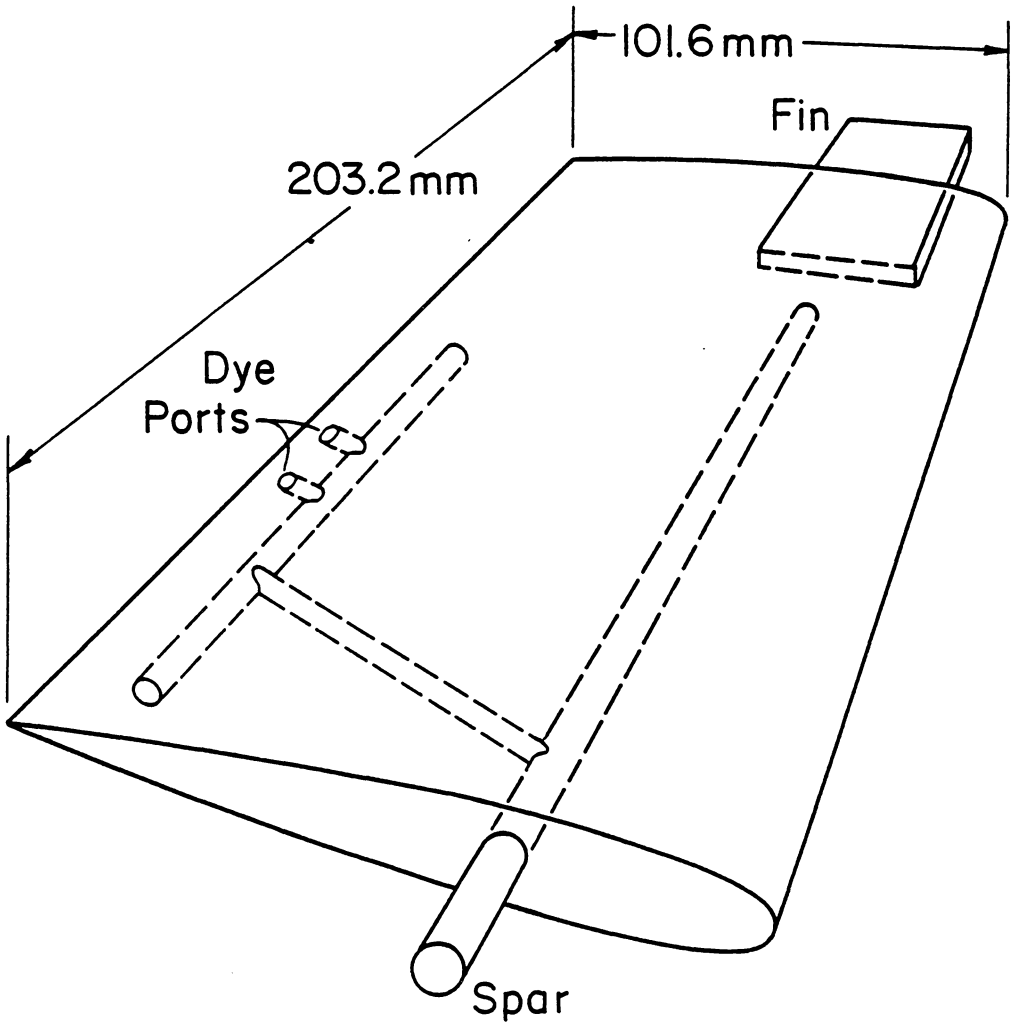

Fig. 2.3.2 NACA 0012 model airfoil instrumented for dye injection at 80% chord.

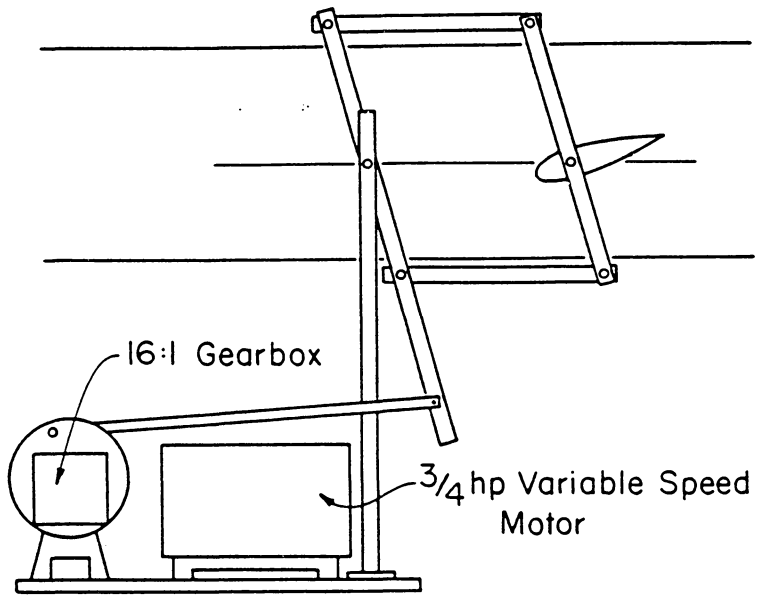

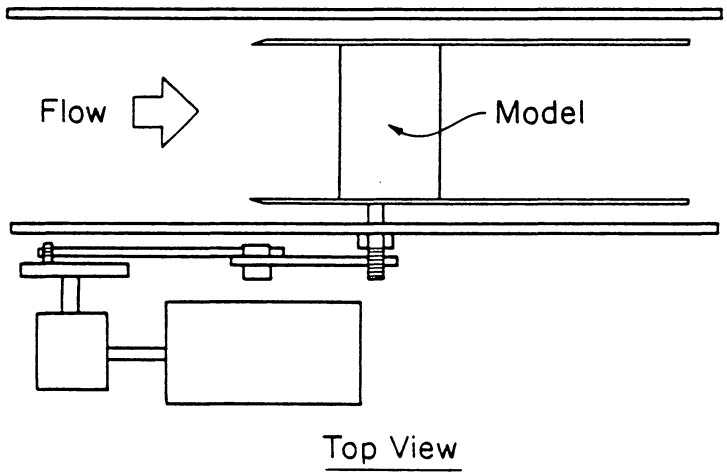

Fig. 2.3.3 Four-bar oscillating mechanism.

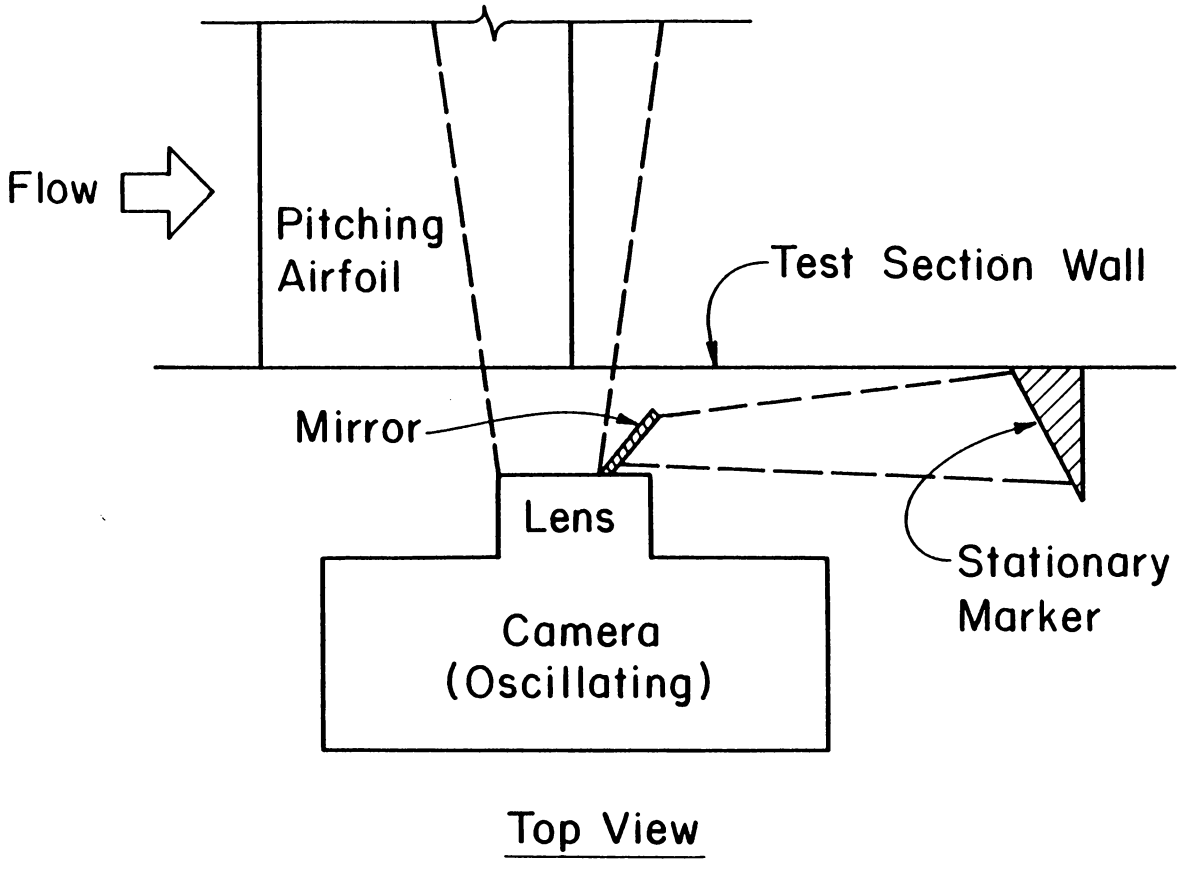

Fig. 2.4.1 Flow visualization configuration using a moving reference frame.

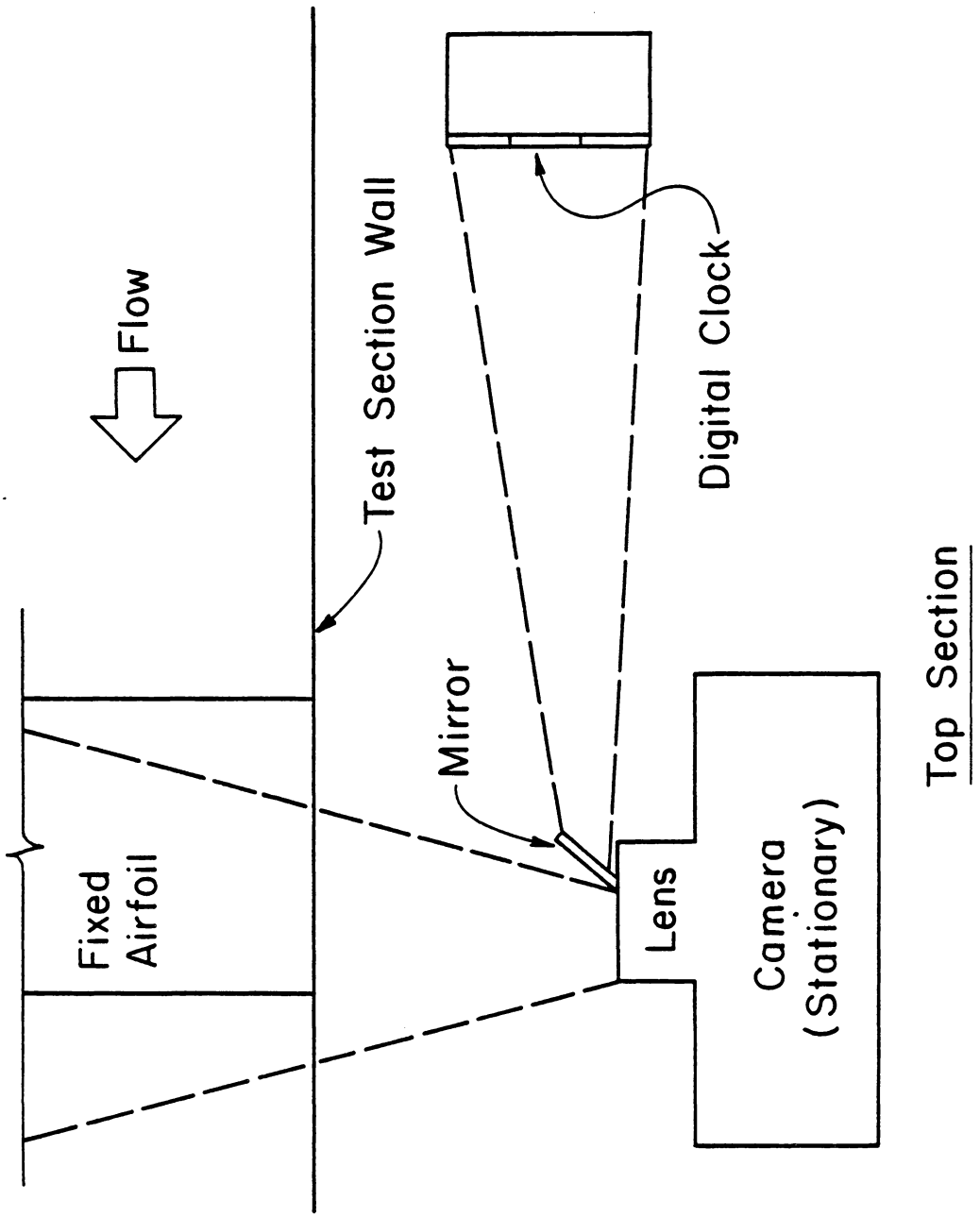

Fig. 2.4.2 Flow visualization configuration using a fixed reference frame.

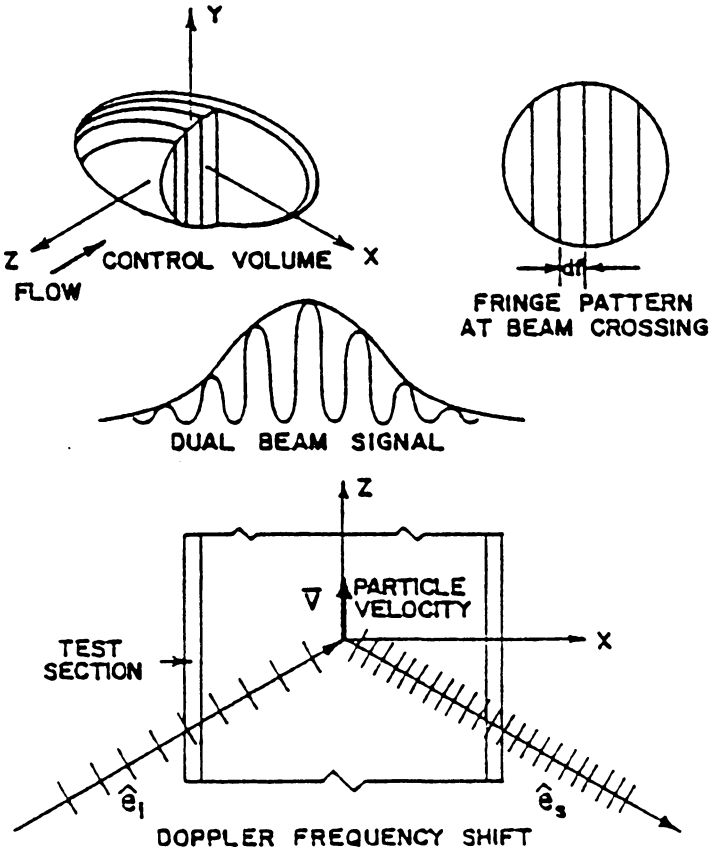

Fig. 2.5.1 Schematic of the principles of laser doppler velocimetry.

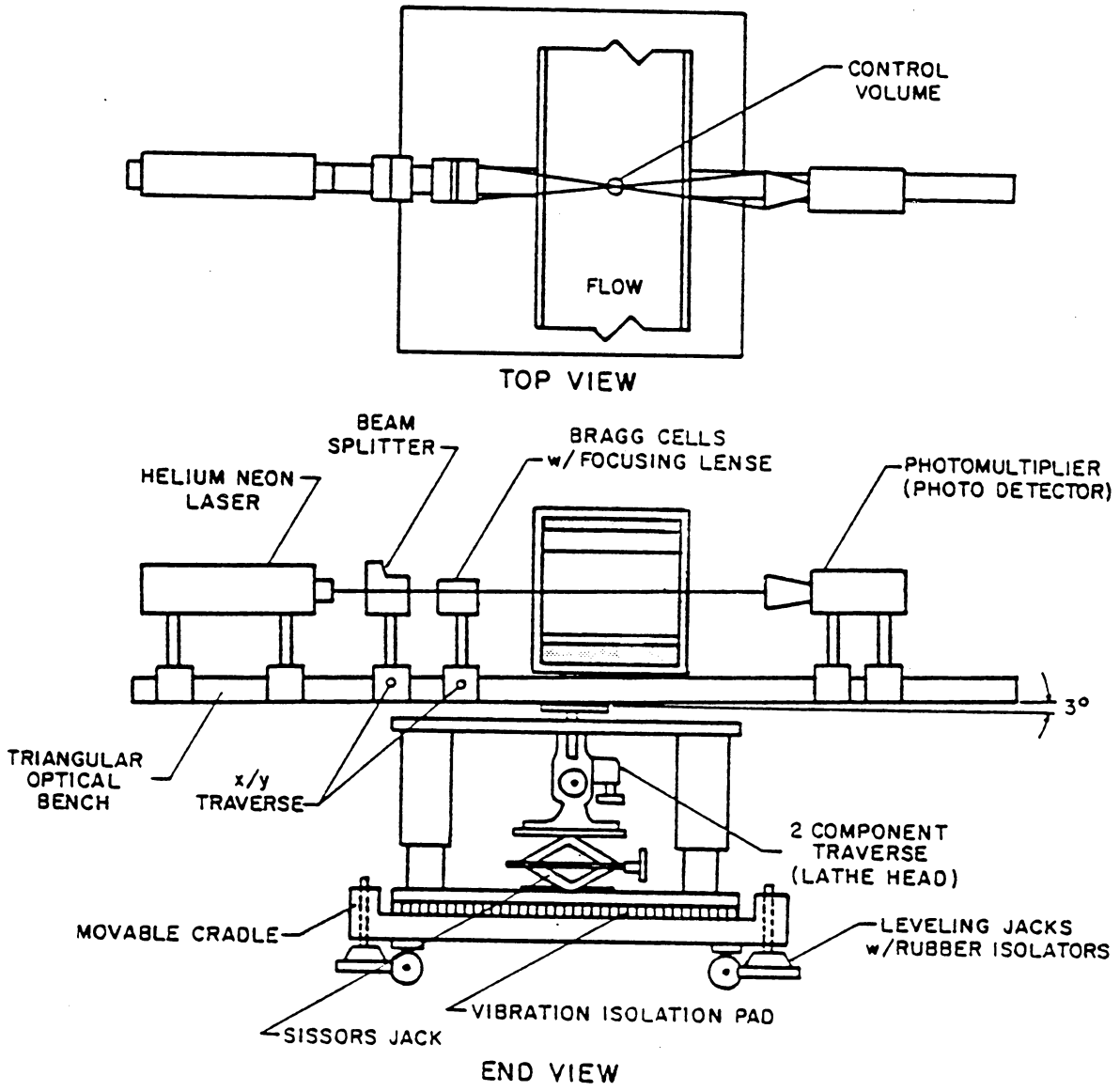

Fig. 2.5.2 The laser traversing mechanism showing ground support and mobility structure.

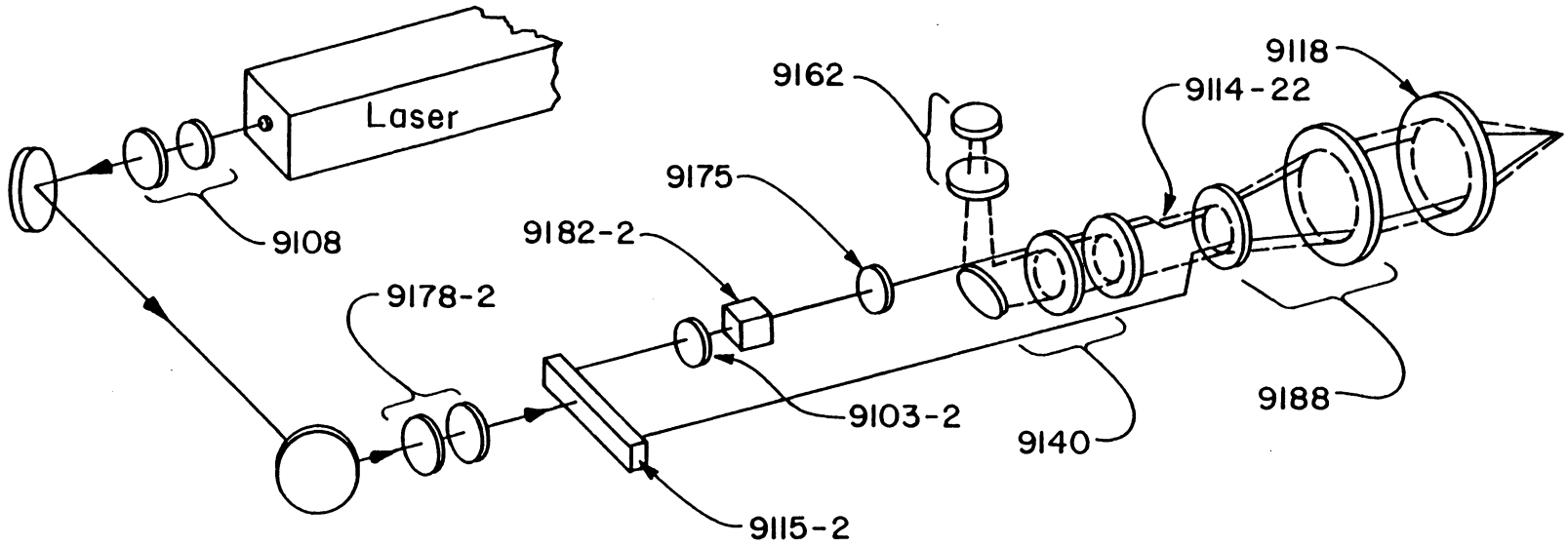

9118	Achromatic lens with focal length 250 mm
9188	Beam expander
9114-22	Beam spacer
9140	Receiving assembly
9162	Photodetector
9175	Beam Steering module
9182-2	Bragg-cell of 40 MHz
9103-2	Polarization rotator
9115-2	Beam splitter of equal intensity
9178-2	Rotating mount
9108	Collimator

Fig. 2.5.3 The TSI optical train.

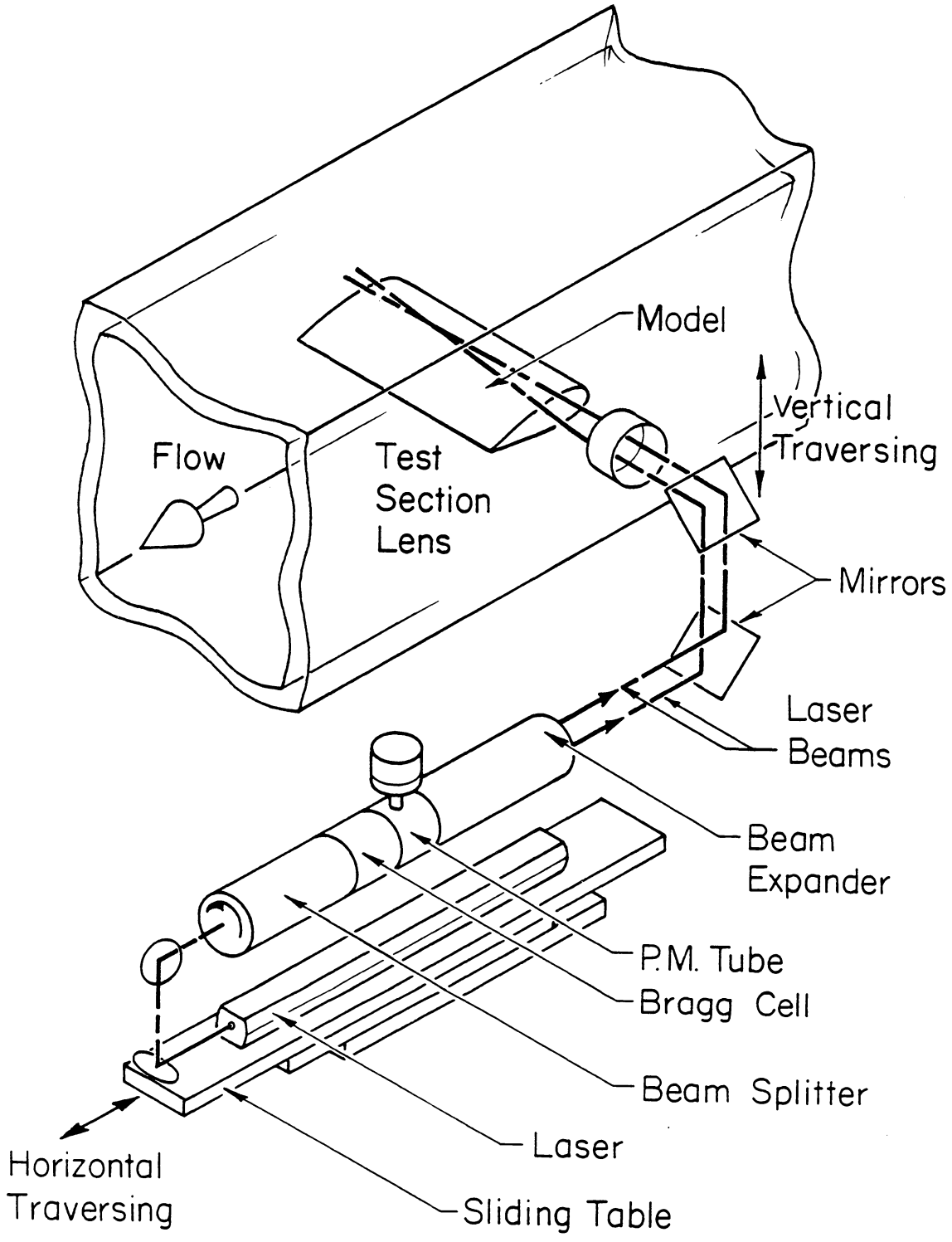

Fig. 2.5.4 Sliding table and traversing mechanism.

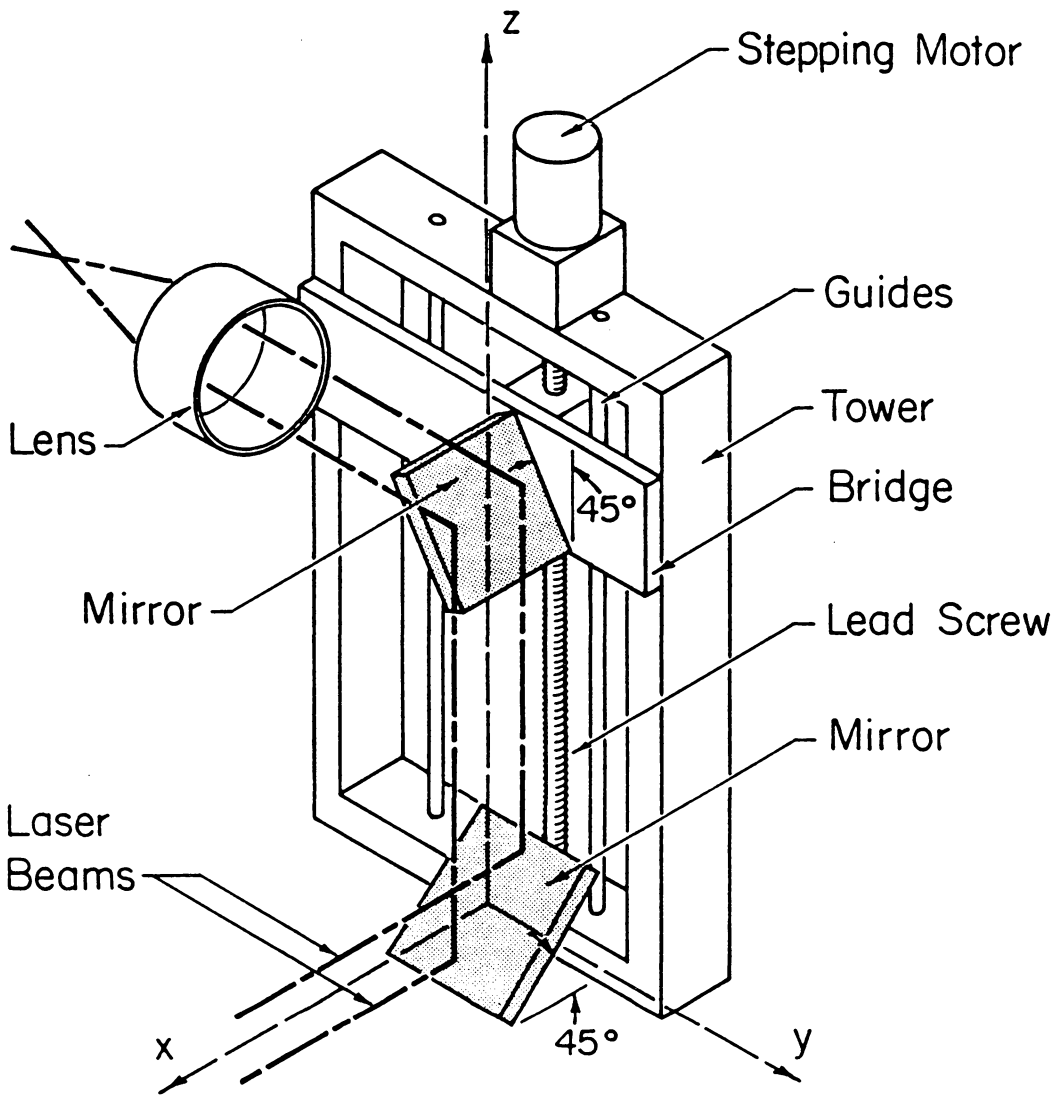

Fig. 2.5.5 Traversing mechanism for LDV measurements.

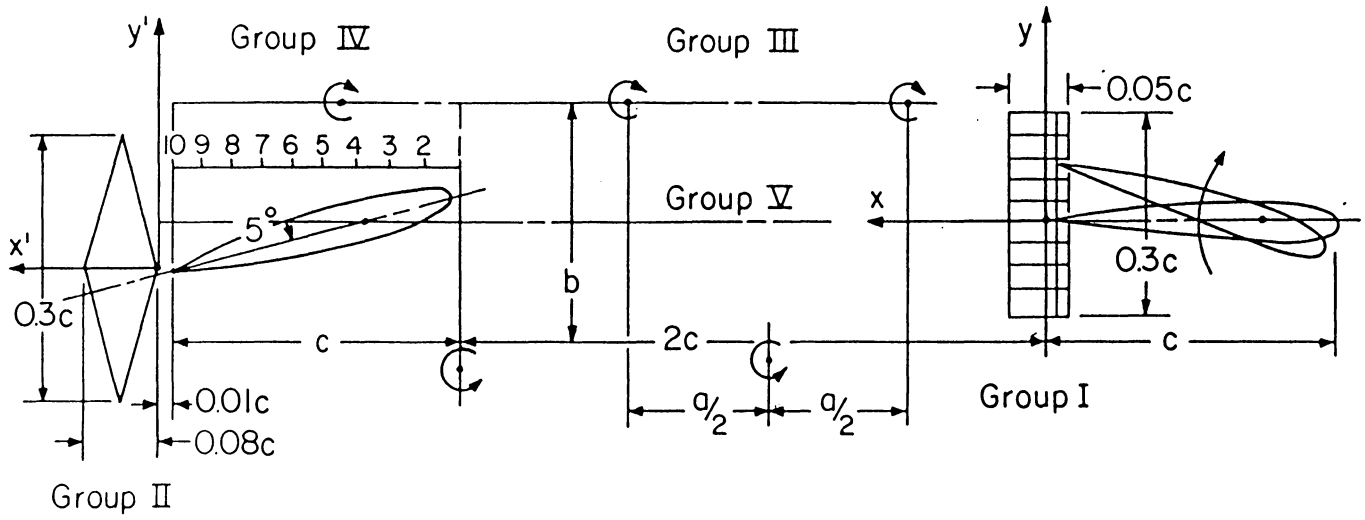

Fig. 3.2.1 Schematic representation of the experimental arrangement. General grid layout showing the 5 groups of measuring points.

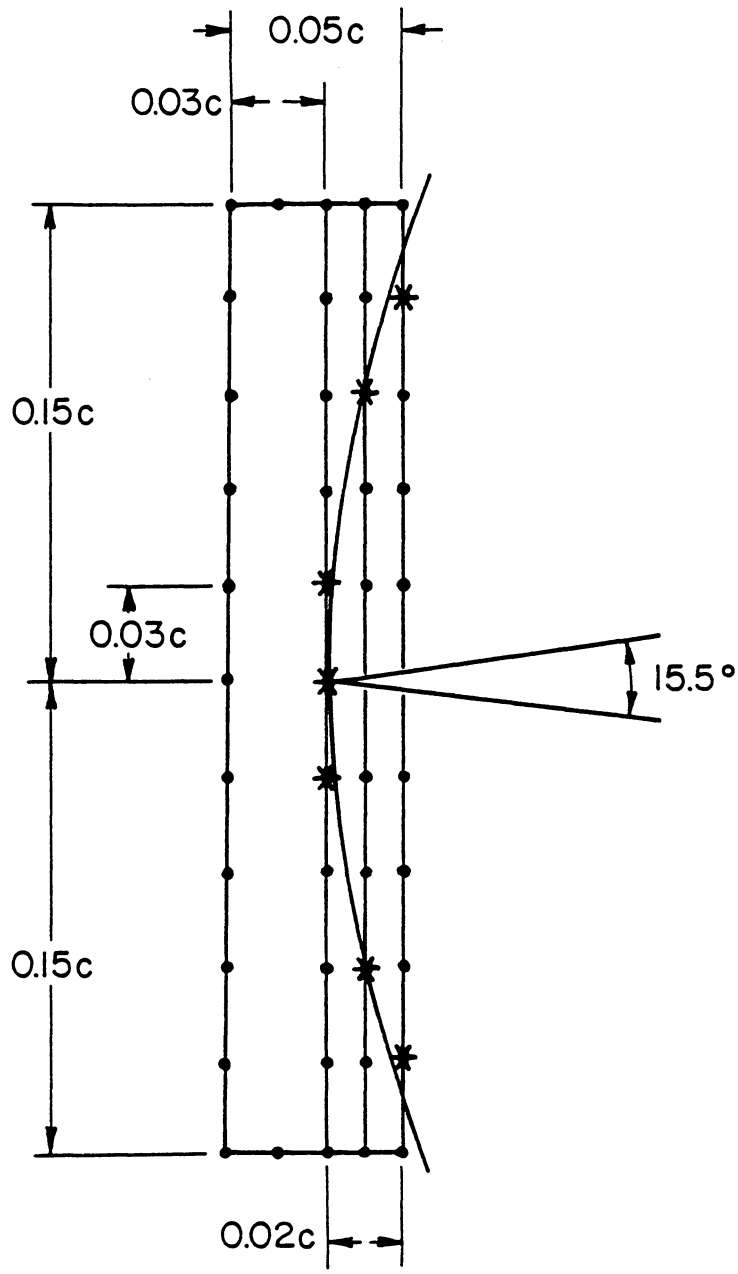

Fig. 3.2.2 The grid points of group I.

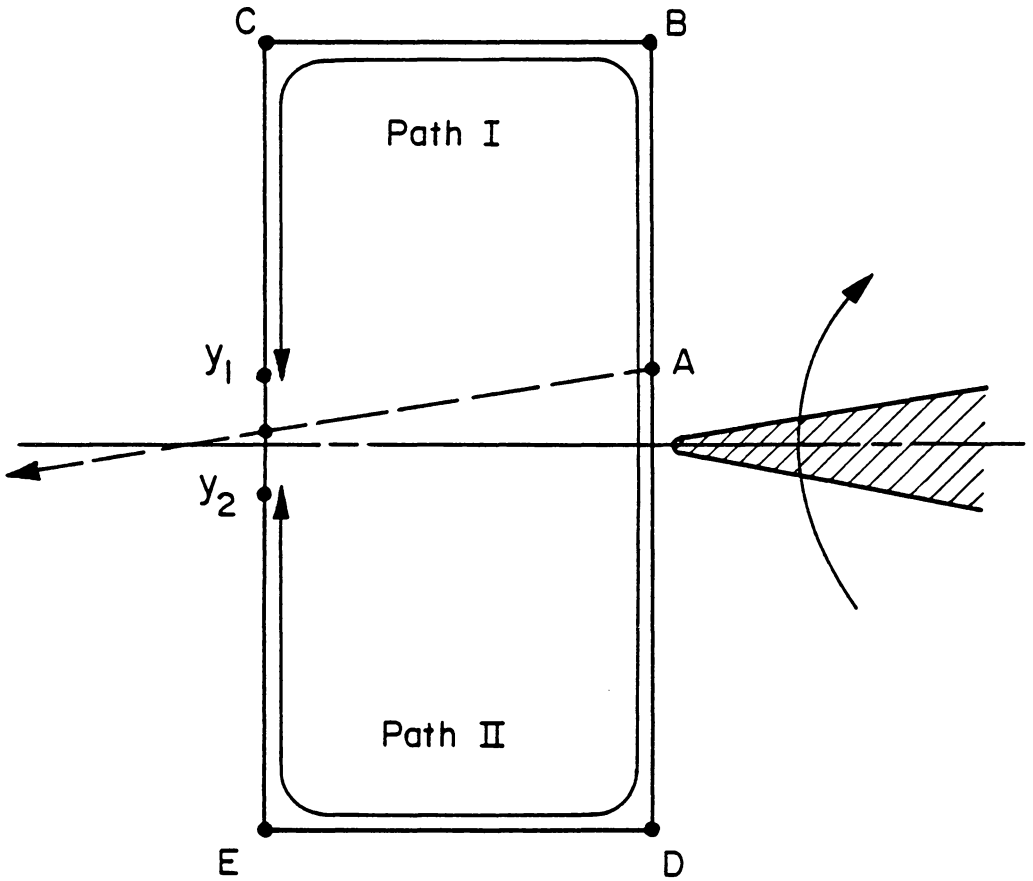

Fig. 3.2.3 Streamline integration paths starting at point A for the pitching airfoil with a non-rotating reference frame.

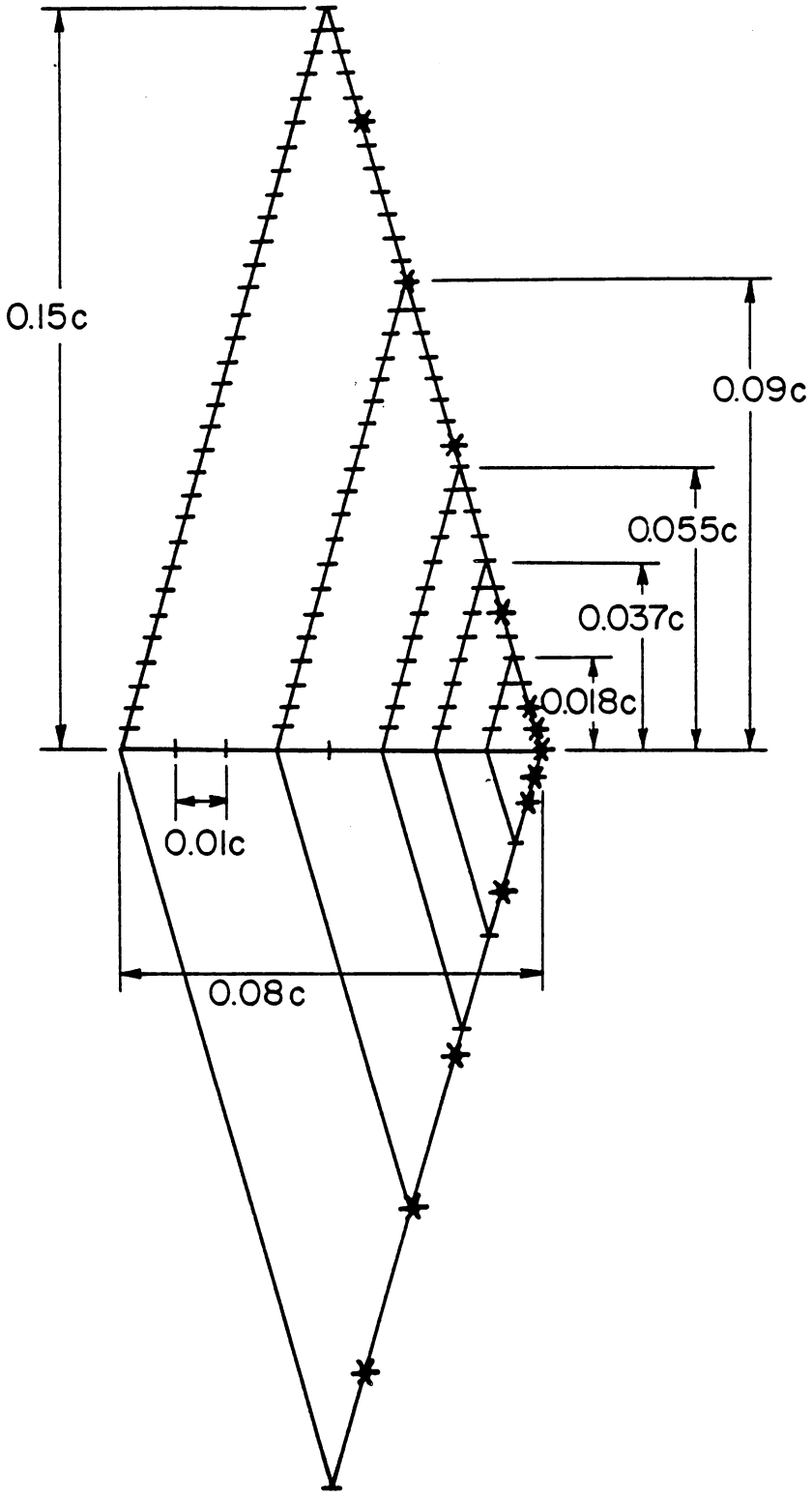

Fig. 3.2.4 The grid points of Group II.

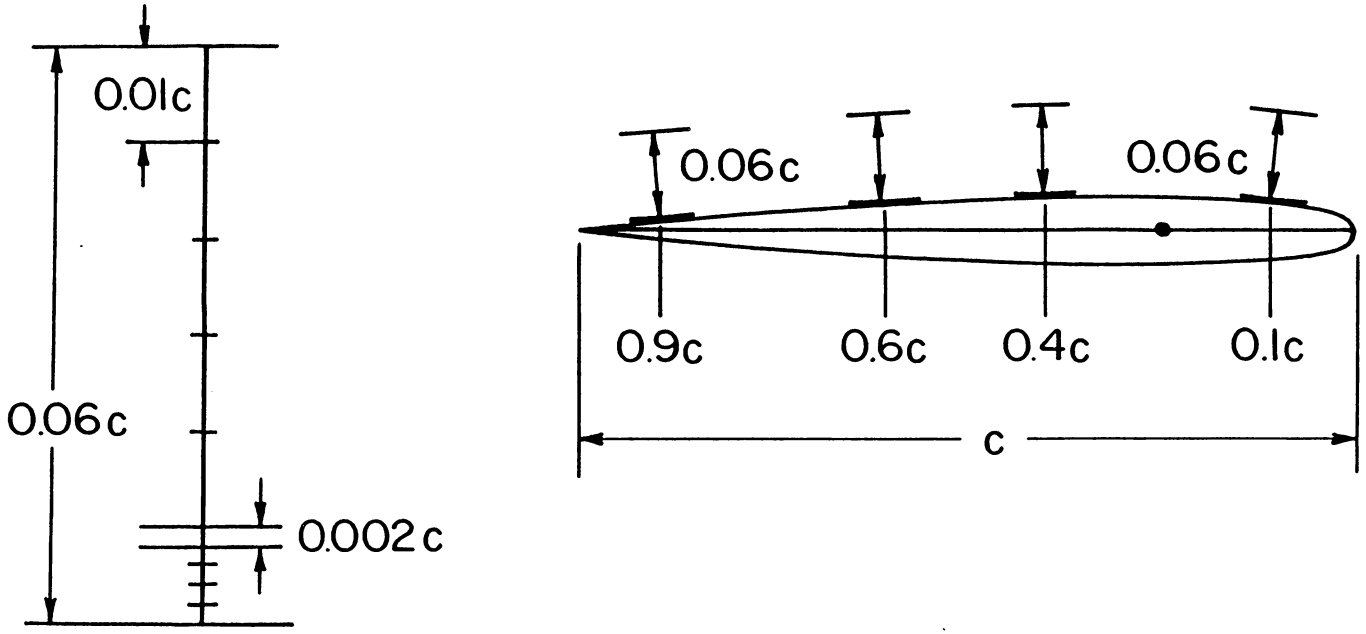

Fig. 3.2.5 Dimensions of the measuring grid for the fixed airfoil boundary layer measurements at a 0° angle of attack.

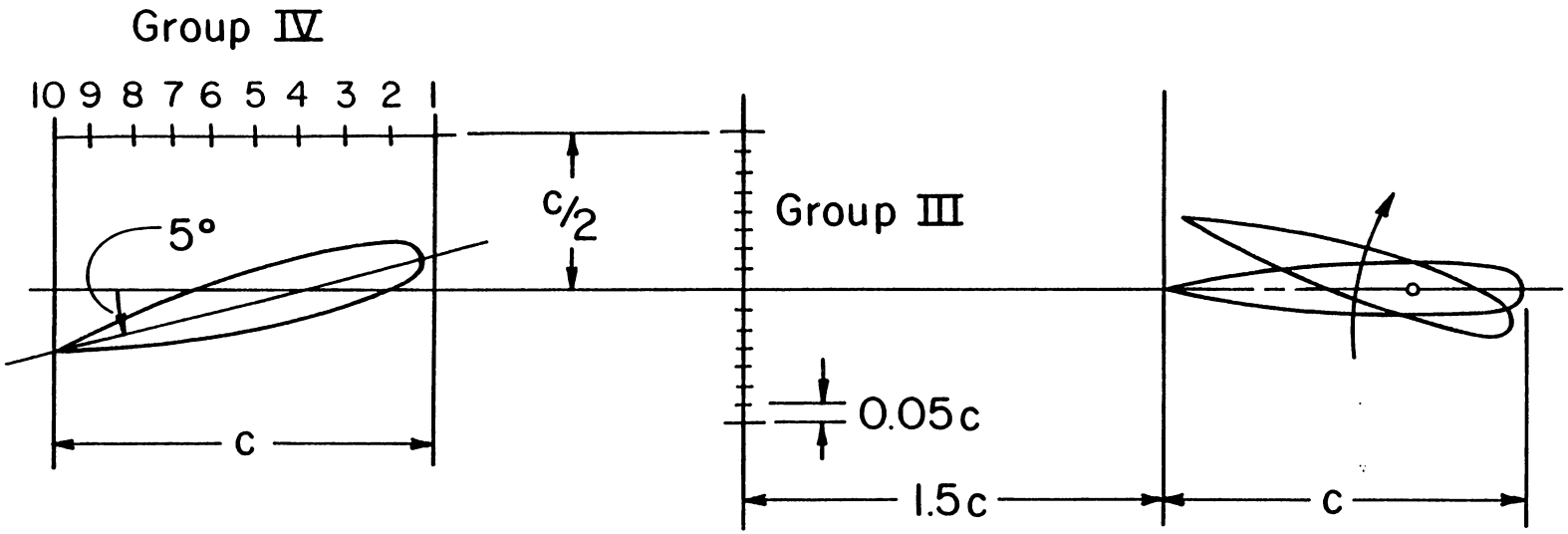

Fig. 3.2.6 Dimensions for the vortex tracking measurements.

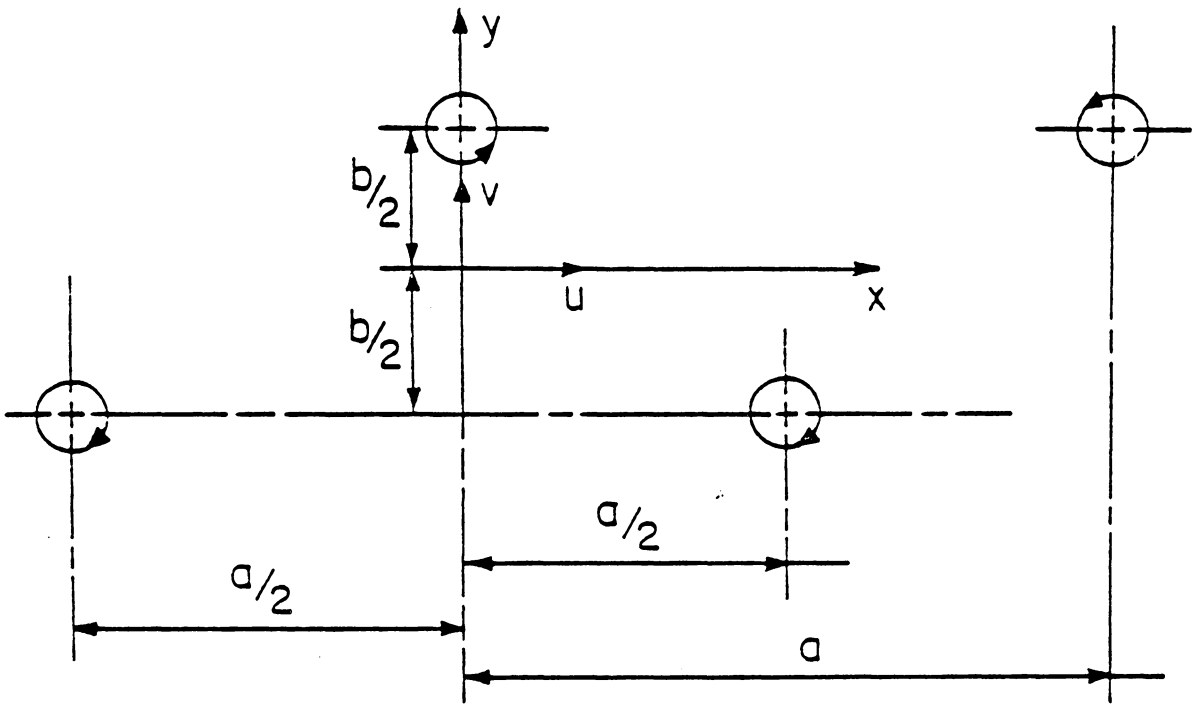

Fig. 3.2.7 Vortex street.

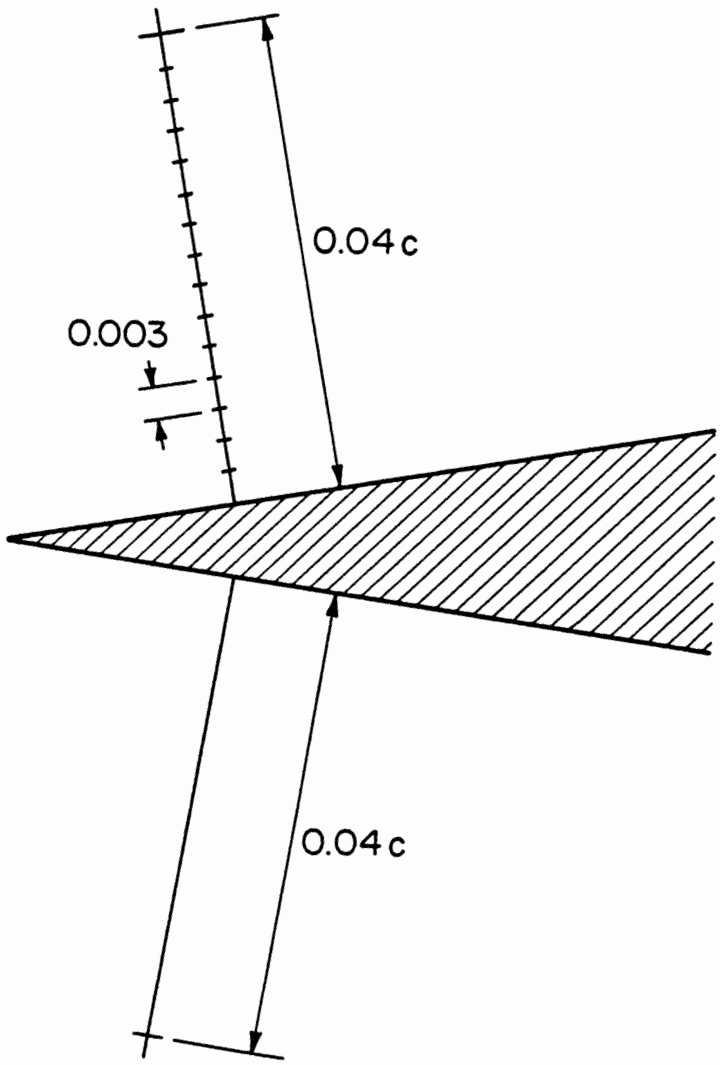

Fig. 3.2.8 Trailing edge boundary layer measuring grid at 98% chord on the fixed airfoil.

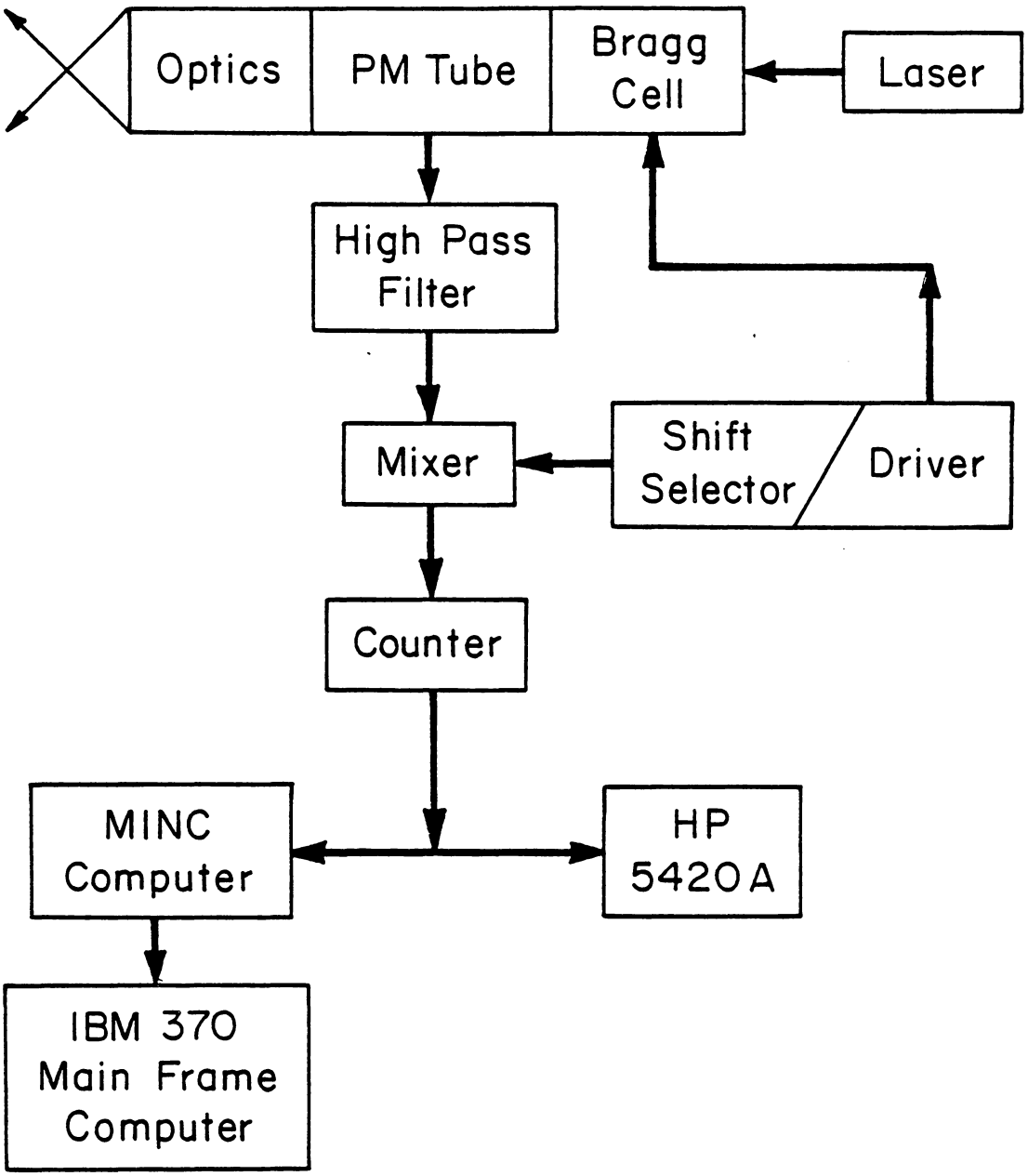

Fig. 3.2.9 Data acquisition system.

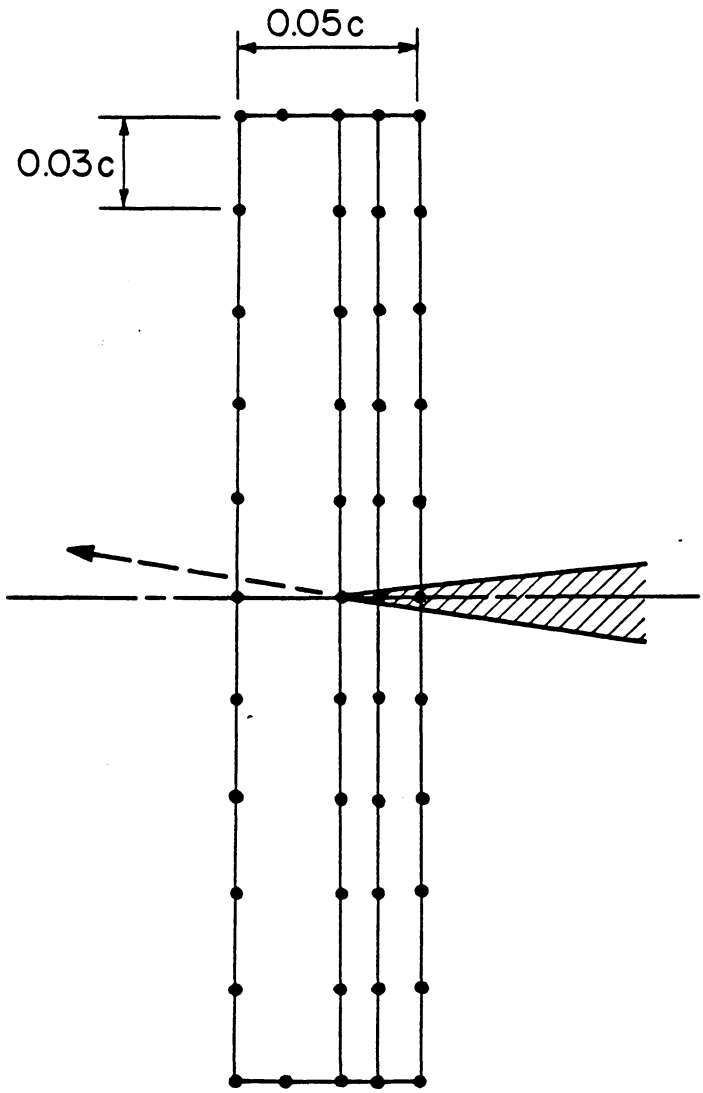

Fig. 3.3.1(a) Instantaneous trailing edge streamline at the instant when $\alpha=0°$ during a downstroke (K=2.4).

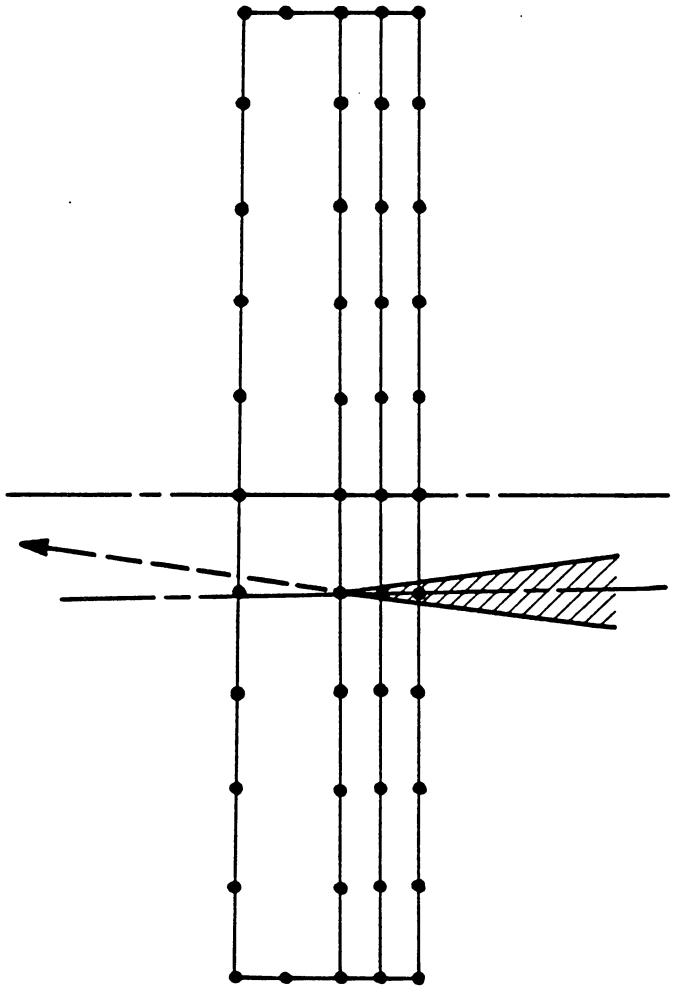

Fig. 3.3.1(b) Instantaneous trailing edge streamline at the instant when α=-2.25° which corresponds to the trailing edge position at x=-0.02c and y=-0.03c during a downstroke (K=2.4).

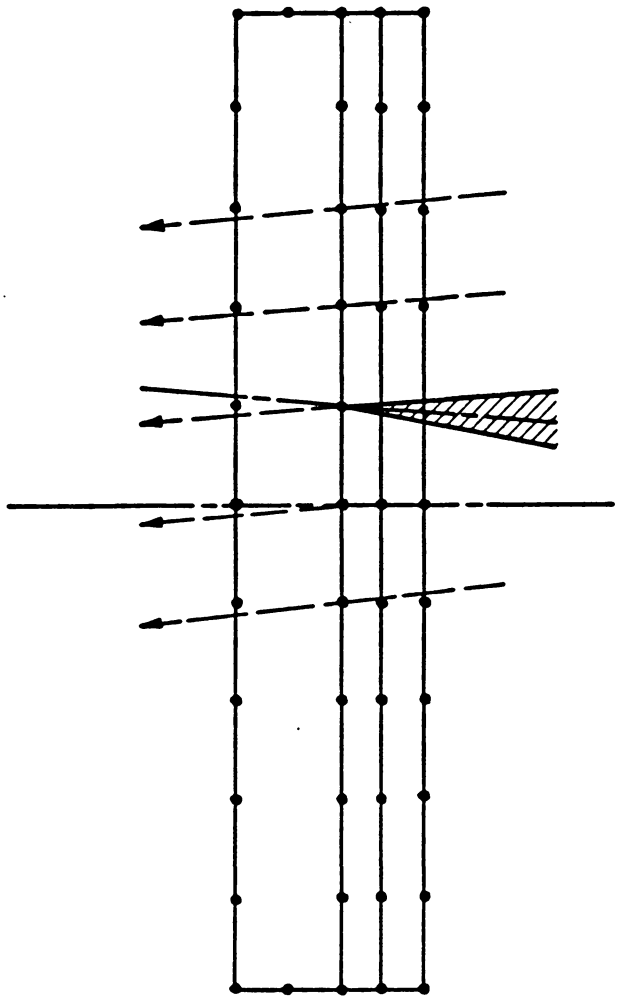

Fig. 3.3.2(a) Instantaneous trailing edge streamline at the instant when α=2.25° which corresponds to the trailing edge position at x=-0.02c and y=0.03c during an upstroke (K=2.4).

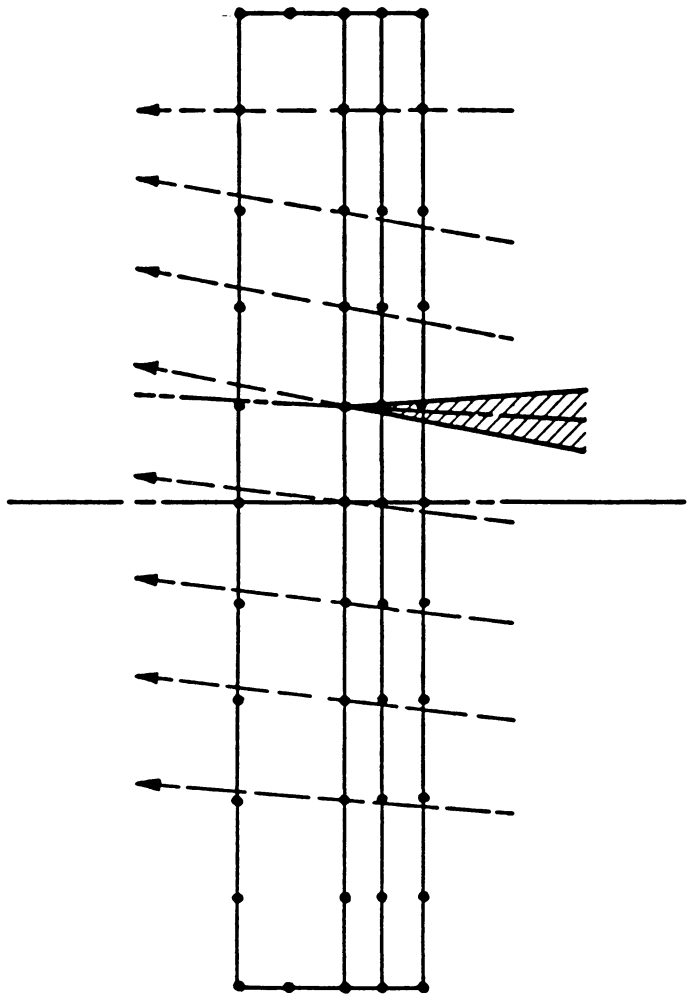

Fig. 3.3.2(b) Instantaneous trailing edge streamline at the instant when α=2.25° which corresponds to the trailing edge position at x=-0.02c and y=0.03c during a downstroke (K=2.4).

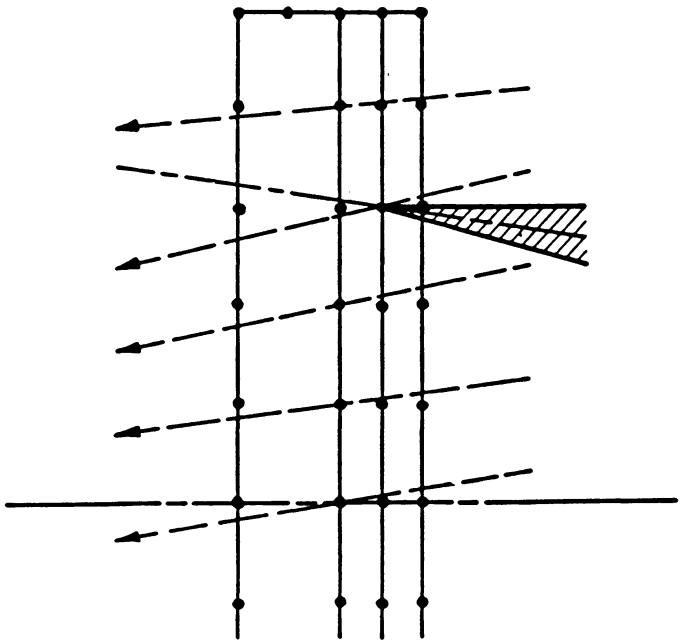

Fig. 3.3.3(a) Instantaneous trailing edge streamline at the instant when α=6.82° which corresponds to the trailing edge position at x=-0.01c and y=0.09c during an upstroke (K=2.4).

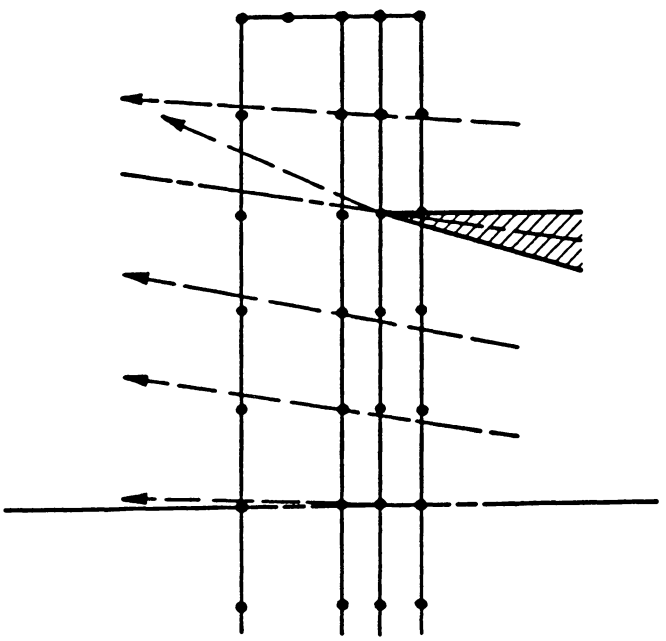

Fig. 3.3.3(b) Instantaneous trailing edge streamline at the instant when α=6.82° which corresponds to the trailing edge position at x=-0.01c and y=0.09c during a downstroke (K=2.4).

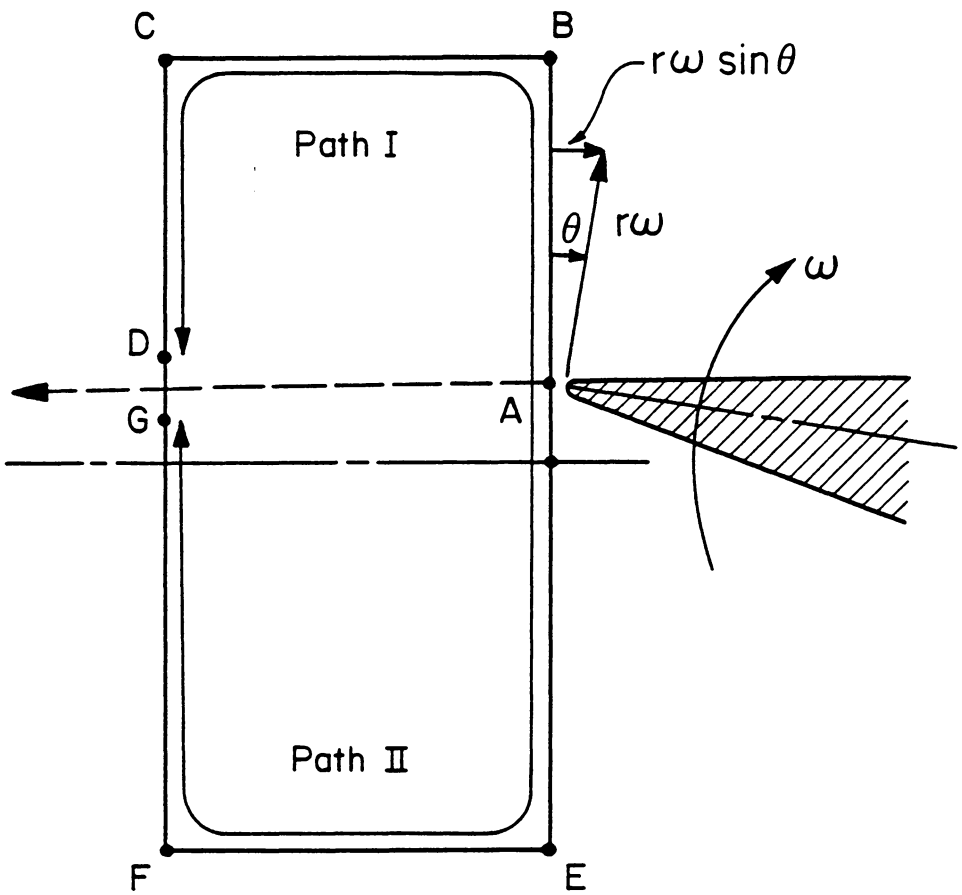

Fig. 3.3.4 Streamline integration paths starting at point A for the pitching airfoil with the frame of reference attached to the airfoil.

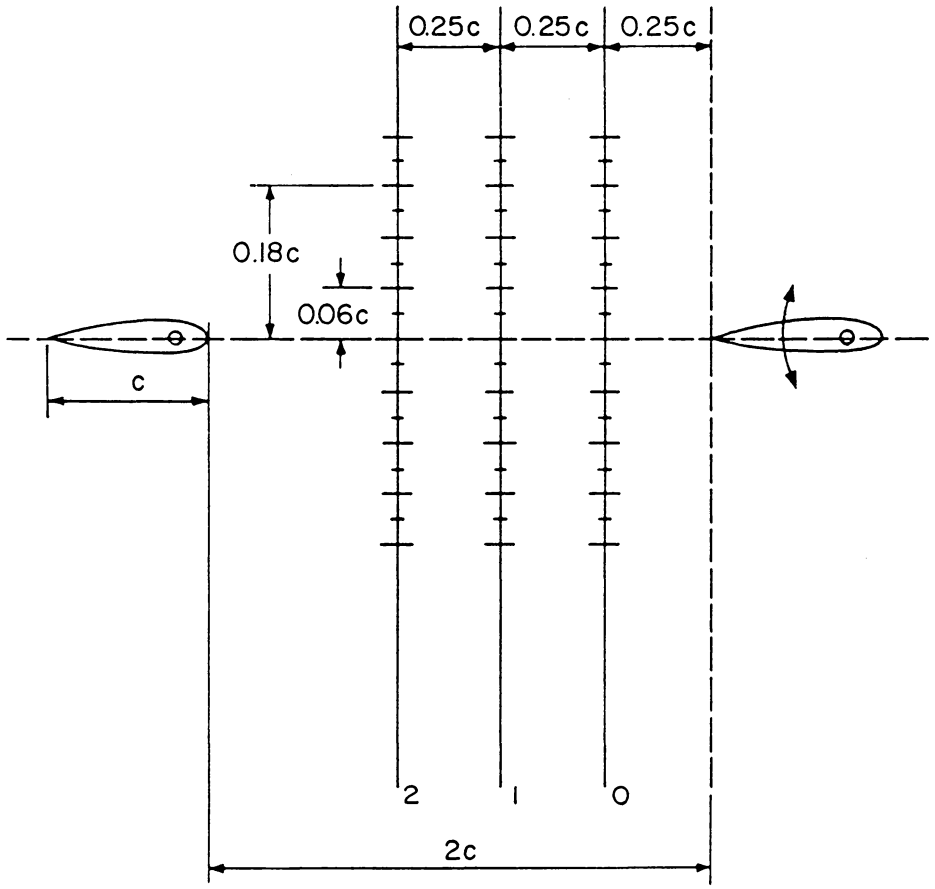

Fig. 3.3.5 The grid points of group V.

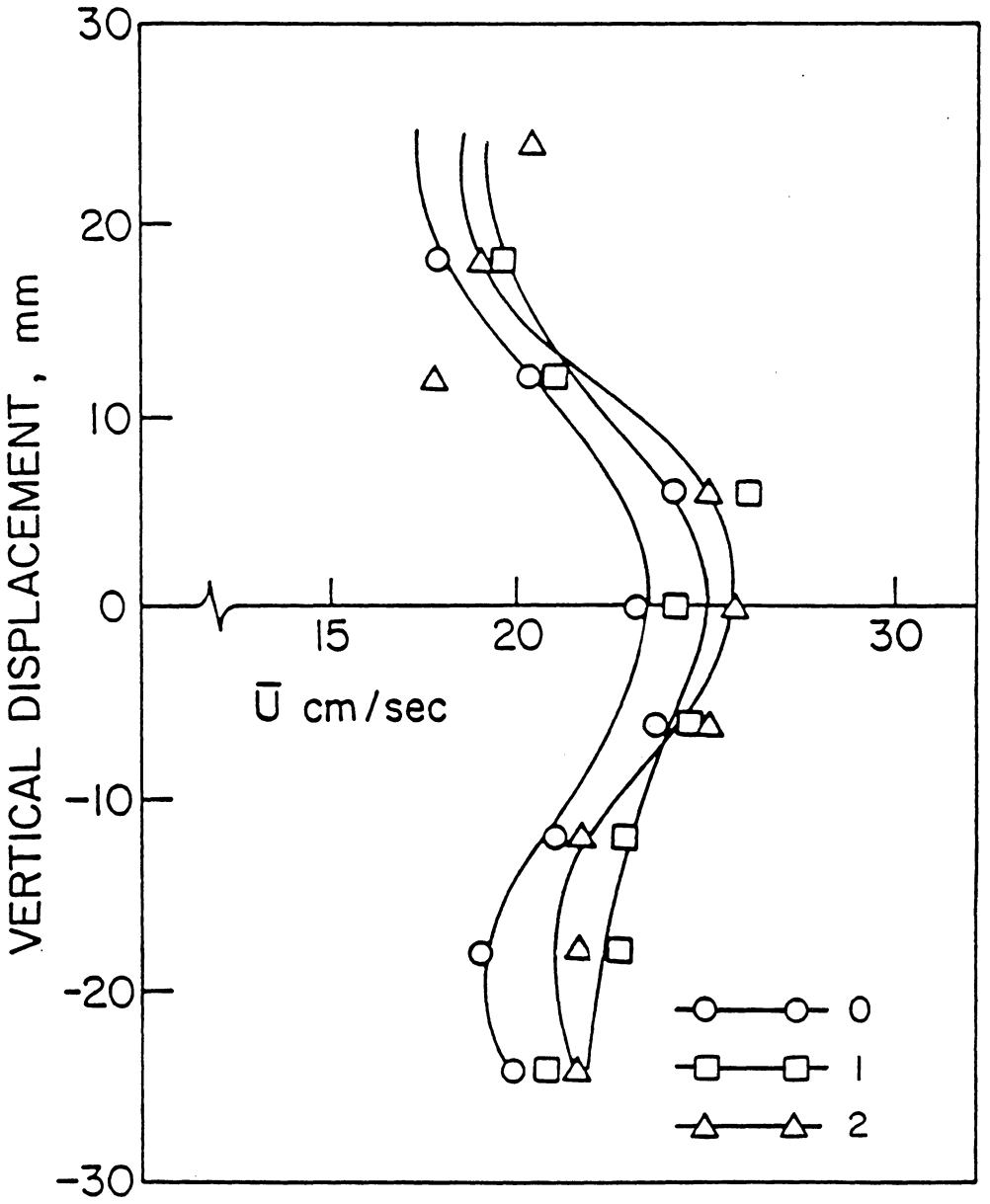

Fig. 3.3.6 Mean velocity in the wake of the oscillating airfoil (refer to Fig. 3.3.5 for the grid position).

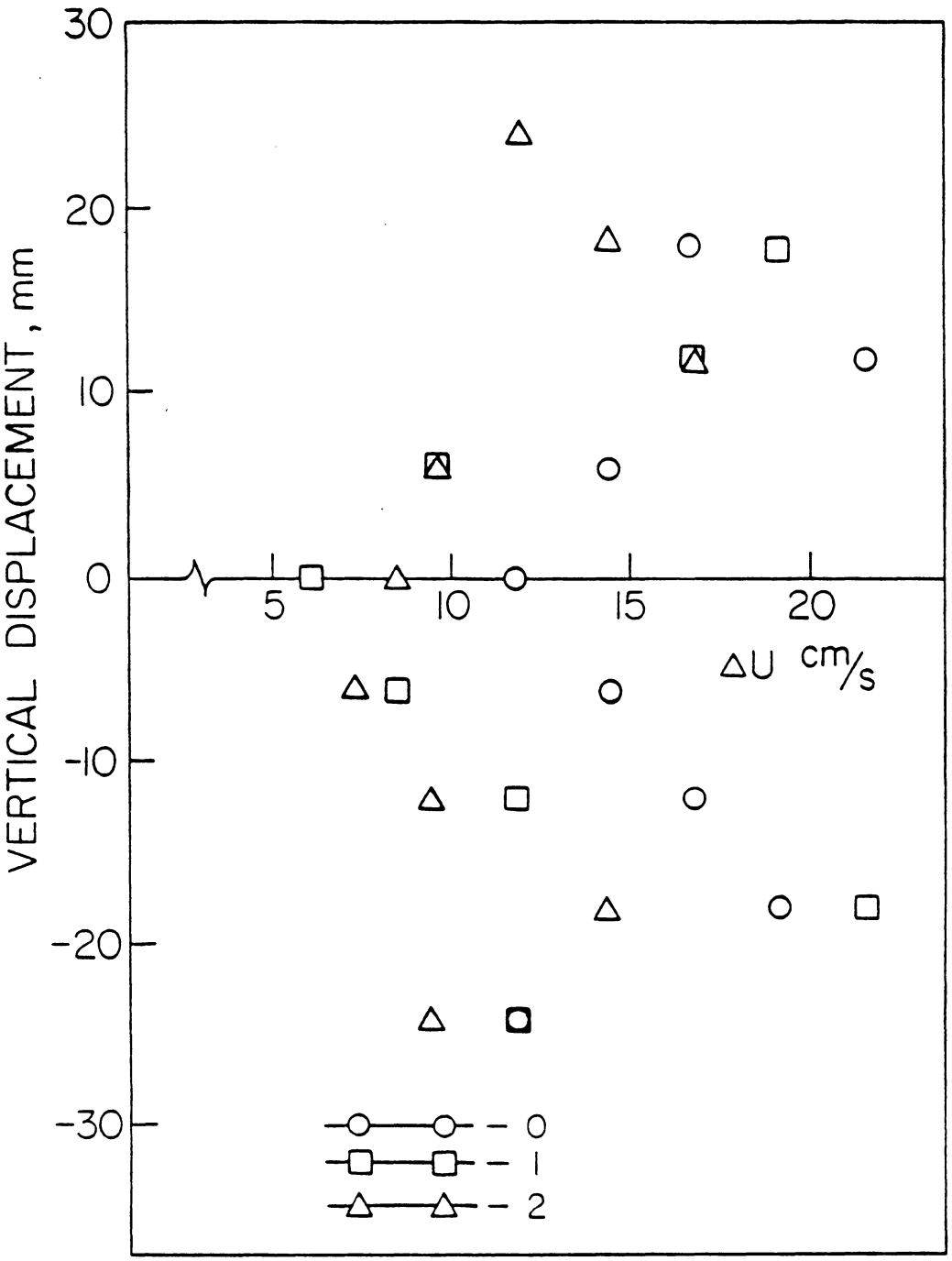

Fig. 3.3.7 Amplitude of the velocity fluctuation in the wake of the pitching airfoil (refer to Fig. 3.3.5 for the grid position).

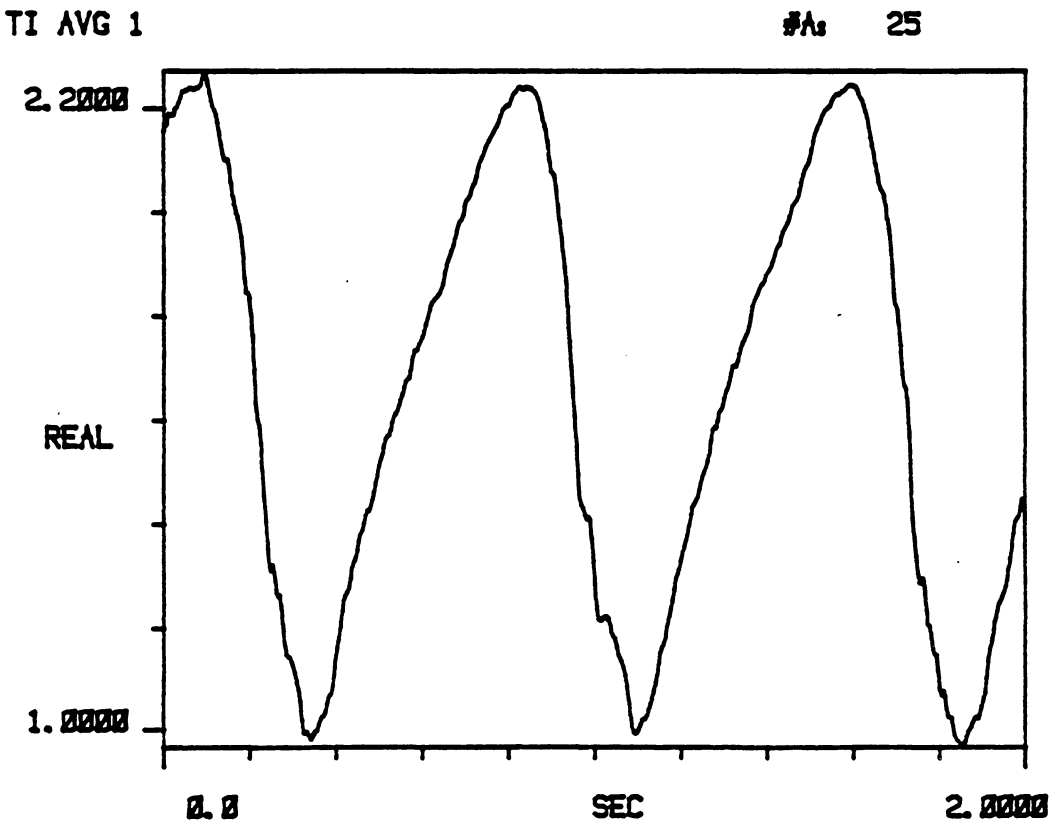

Fig. 3.3.8 Averaged time record of velocity fluctuations. Trailing edge at position x=0.25c and y=0.18c (refer to Fig. 3.3.5 for the grid position).

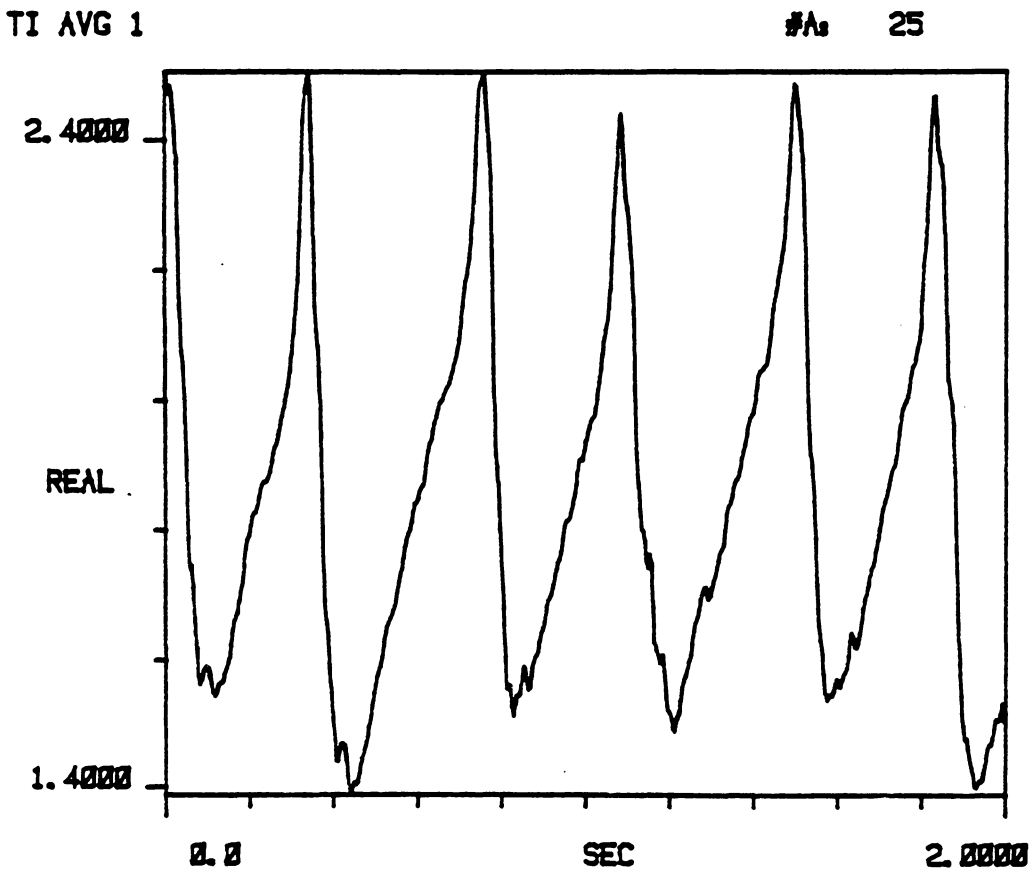

Fig. 3.3.9 Averaged time record of velocity fluctuations. Trailing edge at position x=0.25c and y=0.00 (refer to Fig. 3.3.5 for the grid position).

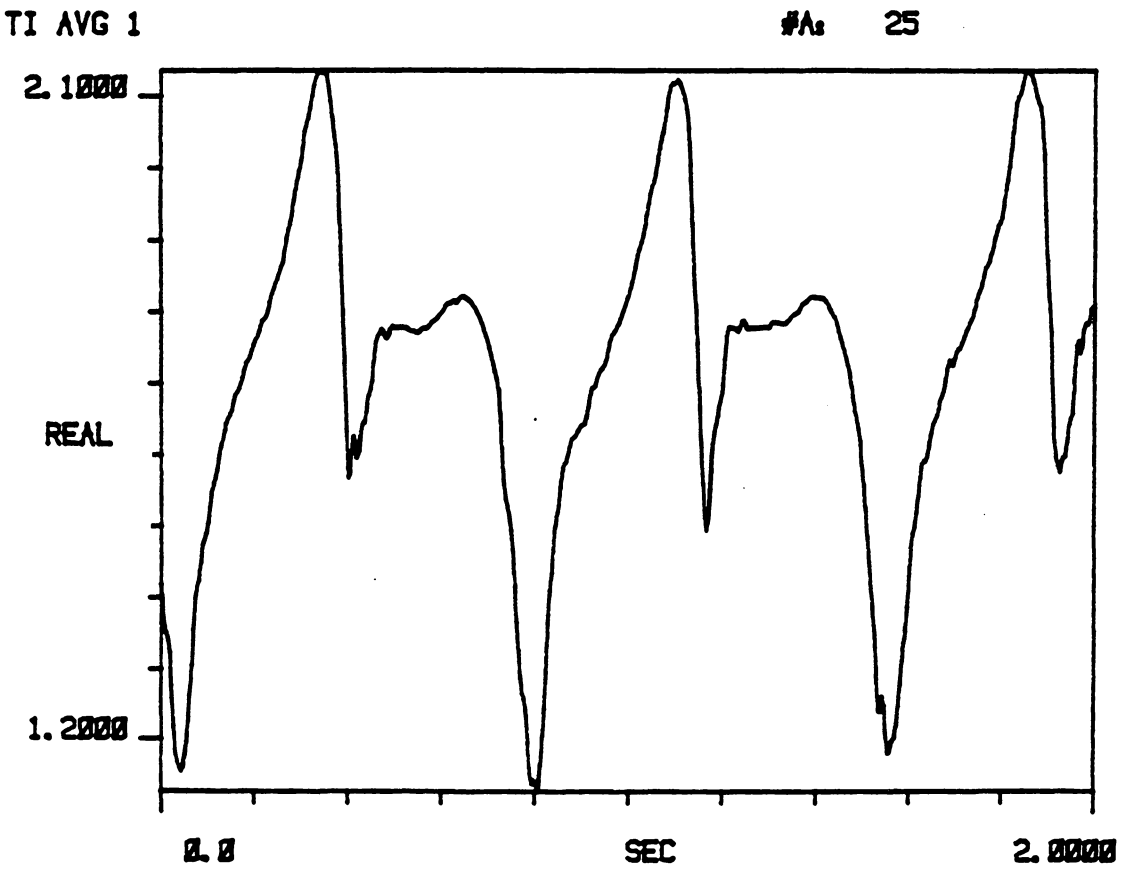

Fig. 3.3.10 Averaged time record of velocity fluctuations. Trailing edge at position x=0.75c and y=0.08c (refer to Fig. 3.3.5 for the grid position).

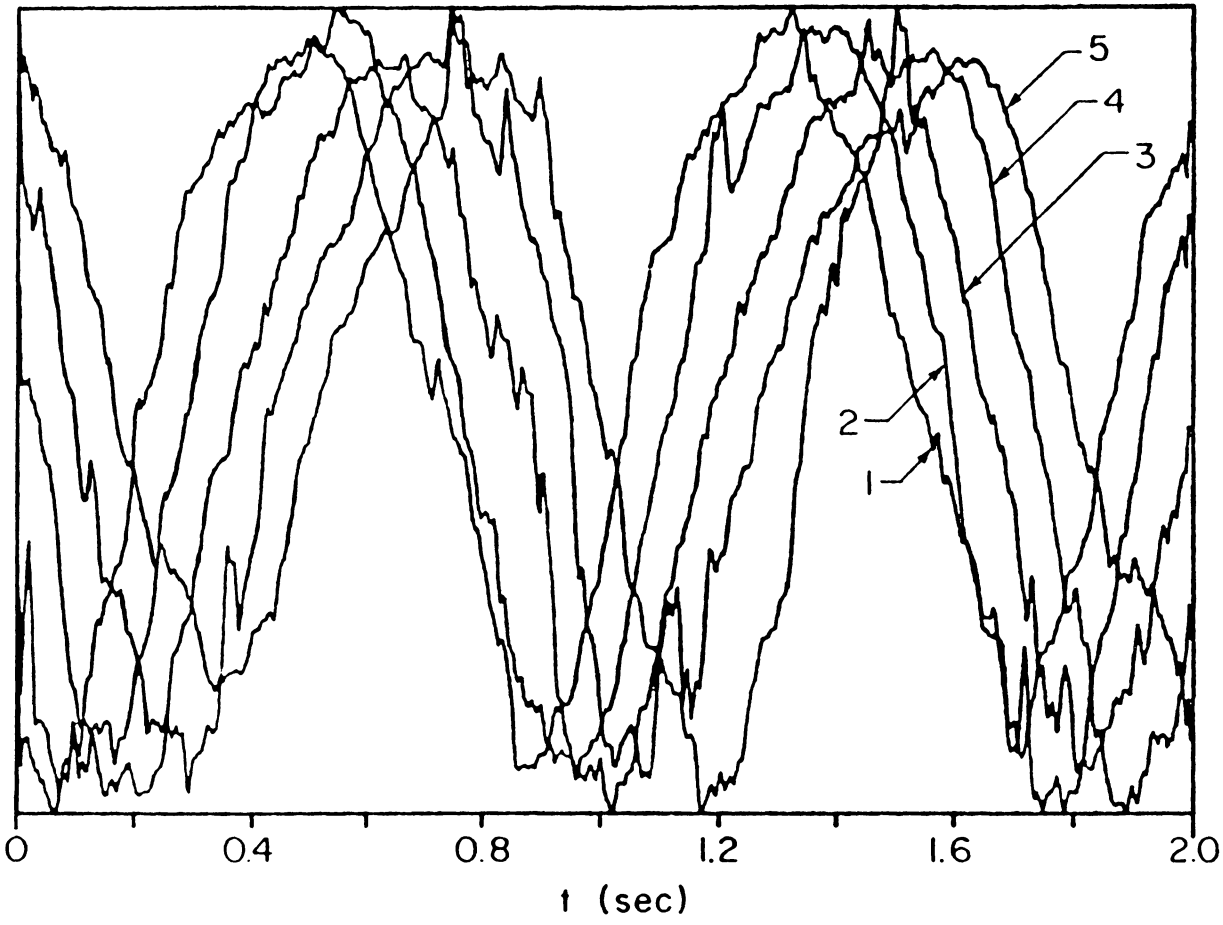

Fig. 3.3.11 Velocity waveforms obtained at grid points of group IV (see Fig. 3.2.1 over the fixed airfoil).

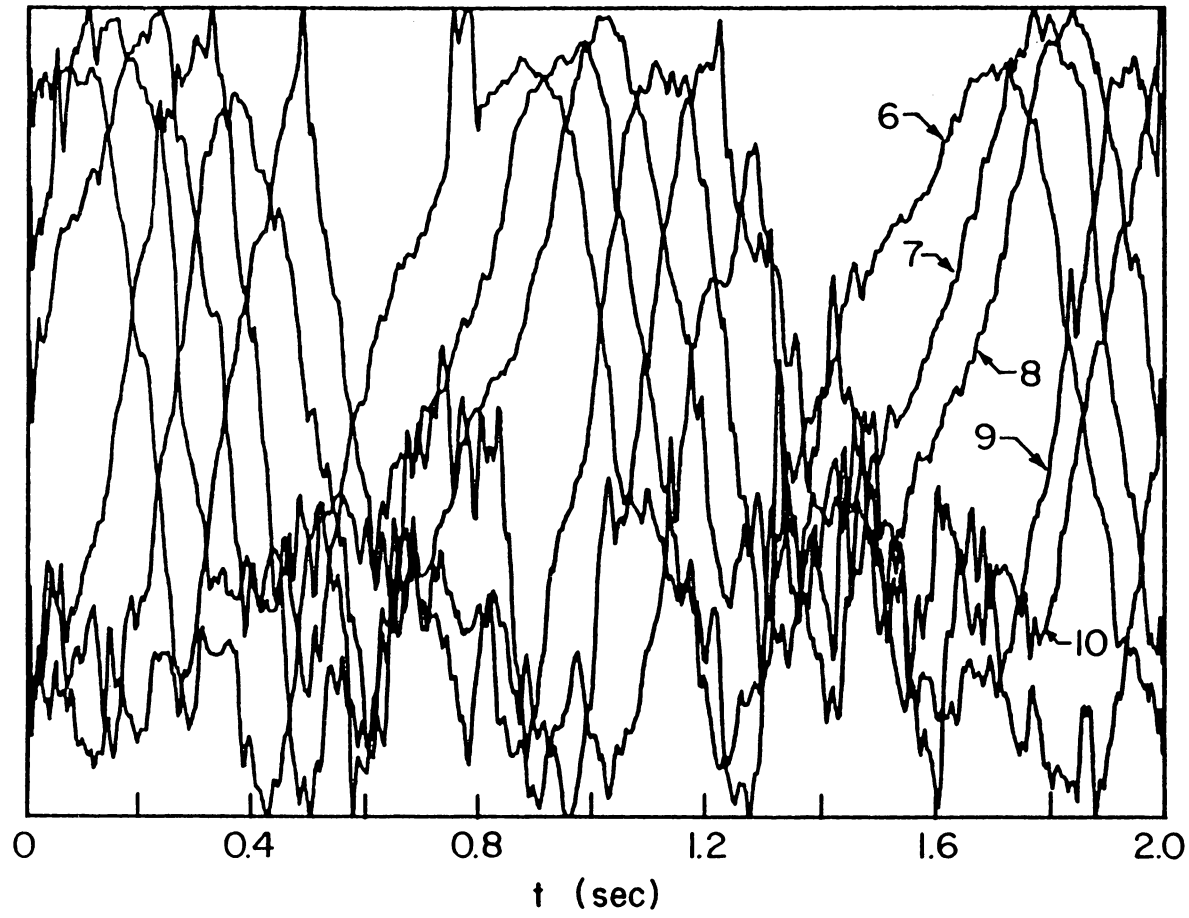

Fig. 3.3.12 Velocity waveforms obtained at grid points of group IV (see Fig. 3.2.1 over the fixed airfoil).

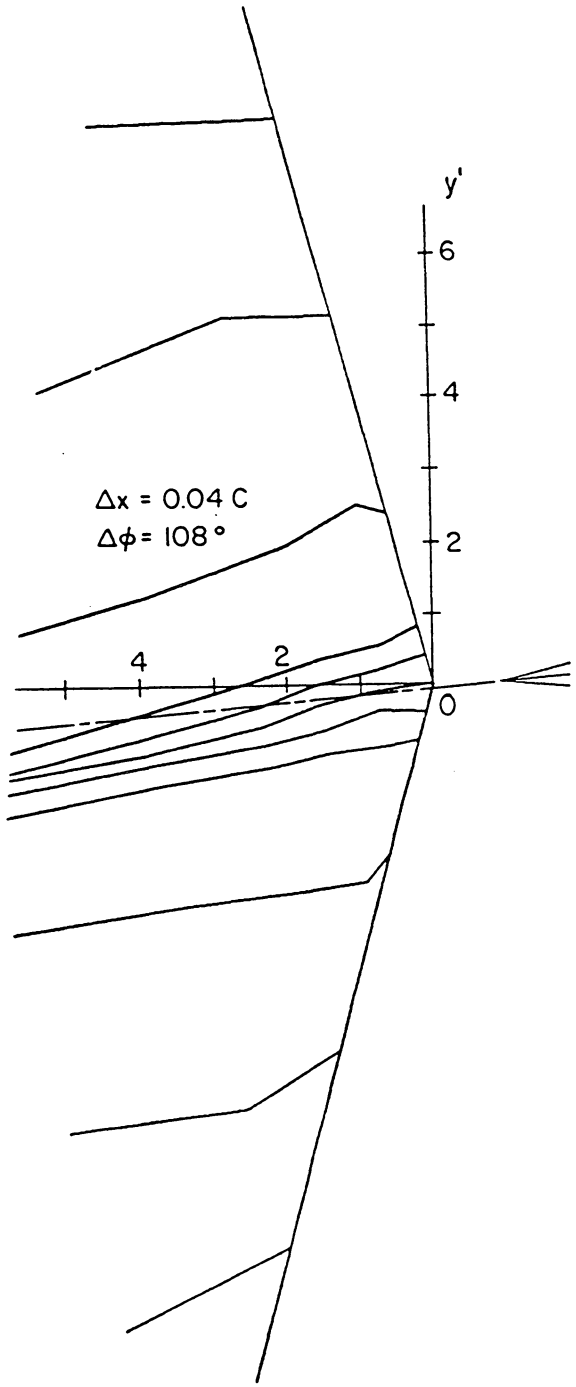

Fig. 3.3.13 Instantaneous streamlines in the neighborhood of the trailing edge of the fixed airfoil as obtained by conditional averaging of the LDV signals.

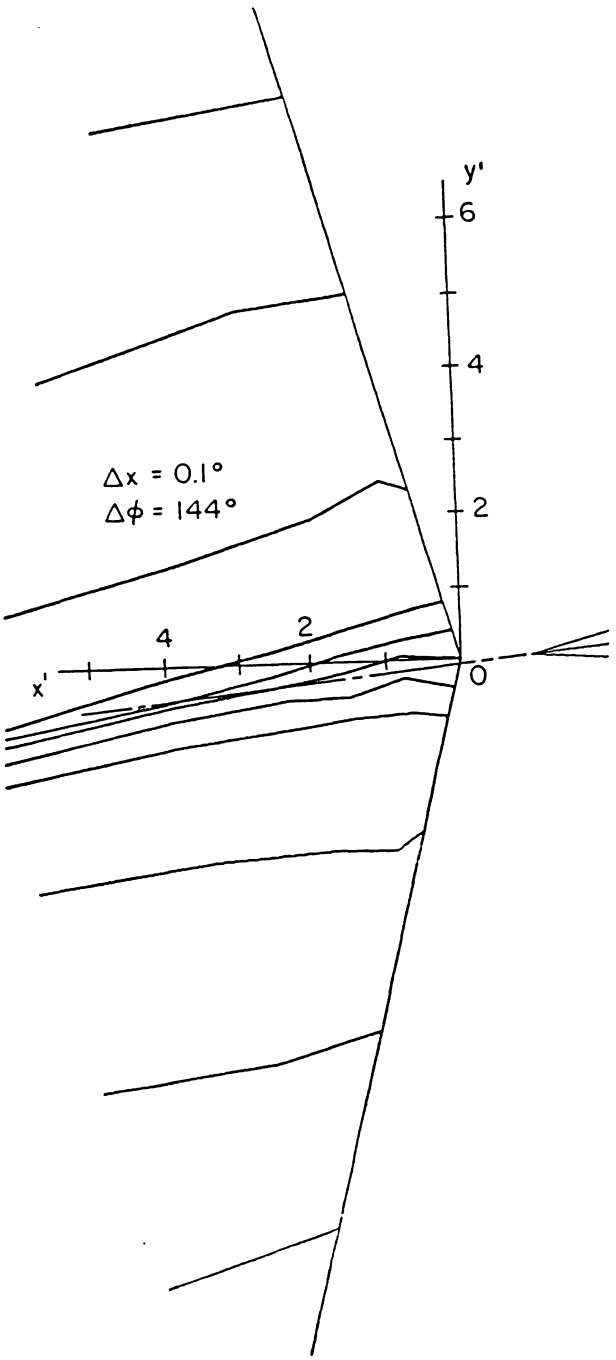

Fig. 3.3.14 Instantaneous streamlines in the neighborhood of the trailing edge of the fixed airfoil as obtained by conditional averaging of the LDV signals.

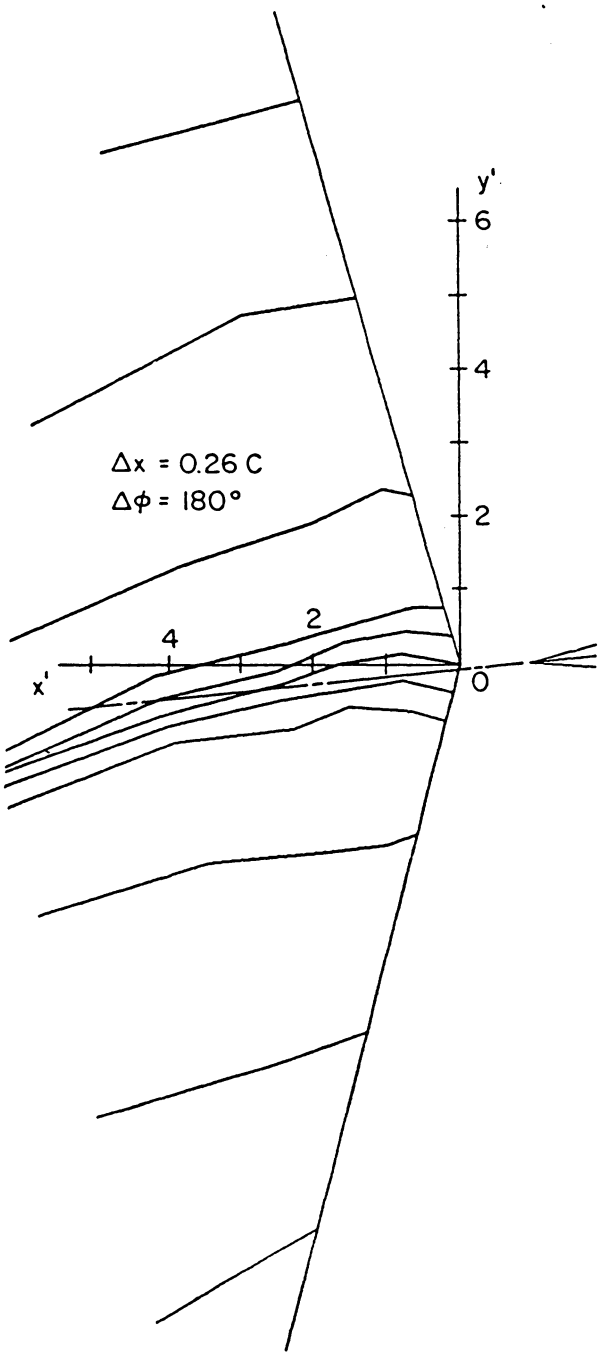

Fig. 3.3.15 Instantaneous streamlines in the neighborhood of the trailing edge of the fixed airfoil as obtained by conditional averaging of the LDV signals.

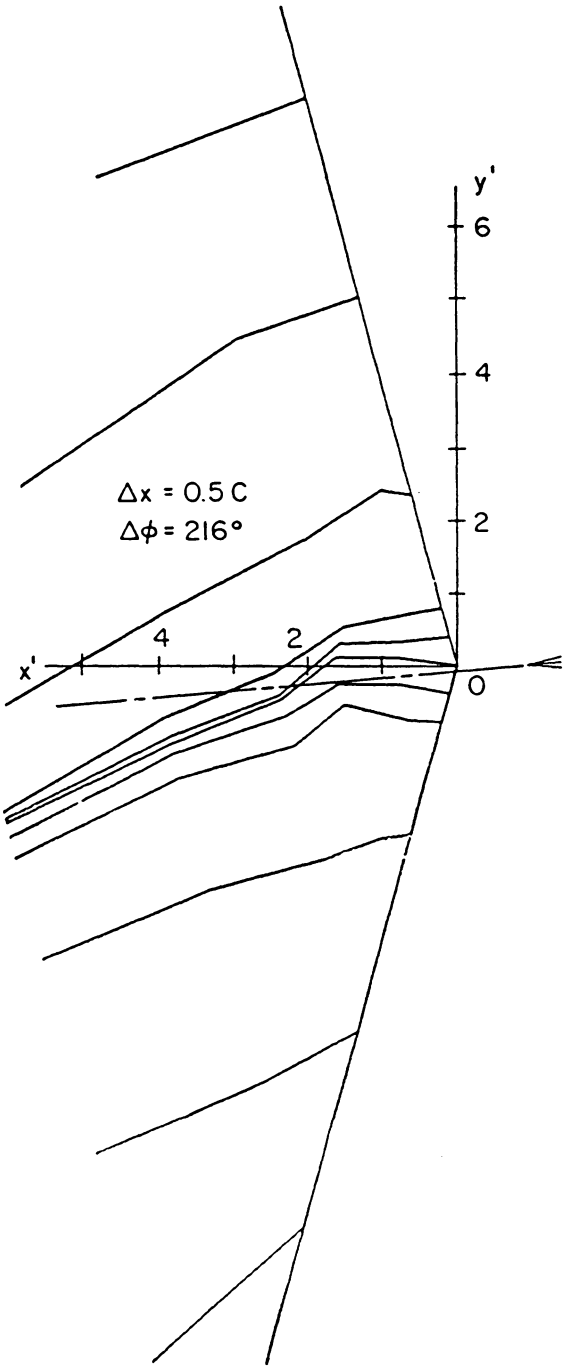

Fig. 3.3.16 Instantaneous streamlines in the neighborhood of the trailing edge of the fixed airfoil as obtained by conditional averaging of the LDV signals.

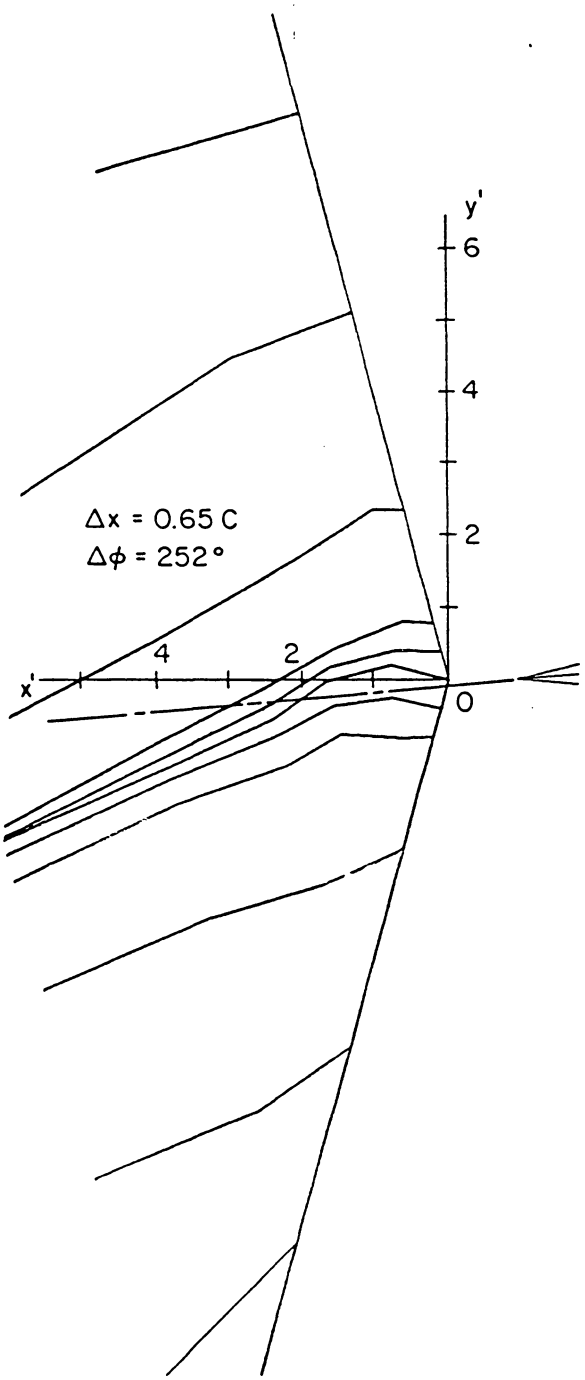

Fig. 3.3.17 Instantaneous streamlines in the neighborhood of the trailing edge of the fixed airfoil as obtained by conditional averaging of the LDV signals.

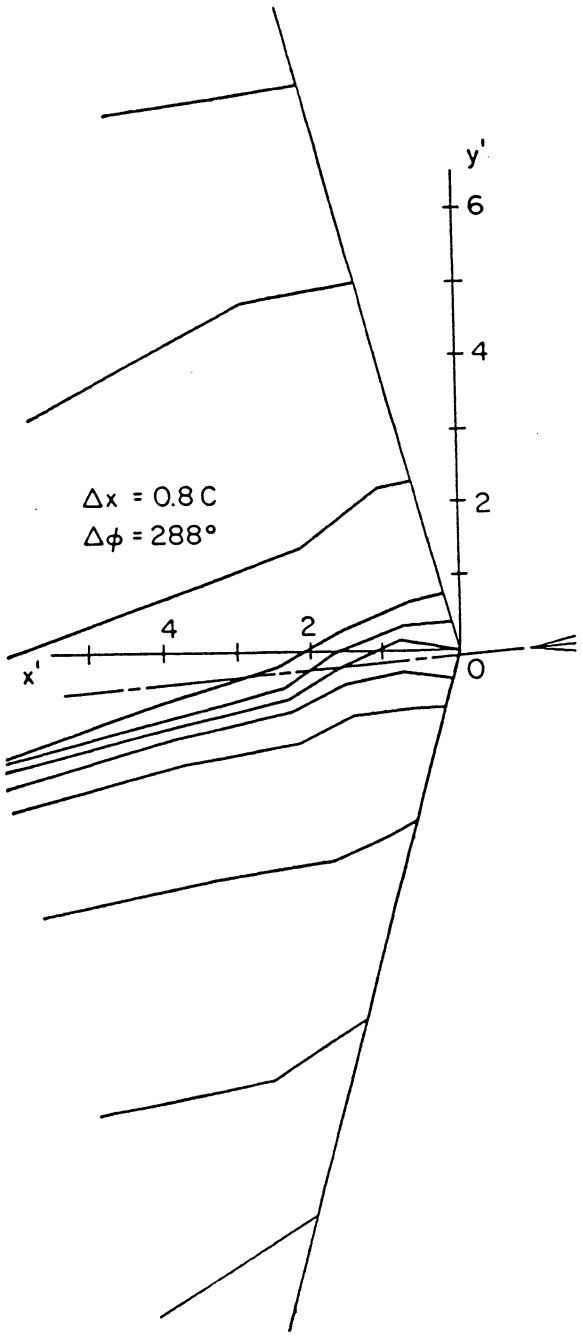

Fig. 3.3.18 Instantaneous streamlines in the neighborhood of the trailing edge of the fixed airfoil as obtained by conditional averaging of the LDV signals.

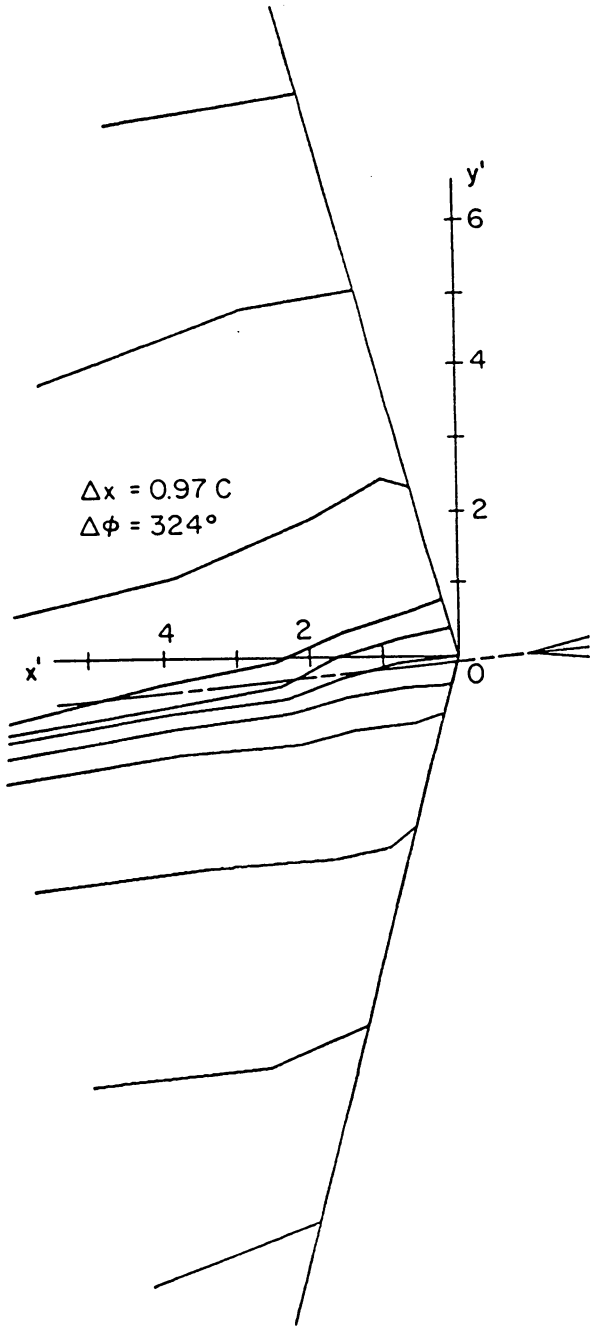

Fig. 3.3.19 Instantaneous streamlines in the neighborhood of the trailing edge of the fixed airfoil as obtained by conditional averaging of the LDV signals.

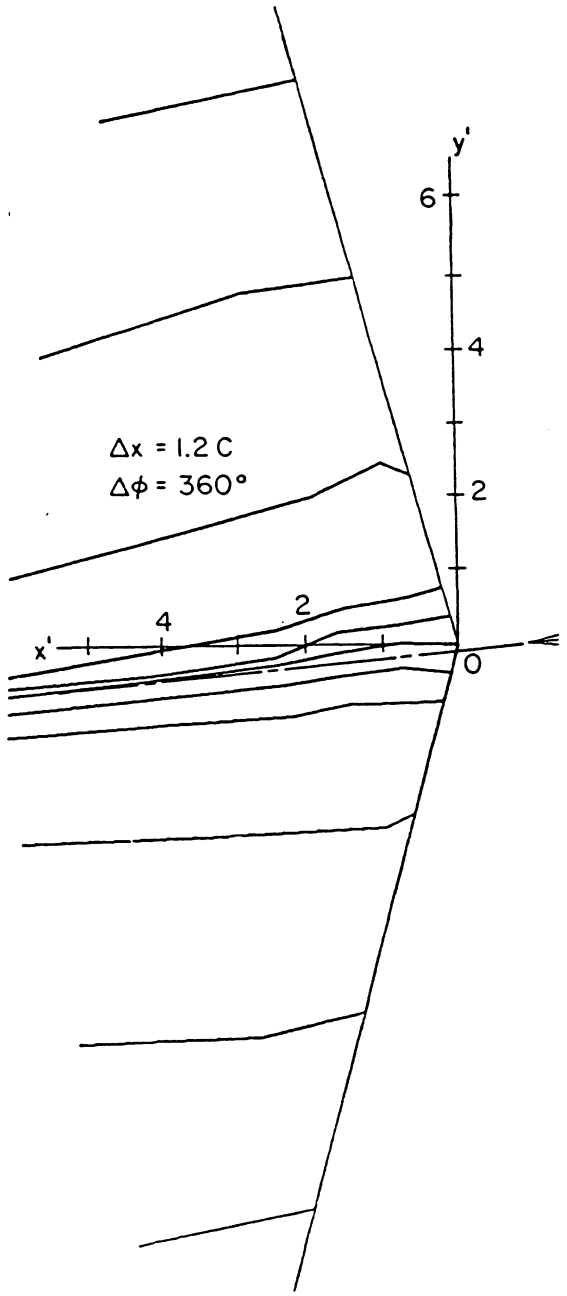

Fig. 3.3.20 Instantaneous streamlines in the neighborhood of the trailing edge of the fixed airfoil as obtained by conditional averaging of the LDV signals.

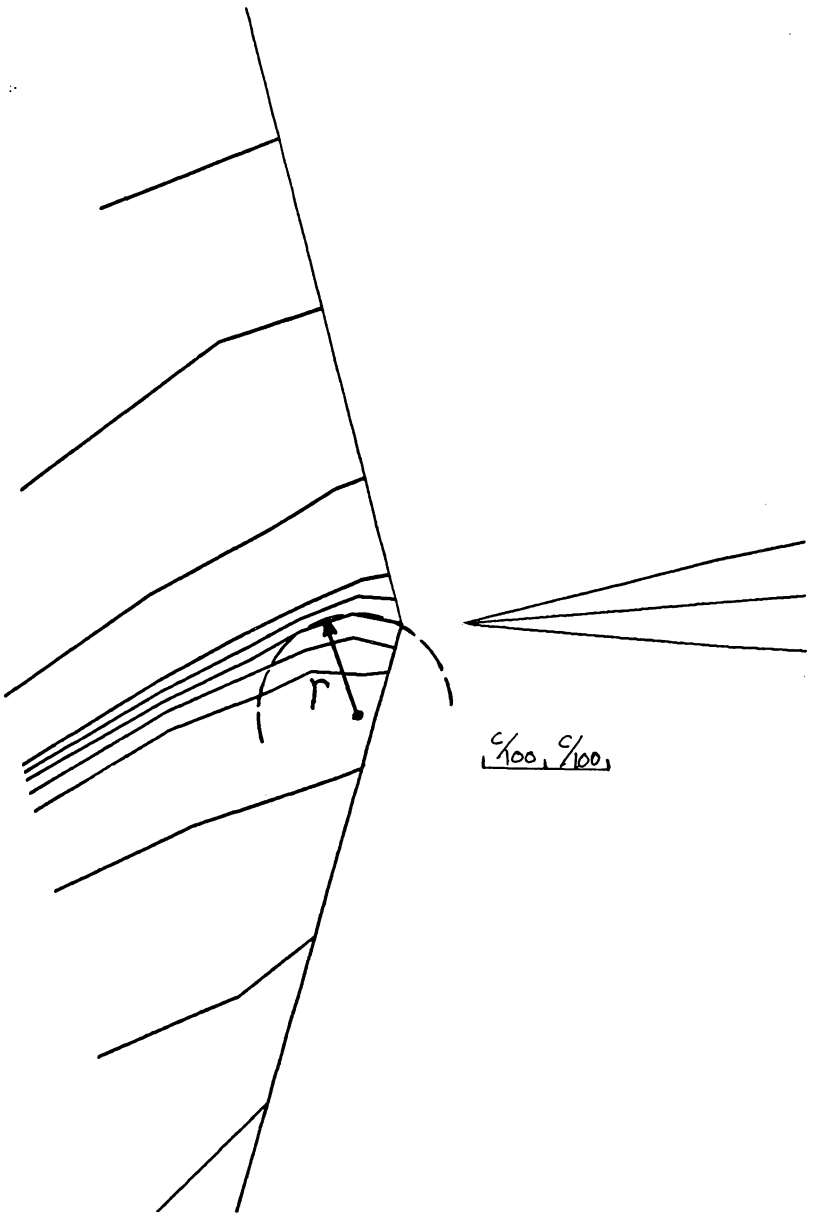

Fig. 3.3.21 Radial measurement of the curvature of the viscous shear-layer aft of the fixed airfoil used in the pressure coefficient calculation at the edge.

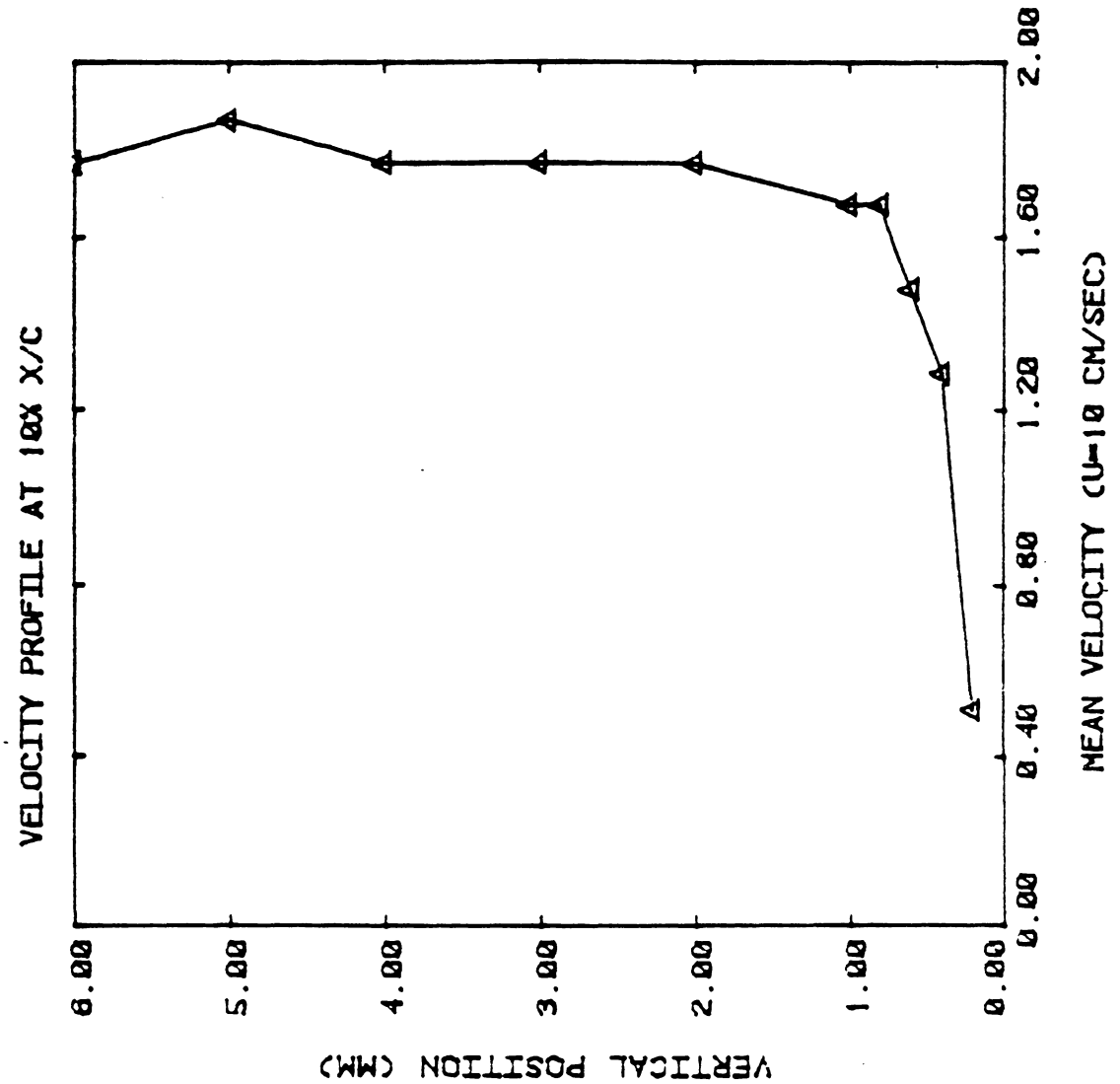

Fig. 3.3.22 Velocity profile over the fixed airfoil at 0.1c and $\alpha=0°$ (K=4.7).

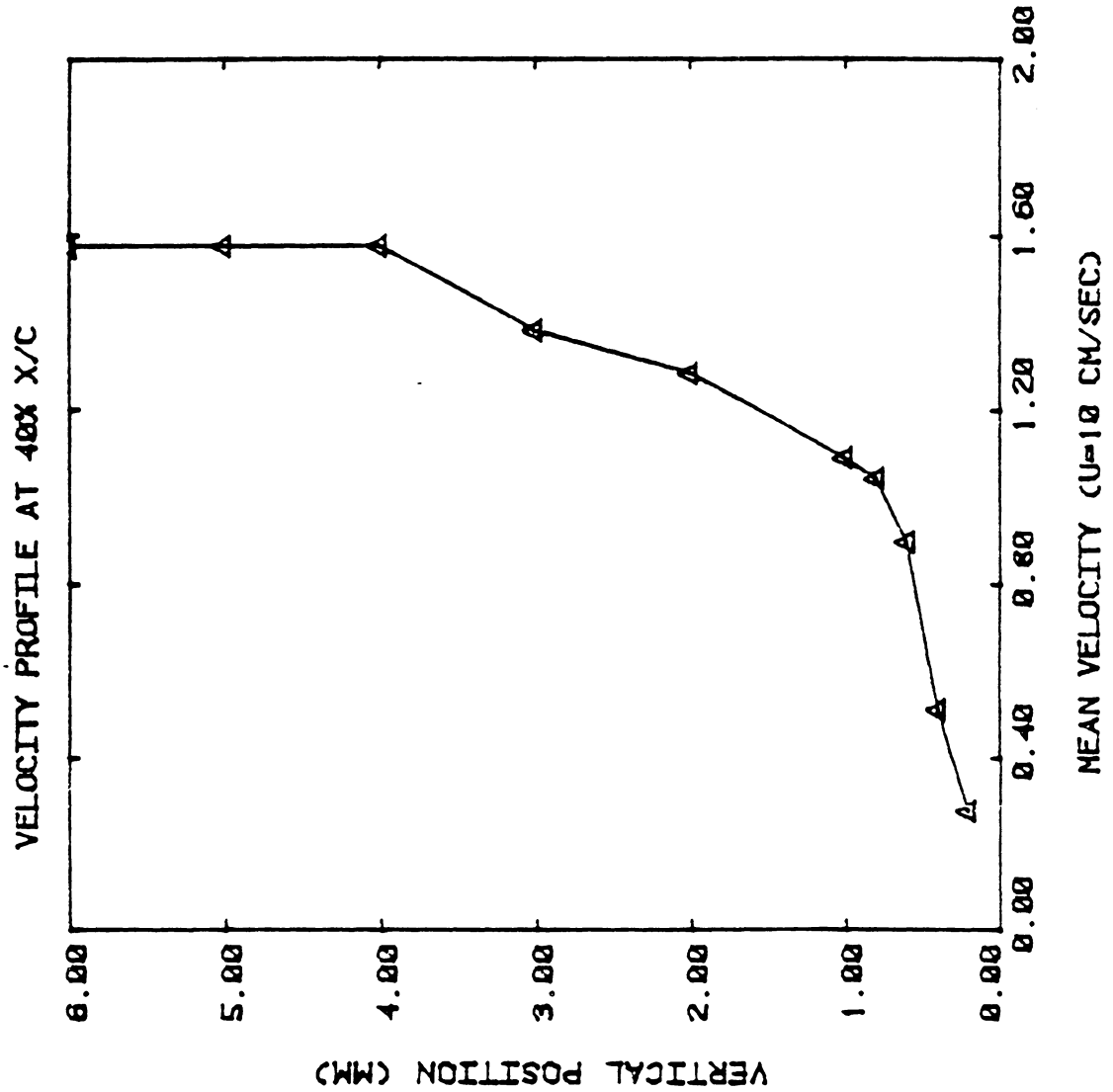

Fig. 3.3.23 Velocity profile over the fixed airfoil at 0.4c and $\alpha=0°$ (K=4.7).

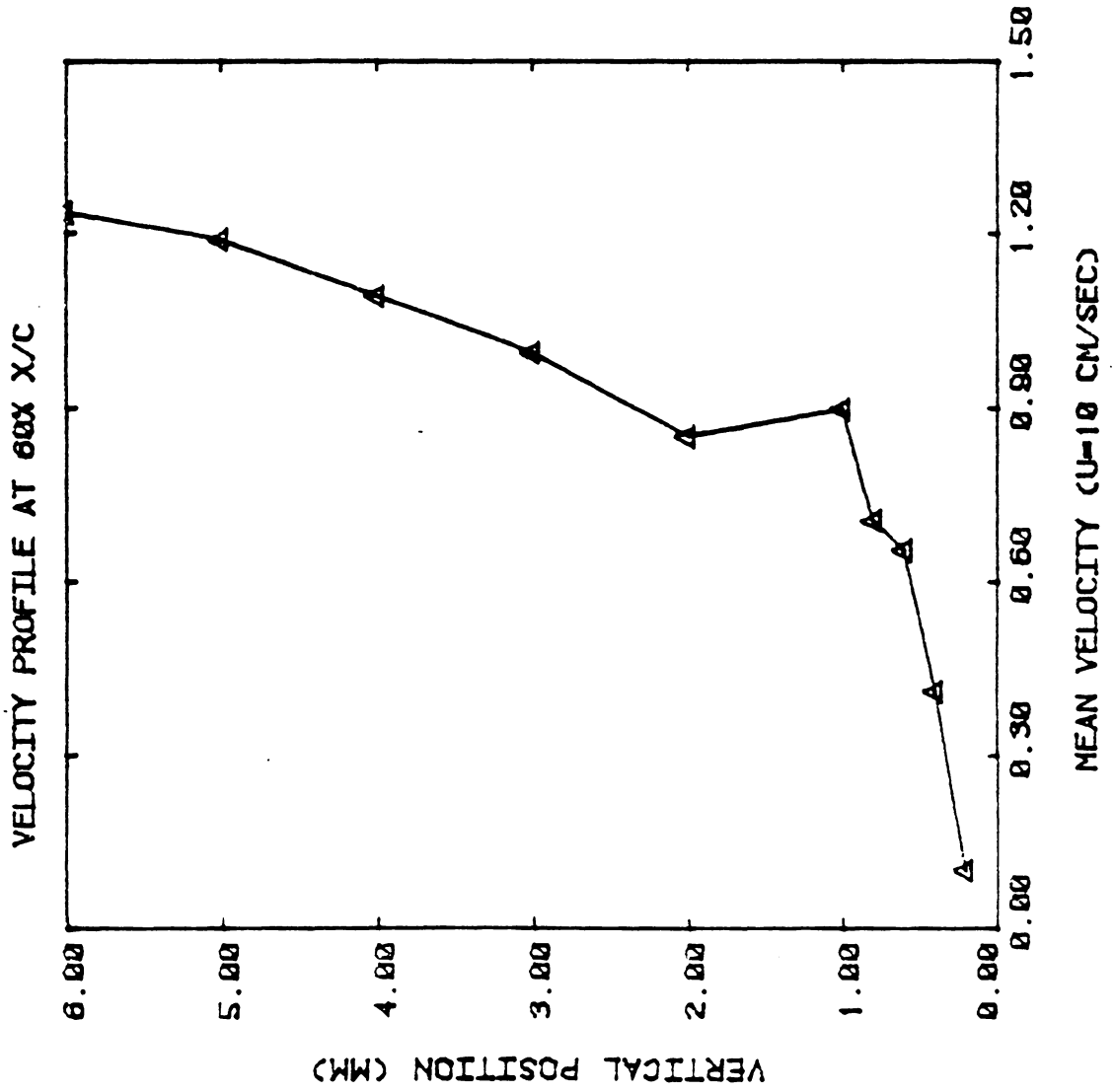

Fig. 3.3.24 Velocity profile over the fixed airfoil at 0.6c and $\alpha=0°$ (K=4.7).

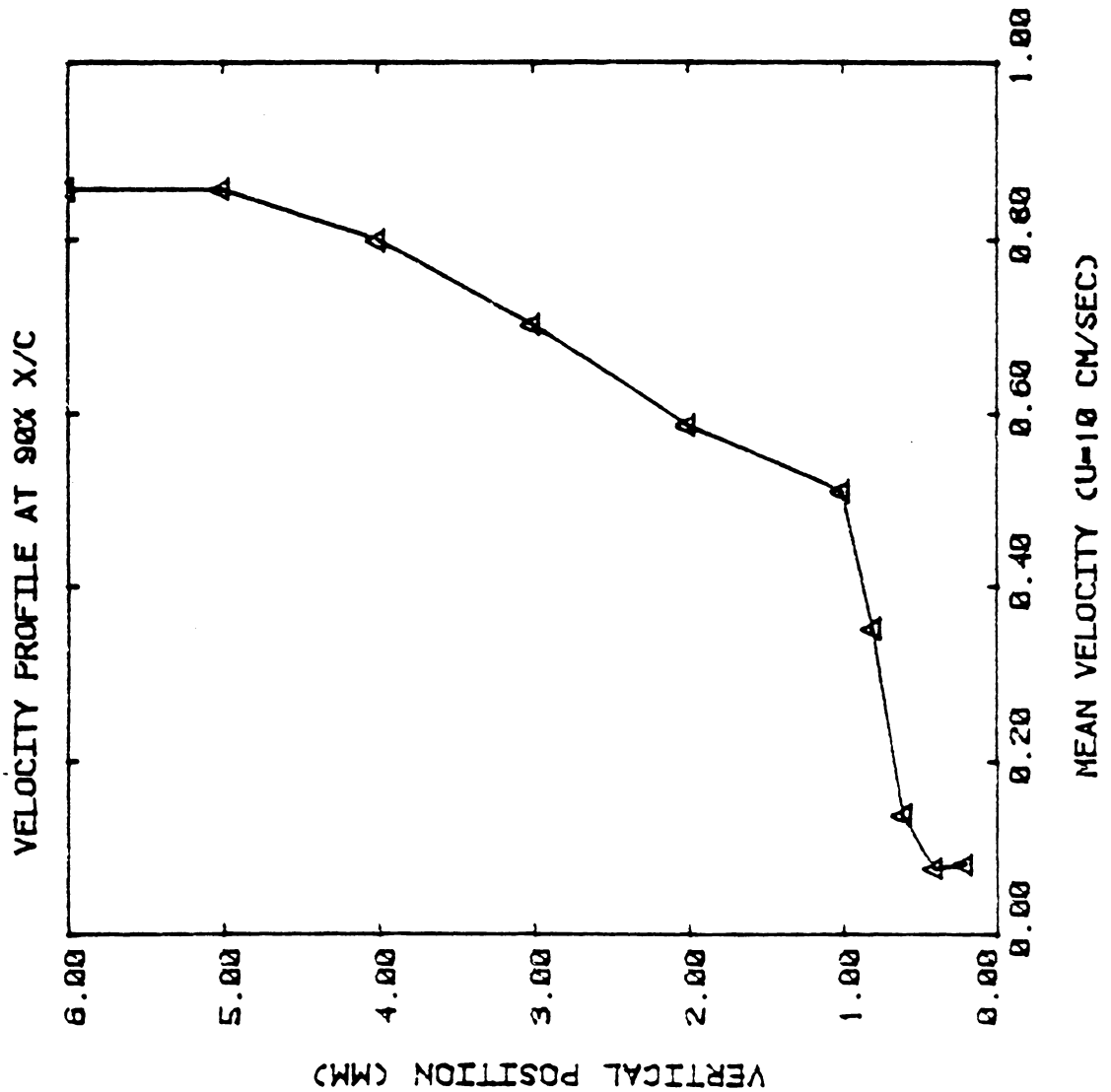

Fig. 3.3.25 Velocity profile over the fixed airfoil at 0.9c and $\alpha=0°$ (K=4.7).

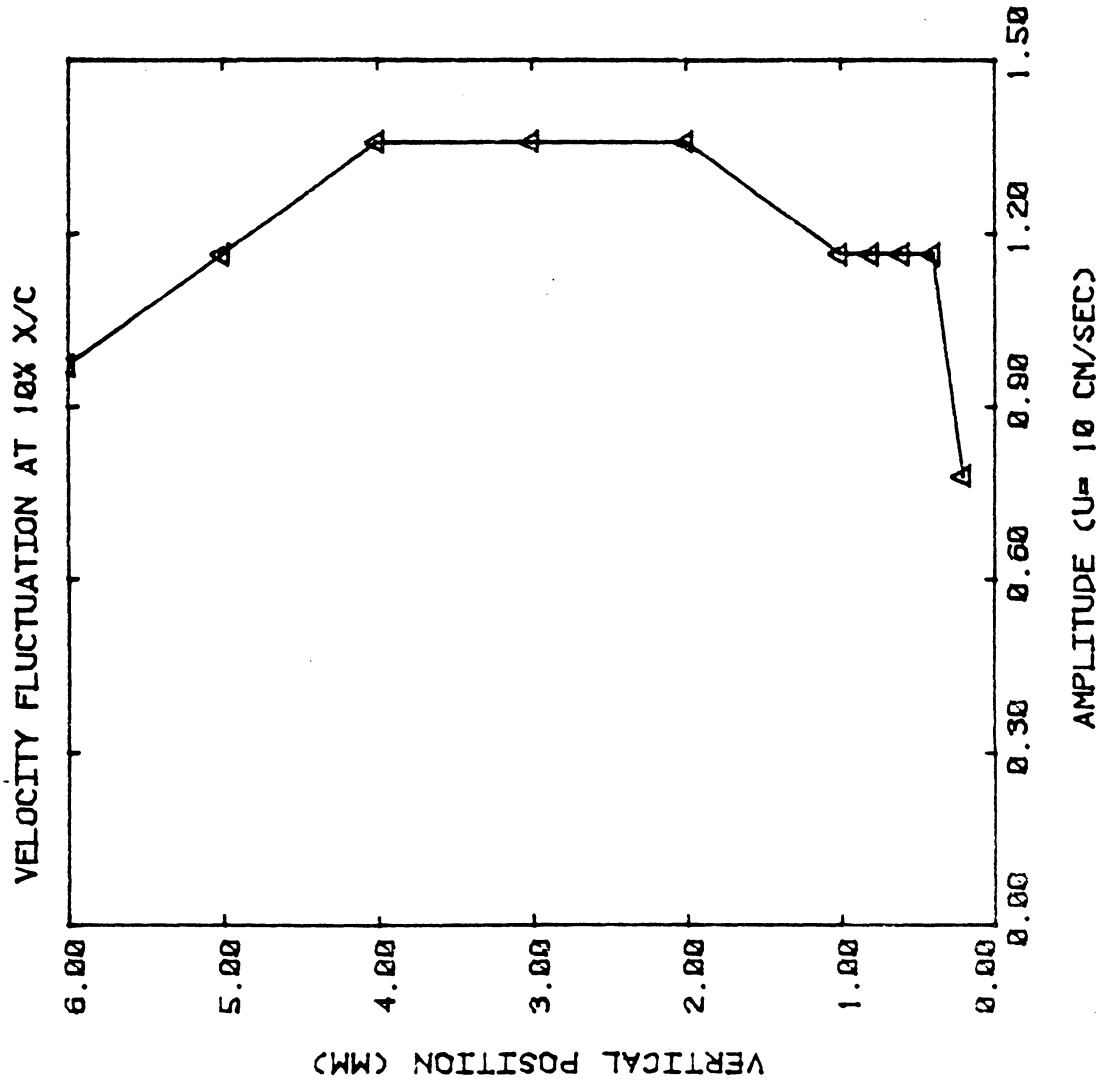

Fig. 3.3.26 Amplitude of the velocity fluctuation over the fixed airfoil at 0.1c and $\alpha=0°$ (K=4.7).

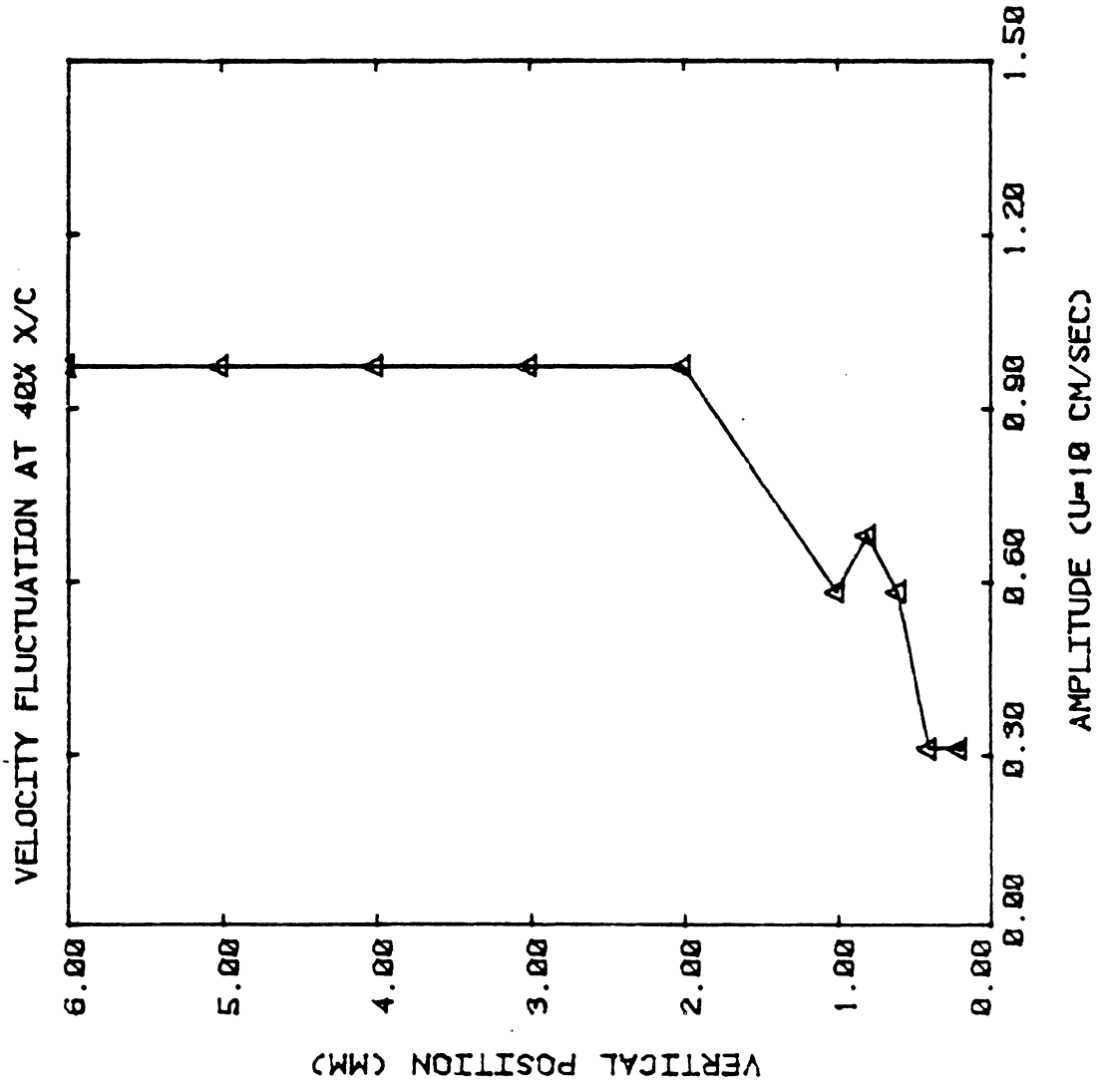

Fig. 3.3.27 Amplitude of the velocity fluctuation over the fixed airfoil at 0.4c chord and $\alpha = 0°$ (K=4.7).

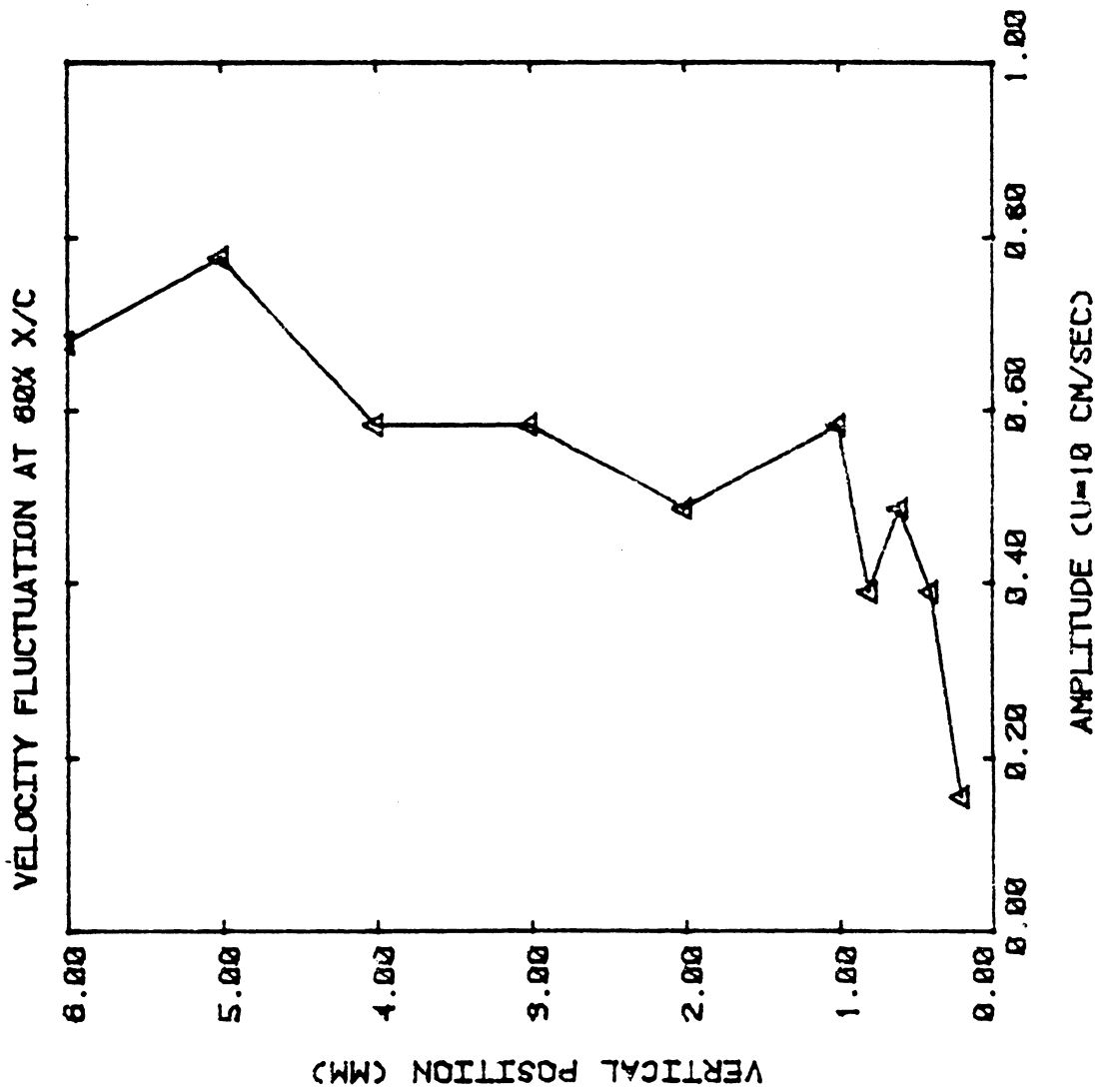

Fig. 3.3.28 Amplitude of the velocity fluctuation over the fixed airfoil at 0.6c chord and $\alpha = 0°$ (K=4.7).

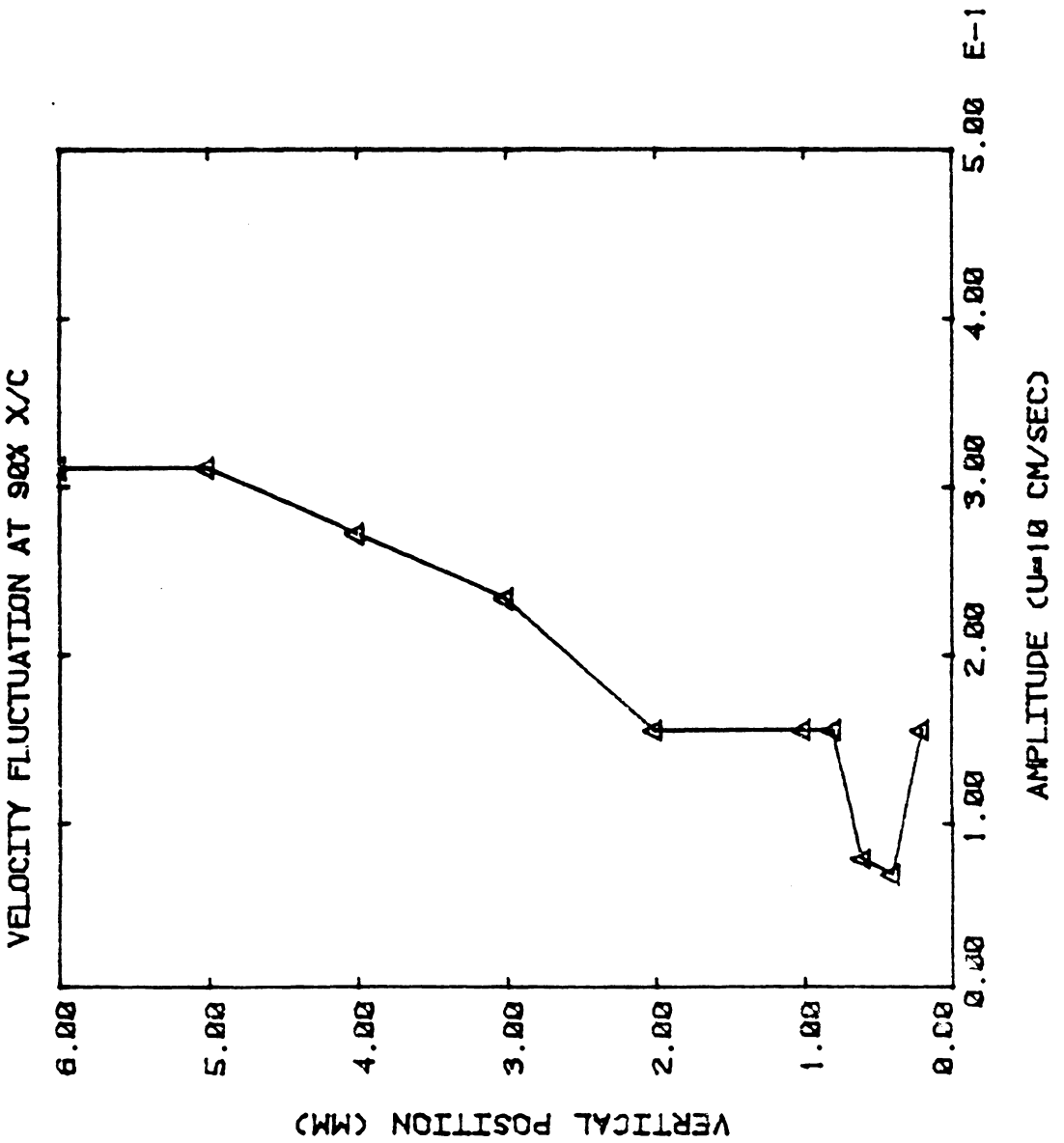

Fig. 3.3.29 Amplitude of the velocity fluctuation over the fixed airfoil at 0.9c chord and $\alpha = 0°$ (K=4.7).

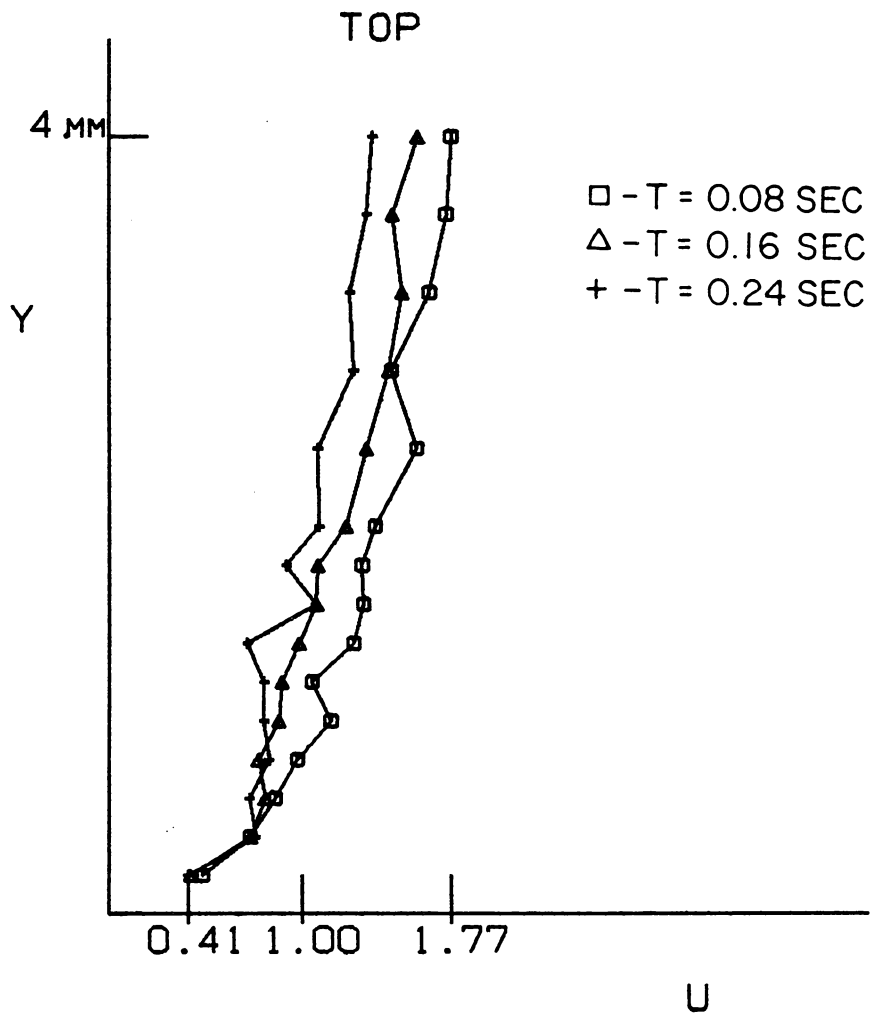

Fig. 3.3.30 Boundary layer velocity profiles at 98% chord. T corresponds to a fraction of the period of the velocity waveform. One full period is 0.8 sec.

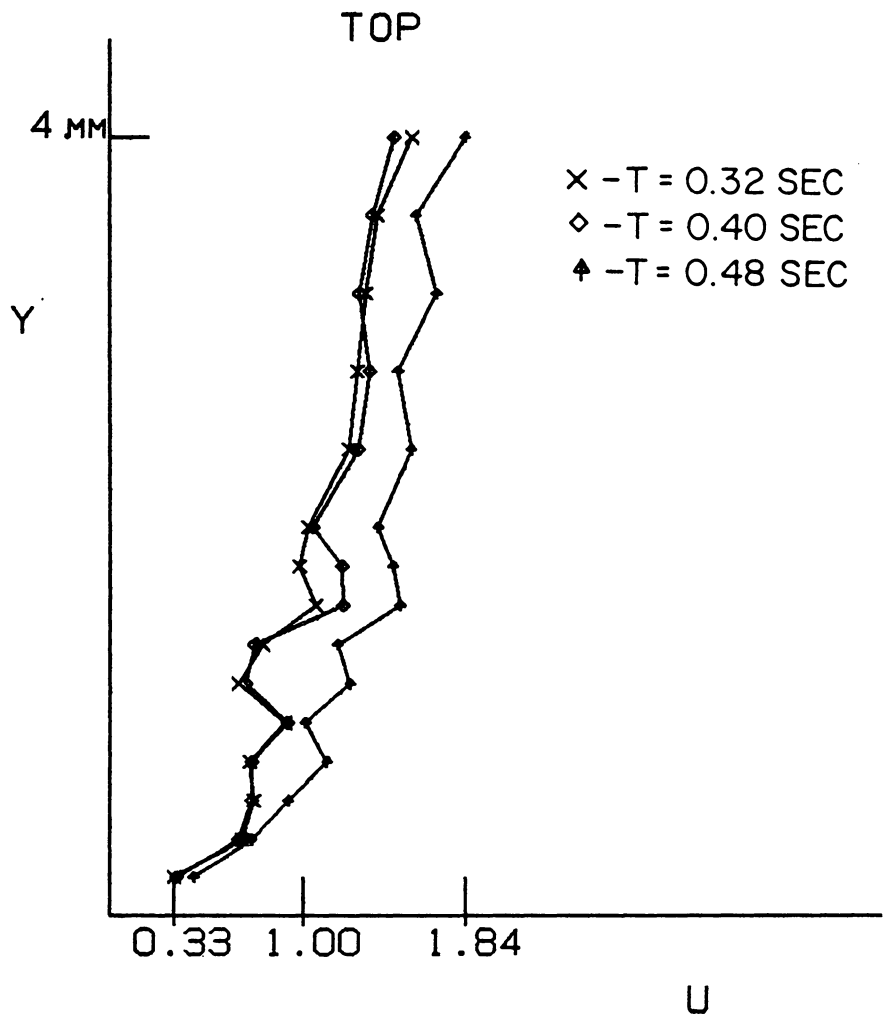

Fig. 3.3.31 Boundary layer velocity profiles at 98% chord. T corresponds to a fraction of the period of the velocity waveform. One full period is 0.8 sec.

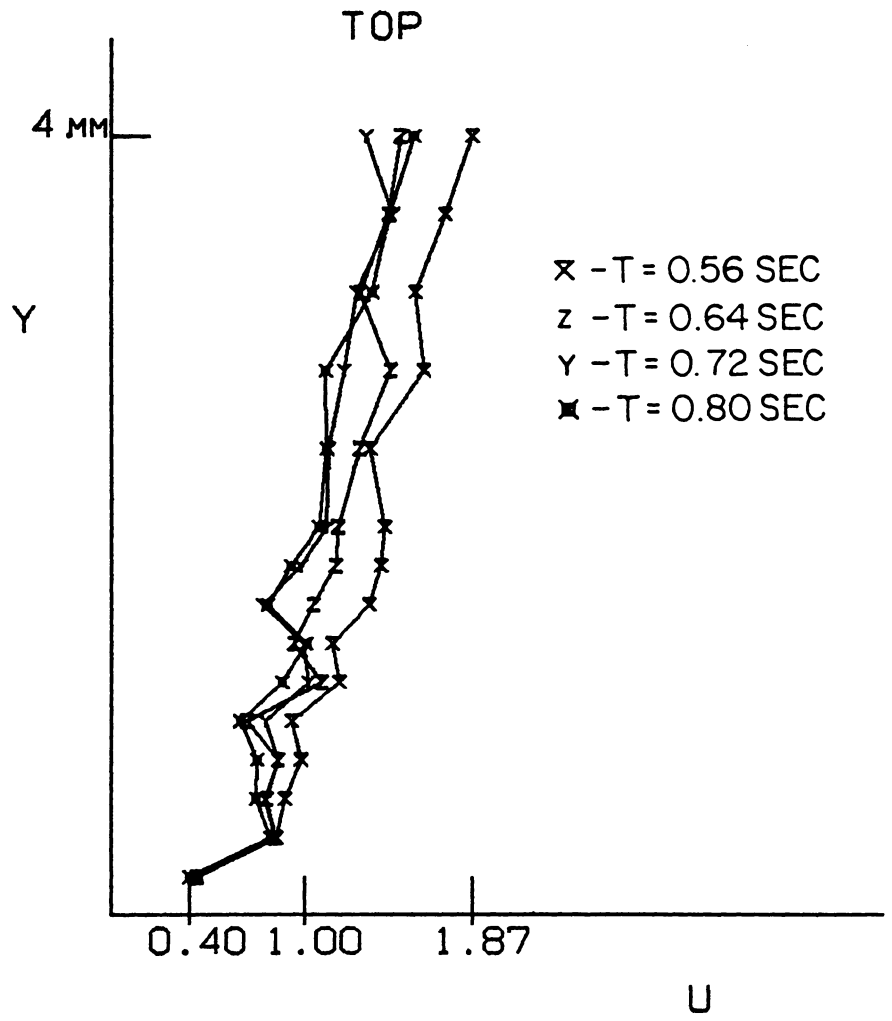

Fig. 3.3.32 Boundary layer velocity profiles at 98% chord. T corresponds to a fraction of the period of the velocity waveform. One full period is 0.8 sec.

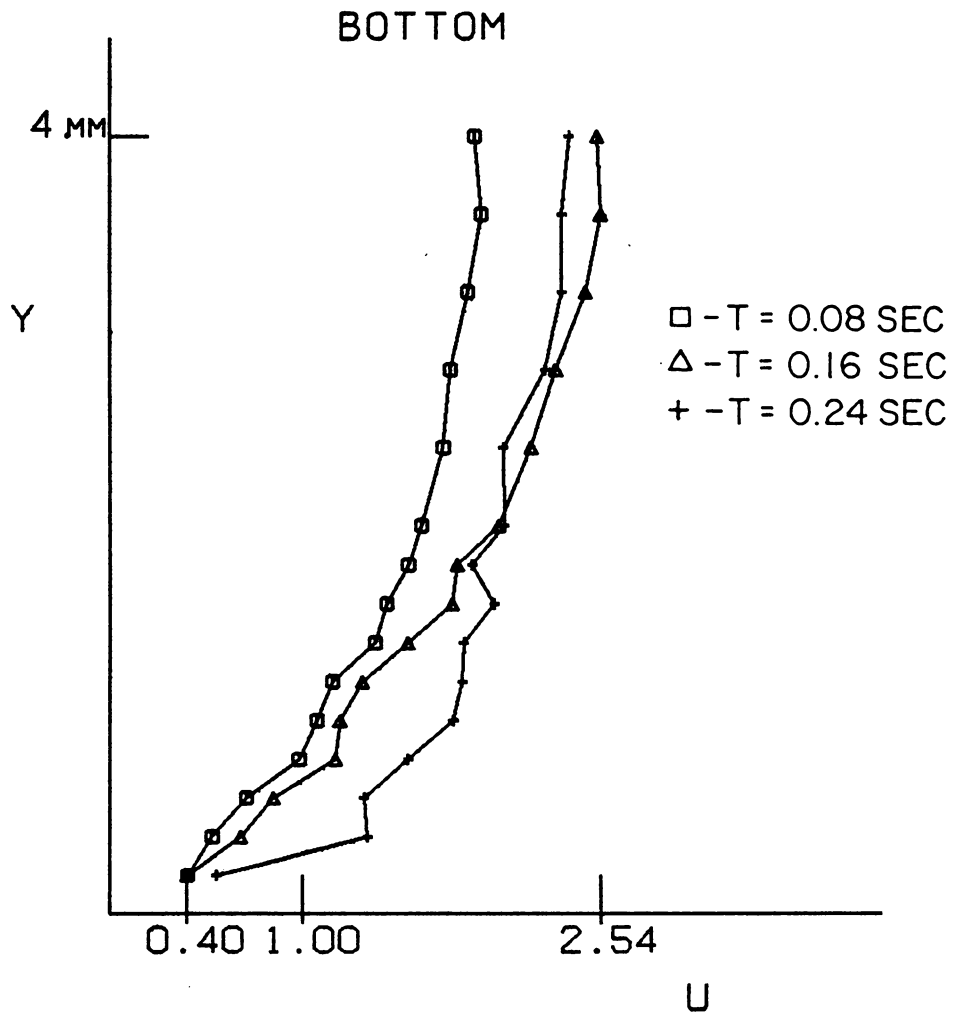

Fig. 3.3.33 Boundary layer velocity profiles at 98% chord. T corresponds to a fraction of the period of the velocity waveform. One full period is 0.8 sec.

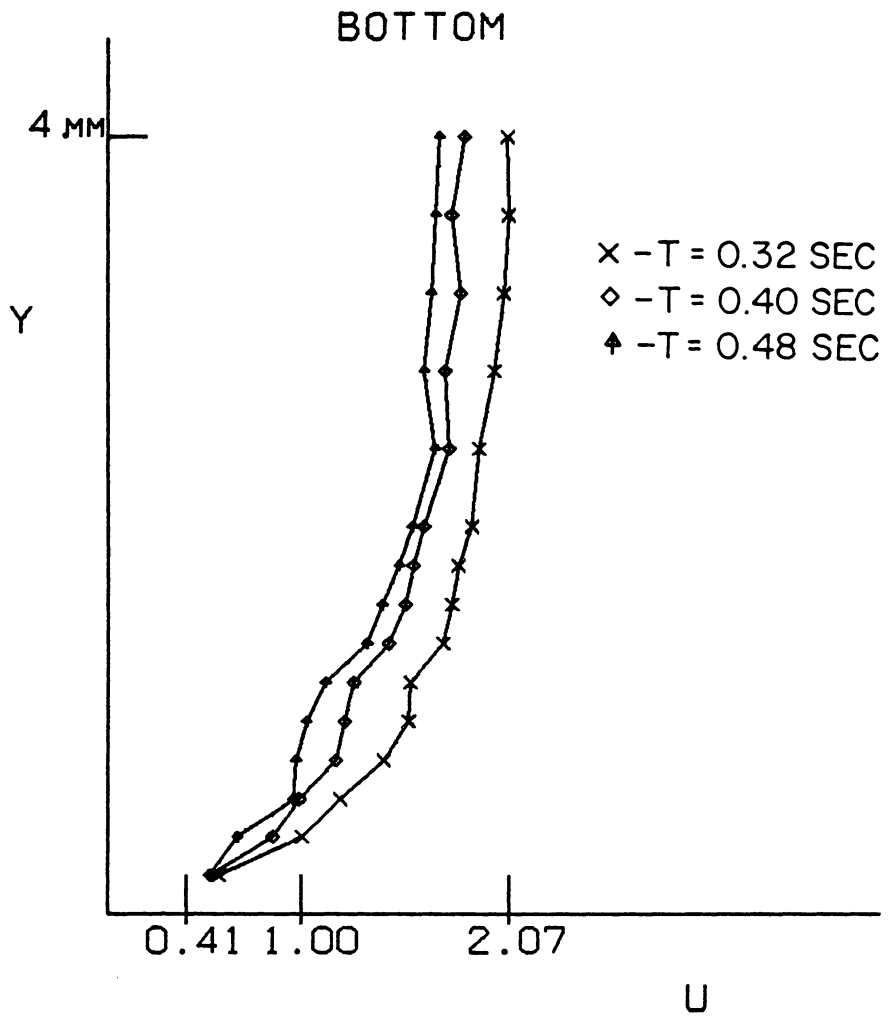

Fig. 3.3.34 Boundary layer velocity profiles at 98% chord. T corresponds to a fraction of the period of the velocity waveform. One full period is 0.8 sec.

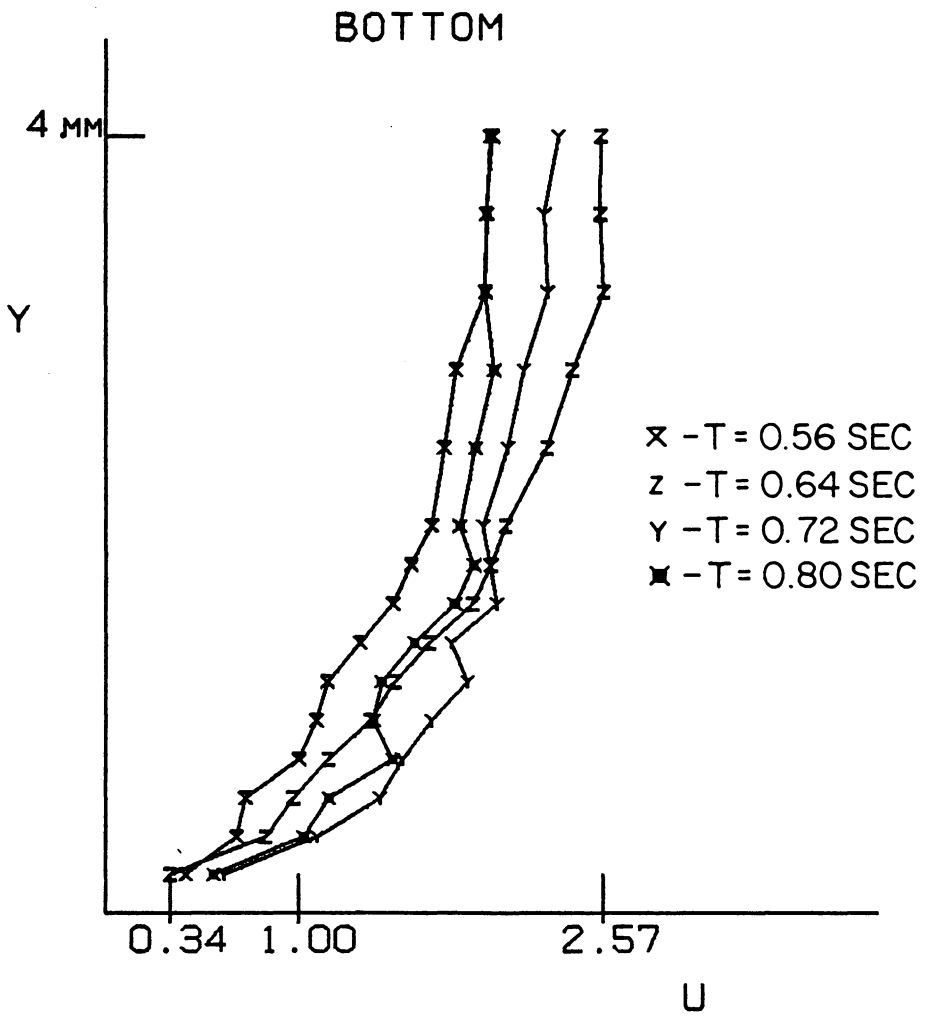

Fig. 3.3.35 Boundary layer velocity profiles at 98% chord. T corresponds to a fraction of the period of the velocity waveform. One full period is 0.8 sec.

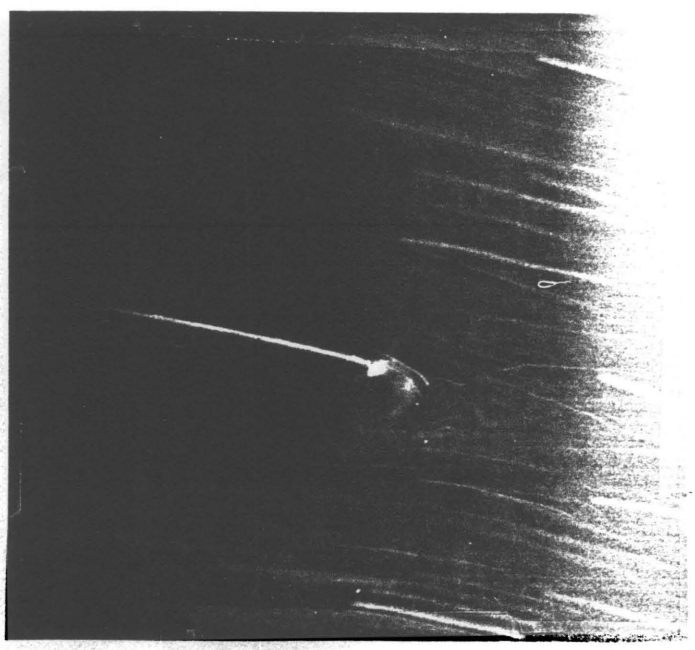

Fig. 3.4.1 Instantaneous flow visualization for K=0.8 and α=0° (downstroke).

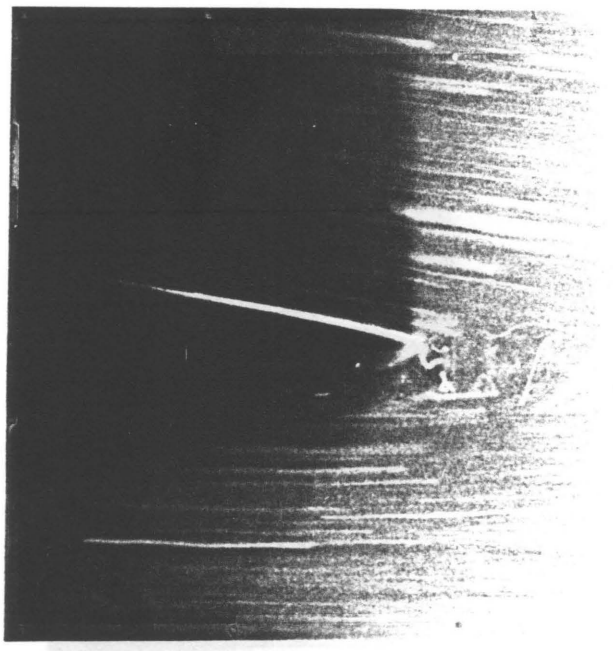

Fig. 3.4.2 Instantaneous flow visualization for K=0.8 and α=-10° (upstroke).

Fig. 3.4.3 Instantaneous flow visulaization for K=1.2 and α=0° (upstorke).

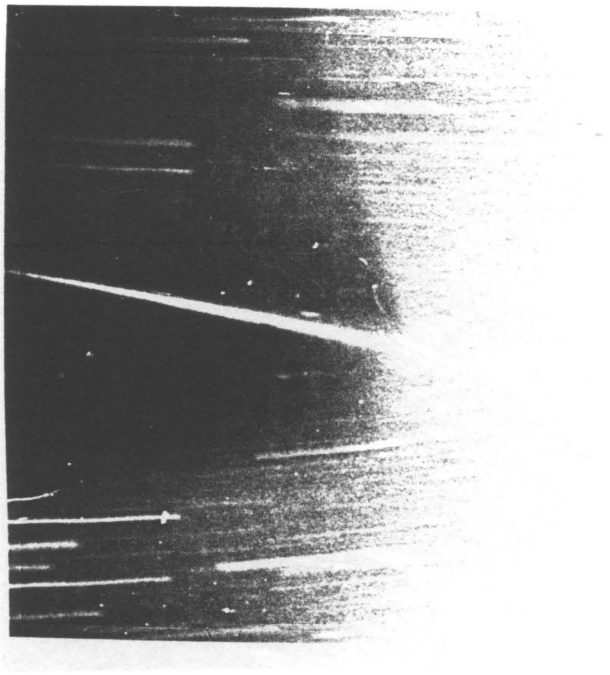

Fig. 3.4.4 Instantaneous flow visualization for K=1.2 and α=+10° (downstroke).

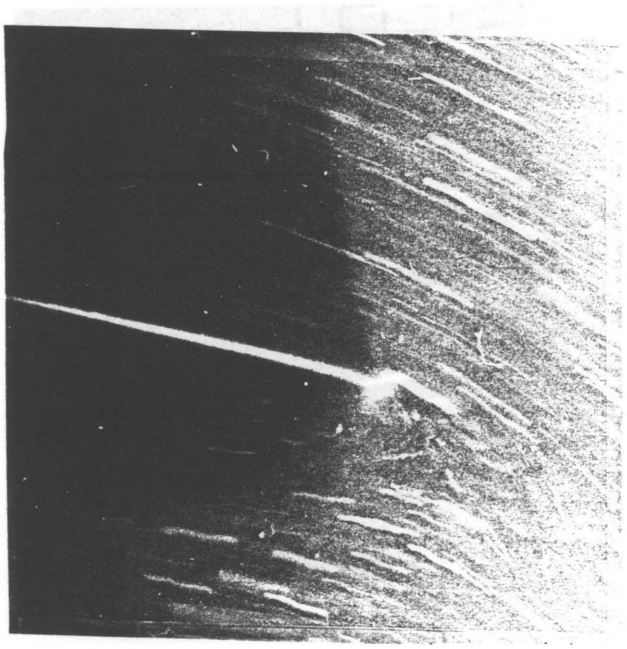

Fig. 3.4.5 Instantaneous flow visualization for K=2.4 and α=0° (upstroke).

Fig. 3.4.6 Instantaneous flow visulaization for K=2.4 and $\alpha=0°$ (downstroke).

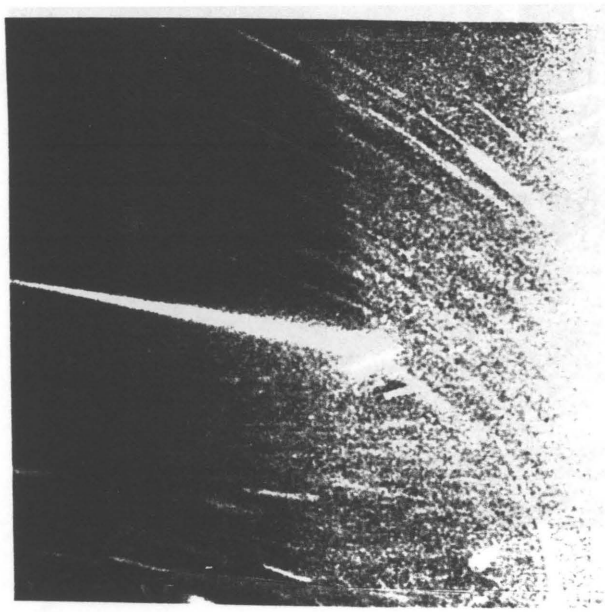

Fig. 3.4.7 Instantaneous flow visualization for K=3.9 and α=0° (upstroke).

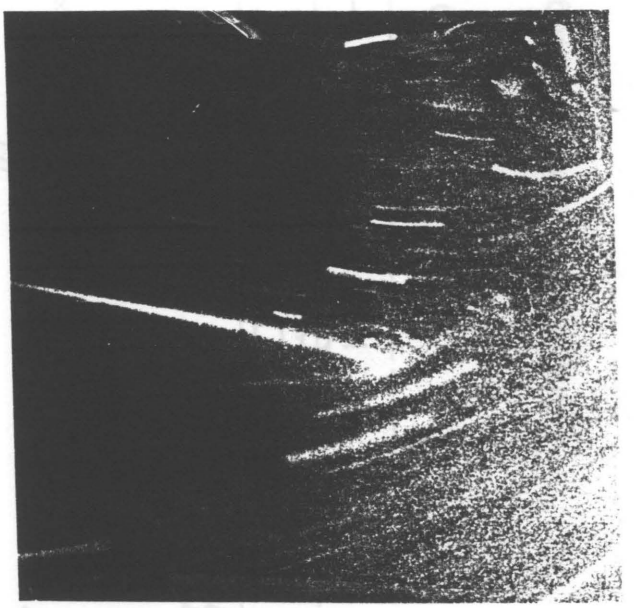

Fig. 3.4.8 Instantaneous flow visualization for K=3.9 and $\alpha=0°$ (downstroke).

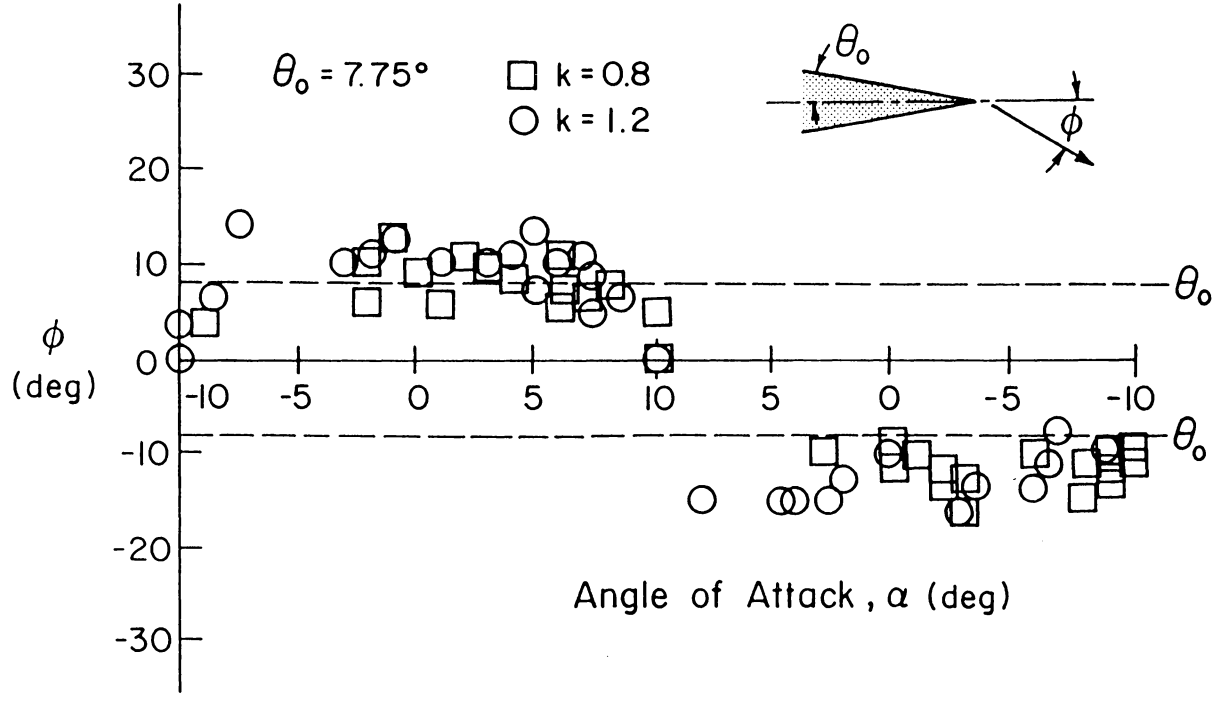

Fig. 3.4.9 Slope of the streamlines at the trailing edge for K=0.8 and 1.2.

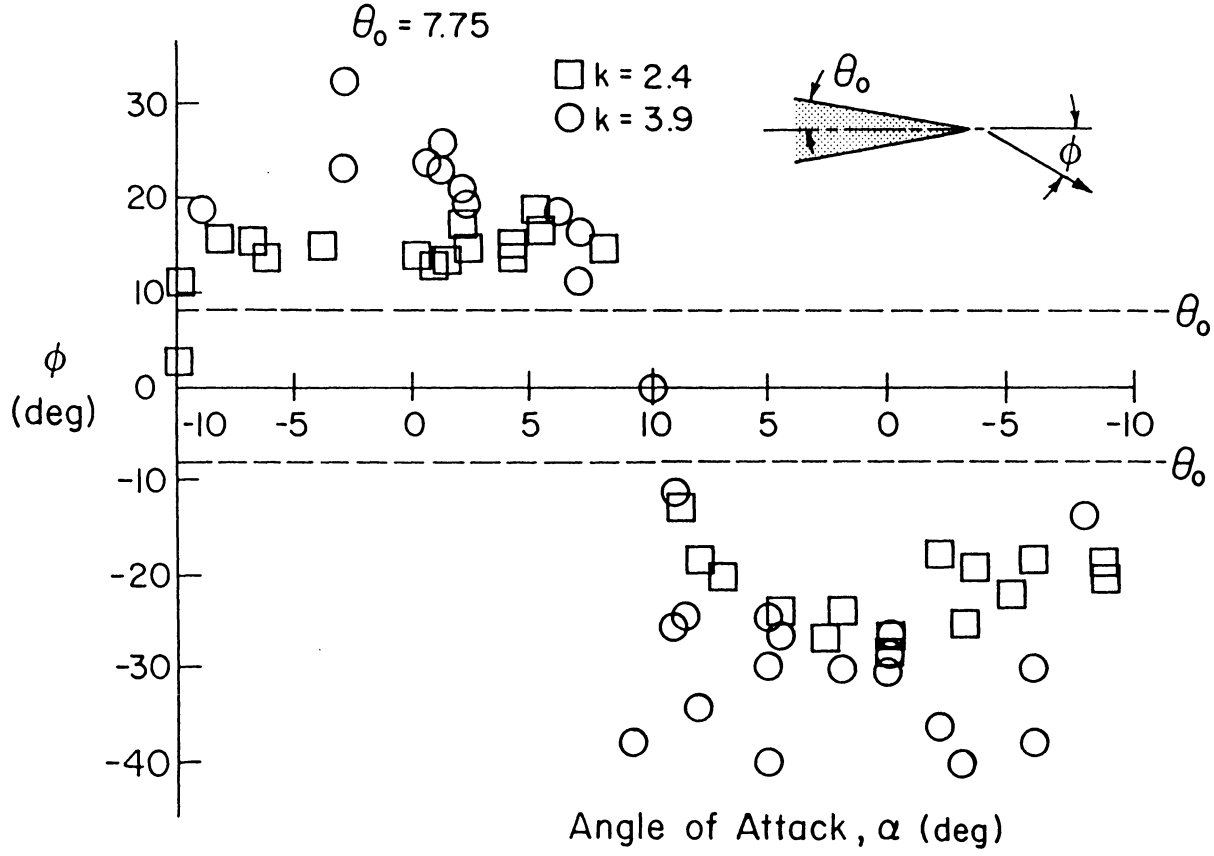

Fig. 3.4.10 Slope of the streamlines at the trailing edge for K=2.4 and 3.9.

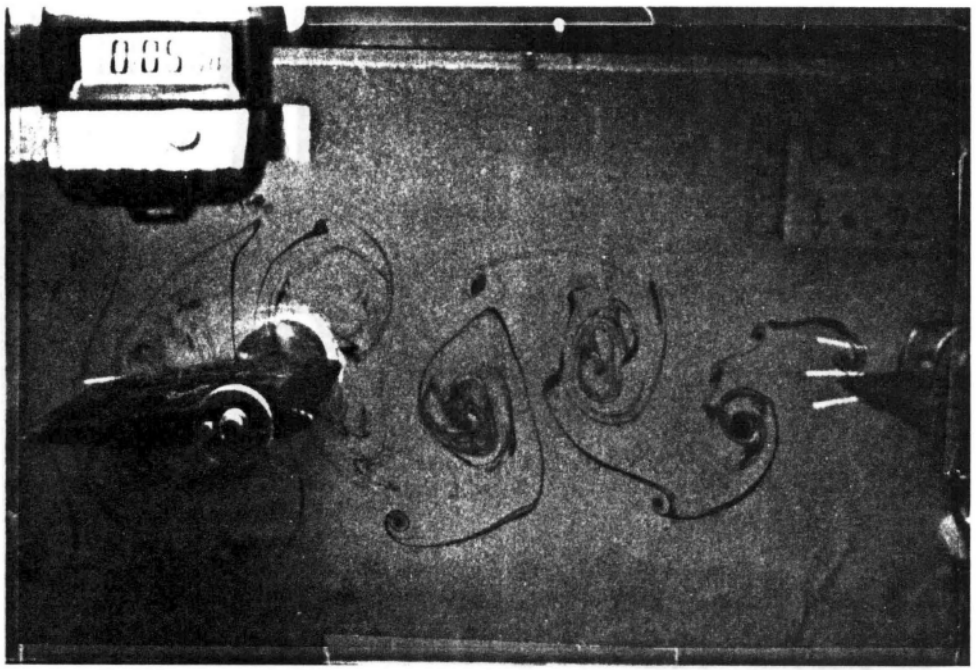

Fig. 3.4.11 Dye visualization behind the pitching airfoil for K=3.9 (t=5.08 sec).

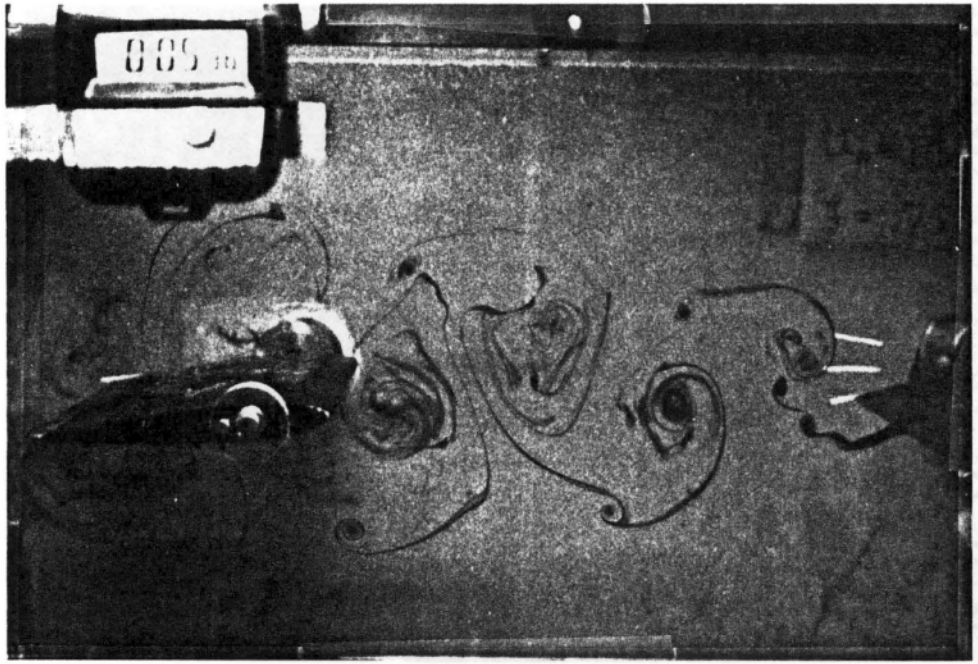

Fig. 3.4.12 Dye visualization behind the pitching airfoil for K=3.9 (t=5.38 sec).

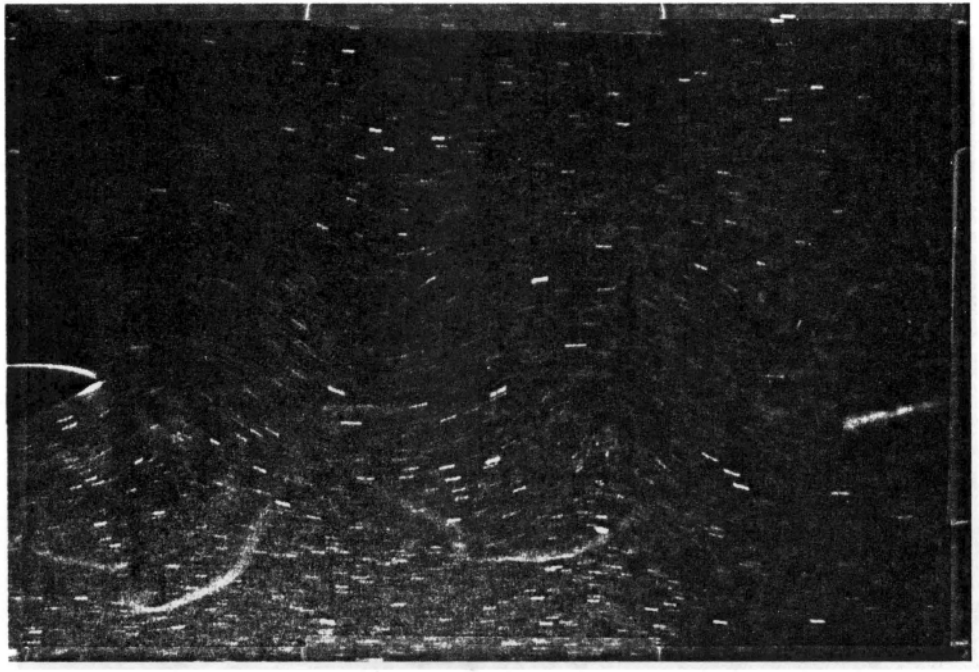

Fig. 3.4.13 Particle and dye visualization behind the pitching airfoil for K=3.9.

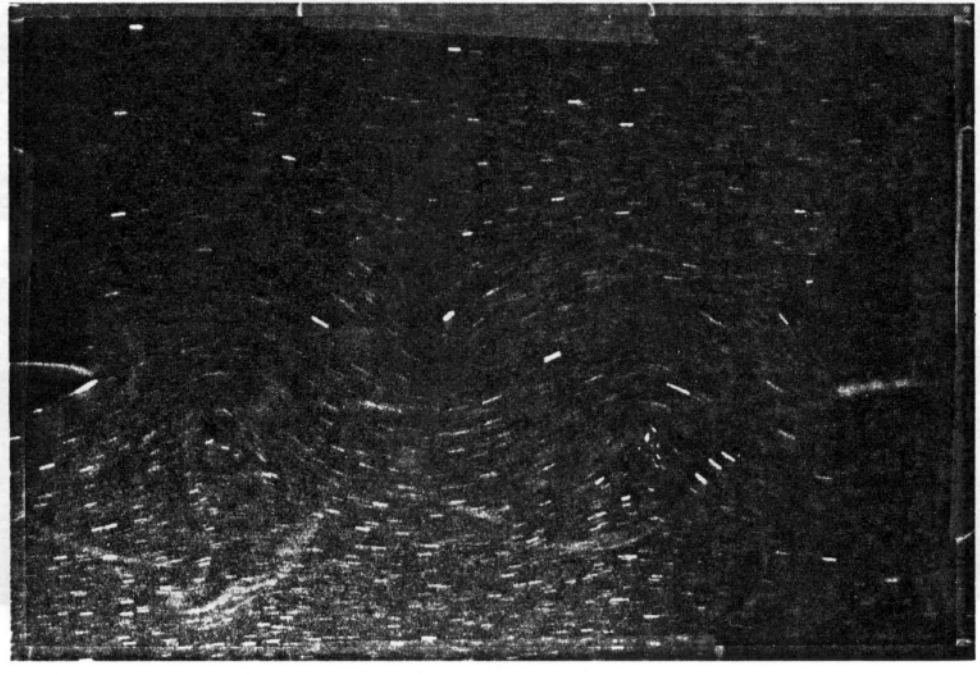

Fig. 3.4.14 Particle and dye visualization behind the pitching airfoil for K=3.9.

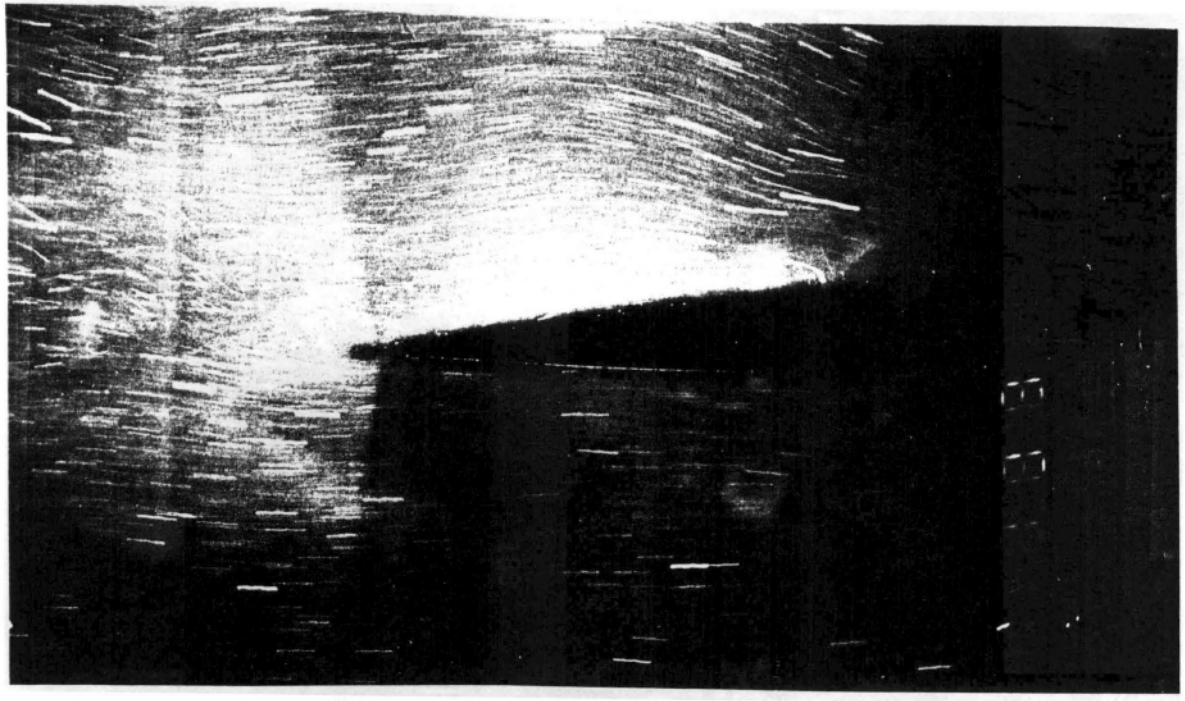

Fig. 3.4.15 Particle visualization at the trailing edge of the fixed airfoil for K=3.9 (t=0.7 sec, one full period is 0.8 sec).

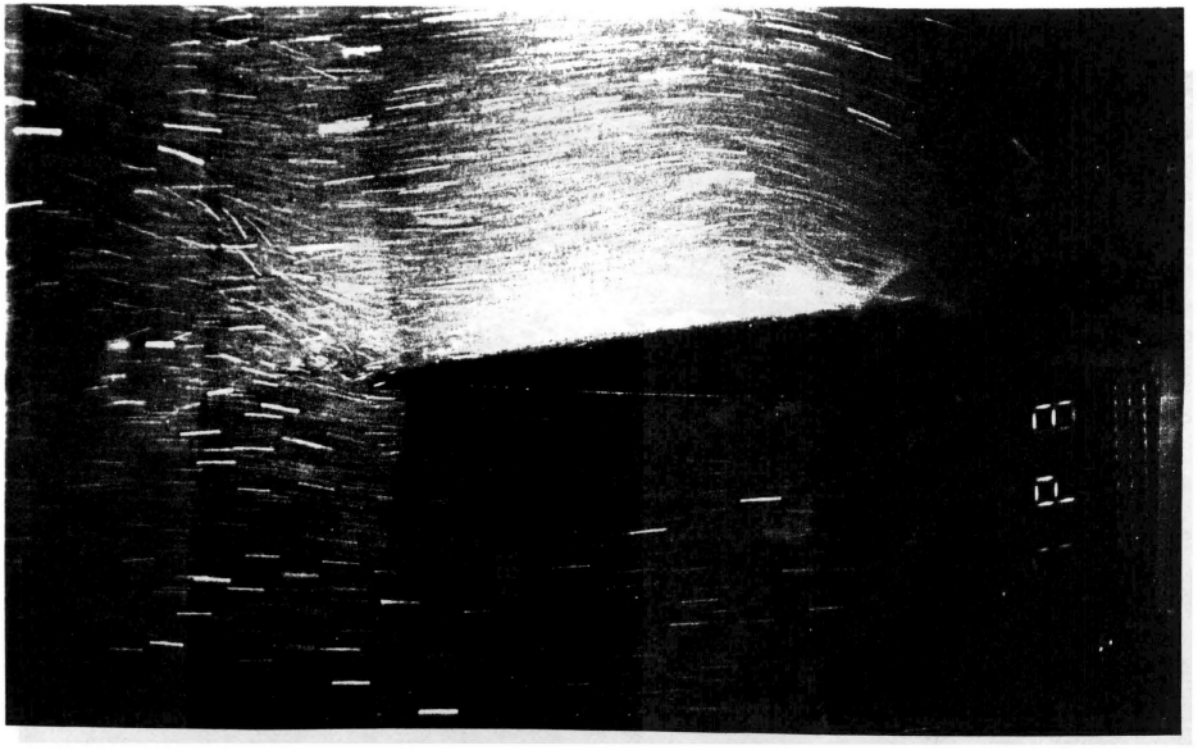

Fig. 3.4.16 Particle visualization at the trailing edge of the fixed airfoil for K=3.9 (t=0.6 sec, one full period is 0.8 sec).

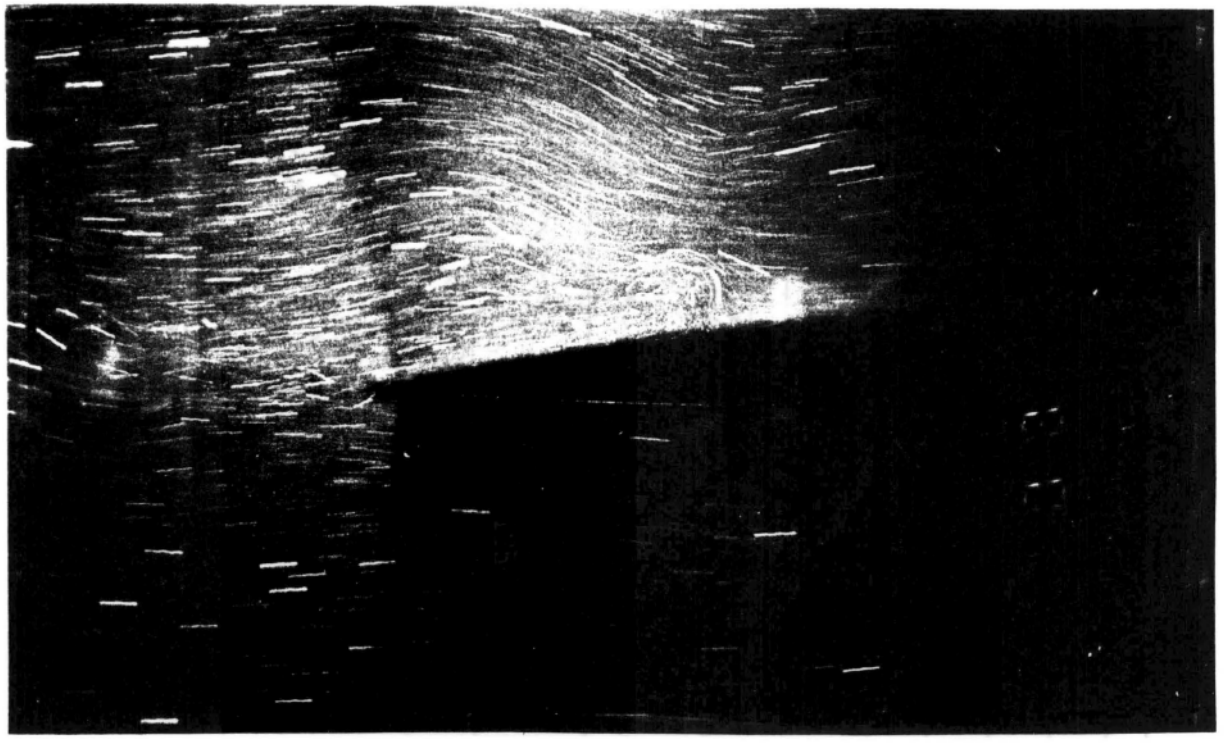

Fig. 3.4.17 Particle visualization at the trailing edge of the fixed airfoil for K=3.9 (t=0.1 sec, one full period is 0.8 sec).

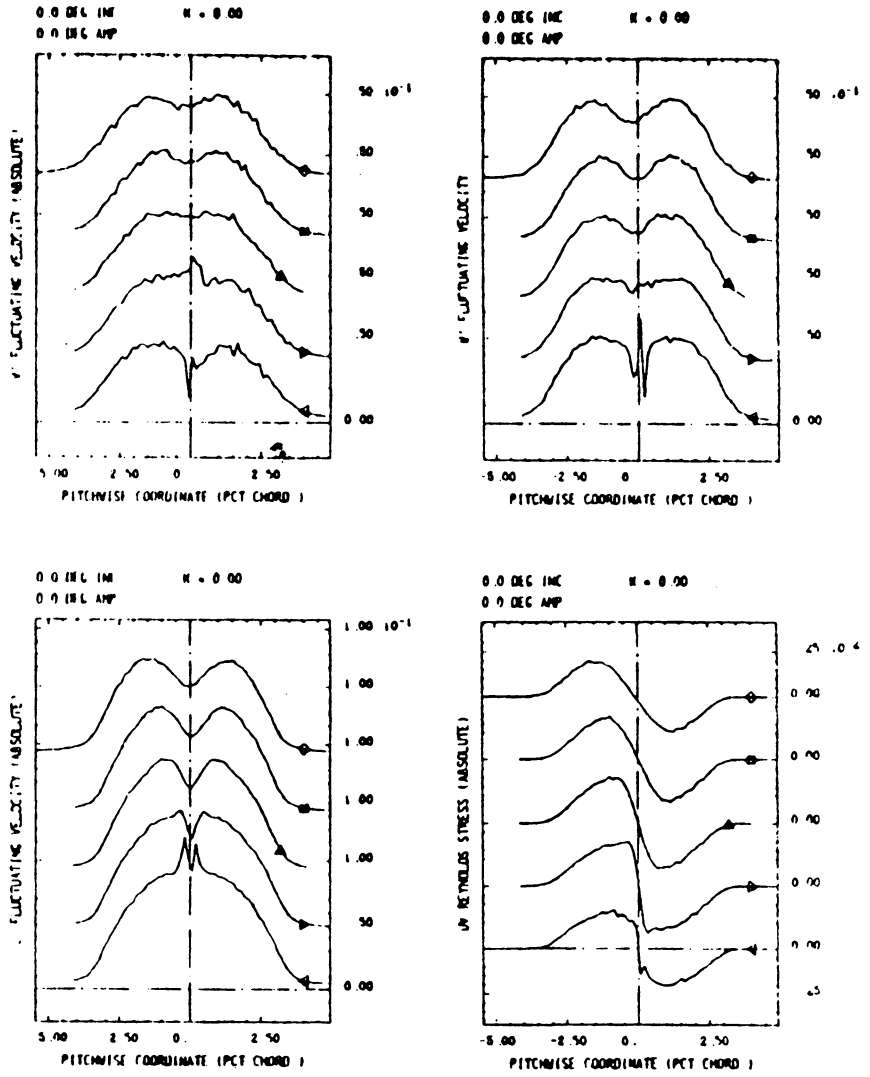

Fig. 3.5.1(a) Velocity profiles in the wake of an oscillating NACA 0012 at K=0.86 (DeRuyck and Hirsch, 1982).

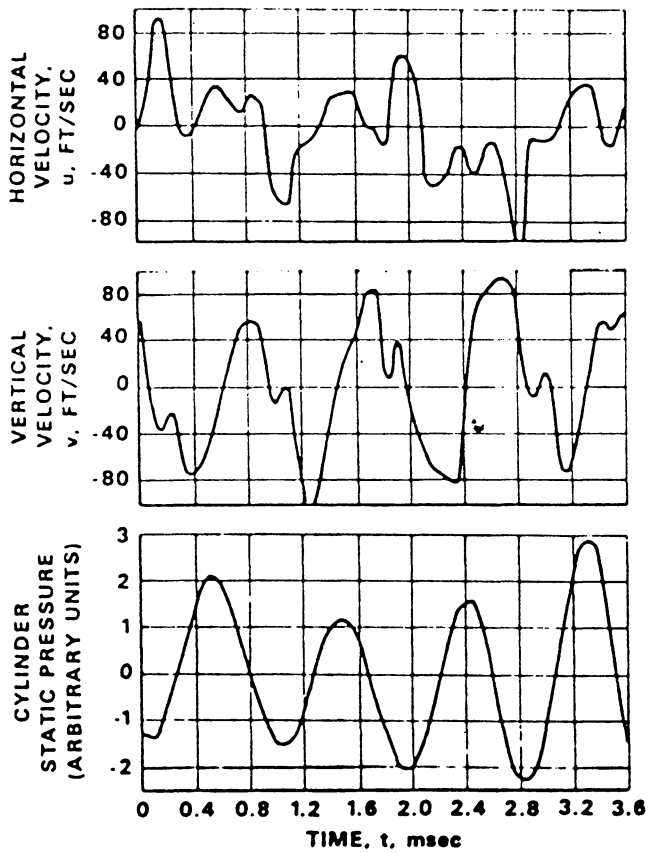

Fig. 3.5.1(b) Velocity response of the fluctuation of the flow aft of a circular cylinder at K=3.9 (Commerford and Carta, 1974).

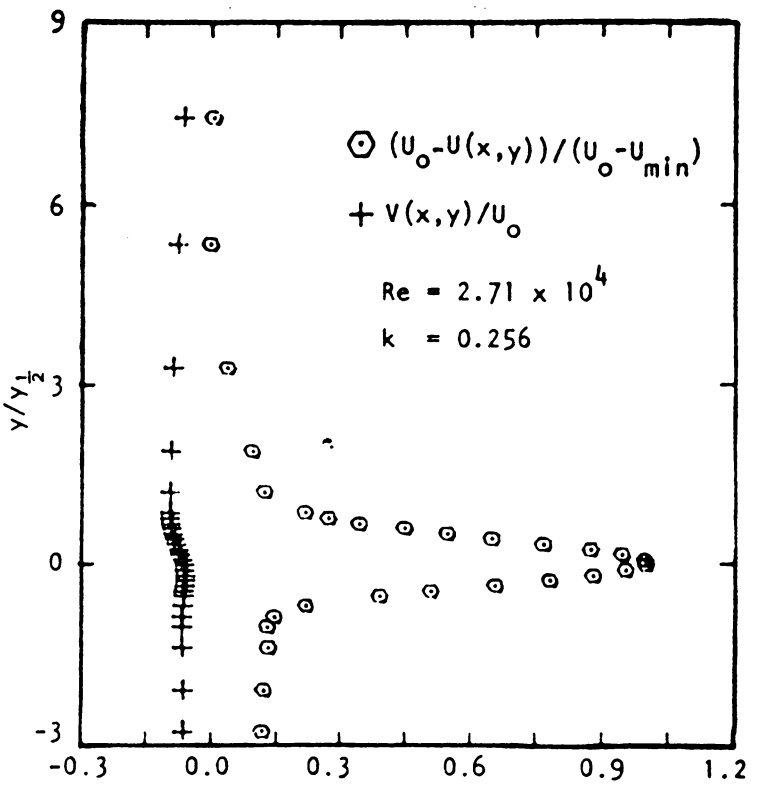

Fig. 3.5.1(c) Streamwise and transverse velocity profiles in the wake of a plunging NACA 0012 airfoil at K=1.0 (Ho and Chen, 1980).

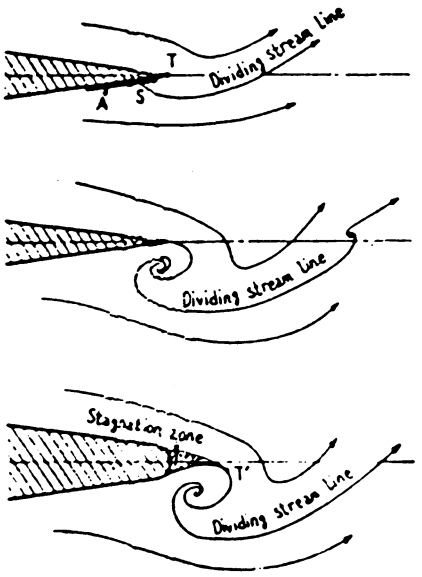

Fig. 3.5.2 Trailing edge flow of a plunging airfoil, (a) sharp edge with stagnation point at A, (b) sharp edge with stagnation point at the edge, (c) rounded edge (Ohashi and Ishikawa, 1972).

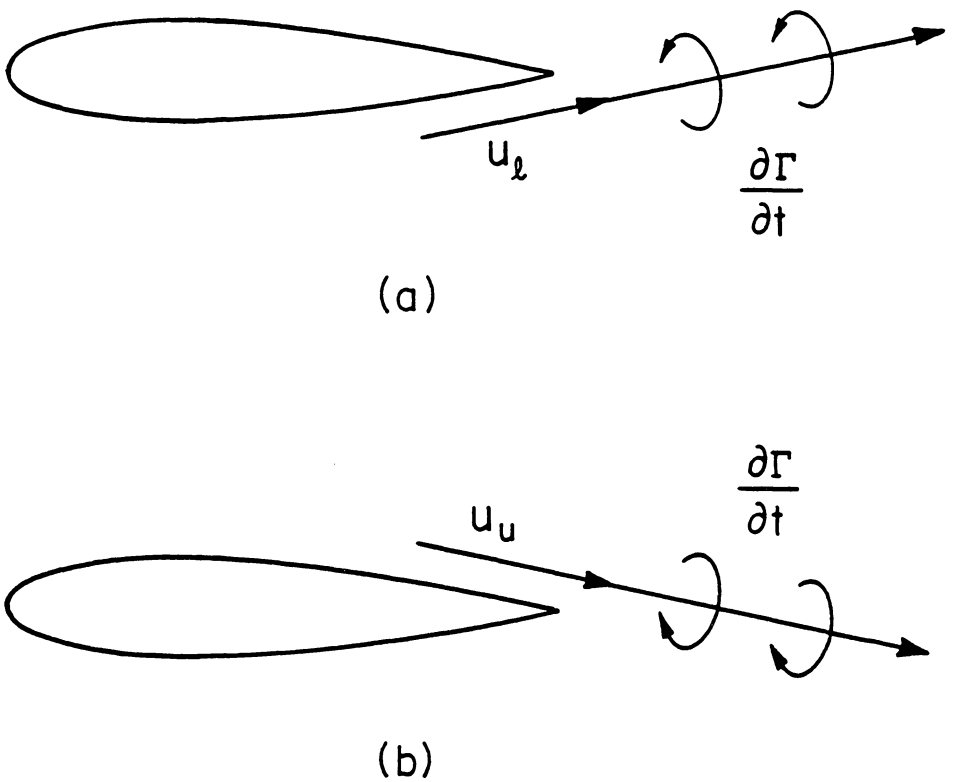

Fig. 4.1.1 Vorticity shedding aft of the trailing edge; (a) counter-clockwise shedding, (b) clockwise shedding.

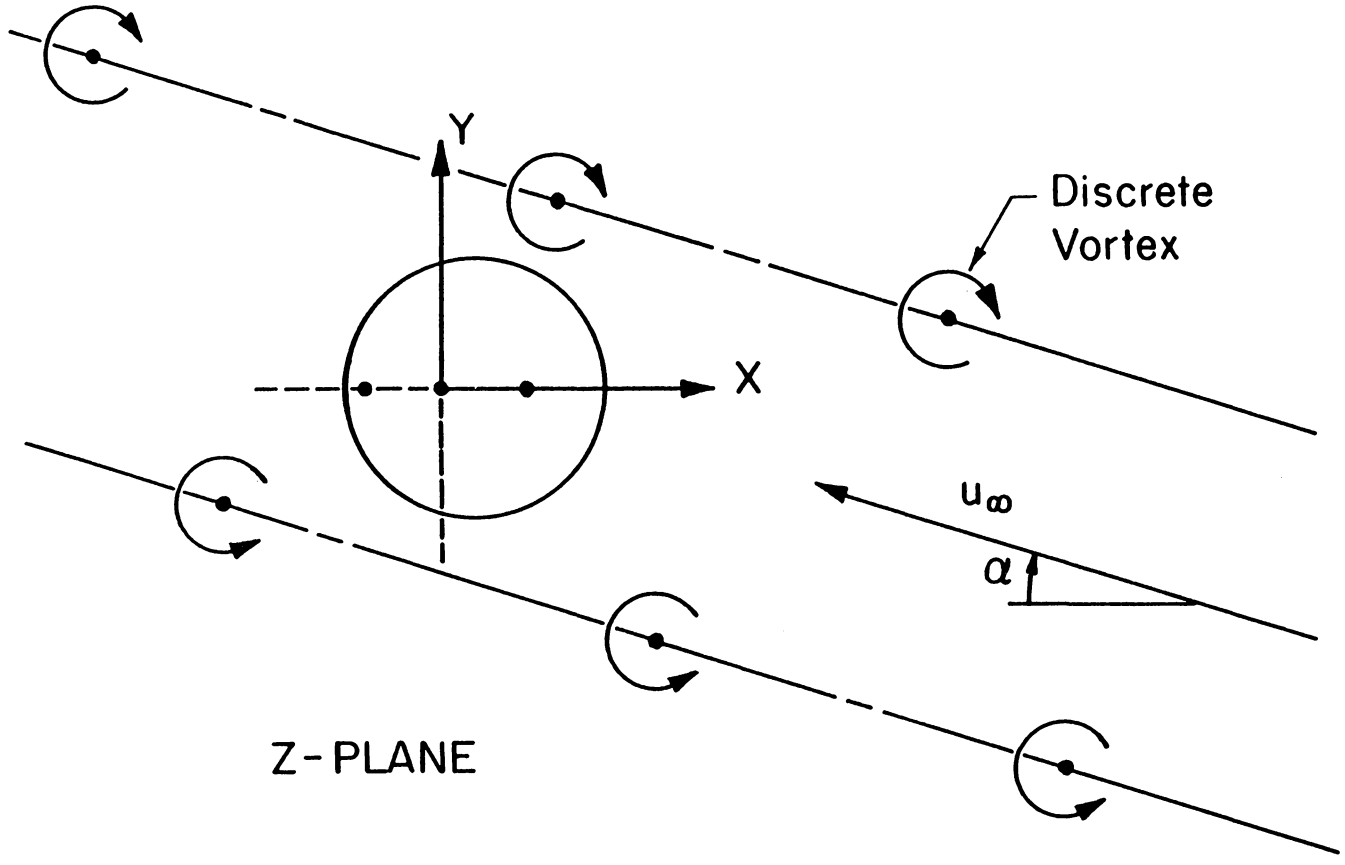

Fig. 4.2.1 The flowfield over a circular cylinder in the z-plane with discrete vortices.

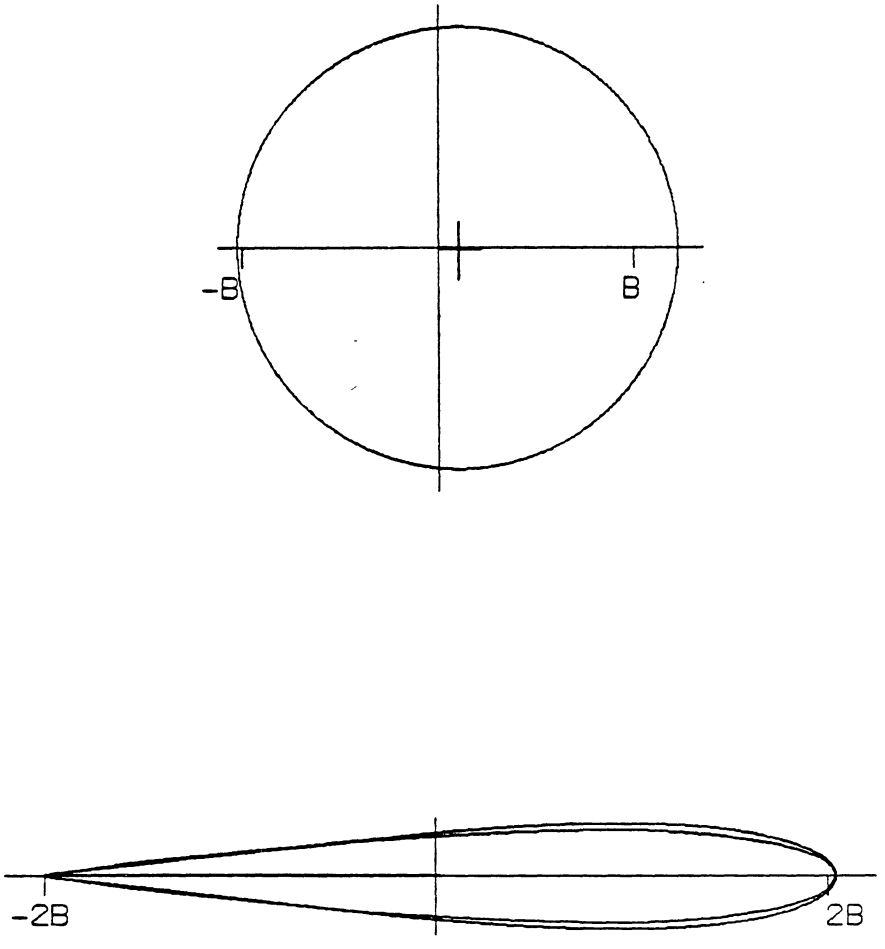

Fig. 4.2.2 Approximation of a Joukowski airfoil to a NACA 0012 via conformal mapping (the inside airfoil is the NACA 0012).

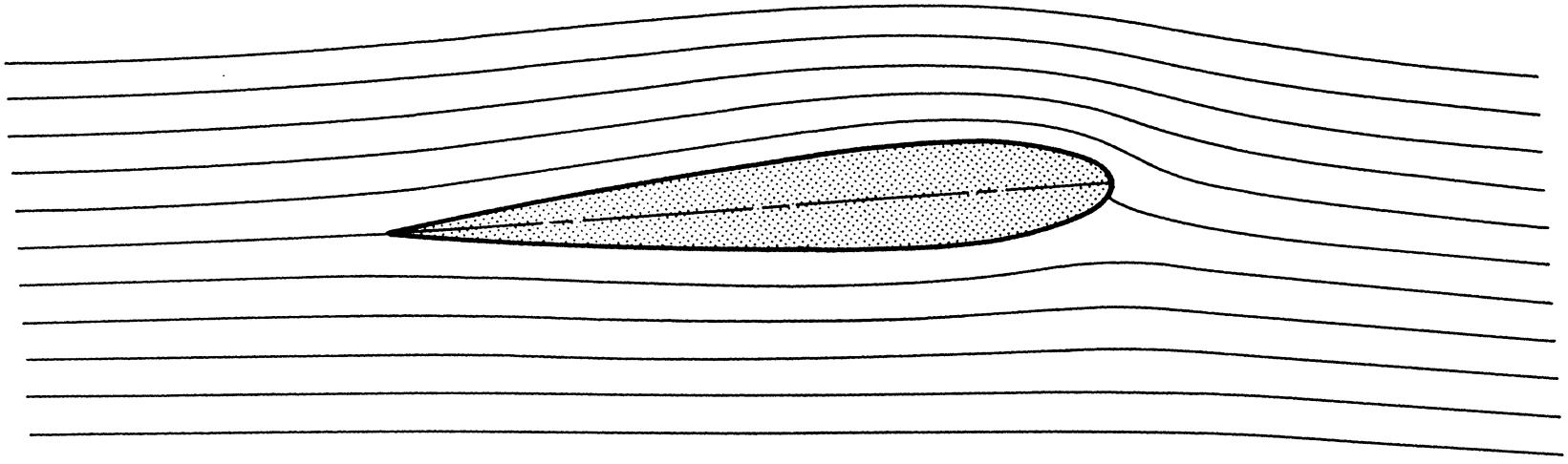

Fig. 4.2.3 Ideal flow pattern of streamlines over the modified Joukowski airfoil at a 5 degree angle of attack.

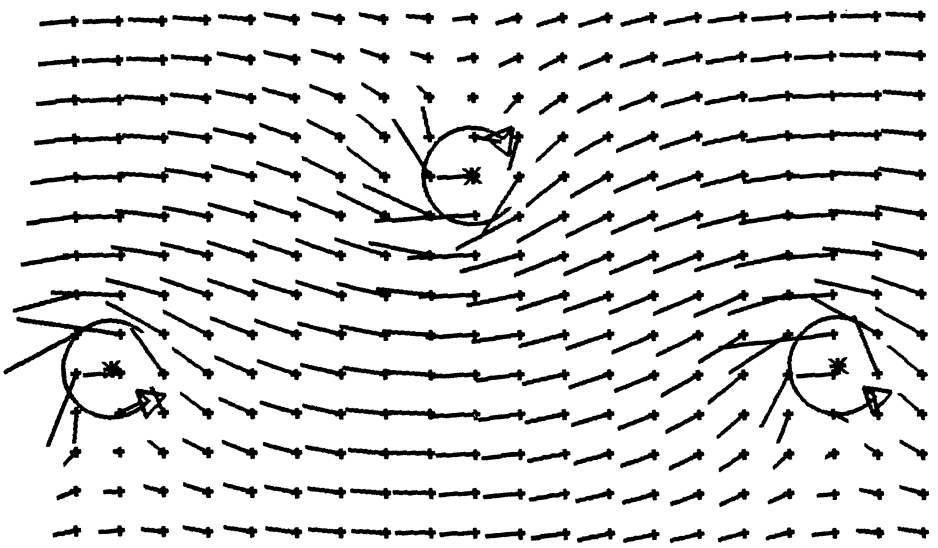

Fig. 5.1.1 The numerically predicted velocity field of the unsteady periodic wake using the results from the experiments of the present work, e/a=0.1915 (K=3.9).

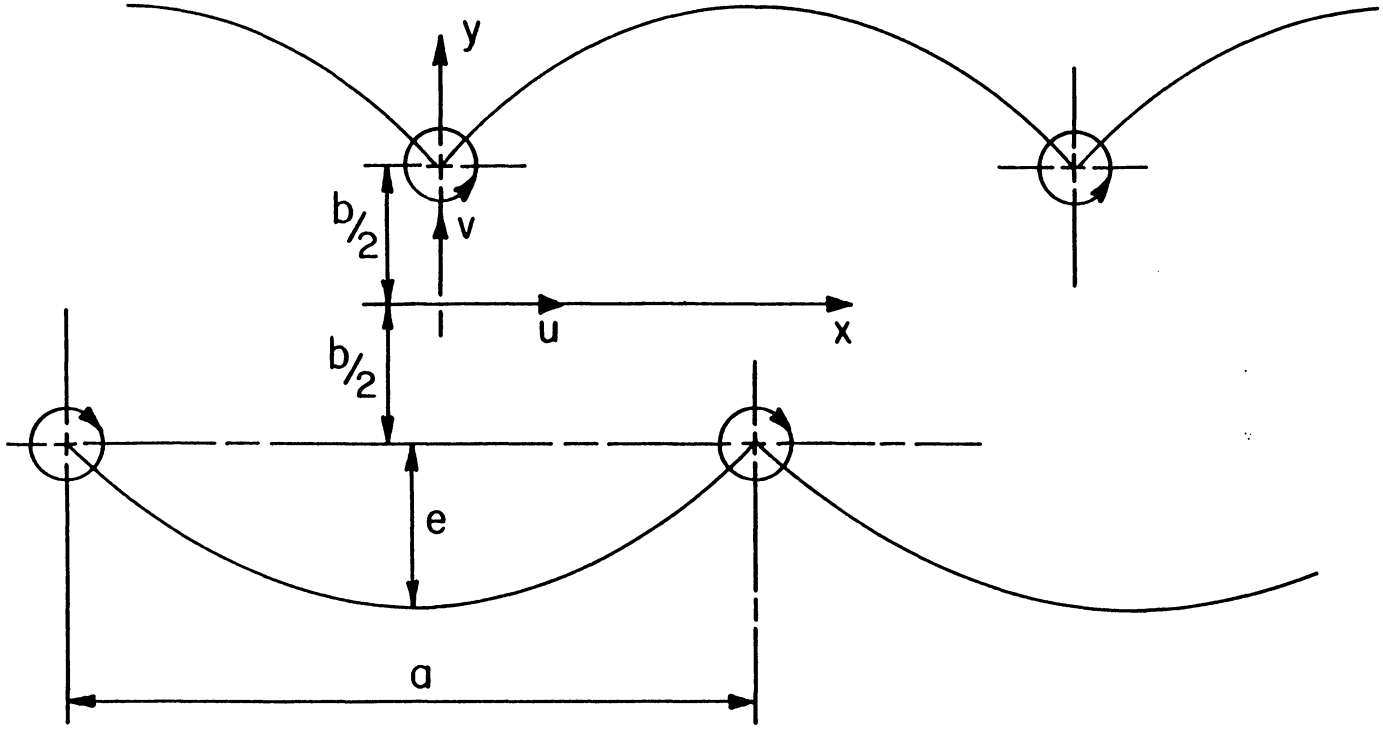

Fig. 5.1.2 Vortex street showing vortex spacing a and wave depth e for the calculation of the ratio e/a.

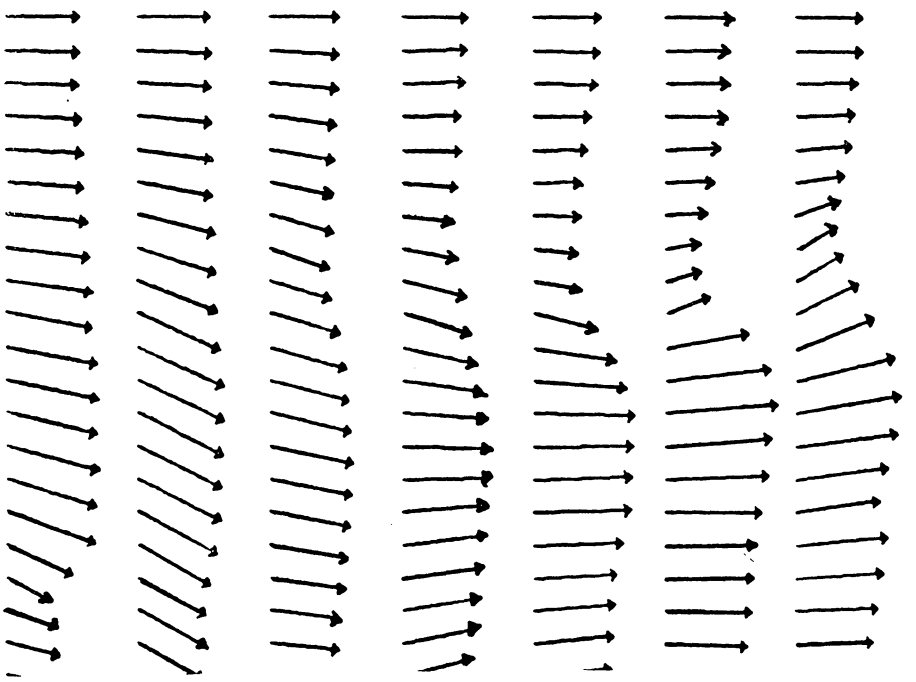

Fig. 5.1.3 The experimental velocity field of Mathioulakis, 1985. The ratio e/a=0.1613 (K=2.77).

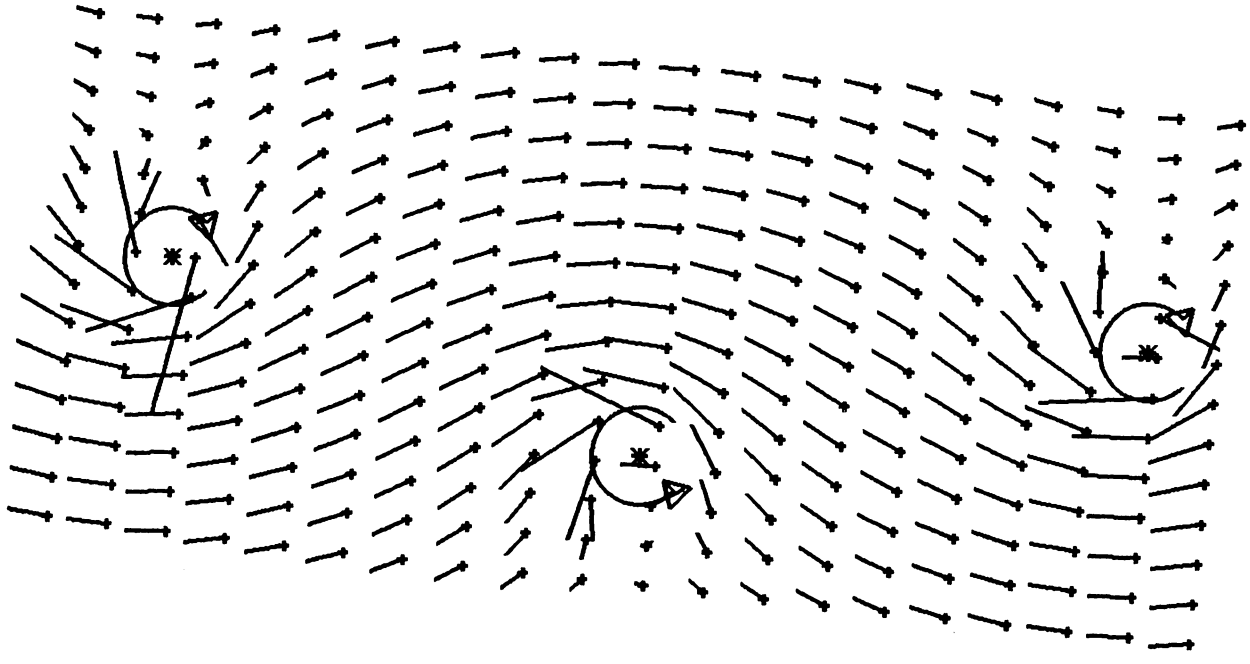

Fig. 5.1.4 The numerically predicted velocity field of the unsteady periodic wake using the results from the experiments of Mathioulakis, 1985. The ratio e/a=0.17460 (K=2.77).

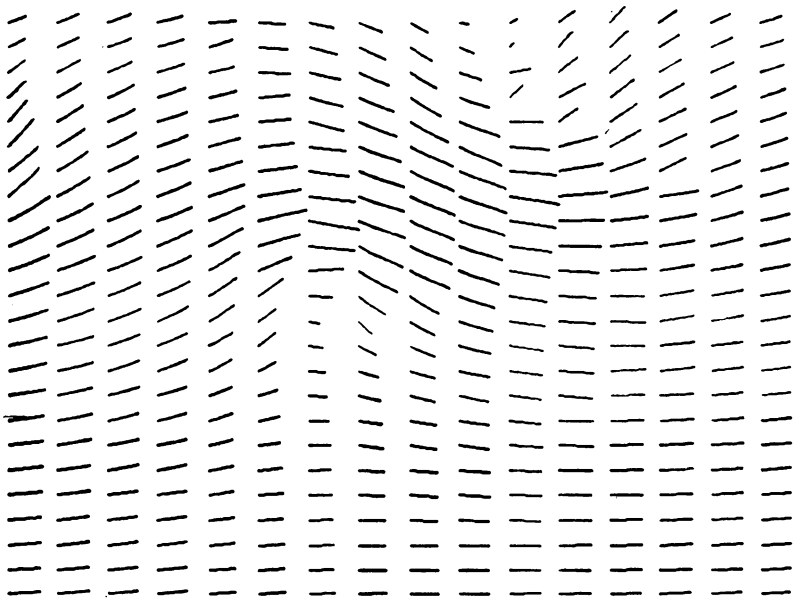

Fig. 5.1.5 The numerically predicted velocity field behind the pitching airfoil from the numerical analysis of Kim and Mook, 1985. The ratio e/a=0.21739 (K=3.9).

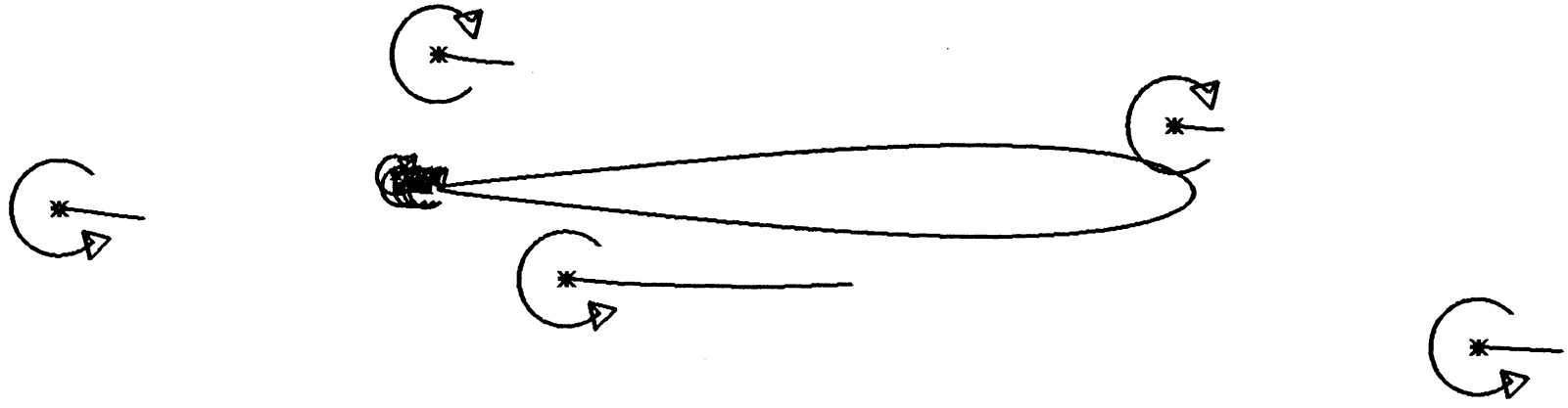

Fig. 5.2.1 Calculated positions of free stream and shed vorticity over the fixed airfoil at an angle of attack of 5° (5th time step).

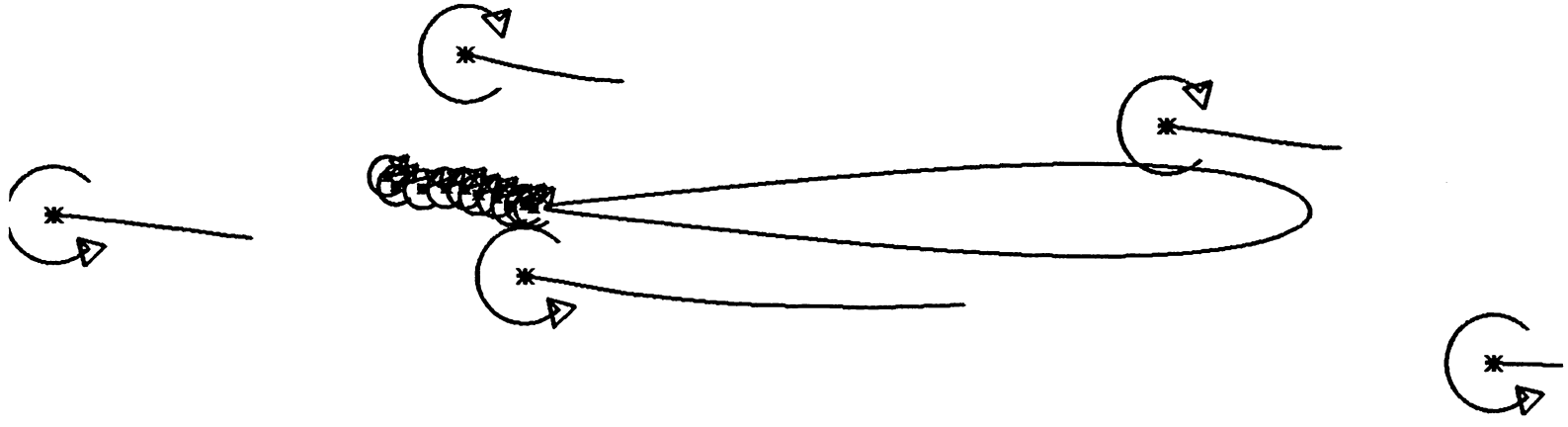

Fig. 5.2.2 Calculated positions of free stream and shed vorticity over the fixed airfoil at an angle of attack of 5° (10th time step).

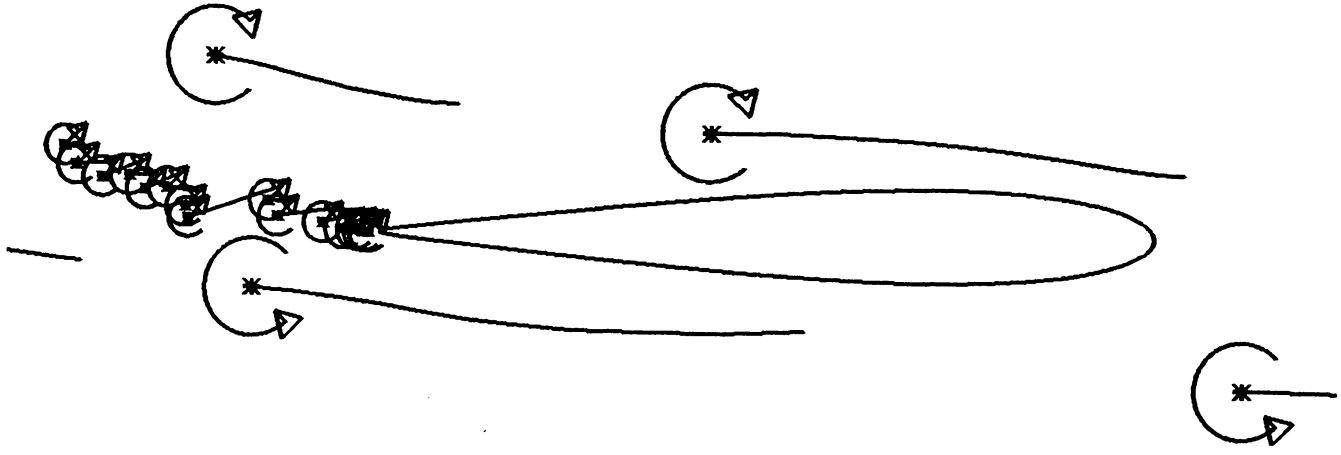

Fig. 5.2.3 Calculated positions of free stream and shed vorticity over the fixed airfoil at an angle of attack of 5° (15th time step).

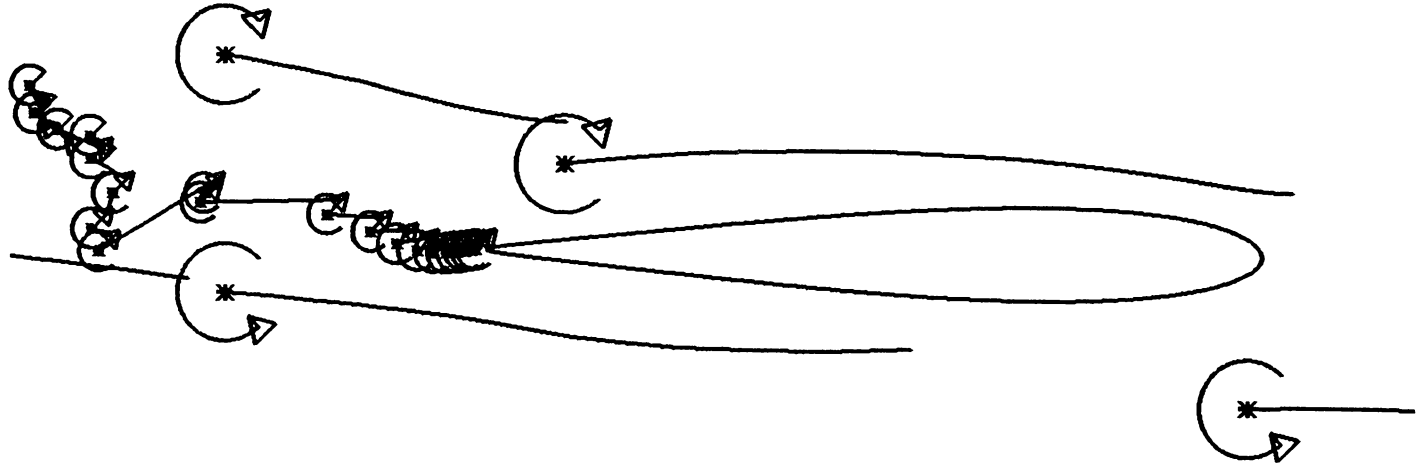

Fig. 5.2.4 Calculated positions of free stream and shed vorticity over the fixed airfoil at an angle of attack of 5° (20th time step).

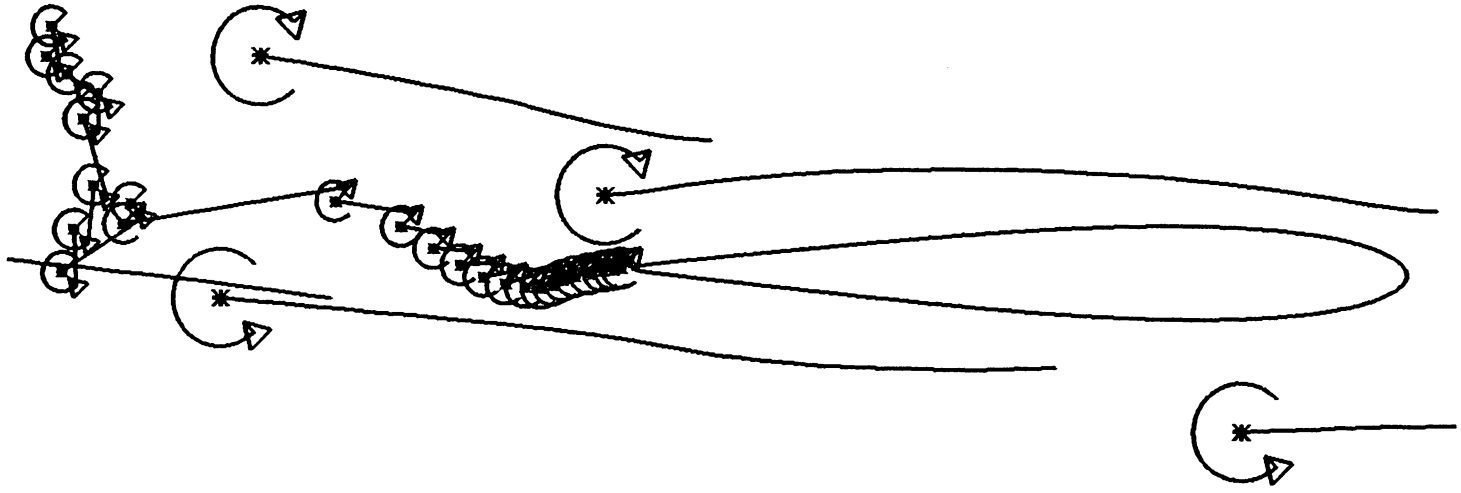

Fig. 5.2.5 Calculated positions of free stream and shed vorticity over the fixed airfoil at an angle of attack of 5° (25th time step).

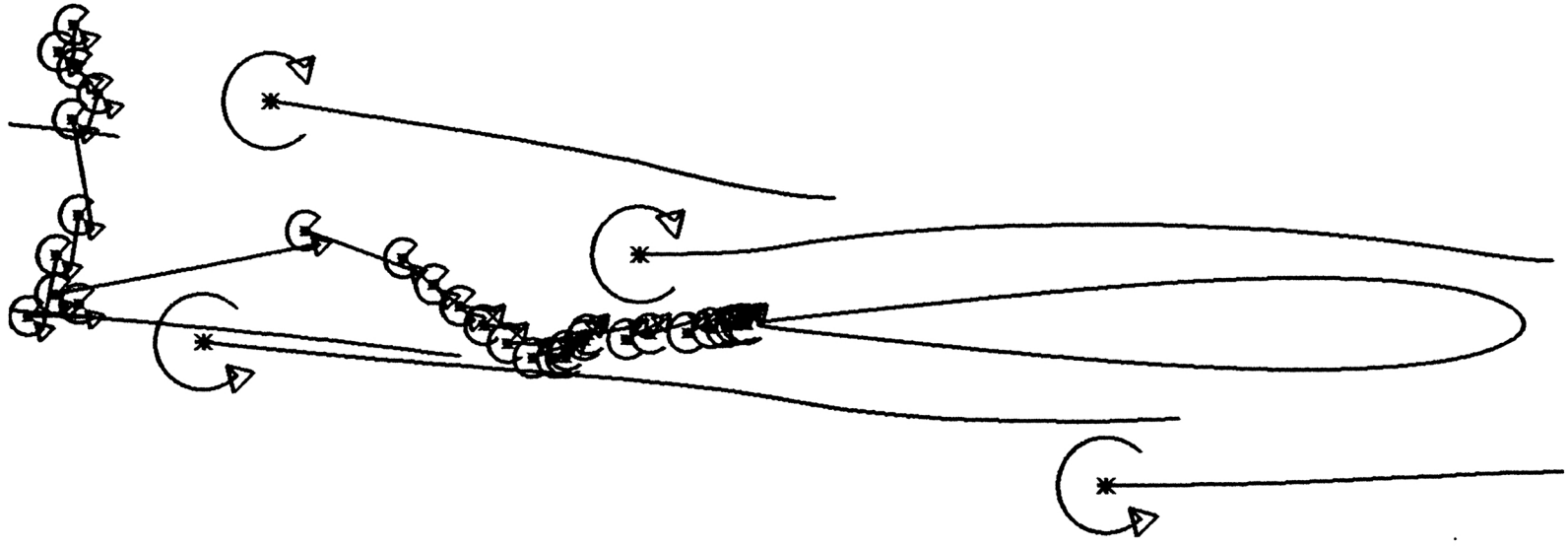

Fig. 5.2.6 Calculated positions of free stream and shed vorticity over the fixed airfoil at an angle of attack of 5° (30th time step).

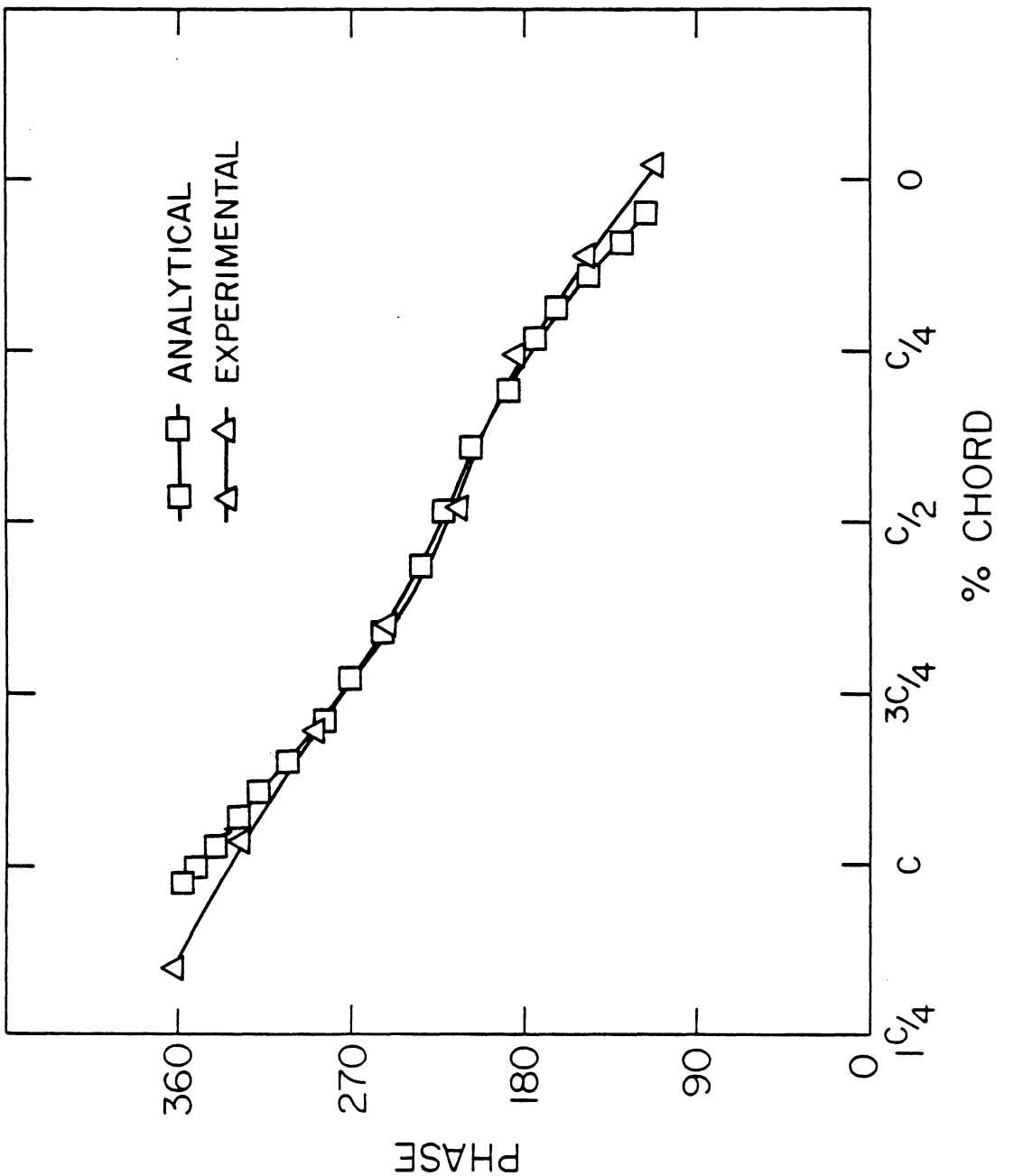

Fig. 5.2.7 The axial distance of a vortex over the fixed airfoil as obtained by numerical analysis and experiment.

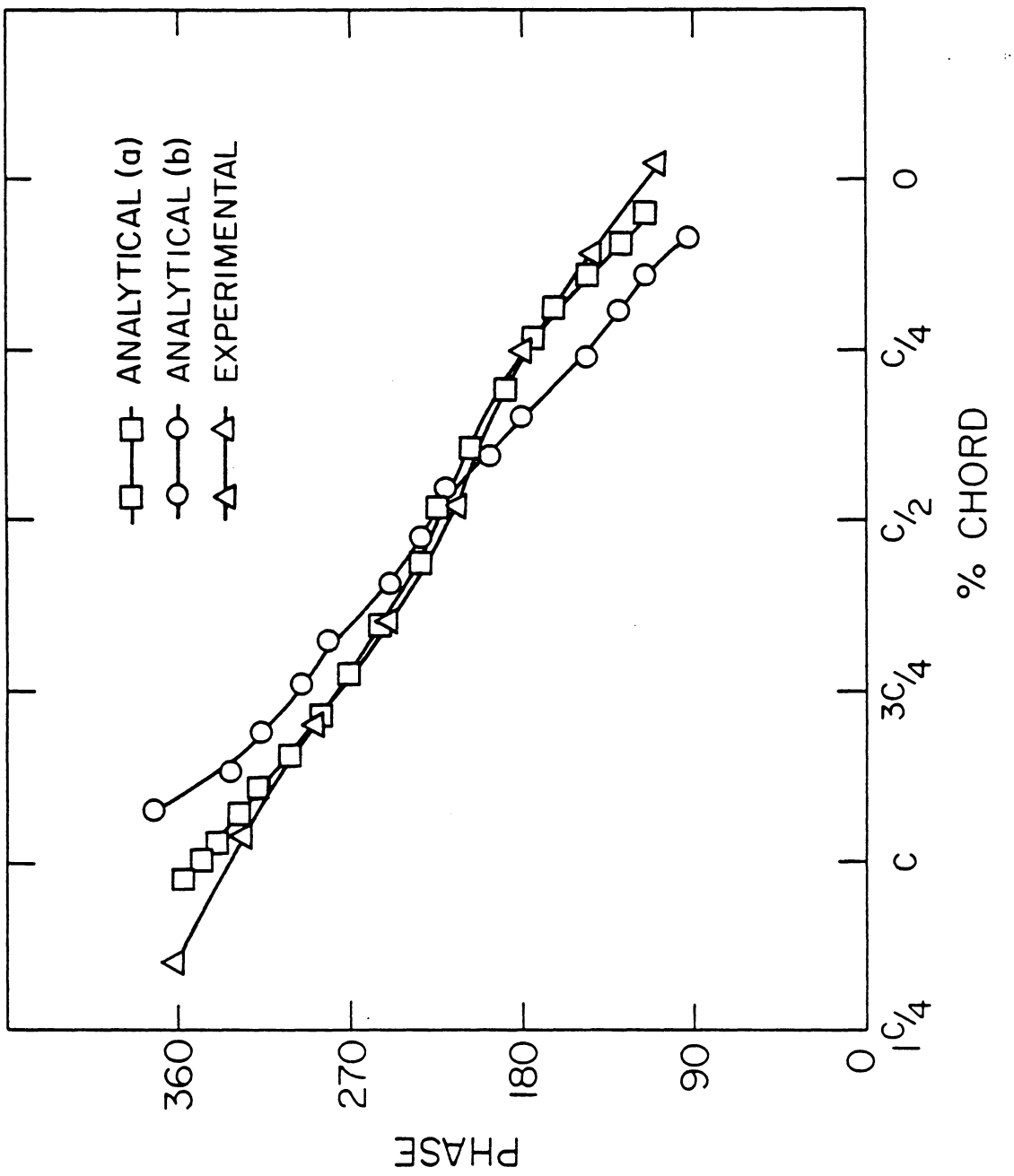

Fig. 5.2.8 The axial distance of a vortex over the fixed airfoil as obtained by numerical analysis and experiment; (a) 20 vortices, (b) 4 vortices.

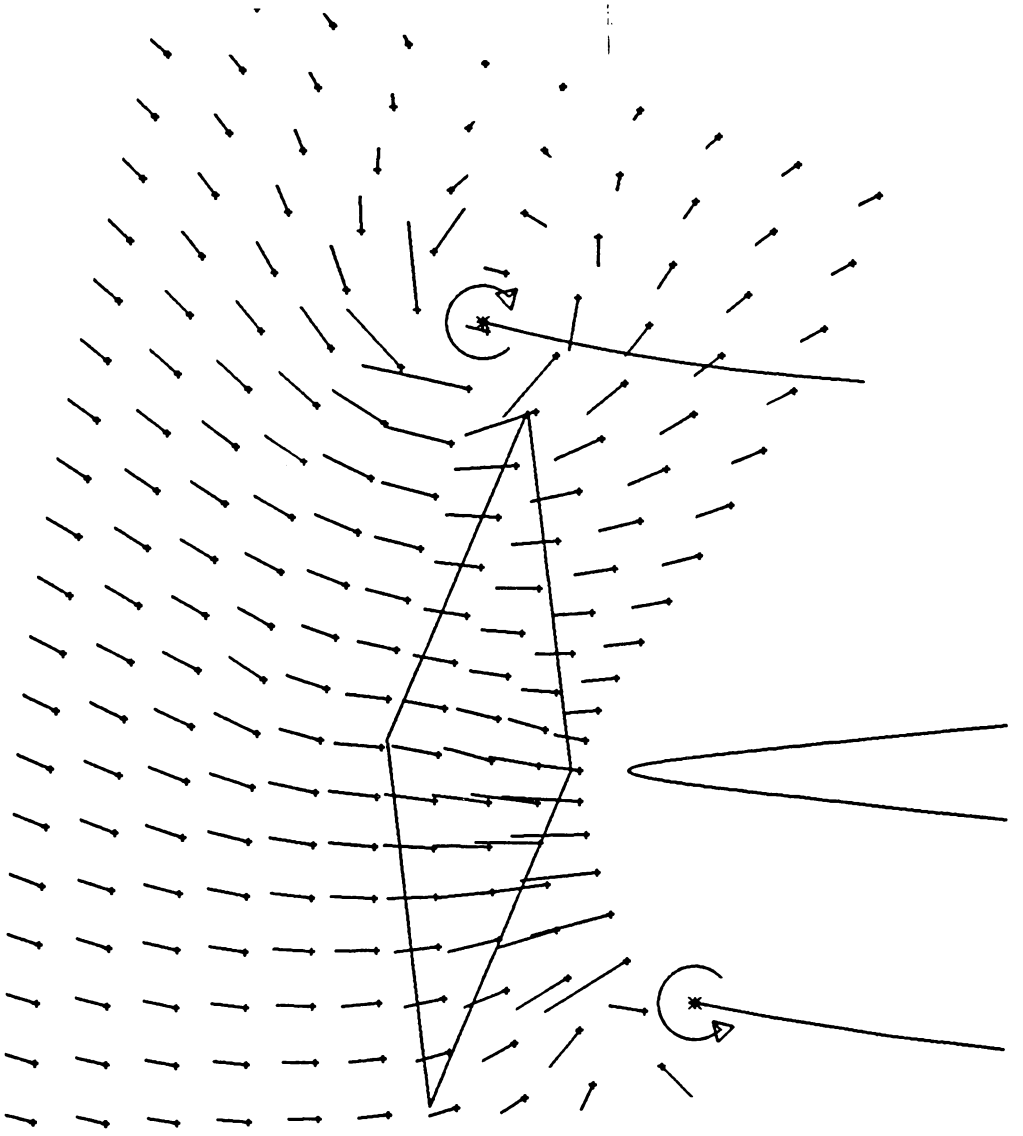

Fig. 5.2.9 The calculated velocity field aft of the trailing edge of the fixed airfoil (8th time step).

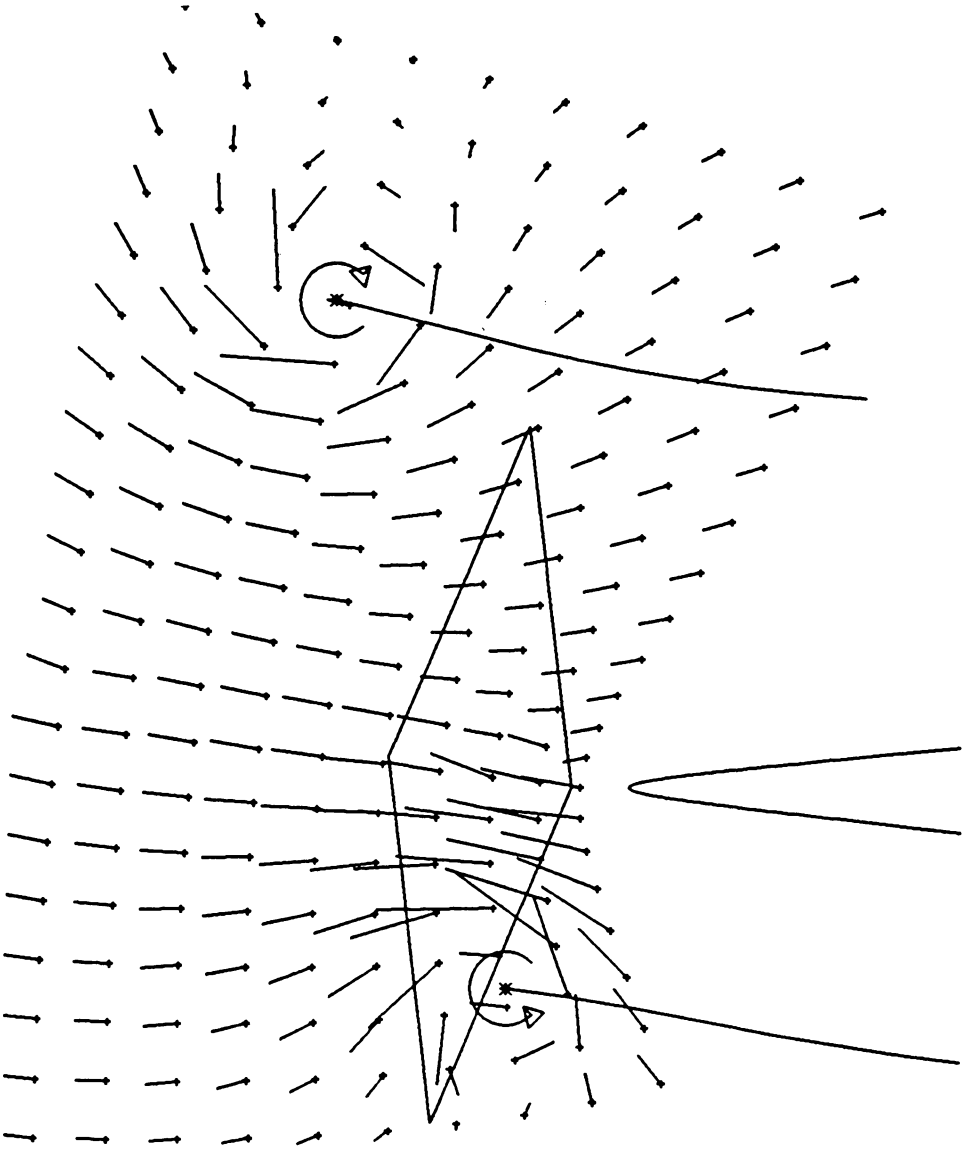

Fig. 5.2.10 The calculated velocity field aft of the trailing edge of the fixed airfoil (11th time step).

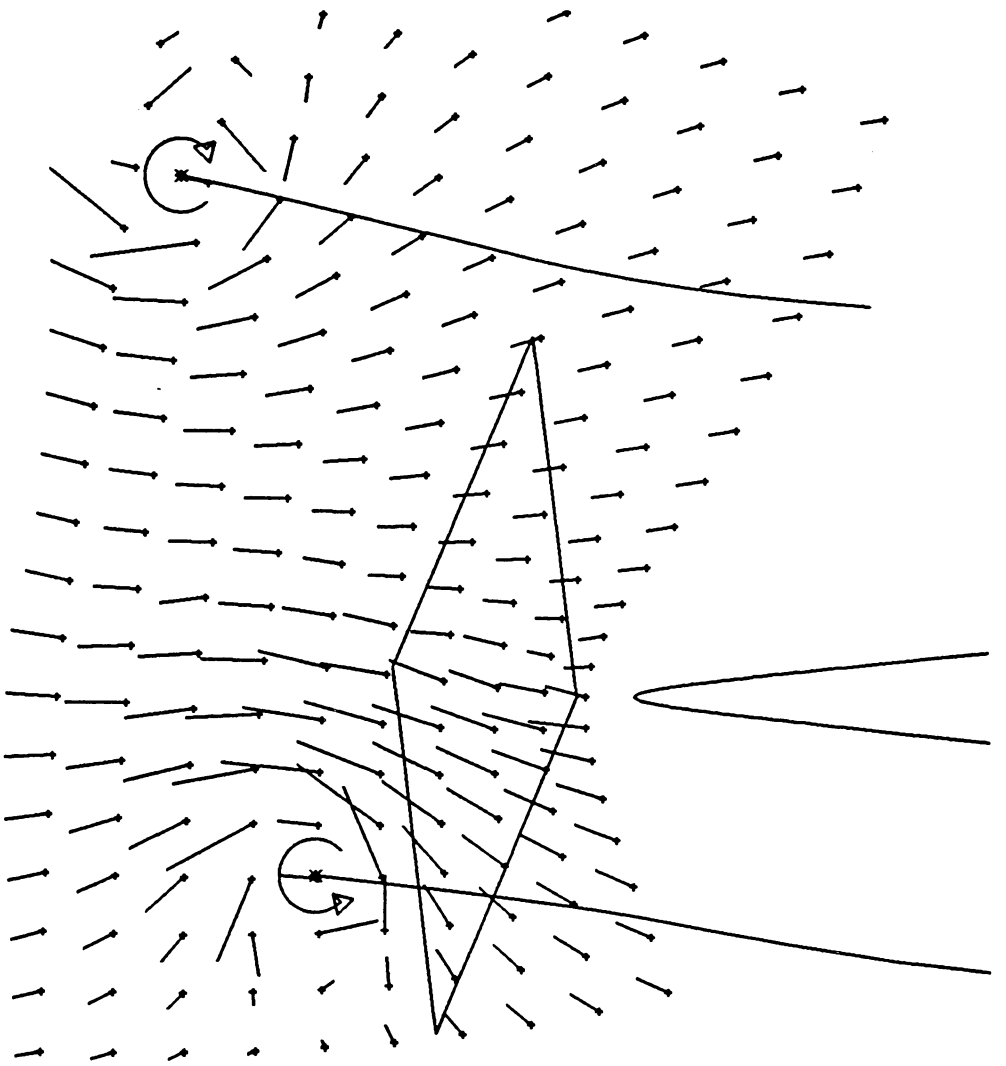

Fig. 5.2.11 The calculated velocity field aft of the trailing edge of the fixed airfoil (14th time step).

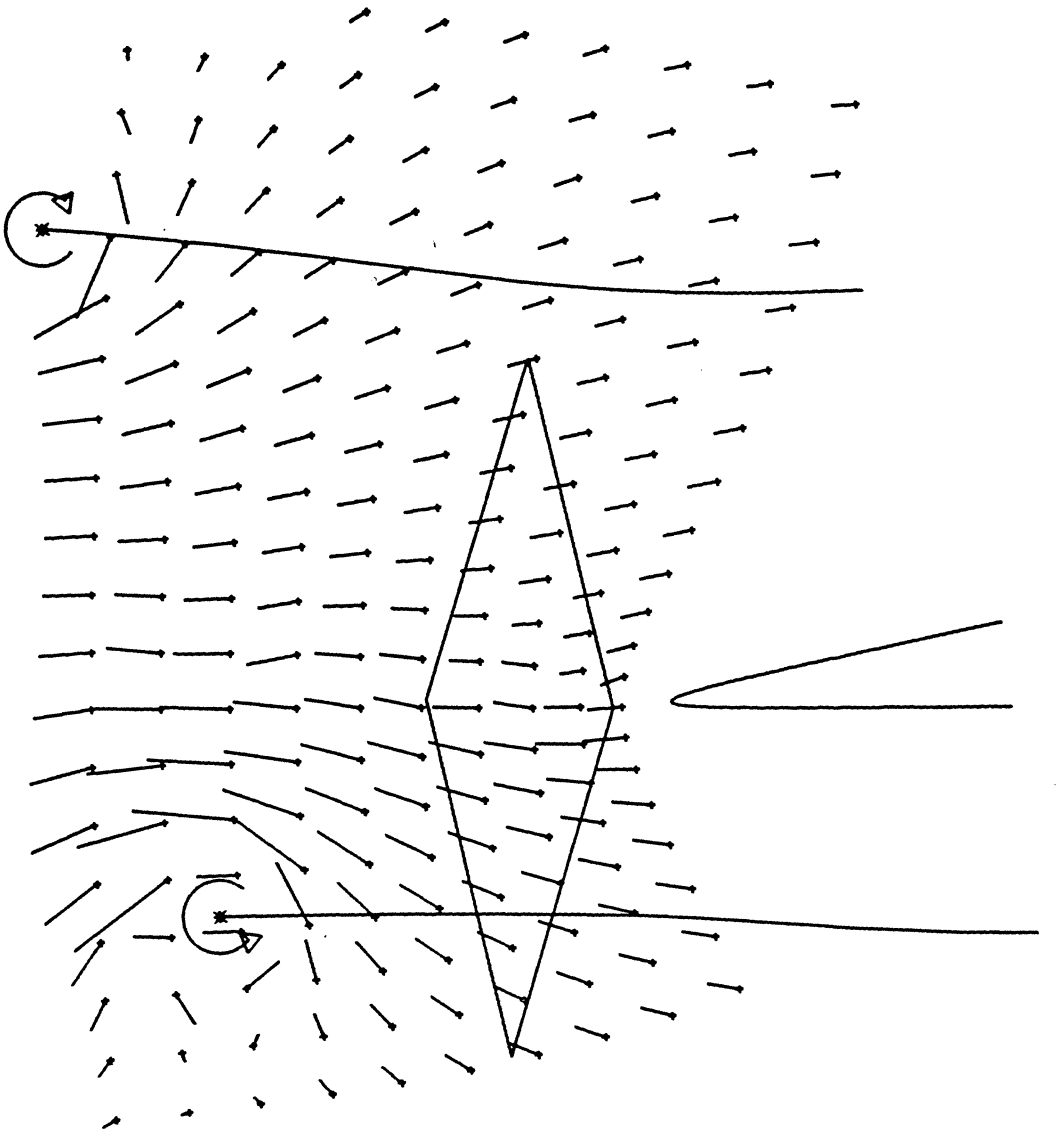

Fig. 5.2.12 The calculated velocity field aft of the trailing edge of the fixed airfoil (16th time step).

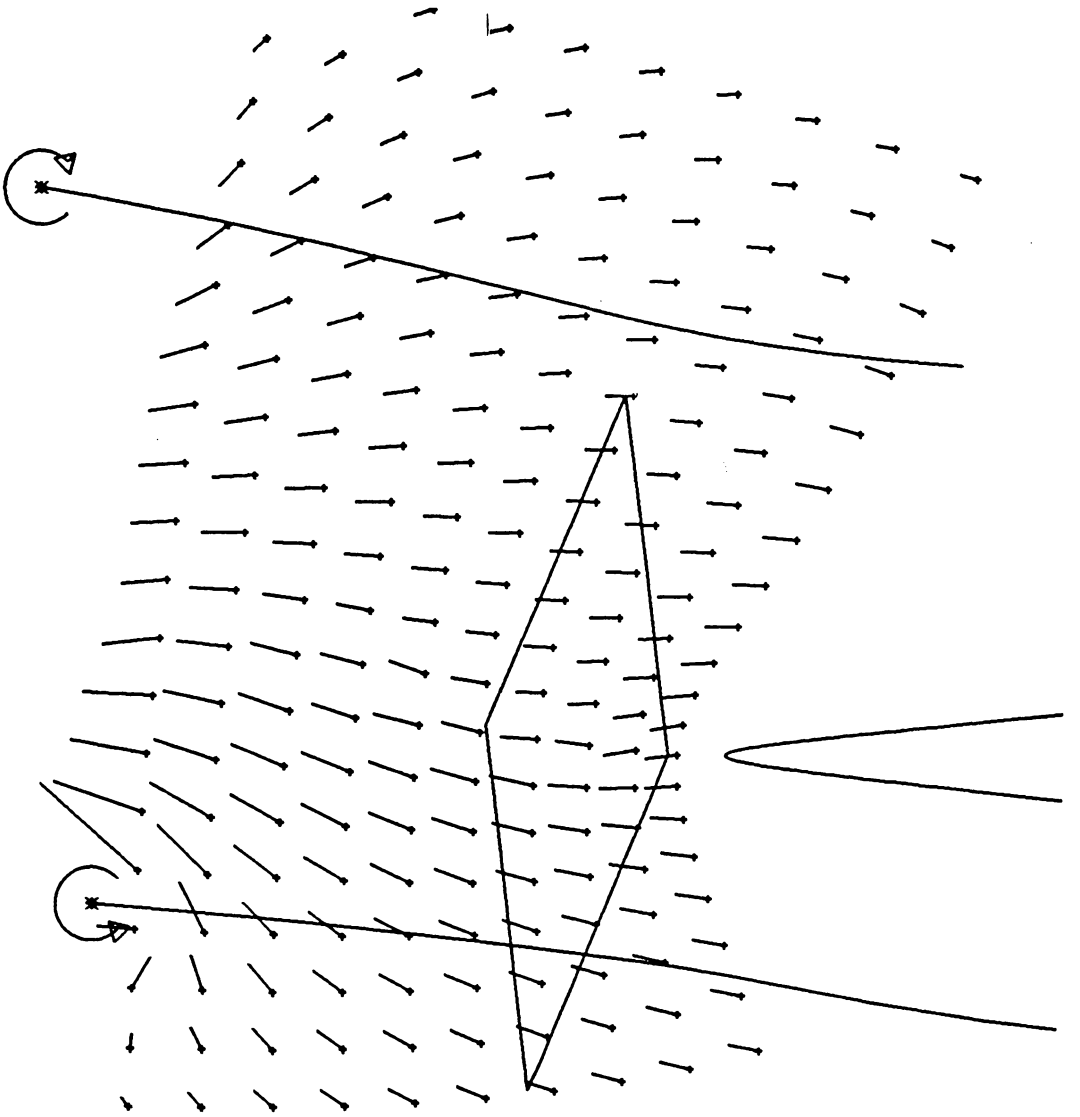

Fig. 5.2.13 The calculated velocity field aft of the trailing edge of the fixed airfoil (18th time step).

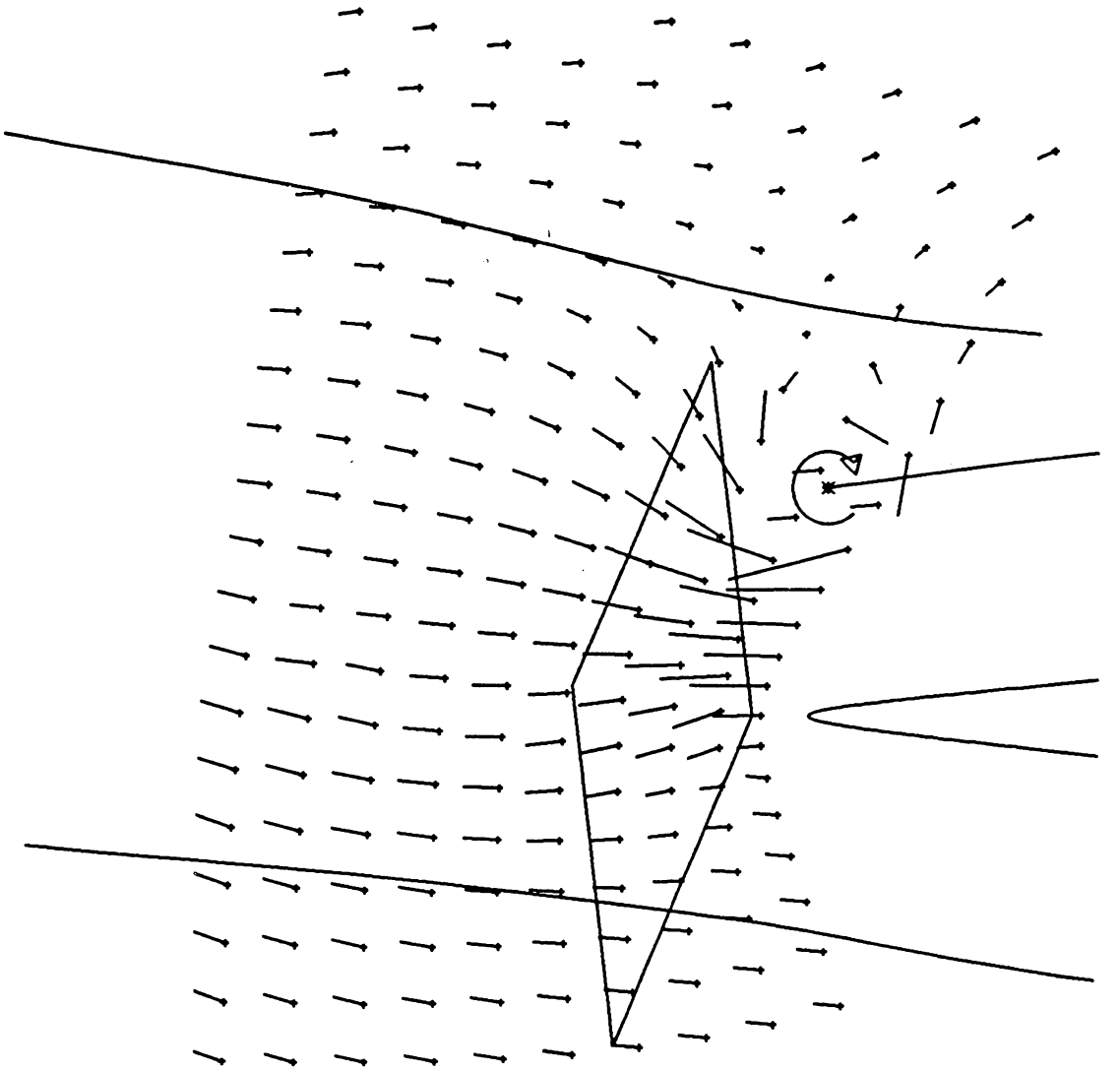

Fig. 5.2.14 The calculated velocity field aft of the trailing edge of the fixed airfoil (23rd time step).

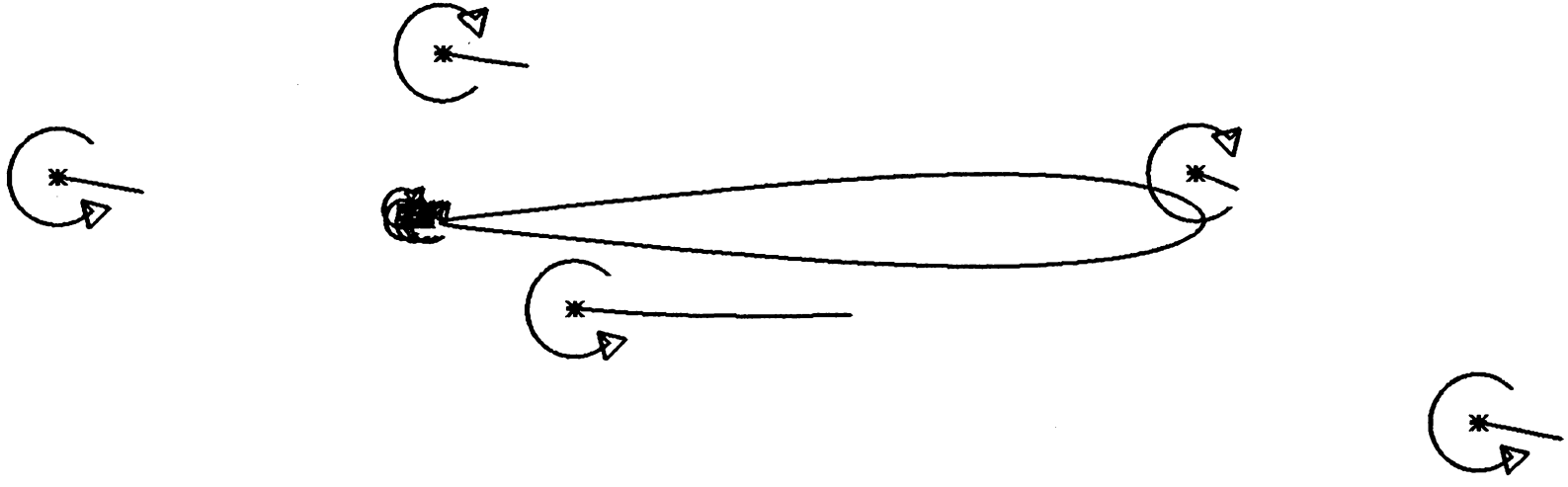

Fig. 5.3.1 Calculated positions of free stream and shed vortices over the fixed airfoil at an angle of attack of 10° (5th time step).

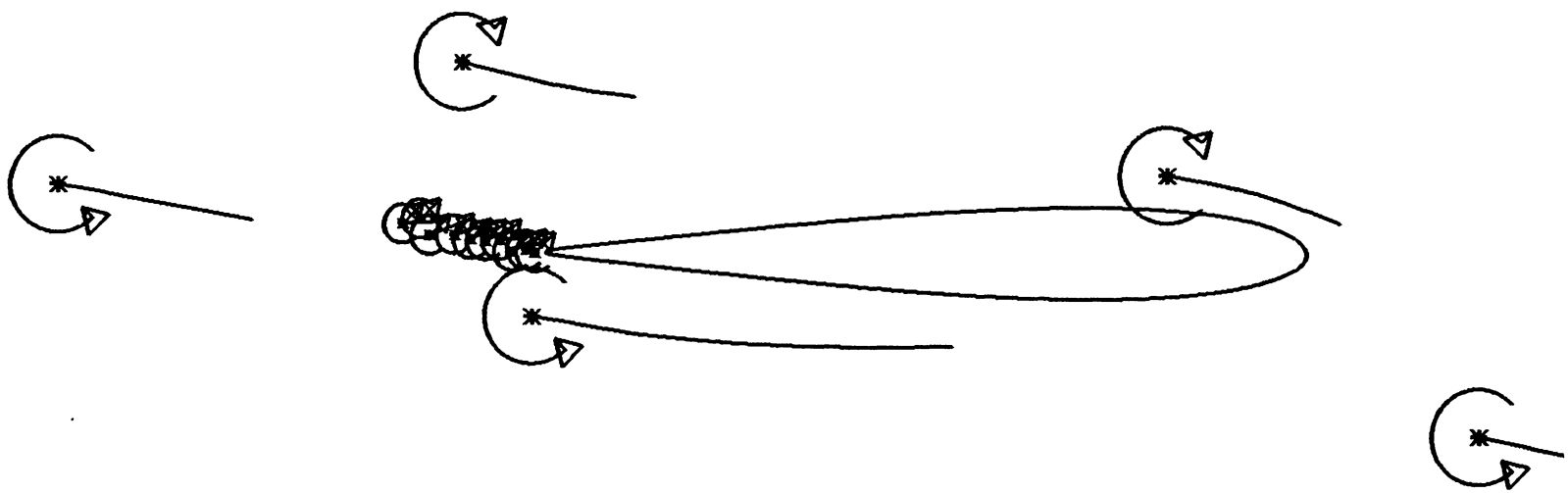

Fig. 5.3.2 Calculated positions of free stream and shed vortices over the fixed airfoil at an angle of attack of 10° (10th time step).

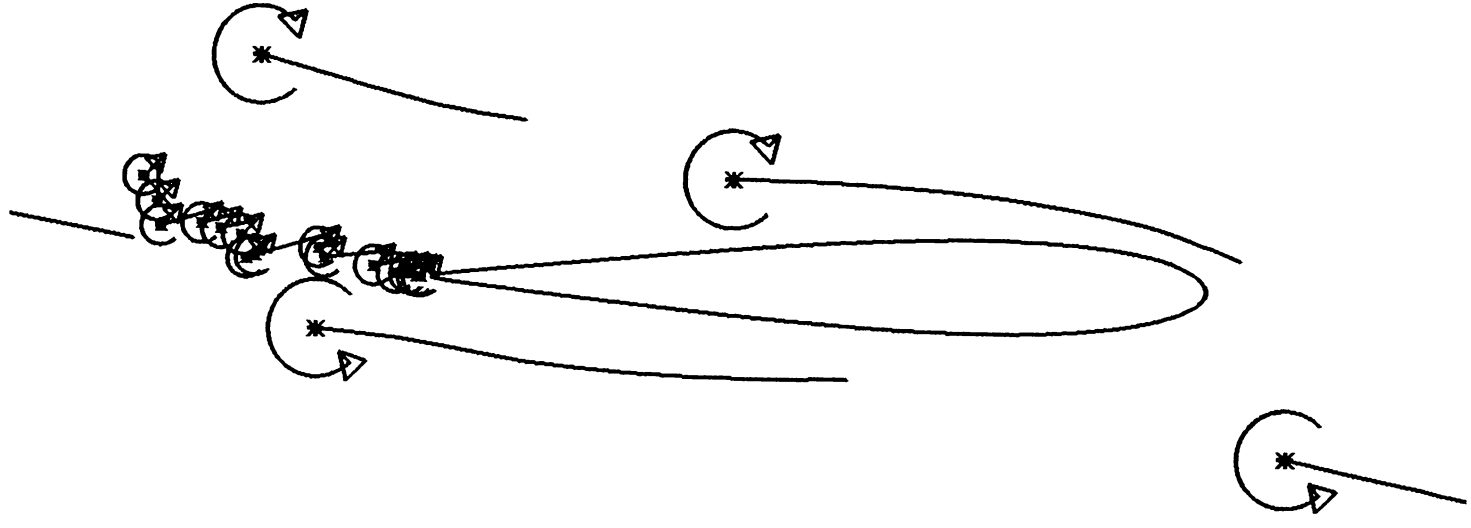

Fig. 5.3.3 Calculated positions of free stream and shed vortices over the fixed airfoil at an angle of attack of 10° (15th time step).

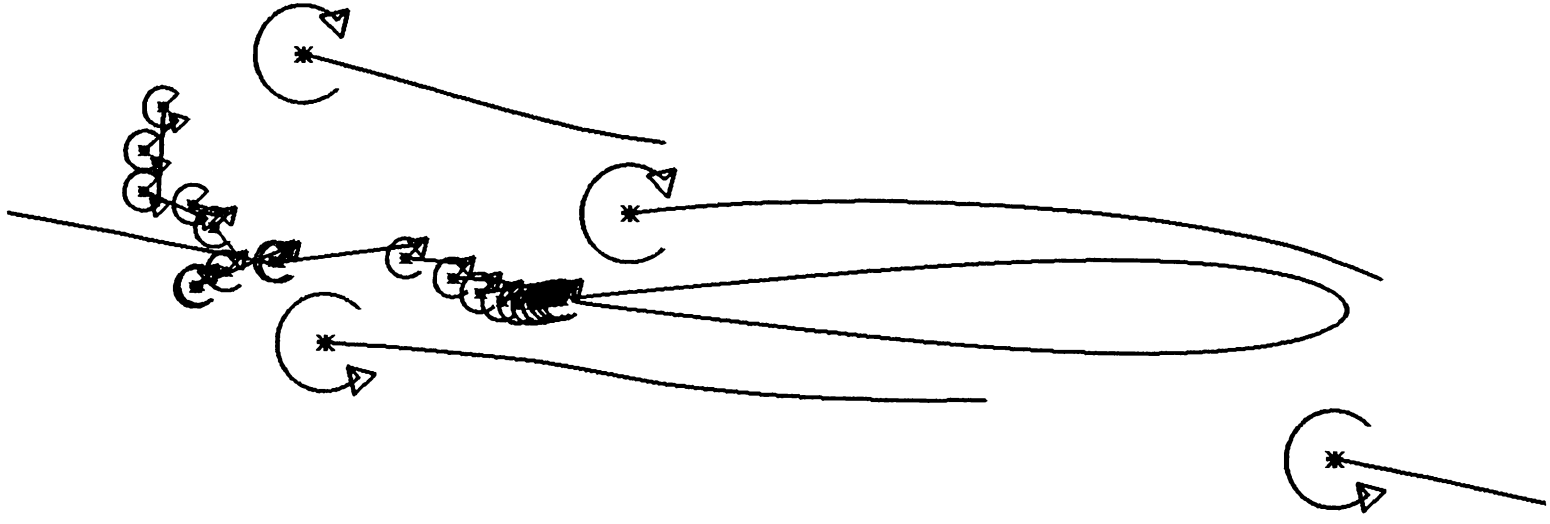

Fig. 5.3.4 Calculated positions of free stream and shed vortices over the fixed airfoil at an angle of attack of 10° (20th time step).

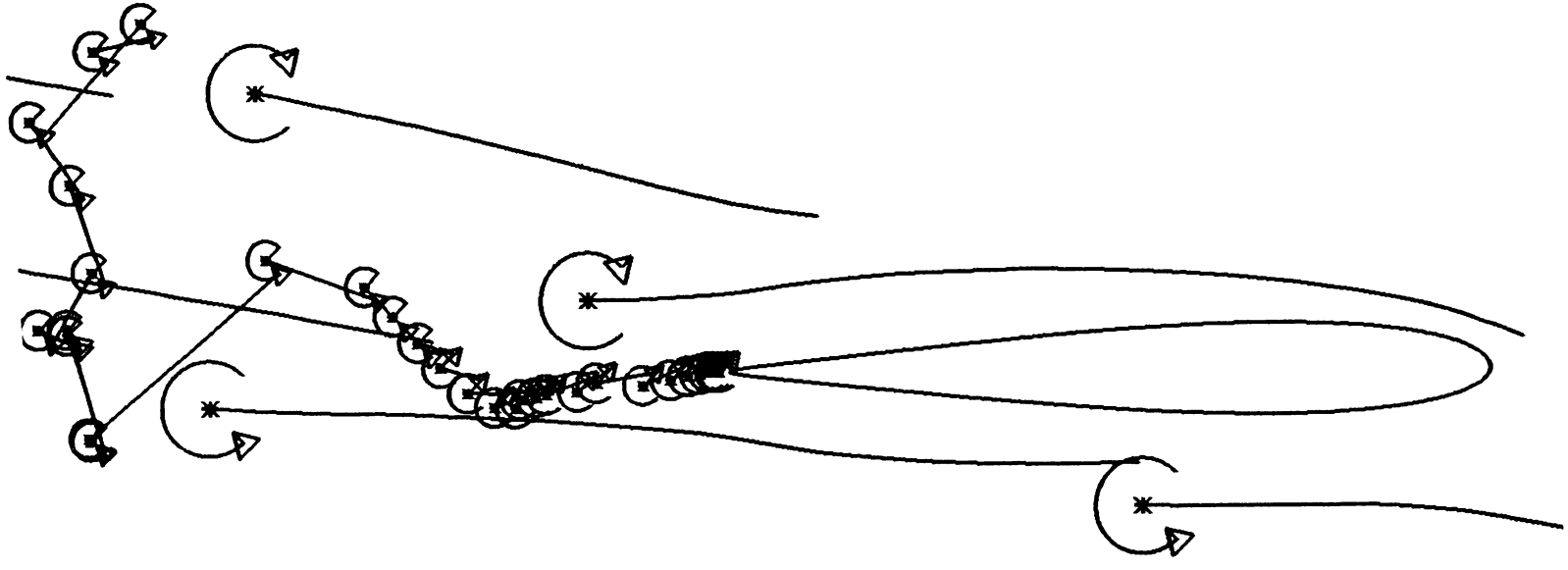

Fig. 5.3.5 Calculated positions of free stream and shed vortices over the fixed airfoil at an angle of attack of 10° (30th time step).

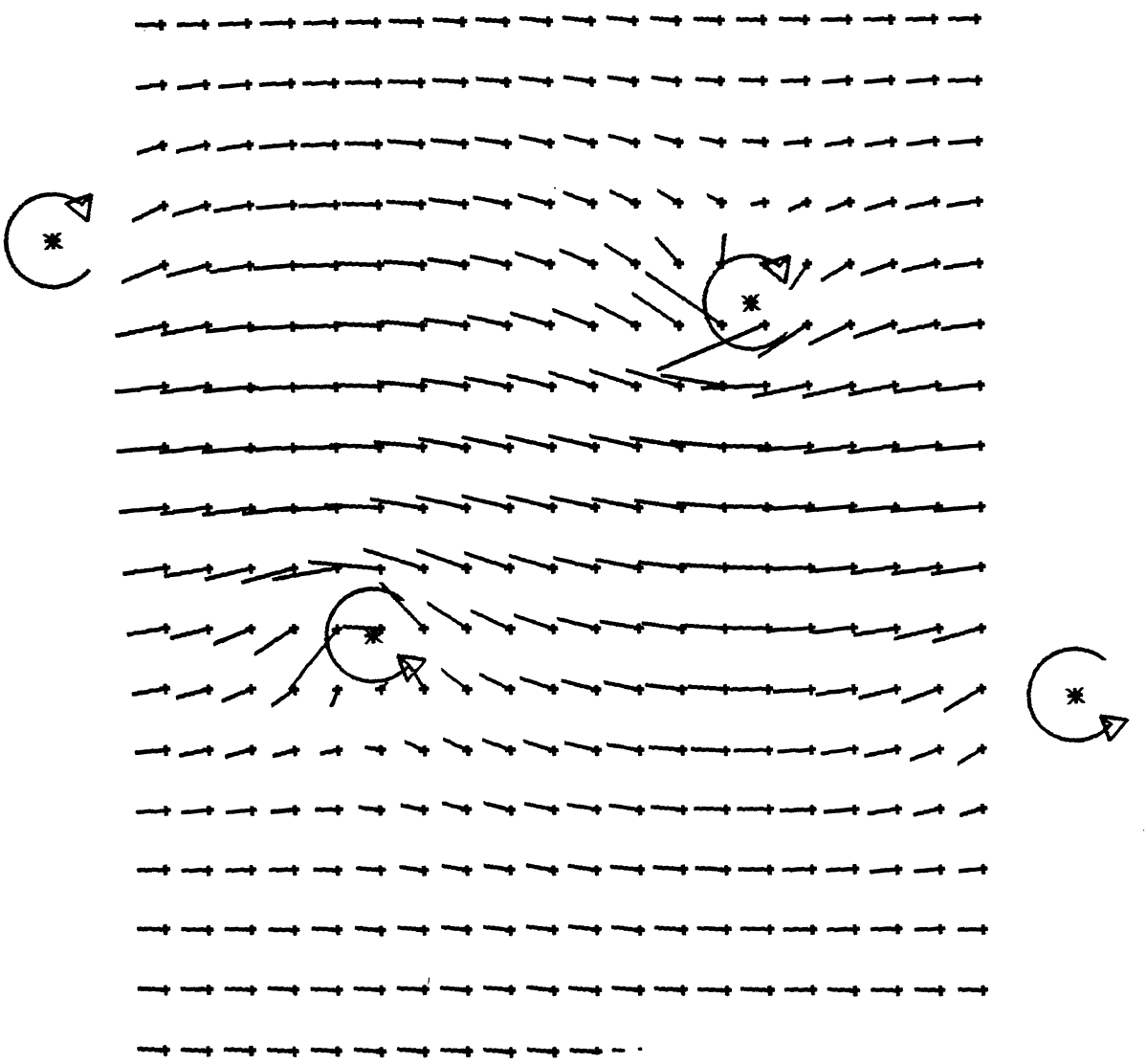

Fig. 5.3.6 The numerically predicted velocity field of the unsteady periodic wake (b=0.5c, e/a=0.1333).

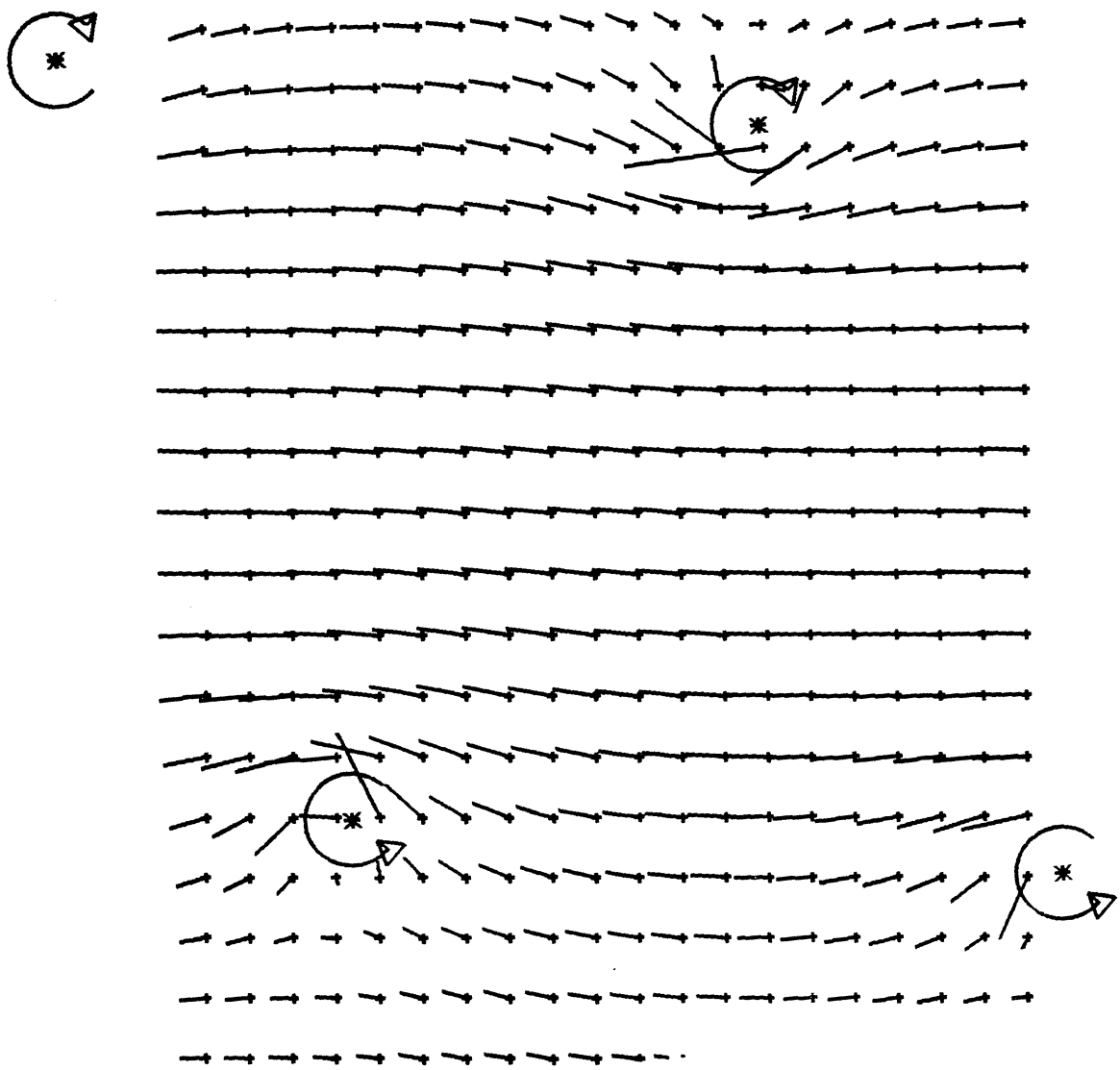

Fig. 5.3.7 The numerically predicted velocity field of the unsteady periodic wake (b=c, e/a=0.1600).

TABLE 3.1

	Satyanarayana and Davis (1978)	Ho and Chen (1981)	DeRuyck and Hirsh (1982)	Poling (present work)
K	< 0.6	0.5-1.0	0.5-1.0	0.8-3.9
ℓ	< 0.0157	0.016-0.320	0.02-0.30	0.105-0.514

Table 3.1 Comparison of the values of the reduced frequency parameter K and the proposed dynamic similarity parameter ℓ. The quasi-steady criterion is not valid for values of $\ell \geq 0.1$.

TABLE 5.1

e/a

	Mathioulakis	Kim	Poling
k = 2.77	0.1613 (experiment)	———	0.1746 (calculated)
k = 3.90	———	0.2173 (calculated)	0.2019 (experiment) 0.1915 (calculated)

Table 5.1 Experimental and calculated values of the ratio of the wave depth e to the vortex spacing a for two different values of the reduced frequency parameter.

REFERENCES

Abbott, I. H. and von Doenhoff, A. E., 1959, Theory of Wing Sections, Dover Edition, 1959.

Archibald, F. S., 1975, "Unsteady Kutta Condition at High Values of the Reduced Frequency Parameter", AIAA Journal, Vol. 12, No. 6, June 1975.

Basu, B. C. and Hancock, G. J., 1978, "The Unsteady Motion of a Two-Dimensional Aerofoil in Incompressible Inviscide Flow", J. Fluid Mech., Vol. 87, pp. 159-178.

Bechert, D. and Pfizenmaier, E., 1975, "Optical Compensation Measurements on the Unsteady exit Condition at a Nozzle Discharge Edge", JFM, Vol. 71, p. 123.

Brayton, D. B., Kalb, H. T. and Crosswy, F. L., 1973, "Two Component Dual-Scatter LDV with Frequency Burst Signal Readout", Appl. Opt., Vol. 12, pp. 1145-1156.

Brown, S. N. and Daniels, P. G., 1975, "On the Viscous Flow About the Trailing Edge of a Rapidly Oscillating Plate", J. Fluid Mech., Vol. 67, pp. 743-761.

Chow, C. Y. and Huang, M. K., 1983, "Unsteady Flows About a Joukowski Airfoil in the Presence of Moving Vortices", AIAA-83-0129.

Commerford, G. L. and Carta, F. O., 1974, "Unsteady Aerodynamic Response of a Two Dimensional Airfoil at High Reduced Frequency", AIAA J., Vol. 12, p. 43.

Covert, E. E., Lorber, P. F. and Vaczy, C. M., 1983, "Measurements of the Near Wake of an Airfoil in Unsteady Flow", AIAA-83-0127.

DeRuyck, J. and Hirsch, C., 1982, "Instantaneous Turbulence Profiles in the Wake of an Oscillating Airfoil", AIAA-82-0353.

Fleeter, S., 1980, "Trailing Edge Conditions for Unsteady Flows at High Reduced Frequency", AIAA Journal, Vol. 18, No. 5, May 1980.

Fox, R. W. and McDonald, A. T., 1973, Introduction to Fluid Mechanics, 1st edition, 1973.

Fujita, H. and Kovasznay, L. S. G., 1974, "Unsteady Lift and Radiated Sound From a Wake Cutting Airfoil", AIAA Journal, Vol. 12, No. 9, Sept. 1974.

Giesing, J. P., 1968, "Nonlinear Two-Dimensional Unsteady Potential Flow with Lift", J. Aircraft, Vol. 5, No. 2, Mar.-Apr. 1968.

Giesing, J. P., 1969, "Vorticity and Kutta Condition for Unsteady Multi-Energy Flows", Trans. ASME, J. Appl. Mech., Vol. 36, pp. 608-613.

Ham, N. D., 1968, "Aerodynamic Loading on a Two-Dimensional Airfoil During Dynamic Stall", AIAA Journal, Vol. 6, No. 10, Oct. 1968.

Hess, J. L. and Smith, A. M. O., 1967. "Calculation of Potential Flow About Arbitrary Bodies", Prog. Aero. Sci., Vol. 8, Pergamon Press, Oxford, 1967, pp. 1-138.

Ho, C. M. and Chen, S. H., 1980, "Unsteady Wake of a Plunging Airfoil", AIAA Paper No. 80-1446.

Ho, C. M. and Chen, S. H., 1981, "Unsteady Kutta Condition of a Plunging Airfoil" in Unsteady Turbulent Shear Flows, Toulouse, France.

Ho, C. M., 1982, Private communication.

Jones, G. S., 1980, "Measurement and Visualization of Vortex Shedding--Natural and Forced", M.S. Thesis, VPI & SU.

Katz, J. and Weihs, D., 1981, "Wake Rollup and the Kutta Condition for Airfoils Oscillating at High Frequency", AIAA-81-4329.

Kim, B. K., 1985, "Boundary-Layer Analysis and Measurement of Newtonian and Non-Newtonian Fluids", Ph.D. Dissertation, VPI & SU.

Kim, M. J. and Mook, D. T., 1985, "Application of Continuous Vorticity Panels to General Unsteady Two-Dimensional Lifting Flows", AIAA-85-0282.

Kinney, R. B. and Cielak, Z. M., 1977, "Analysis of Unsteady Viscous Flow Past an Airfoil: Part I - Theoretical Development", AIAA Journal, Vol. 13, No. 12, 1977.

Kinney, R. B. and Cielak, Z. M., 1978, "Analysis of Unsteady Viscous Flow Past an Airfoil: Part II - Numerical Formulation and Results", AIAA Journal, Vol. 16, No. 2, Feb. 1978.

Koromilas, C. A., 1978, "Experimental Investigation of Unsteady Separation", Ph.D. Dissertation, VPI & SU.

Koromilas, C. A. and Telionis, D. P., 1980, "Unsteady Laminar Separation; an Experimental Study", J. Fluid Mech., Vol. 97, pp. 347-384.

Kovasznay, L. S. G. and Fujita, H., 1972, "Unsteady Boundary Layer and Wake Near the Trailing Edge of a Flat Plate", Proc. IUTAM Symp. at Laval, Canada, p. 805.

Maskell, E. C., 1971, "On the Kutta-Joukowski Condition in Two-Dimensional Unsteady Flow", unpublished note, Roy. Aircraft Establishment, Farmborough.

Mathioulakis, D., 1982, "Steady and Unsteady Cascade Measurements", M.S. Thesis, VPI & SU.

Mathioulakis, D. and Telionis, D. P., 1983, "Modeling of Rotating Stall by Vortex Dynamics", AIAA Paper No. 83-0002, Jan. 1983.

Mathioulakis, D., 1985, "Vorticity Shedding Over Two-Dimensional Bodies", Ph.D. Dissertation, VPI & SU.

Mathioulakis, D. S., Kim, M. J., Telionis, D. P. and Mook, D. T., 1985, "On the Wake of a Pitching Airfoil", AIAA-85-1621.

McAlister, K. W. and Carr, L. W., 1978, "Water-Tunnel Experiments on an Oscillating Airfoil at R_e=21,000", NASA TM-78446.

McCroskey, W. J., 1973, "Inviscid Flowfield of an Unsteady Airfoil", AIAA Journal, Vol. 11, No. 8, Aug. 1973, pp. 1130-1137.

McCroskey, W. J., 1977, "Some Current Research in Unsteady Fluid Dynamics--The 1976 Freeman Scholar Lecture", J. Fluid Eng., Vol. 99, pp. 8-38.

McCroskey, W. J., 1981, "The Phenomenon of Dynamic Stall", NASA TM-81264.

McCroskey, W. J., 1982, "Unsteady Airfoils", Ann. Rev. Fluid Mech., Vol. 14, pp. 285-311.

Mehta, U. B. and Lavan, Z., 1975, "Starting Vortex, Separation Bubbles and Stall: a Numerical Study of Laminar Unsteady Flow Around an Airfoil", J. Fluid Mech. (1975), Vol. 67, part 2, pp. 227-256.

Mezaris, T. B., 1979, "Visualization and LDV Measurements of Separating Oscillatory Laminar Flows", M.S. Thesis, VPI & SU.

Mezaris, T. B. and Telionis, D. P., 1980, "Separation and the Near Wake of a Pulsating Laminar Flow", AIAA-80-1420.

Milne-Thompson, L. M., 1960, Theoretical Hydrodynamics, 4th edition, 1960.

Ohashi, H. and Ishikawa, N., 1972, "Visualization Study of Flow Near the Trailing Edge of an Oscillating Airfoil", Bulletin of the JSME, Vol. 15, pp. 840-847.

Ono, K., Kuwahara, K. and Osima, K., 1981, "Numerical Analysis of Dynamic Stall Phenomena of an Oscillating Airfoil by the Discrete-Vortex Approximation", 7th Intl. Conf. on Numerical Methods in Fluid Dynamics, in Lecture Notes in Physics, Ed. W. C. Reynolds, R. W. MacCormack, Springer, 1981.

Osdiek, F. R., 1975, "A Cascade in Unsteady Flow", AGARD CP 177.

Sarpkaya, T. and Schoaff, R. L., 1979, "Inviscid Model of Two-Dimensional Vortex Shedding by a Circular Cylinder", AIAA Journal, Vol. 17, Nov. 1979.

Satyanarayana, B. and Davis, S., 1978, "Experimental Studies of Unsteady Trailing Edge Conditions", AIAA J., Vol. 16, No. 2, p. 125.

Scheiman, J. and Brooks, J. D., 1980, "Comparison of Experimental and Theoretical Turbulence Reduction from Screens, Honeycomb and Honeycomb-Screen Combinations", AIAA-80-0433R.

Schubauer, G. B., "Air Flow in a Separating Laminar Boundary Layer", NACA Technical Report No. 527.

Sears, W. R., 1955, "Rotating Stall in Axial Compressors", J. Appl. Math. Phys., Vol. 6, pp. 429-455.

Sears, W. R., 1975, "Unsteady Motion of Airfoils with Boundary-Layer Separation", AIAA Journal, Vol. 14, pp. 216-220.

Stewartson, K., 1974, "Multi-Structured Boundary Layers on Flat Plates and Related Bodies", Advances in Mechanics, Vol. 14, pp. 145-239.

Tan-Atichat, J., Nagib, H. M. and Loehrke, R. I., 1982, "Interaction of Free-Stream Turbulence with Screens and Grids: a Balance Between Turbulence Scales", J. Fluid Mech., Vol. 114, pp. 501-528.

Telionis, D. P., Mathioulakis, D., Kim, B., Jones, G. S., 1984, "Calibration of the ESM Water Tunnel", to appear as a VPI & SU report.

T. S. I. Manual, "Laser Velocimetry Systems".

Van De Vooren, A. I. and Van De Vel, H., 1964, "Unsteady Profile Theory in Incompressible Flow", Archiwum Mechaniki Stosowanej, Vol. 3, No. 16, 1964.

Vatsa, V. N., Werle, M. J. and Verdon, J. M., 1982, "Viscid/Inviscid Interaction at Laminar and Turbulent Symmetric Trailing Edges", AIAA paper No. 82-0165, Jan.

Yates, J., 1977, "Pressure Distribution on the Trailing Edge of a Semi-Infinite Airfoil Oscillating in a Shear Layer", A.R.A.P. Report No. 77-157, 1977.

APPENDIX I

FORTRAN PROGRAM FOR UNSTEADY FLOW

A copy of the Fortran program used to control the MINC-II minicomputer for the data obtained aft of the trailing edge of the fixed airfoil (group-II) is shown in this section. A description of all of the basic functions of the program can be found in Appendix V of Mathioulakis (1985). The main difference in the program of the present work and the one of Mathioulakis is in the statements that control the traversing. Since the data of group-II employed a diamond shape measuring grid it was necessary to traverse the measuring volume in increments that involved both horizontal and vertical movements. this enabled the control volume to follow the contour of the diamond shape grid. These statements that control the traversing are written as "IF" statements and can be found just prior to the statements that control the movement of both the horizontal and vertical stepping motors.

```
      PROGRAM UNSTED
C
CC    THIS ROUTINE makes average in time domain of ONE channel
CCC   USING EXTERNAL TRIGGER FOR  UNSTEADY  FLOW;ALSO IT
CCC   COMPUTES THE RMS (PLUS  AC OUTPUT OF TEKTRONIX PREAMP
CCC   IN A/D  CONVERTER
CC    USE OF DIGITAL OUTPUT    FOR CONTROL OF TRANSLATOR
      INTEGER*2 INFO(40),IBUF(1024,1),IGINFO(30),FNAME(15) '
      REAL*4 X(512,1),ba(512,2),x11(512)
      LOGICAL*1 EFLG
C
CC    PUT IN SPECIAL TT MODE SO THIS WILL WORK IN FB (ALLOW
CCC   BUSY WAIT.
C
      CALL IPOKE('44,IPEEK('44).OR.'100)
C
CCC   PROMPT FOR PARAMETERS
C     MPAR IS  THE INDEX OF the POSITION OF THE LASER
      JST=0
      Jstv=0
      type 1
1     FORMAT('$ENTER THE INITIAL CHANNEL NUMBER:  ')
      ACCEPT *,IFIRST
      TYPE 2
2     FORMAT('$ENTER THE SAMPLE PERIOD IN SECONDS:  ')
      ACCEPT *,PERIOD
      type 12
 12   format('$enter THE number of points per sample:  ')
      accept *,ne
      DO 30 I=1,NE
30    X11(I)=I*PERIOD
      type 13
 13   format('$ENTER THE NUMBER OF ENSEMBLES: ')
      accept *,ms
      type 3
3     FORMAT('$ENTER THE FILENAME OF THE DATA FILE:  ')
      CALL GETSTR(5,FNAME,14,EFLG)
      OPEN (NAME=FNAME,TYPE='NEW',UNIT=10)
      TYPE 24
24    FORMAT('$INPUT INDEX OF POSITION (INITIAL=1 ): ')
      ACCEPT *,MPAR
      TYPE 26
26    FORMAT('$INPUT NUMBER OF COUNTS FROM ORIGINAL X-POSITION
      ACCEPT *,JST1
      type 77
77    format('$input number of counts from original x-position
      accept *,Jstv1
C
CCC   GET CLOCK RATE AND PRESET VALUE.
C
      CALL XRATF(PERIOD,IRATF,IPRE)
      CALL CLOCKA(IRATE,IPRE,IND)
      IF(IND.EQ.0) STOP 'CLOCKA ERROR'
C
C     INITIALIZE BUFFER SYSTEM.
C     DELAY LOOP
55    TYPE 35
35    FORMAT(' DELAY LOOP STARTED  ')
      DO 23 I1=1,80
      DO 23 I2=1,80
      DO 23 I3=1,80
23    CONTINUE
      TYPE 36
36    FORMAT('$DELAY LOOP FINISHED ')
C4     format(a2)
      MP=NE
```

```
c start a/d  conversion  with  external  trigger
      DCV=0.
      DO 22 I=1,NE
22    BA(I,1)=0.0
      ML=MS*NE
      PAR4=1./FLOAT(ML)
      PAR5=1./FLOAT(MS)
      do  15 J=1,ms
      CALL  SETIBF(INFO,IND,,IBUF(1,1))
      CALL RLSBUF(INFO,IND,0)
      CALL ADSWP(INFO,MP,1,256,,,,)FIRST,1)
      WRITE(7,27) J,MPAR
27    FORMAT(10X,I5,4X,I5)
C
C     WAIT FOR BUFFER OR CARRIAGE RETURN.  IF BUFFER BECOMES
c     AVAILABLE, SAVE THE DATA.
      write(7,40)  info(1)
      CALL IWTBUF(INFO,,IBUFN,IND)
      WRITE(7,40)  IND
      IF(ITTINR().GE.0) GO TO 510
      DO 16 I=1,NE
      VNUM=((IBUF(I,IBUFN+1),AND,'7777)-2048)*.0025
      X(I,1)=VNUM*PAR5+BA(I,1)
      ba(i,1)=x(i,1)
      DCV=DCV+VNUM*PAR4
16    CONTINUE
15    continue
40    format(i5)
C          COMPUTE  RMS
C     RMS=SQRT(P1)
c     NDIR=1
c     IF(NDIR.EQ.0)  GO TO 60
c     IF(NDIR.EQ.1) JST=-JST
c     jstv=-jstv
c     JST1=JST1+JST
c     Jstv1=Jstv1+Jstv
c60   CONTINUE
C     STORE  THE DATA
C     CALL BOUNDS(1,BA(1,1),VMAX,VMIN,NE)
      DU=VMAX-VMIN
      WRITE(7,505) MPAR,DCV,RMS,DU,JST1,JST
505   FORMAT(2X,I5,3(5X,F8.4),2(5X,I5))
      WRITE(10,503) MPAR,DCV
503   FORMAT(5X,I5,5X,F8.3)
c     write(10,599) Jstv,Jstv1
c599  format(2(5x,i5))
c     WRITE(10,504) VMAX,VMIN
c504  FORMAT(2(5X,F8.3))
      WRITE(10,501) (BA(J,1),J=1,ne,20)
501   FORMAT(1X,3F8.3)
C     PLOT RESULTS
      CALL GRINIT(IGINFO)
      CALL GRREON(IGINFO,0,3)
      CALL GRAPHS(IGINFO,,X11,BA,NE,,,0)
C     dvel=.11625*dcv
      WRITE(7,509) MPAR,DCV
509   format(2x,i5,1x,f6.3)
C     CHECK IF THE VELOCITY IS CLOSE TO  ZERO .IF SO INCREASE
C     NUMBER OF ENSEMBLES
c     IF(DCV.LE.1.75)  MS=15
C     DELAY LOOP OF ABOUT 3 SECS
      DO 43 I1=1,60
      DO 43 I2=1,60
c     DO 43 I3=1,60
```

```
43      CONTINUE
C       ACCEPT 4,I
C4      FORMAT(A2)
        CALL VTCLR
C       TRAVERSE THE LASER SYSTEM
C       TYPE 18
C18     FORMAT('$TO DO IT AGAIN TYPE 0 : ')
        Jstv=37
        Jst=31
        ndir=1
        ndirv=1
        if(mpar.eq.33) ndirv=4
        if(mpar.eq.33) ndir=4
        if(mpar.eq.33) Jstv=37*36
        if(mpar.eq.33) Jst=31*28
        if(mpar.eq.38) ndirv=4
        if(mpar.eq.38) ndir=4
        if(mpar.eq.38) Jstv=37*8
        if(mpar.eq.38) Jst=0
        if(mpar.eq.47) ndirv=4
        if(mpar.eq.47) ndir=4
        if(mpar.eq.47) Jstv=47*12
        if(mpar.eq.47) Jst=31*
        if(mpar.eq.60) ndirv=4
        if(mpar.eq.60) ndir=4
        if(mpar.eq.60) Jstv=37*20
        if(mpar.eq.60) Jst=31*4
C       if(mpar.eq.77) ndirv=4
C       if(mpar.eq.77) ndir=4
C       if(mpar.eq.77) Jstv=37*20
C       if(mpar.eq.77) Jst=31*12
        if(mpar.eq.81) ndirv=4
        if(mpar.eq.81) ndir=4
        if(mpar.eq.81) Jstv=37*32
        if(mpar.eq.81) Jst=31*8
        if(mpar.eq.114) go to 510
C********MOVE HORIZONTAL MOTOR********
        CALL IPOKE('171066,0)
        DO 80 L=1,JST
        CALL IPOKE ('171262,NDIR)
C       DELAY LOOP
        DO  85 K=1,150
85      CONTINUE
        CALL IPOKE('171262,0)
C       DELAY LOOP
        DO 80 K=1,10
80      CONTINUE
C********MOVE VERTICAL MOTOR**********
        CALL IPOKE('171066,4095)
        DO 100 J=1,JSTV
        CALL IPOKE('171262,NDIRV)
        DO 105 K=1,150
105     CONTINUE
        CALL IPOKE('171262,0)
        DO 100 K=1,10
100     CONTINUE
        MPAR=MPAR+1
        GO TO 55
510     CALL STPSWP(INFO,,IND)
        CLOSE(UNIT=10)
c       JST1=JST1+JST
        WRITE(7,28) MPAR
28      FORMAT(1X,5X,I5)
        STOP
        END
```

APPENDIX II

DATA TRANSFER FROM THE MINC-II TO THE IBM 370

The steps involved in transferring the data from the MINC-II minicomputer to the IBM 370 mainframe computer are outlined in this section.

The 100 baud rate modem must be connected to the MINC to activate the data transfer to the IBM 370. With the system and data storage diskettes in the left and right hand drives of the MINC respectively, perform the following steps:

type R_XFMAIN

dial 7211 on the phone/modem

type RS (response will be request:)

type VM1 (now you can log on)

type L_(user-id)_(password)

type LDISK_HAND1 (the screen will request a password)

type MICRO (MICRO is the password)

type XFER_(filename)_(filetype)_(IN_RECFM_F

type MINC (MINC is the local file spec)

Upon completion of all of these steps change the record length of the data file (now in the IBM 370) from 132 to 80 in the following way:

type COPY_(filename)_(filetype)_A1_(filename)_(filetype)_A1_
(LRECL_80)

At this point wait for the indication by the computer that the record length has been changed, then either transfer another data file or log off.

APPENDIX III

FORTRAN PROGRAM OF THE NUMERICAL ANALYSIS "VORTX"

This section describes basically the computer program that performs the calculations of the field of N number of discrete vortices convected over the modified Joukowski airfoil at an angle of attack.

The program entitled "VORTX" is set up to run interactively either on the Tektronix graphics terminal or the Memorex, IBM, TAB or HP terminals. If the program is run on a terminal other than a designated graphics terminal, symbols in the form of letters, numbers, etc. will appear on the screen as results. The only advantage of running the program on non-graphics terminals would be for quick turn-around when writing to a data file. This program cannot be submitted through batch (i.e. with JCL) due to the "call-plot" statements that interact with the Versatec plotting system.

The program has several comment cards identifying terms and variables as well as identifying various routines throughout. To start the program just type VORTX. VORTX activates an exec routine (VORTX EXEC) that loads the program into the system. Questions will then appear on the screen which must be answered to continue running the program. These questions are located at the beginning and end of the program. After answering the questions in the beginning of the program the screen will respond with the word "option". The following letters identify the options most commonly used:

F - Opens the "hardcopy data" file that stores all data for plotting. Press F only if you want a printed version of the plot.

W - This is a window that enables all or just part of the plot to be seen on the screen. The usual window size for this program is 6., 0. (hit return) and 20., 12. (& hit return).

E - Erases the screen.

C - Continue, runs the program.

Q - Quit command, prevents the program from executing and puts you back in the CMS mode.

N - Cancels the "F" command. i.e. will not transfer data for plotting. This option basically closes the "hardcopy data" file in the event that you do not wish to make a Versatec plot (press N only if you have already pressed F).

```
C
C       THIS PROGRAM CONVECTS 20 VORTICES OVER THE FIXED AIRFOIL
C      (ALL 20 VORTICES ARE PLACED OVER THE AIRFOIL INITIALLY
C       AND THEN CONVECTED DOWNSTREAM)
C
       DOUBLE PRECISION WA,XNEW,YNEW,XP,YP,THT,X,Y,DFZ,R,BTA,PI,EX,EY,
      1ALF,GMMA,GRLF,PSI,XPSI,DT3,DT4,DFZ2,DFZ4,YSI1,BX,DTME,GG,
      1THTA,DDR,DFZ1,XPSI1,XPSI2,YPSI1,YPSI2,XDSI,YDSI,DPSI,XSTG1,YSTG1,
      1XSTG2,YSTG2,RRX,RRY,PHI,TH1,RR,ZZRX,XINTR,WWXX,WWYY,ZRZX,
      1  XPT,YPT, GRRL(1,30),DGDTT,ZRX,ZRX1,WWX,WWY,CHETA,HETA,DHETA
C
       COMPLEX*8 ZGP1,ZGP(40,40),DGPY1,DGPY2,ZEGP(40,40),ZGGP
C
C          THE FOLLOWING VARIABLES ARE DESIGNATED AS AS BEING DOUBLE
C          PRECISION AND COMPLEX
       COMPLEX*16 ZNEW(21,60),ZI,ZETA,ZTE,BI(2),AI(2,2),VELOC,W(21,60),
      1VA1,VA2,BT,CT,DT,ET,GI,CUTOFF,GCL(60),GRL(21,60),ZNT,Z(21,60),ZF,
      1ZR,VEL1,VEL3,ZSUR,FZ,PRS,ZZS,ZSS,PRES,ZSX,ZPSI(61,5),FZN,ZTSI,FZ2,
      1FZ4,FZ1,ZEPSI(61,5),ZZETA,ZT(21,60),ZCZ(21,1),DGDT,WVEL(20,20),TRE
      1,ZRR,ZZRY,ZRY,WVU,ZRZY,ZRXC,ZZRXC
C         THE FOLLOWING VARIABLES ARE NOT COMPLEX
       DIMENSION X(720,2),Y(720,2),XN(38),YN(38),WA(4),DFZ(180,60),
      1XNEW(21,60),YNEW(21,60),ZETA(21,60),XP(21,60),YP(21,60),PRS(180,60
      1),PSI(21),GRLF(21),NR(21),XCP(21,1),ZZGPX(20,20),ZZGPY(20,20),
      1XW(360),YW(360)
 1000 WRITE(4,104)
  104 FORMAT(//,10X,'INPUT THE MAX NUMBER OF TIME STEPS (ISTP)')
       READ(8,*) ISTP
C      WRITE(4,105)
C 105 FORMAT(//,10X,'INPUT THE INITIAL POSITION OF THE DWNSTRM VORTEX')
C      READ(8,*) ZRX, ZRY
       WRITE(4,106)
  106 FORMAT(//,10X,'INPUT THE ANGLE OF ATTACK')
       READ(8,*) ALFA
       WRITE(4,102)
  102 FORMAT(10X,'DO YOU WANT TO PLOT THE PRESSURE DISTRIBUTION? 1=YES')
       READ(8,*) SQP
       WRITE(4,115)
  115 FORMAT(10X,'DO YOU WANT TO PLOT THE VELOCITY OF THE WAKE? 1=YES')
       READ(8,*) IPP
       WRITE(4,103)
  103 FORMAT(/,10X,'DO YOU WANT TO PLOT STREAMLINES?  1=YES')
       READ(8,*) IRP
       IF(IRP.GT.1) GO TO 111
       WRITE(4,112)
  112 FORMAT(10X,'FOR WHICH TIME STEP DO YOU WANT PSI LINES PLOTTED?')
       READ(8,*) IPQ
       GO TO 113
  111 WRITE(4,116)
  116 FORMAT(10X,'FOR WHICH TIME STEP DO YOU WANT THE AIRFOIL AND VORTIC
     1ES PLOTTED?')
       READ(8,*) IPQ
C
C************  DEFINITION OF TERMS AND VARIABLES **********************
C
C     ALF IS THE ANGLE OF ATTACK IN RADIANS (READ IN AS DEGREES)
C     GMMA IS THE INITIAL AMOUNT OF CIRCULATION REQUIRED TO SATISFY
C        THE KUTTA CONDITION
C     DTME IS THE TIME INCREMENT FOR THE NEW POSITION OF EACH VORTEX
C     ZF IS THE INITIAL POSITION OF THE VORTEX THAT IS PLACED IN
C        THE FLOW UPSTREAM OF THE AIRFOIL
C     GCL(KM) IS THE TOTAL CIRCULATION OF THE CYLINDER AFTER EACH
C        TIME STEP  (THE BOUND CIRCULATION)
C     GRL(1,KM) IS THE CIRCULATION OF THE SHED VORTEX DOWNSTREAM
C        OF THE AIRFOIL
C     GRL(IVX,KM) IS THE MAGNITUDE OF THE CIRCULATION OF THE ONCOMING
C        VORTICES
```

```
C     ZNT IS THE COMPLEX POSITION OF THE CYLINDER (WITH COMPONENTS
C        EX AND EY)
C     ZTE IS THE POSITION ON THE CIRCLE CORRESPONDING TO THE
C        TRAILING EDGE OF THE AIRFOIL
C     N IS THE NO. OF POINTS USED TO PLOT THE AIRFOIL
C     BX IS THE CONSTANT IN THE JOUKOWSKI TRANSFORMATION
C        (BX IS DIMENSIONAL)
C     ISTP IS THE STOPPING POINT
C     SSTP IS A COUNTER WHICH IS USED TO DENOTE THE TIME STEP AT
C         EACH PLOT OF THE AIRFOIL AND VORTICES ON THE PRINTOUT
C     BTA IS THE ANGLE ON THE CIRCLE REQUIRED TO SATISFY THE
C         KUTTA CONDITION
C     SCALE IS THE SCALE FACTOR USED FOR PLOTTING
C     GRLF IS THE MAGNITUDE OF THE CIRCULATION OF THE FIRST VORTEX
C         PLACED UPSTREAM OF THE AIRFOIL (+ IS CCW AND - IS CW)
C     GRLF() IS THE MAGNITUDE OF THE CIRCULATION OF THE ONCOMING VORTICES
C         PLACED UPSTREAM OF THE AIRFOIL (- IS CCW AND + IS CW)
C     NR() IS THE TIME STEP WHEN THE ONCOMING VORTICES ARE PLACED IN
C         FRONT OF THE AIRFOIL
C     NV IS THE NUMBER OF VORTICES PLACED IN FRONT OF THE AIRFOIL
C     VEL3 IS THE VELOCITY ON THE SURFACE OF THE AIRFOIL
C     PRS IS THE PRESSURE ON THE SURFACE OF THE AIRFOIL
C     ZSUR IS THE POSITION OF THE COORDINATES ON THE SURFACE
C         OF THE AIRFOIL
C     ZR IS THE INITIAL POSITION OF THE VORTEX SHED BEHIND THE
C         TRAILING EDGE OF THE AIRFOIL
C     GI IS THE IMAGINARY NUMBER, I
C     ZPSI( , ) ARE THE X AND Y POSITIONS OF THE STREAMLINES
C     CUTOFF DOESNT ALLOW VORTICES TO GET CLOSER THAN A DISTANCE OF .1
C     NOP IS THE NUMBER OF PERIODS TO THE LEFT OF THE ORIGIN WHERE THE
C         FIRST VORTEX IS PLACED
C     TAU IS ONE FULL WAVE LENGTH BETWEEN TWO VORTICES ON THE SAME ROW
C     CC IS DEFINED AS THE QUARTER CORD POINT
C     YBB IS HALF OF THE AMPLITUDE BETWEEN THE TOP ROW AND BOTTOM ROW
C         OF THE VORTEX STREET  YBB=0.5(30% CHORD) FOR K=3.9
C     ZT(2,1) IS THE POSITION OF THE FIRST ONCOMING VORTEX
C     XPSI IS THE X COORDINATE OF THE INITIAL POSITION OF THE STREAMLINES
C     AA IS THE HORIZONTAL DISTANCE TO THE FIRST VORTEX PLACED ON THE
C         TOP ROW OF THE STREET TO THE RIGHT OF THE ORIGIN. AA, TAU, AND
C         YBB ARE ADJUSTED TO INSURE THAT THE INITIAL POSITION OF THE
C         VORTICES MATCHES THE APPROPRIATE REDUCED FREQUENCY PARAMETER.
C         THE REDUCED FREQUENCY IS GOVERNED BY THE AMPLITUDE, WAVELENGTH
C         AND INITIAL POSITION OF THE VORTEX STREET.
C     FETA IS THE TRAILING EDGE BISECTOR ANGLE
C     XINTR IS THE INTERSECTION POINT OF THE TRAILING EDGE BISECTOR
C
C*************************************************************************
C
113    SSTP=1.
       PI=4.D0*DATAN(1.D0)
       R=1.111D0
       EX=0.079D0
       EY=0.D0
       RW=.10
       N=720
       NV=20
       XINTR=2.0531912
       FETA=7.305452*PI/180.
       FFETA=7.305452
       JD2=N
       BX=1.D0
       DP=15.
       DDP=6.
       ITME=1
       KK=0
       NK=1
       NZ=NV+1
```

```
      DTME=.0975D0
      TAUME=2.2/DTME
      GI=DCMPLX(0.D0,1.D0)
      BTA=DATAN(EY/(EX+1.D0))
      ALF=ALFA*PI/180.
      GMMA=-2.*DSIN(ALF+BTA)
      ZTE=-(DCOS(BTA)-EX/R)
      ZNT=EX/R+GI*EY/R
C     ZNT=EX+GI*EY
C
C                GRLF() SIGN CONVENTION:
C        CCW ROTATION IS -  AND CW ROTATION IS +
C
      GRLF(1)=.4034D0
C     GRLF(1)=.5800D0
      IQJ=1
      DO 771 IVX=2,NV
      IQJ=-IQJ
      GRLF(IVX)=IQJ*GRLF(1)
  771 CONTINUE
C
      ZRX=-1.15D0
C
      ZRY=0.D0
      ZR=ZRX+GI*ZRY
      Z(1,1)=ZR
C      THE FOLLOWING VALUES ARE USED IN THE STREAMLINE ROUTINE
      DT3=2.D0*PI/180.D0
      DT4=8.D0*PI/180.D0
      THTA=0.D0
      DDR=.15D0
      XSTG1=(R+EX)*DCOS(ALF)+.1D0
      YSTG1=-(R+EY)*DSIN(ALF)
C
      CALL CIRCLE(X,Y,N,EX,EY,R)
C
C     DO 687 IVA=1,720
C     WRITE(9,688) IVA,X(IVA,1),Y(IVA,1)
C 688 FORMAT(5X,I5,2X,F10.7,2X,F10.7)
C 687 CONTINUE
C
      CALL JWKSK(X,Y,N,BX,XSTG1,YSTG1,XSTG2,YSTG2)
C
      CALL NACA(XN,YN)
C
      CALL ARROW(XW,YW,RW)
C
      XMAX=X(1,1)
      XJMAX=X(1,2)
      YMAX=Y(1,1)
      YJMAX=Y(1,2)
      XMIN=X(1,1)
      XJMIN=X(1,2)
      YMIN=Y(1,1)
      YJMIN=Y(1,2)
      DO 3 I=1,N
      IF(XMAX.LT.X(I,1)) XMAX=X(I,1)
      IF(XJMAX.LT.X(I,2)) XJMAX=X(I,2)
      IF(YMAX.LT.Y(I,1)) YMAX=Y(I,1)
      IF(YJMAX.LT.Y(I,2)) YJMAX=Y(I,2)
      IF(XMIN.GT.X(I,1)) XMIN=X(I,1)
      IF(XJMIN.GT.X(I,2)) XJMIN=X(I,2)
      IF(YMIN.GT.Y(I,1)) YMIN=Y(I,1)
      IF(YJMIN.GT.Y(I,2)) YJMIN=Y(I,2)
    3 CONTINUE
      SCFX=4.D0/(XMAX-XMIN)
      SCFXX=4.D0/(XJMAX-XJMIN)
```

```
      SCFY=4.D0/(YMAX-YMIN)
      SCFYY=4.D0/(YJMAX-YJMIN)
      SCALE=SCFX
      IF(SCALE.GT.SCFXX) SCALE=SCFXX
      IF(SCALE.GT.SCFY) SCALE=SCFY
      IF(SCALE.GT.SCFYY) SCALE=SCFYY
C     SCALE=4.
C     SCALE=1.25
      XPSI=X(360,1)-.2D0
      ZPSI(1,1)=XPSI-.10D0-.08D0+GI*(.7D0)
      ZPSI(1,2)=XPSI-.10D0-.04D0+GI*(.35D0)
C     ZPSI(1,3)=XPSI-.1D0-.02D0+GI*(0.D0)
      ZPSI(1,4)=XPSI-.10D0-.04D0-GI*(.35D0)
      ZPSI(1,5)=XPSI-.10D0-.08D0-GI*(.7D0)
      CALL PLOTS(0,0,50)
      CHORD=DABS(X(720,2)-X(360,2))*SCALE
      CHOR=CHORD/SCALE
C
C
C  *****  ZT IS DEFINED AS THE TEMPORARY POSITION OF THE ONCOMING
C       VORTICES  *********
C
      TAU=0.95*4.00
C     TAU=1.3*4.00
      NOP=4
C     AA=1.60
      AA=1.900
      CC=.25
      YBB=.50
C     YBB=.400
      DD=TAU-(CC+AA)
      IQJ=1
      ZT(2,1)=-(DD+NOP*TAU)+GI*YBB
      DTAU=.5*TAU
      DO 801 IVX=3,NZ
      IQJ=-IQJ
      ZT(IVX,1)=ZT(IVX-1,1)+DTAU+GI*IQJ*2.00*YBB
  801 CONTINUE
C
C   **** NOW CALCULATE THE ACTUAL POSITION OF THE ONCOMING VORTICES OVER
C         THE FIXED AIRFOIL, THEN GO THRU THE REVERSED TRANSFORMATION
C         (IE; ROTATE THE LINE OF VORTICES THRU THE ANGLE ALF).
C
      DO 802 IVX=2,NZ
      RRX=ZT(IVX,1)-CC
      RRY=(-GI)*ZT(IVX,1)
      RR=(RRX**2+RRY**2)**.5D0
      PHI=DATAN(DABS(RRY/RRX))
      IF(RRX.LT.0.D0.AND.RRY.LT.0.D0) GO TO 803
      IF(RRX.GT.0.D0.AND.RRY.GT.0.D0) GO TO 804
      IF(RRX.GT.0.D0.AND.RRY.LT.0.D0) GO TO 805
      TH1=PHI+ALF
      Z(IVX,1)=-(RR*DCOS(TH1)-CC)+GI*RR*DSIN(TH1)
      GO TO 809
  803 TH1=PHI-ALF
      Z(IVX,1)=-(RR*DCOS(TH1)-CC)-GI*RR*DSIN(TH1)
      GO TO 809
  804 TH1=PHI-ALF
      Z(IVX,1)=RR*DCOS(TH1)+CC+GI*RR*DSIN(TH1)
      GO TO 809
  805 TH1=PHI+ALF
      Z(IVX,1)=RR*DCOS(TH1)+CC-GI*RR*DSIN(TH1)
  809 CONTINUE
  802 CONTINUE
C
C     *****  NOW, THRU THE REVERSED TRANSFORMATION, TRANSFORM THESE
C        POINTS BACK TO THE ZEE PLANE (I.E., THE PLANE OF THE CIRCLE)
```

```
C
      DO 806 IVX=2,NZ
      XCP(IVX,1)=Z(IVX,1)
      IF(XCP(IVX,1).LT.0.D0) GO TO 808
      ZCZ(IVX,1)=Z(IVX,1)
      Z(IVX,1)=(ZCZ(IVX,1)/R+CDSQRT((ZCZ(IVX,1)/R)**2-4.D0*((BX/R)**2)))
     1/2.D0
      GO TO 810
  808 ZCZ(IVX,1)=Z(IVX,1)
      Z(IVX,1)=(ZCZ(IVX,1)/R-CDSQRT((ZCZ(IVX,1)/R)**2-4.D0*((BX/R)**2)))
     1/2.D0
  810 CONTINUE
  806 CONTINUE
C
C     THIS PORTION OF THE PRGM DETERMINES THE POSITION OF THE VORTICES
C     (THESE ARE NECESSARY CALCULATIONS PRIOR TO DOING THE CONVECTION
C      OF THE VORTICES)
C
C     WRITE(9,3016)
C3016 FORMAT(2X,'THIS IS; ITME, GRL(ITME) AND DG/DT')
      DO 800 IVX=1,NV
      BT=CDEXP(GI*ALF)-(1./((ZTE-ZNT)**2))*CDEXP(-GI*ALF)-GI*GRLF(IVX)*
     1(1./(ZTE-Z(IVX+1,1))-1./(ZTE-ZNT-1./(DCONJG(Z(IVX+1,1))-DCONJG(ZNT
     1)))+1./(ZTE-ZNT))
      CT=GMMA-GRLF(IVX)
  800 CONTINUE
      DT=GI*(1./(ZTE-Z(1,1))-1./(ZTE-ZNT-1./(DCONJG(Z(1,1))-DCONJG(ZNT))
     1)+1./(ZTE-ZNT))
      ET=GI/(ZTE-ZNT)
      VA1=BT
      VA2=CT
      IF(ITME.EQ.1) GO TO 300
  395 NK=NK+1
      KK=KK+1
C
      VA1=CDEXP(GI*ALF)-(1./((ZTE-ZNT)**2))*CDEXP(-GI*ALF)
      DO 774 IVX=1,NV
C     VA1=VA1+CDEXP(GI*ALF)-(1./((ZTE-ZNT)**2))*CDEXP(-GI*ALF)-GI*GRLF(I
      VA1=VA1-GI*GRLF(IVX)*
     1(1./(ZTE-Z(IVX+1,NK))-1./(ZTE-ZNT-1./(DCONJG(Z(IVX+1,NK))
     1-DCONJG(ZNT)))+1./(ZTE-ZNT))
  774 CONTINUE
C
  313 DO 301 NN=1,KK
      VA1=VA1-GI*GRL(1,NN)*(1./(ZTE-Z(1,NK))-1./(ZTE-ZNT-1./(DCONJG(Z(1,
     1NK))-DCONJG(ZNT)))+1./(ZTE-ZNT))
      NK=NK-1
  301 CONTINUE
      NK=NK+KK
      VA2=CT
C
      DO 341 JT=2,ITME
      VA2=VA2-GRL(1,JT-1)
  341 CONTINUE
  300 BI(1)=VA1
      BI(2)=VA2
C**********  NOW DEFINE THE TERMS IN SUBROUTINE LEQT1C  **********
      AI(1,1)=ET
      AI(1,2)=DT
      AI(2,1)=1.
      AI(2,2)=1.
      M=1
      IA=2
      IB=2
      NI=2
      IJOB=0
C***********  LEQT1C SOLVES A SYSTEM 2X2 WITH COMPLEX CONSTANTS  *****
```

```
      CALL LEQT1C(AI,NI,IA,BI,M,IB,IJOB,WA,IER)
C************  BI(1) AND BI(2) ARE THE ANSWERS (GCL AND GRL)  *******
      KM=ITME
      KM1=ITME-1
C
      GCL(KM)=BI(1)
      GRL(1,KM)=BI(2)
C      THIS LOOP MAKES ALL THE ONCOMING VORTICES CONSTANT
      DO 776 IVX=2,NZ
      GRL(IVX,KM)=GRLF(IVX-1)
  776 CONTINUE
C
      IF(ITME.EQ.1) GO TO 311
      DGDT=GRL(1,KM)/DTME
C     WRITE(9,7102) ITME
C7102 FORMAT(2X,I5)
C
C
C      DETERMINE THE DIRECTION OF THE VELOCITY AT THE TRAILING EDGE
C
C
      ZRX1=-.6000D0
      ZZRX=ZRX1+(BX**2)/ZRX1
C     WRITE(9,891)
C 891 FORMAT(3X,'THE DIRECTION OF THE VELOCITY AT THE EDGE IS')
      ZZRY=0.400
      ZRY=(ZZRY+CDSQRT((ZZRY)**2-4.D0*(BX**2)))/2.D0
      DGDTT=DGDT
      IF(DGDTT.GT.0.D0) ZRR=ZRX1-ZRY
      IF(DGDTT.LT.0.D0) ZRR=ZRX1+ZRY
C
      VELOC=-CDEXP(GI*ALF)+GI*GCL(ITME)/(ZRR-ZNT)+CDEXP(-GI*ALF)/
     1((ZRR-ZNT)**2)
      DO 888 IN=1,NZ
      KM=ITME
      DO 888 JN=1,ITME
      DO 889 IVX=2,NV
      IF(IN.EQ.IVX.AND.JN.GE.2) GO TO 888
      IF(IN.EQ.(NV+1).AND.JN.GE.2) GO TO 848
  889 CONTINUE
C
      IF(JN.EQ.1) GO TO 887
      KM=KM-1
  887 CUTOFF=ZRR-Z(IN,KM)
      IF(CDABS(CUTOFF).LE..1) GO TO 888
C
      VELOC=VELOC+GI*GRL(IN,JN)*(1./(ZRR-Z(IN,KM))-1./(ZRR-ZNT-1./
     1(DCONJG(Z(IN,KM))-DCONJG(ZNT)))+1./(ZRR-ZNT))
  888 CONTINUE
  848 WVU=VELOC/(1.-(BX**2)/((R**2)*(ZRR**2)))
      WWX=WVU
      WWY=-GI*WVU
C
C     NOW CALCULATE THE DIRECTION OF THE VELOCITY AT ZRR
C
      WWXX=DABS(WWX)
      WWYY=DABS(WWY)
      CHETA=DATAN(WWYY/WWXX)
      HETA=CHETA*180./3.141593
      DHETA=DABS(HETA-FFETA)
C
C*****       NOW DETERMINE THE VELOCITY OF THE VORTICES
C*****       W(1,J) IS THE VELOCITY OF THE SHED VORTEX
C*****       W(NV,J) IS THE VELOCITY OF THE ONCOMING VORTICES
C*****      (NV IS THE NUMBER OF VORTICES APPROACHING THE AIRFOIL)
C
  311 DO 302 I=1,NZ
```

```
      DO 302 J=1,ITME
      DO 778 IVX=2,NZ
      IF(I.EQ.IVX.AND.J.NE.ITME) GO TO 302
  778 CONTINUE
C
      VELOC=-CDEXP(GI*ALF)+GI*GCL(ITME)/(Z(I,J)-ZNT)+CDEXP(-GI*ALF)/
     1((Z(I,J)-ZNT)**2)
      DO 303 IN=1,NZ
      KM=ITME
      DO 303 JN=1,ITME
C
      DO 779 IVX=2,NV
      IF(IN.EQ.IVX.AND.JN.GE.2) GO TO 303
      IF(IN.EQ.(NV+1).AND.JN.GE.2) GO TO 348
  779 CONTINUE
C
      IF(JN.EQ.1) GO TO 304
      KM=KM-1
  304 CUTOFF=Z(I,J)-Z(IN,KM)
      IF(CDABS(CUTOFF).LE..1) GO TO 303
      VELOC=VELOC+GI*GRL(IN,JN)*(1./(Z(I,J)-Z(IN,KM))-1./(Z(I,J)-ZNT-1./
     1(DCONJG(Z(IN,KM))-DCONJG(ZNT)))+1./(Z(I,J)-ZNT))
  303 CONTINUE
  348 W(I,J)=VELOC
  302 CONTINUE
C
C *********      NOW CONVECT THE VORTICES   **********
C              (CALCULATE THE NEW POSITIONS)
C       Z(I,JP) IS THE NEW POSITION OF THE VORTICES
      DO 305 IL=1,NZ
      DO 305 JL=1,ITME
      XNEW(IL,JL)=Z(IL,JL)+W(IL,JL)*DTME
      YNEW(IL,JL)=(-GI)*(Z(IL,JL)-W(IL,JL)*DTME)
      ZNEW(IL,JL)=DCMPLX(XNEW(IL,JL),YNEW(IL,JL))
  305 CONTINUE
      DO 320 I=1,NZ
      DO 320 J=1,ITME
      JP=J+1
      Z(I,JP)=ZNEW(I,J)
  320 CONTINUE
C ***** NOW TRANSFORM ZNEW TO THE ZETA PLANE  ****
      DO 307 IL=1,NZ
      DO 307 JL=1,ITME
C
      DO 783 IVX=2,NZ
      IF(IL.EQ.IVX.AND.JL.NE.ITME) GO TO 307
  783 CONTINUE
C
C              THIS IS ROUTHS' THEOREM
C     ZETA(IL,JL)=R*Z(IL,JL)+W(IL,JL)/(1.-(BX**2)/((R**2)*(Z(IL,JL)**2))
C    1)-(2.*(BX**2)/((R**2)*(Z(IL,JL)**3)))*((1./(1.-(BX**2)/((R**2)*(Z(
C    1IL,JL)**2))))**2)
C        THIS IS THE REGULAR TRANSFORMATION
C        THIS IS THE DIMENSIONAL FORM OF THE TRANSFORMATION (ZETA)
      ZETA(IL,JL)=R*Z(IL,JL)+(BX**2)/(R*Z(IL,JL))
      XP(IL,JL)=ZETA(IL,JL)
      YP(IL,JL)=(-GI)*ZETA(IL,JL)
C
  307 CONTINUE
      IF(IPQ.EQ.ITME) GO TO 638
      IF(SQP.NE.1.) GO TO 640
      IF(ITME.EQ.(IPQ-1)) GO TO 389
      IF(ITME.EQ.IPQ) GO TO 389
C
C     *** CALCULATION OF THE POTENTIAL AT POINTS ON THE CIRCLE *****
C
  389 IA=4
```

```
      DO 400 ID=1,180
      ZSUR=X(IA,1)/R+GI*Y(IA,1)/R
      FZ=-(ZSUR-ZNT)*CDEXP(GI*ALF)-(CDEXP(-GI*ALF))/(ZSUR-ZNT)+GI*GCL(IT
     1ME)*CDLOG(ZSUR-ZNT)
      DO 401 IN=1,NZ
      KM=ITME
      DO 401 JN=1,ITME
C
      DO 785 IVX=2,NV
      IF(IN.EQ.IVX.AND.JN.GE.2) GO TO 401
  785 CONTINUE
      IF(IN.EQ.(NV+1).AND.JN.GE.2) GO TO 431
C
      IF(JN.EQ.1) GO TO 403
      KM=KM-1
  403 FZ=FZ+GI*GRL(IN,JN)*(CDLOG(ZSUR-Z(IN,KM))-CDLOG(ZSUR-ZNT-1./(DCONJ
     1G(Z(IN,KM))-DCONJG(ZNT)))+CDLOG(ZSUR-ZNT)-CDLOG(-(DCONJG(Z(IN,KM))
     1-DCONJG(ZNT))))
  401 CONTINUE
  431 DFZ(ID,ITME)=FZ
      IA=IA+4
  400 CONTINUE
C
C     ** PUT IN ITME STATEMENTS TO BYPASS LOOP 404 AND PLOT STMNTS *****
C     ******  LOOP 404 CALCULATES THE PRESSURE ON THE SURFACE  **********
C
      IF(ITME.EQ.1) GO TO 390
      IF(ITME.EQ.(IPQ-1)) GO TO 390
C
C  **  GENERATE THE GRID POINTS FOR THE WAKE VELOCITY FIELD  ***
C
  638 IF(IPP.GT.1) GO TO 644
      NG=18
      NNGG=18
      NGD=20
      NGB=20
      YBB1=2.7
      DXBB=TAU/NG
      DYBB=2.0*YBB1/NNGG
      ALFF=ALF
C
C      TO PLOT THE WAKE VELOCITY FIELD UPSTREAM OF THE AIRFOIL LET
C
C     NG=18
C     NNGG=18
C     NGD=20
C     NGB=12 TO 20
C     YBB1=1.7
C     ZGP1=(4.*AA+TAU)+GI*(0.5*YBB1)  (THIS IS THE LOCATION OF THE FIRST
C         GRID POINT)
C     ZGPX=ZGP1
C     ZGPY=-GI*ZGP1
C     ZGP(1,1)=+ZRGP*COS(PETA)+.............
C
C      TO PLOT THE WAKE VELOCITY VECTORS AT THE TRAILING EDGE LET
C
C     NG=30
C     NNGG=22
C     NGD=10
C     NGB=20
C     YBB1=1.15
C     ZGP1=-1.2+GI*YBB1  (THIS IS THE LOCATION OF THE FIRST GRID POINT)
C     ZGPX=ZGP1
C     ZGP(1,1)=-ZRGP*COS(PETA)+GI*.............
      ZGP1=(4.0*AA+TAU)+GI*(0.5*YBB1)
C     ZGP1=-1.200+GI*(YBB1)
      ZGPX=ZGP1
```

```
      ZGPY=-1.0*GI*ZGP1
      GETA=ATAN(ZGPY/ZGPX)
      PETA=ABS(GETA-ALFF)
      ZRGP=(ZGPX**2+ZGPY**2)**0.5
      ZGP(1,1)=ZRGP*COS(PETA)+GI*ZRGP*SIN(PETA)
C     ZGP(1,1)=-ZRGP*COS(PETA)+GI*ZRGP*SIN(PETA)
      DGPX1=DYBB*SIN(ALFF)
      DGPY1=DYBB*COS(ALFF)*GI
      DGPX2=DXBB*COS(ALFF)
      DGPY2=DXBB*SIN(ALFF)*GI
      DO 440 IBJ=1,NGD
      DO 441 IBB=1,NGB
      ZGP(IBB+1,IBJ)=ZGP(IBB,IBJ)-DGPX1-DGPY1
  441 CONTINUE
      ZGP(1,IBJ+1)=ZGP(1,IBJ)-DGPX2+DGPY2
  440 CONTINUE
C
C   **  TRANSFORM THESE GRID POINTS TO THE ZETA PLANE ****
C
      DO 447 IBJ=1,NGD
      DO 447 IBB=1,NGB
      ZEGP(IBB,IBJ)=R*ZGP(IBB,IBJ)+(BX**2)/(R*ZGP(IBB,IBJ))
  447 CONTINUE
C
C   ****  DETERMINE THE VELOCITY OF THE WAKE AT THESE GRID POINTS ***
C
C     WRITE(9,468)
C 468 FORMAT(/,3X,'THESE ARE THE WAKE VELOCITY VALUES')
      DO 461 IBJ=1,NGD
      DO 461 IBB=1,NGB
      ZGGP=ZGP(IBB,IBJ)
      VELOC=-CDEXP(GI*ALF)+GI*GCL(ITME)/(ZGGP-ZNT)+CDEXP(-GI*ALF)/((ZGGP
     1-ZNT)**2)
      DO 465 IN=1,NZ
      KM=ITME
      DO 465 JN=1,ITME
C
      DO 464 IVX=2,NV
      IF(IN.EQ.IVX.AND.JN.GE.2) GO TO 465
      IF(IN.EQ.(NV+1).AND.JN.GE.2) GO TO 462
  464 CONTINUE
      IF(JN.EQ.1) GO TO 466
      KM=KM-1
  466 CUTOFF=ZGGP-Z(IN,KM)
      IF(CDABS(CUTOFF).LE..1) GO TO 465
      VELOC=VELOC+GI*GRL(IN,JN)*(1./(ZGGP-Z(IN,KM))-1./(ZGGP-ZNT-1./(DCO
     1NJG(Z(IN,KM))-DCONJG(ZNT)))+1./(ZGGP-ZNT))
  465 CONTINUE
  462 WVEL(IBB,IBJ)=VELOC/(1.-(BX**2)/((R**2)*(ZGGP**2)))
      WVELX=WVEL(IBB,IBJ)
      WVELY=GI*WVEL(IBB,IBJ)
C     WRITE(9,467) IBJ,IBB,WVELX,WVELY
C 467 FORMAT(3X,I5,3X,I5,3X,F10.7,3X,F10.7)
  461 CONTINUE
C
  644 IF(SQP.NE.1.) GO TO 640
      IA=4
      DO 404 ID=1,180
      ZSUR=X(IA,1)/R+GI*Y(IA,1)/R
      VELOC=-CDEXP(GI*ALF)+GI*GCL(ITME)/(ZSUR-ZNT)+CDEXP(-GI*ALF)/((ZSUR
     1-ZNT)**2)
      DO 405 IN=1,NZ
      KM=ITME
      DO 405 JN=1,ITME
C
      DO 786 IVX=2,NV
      IF(IN.EQ.IVX.AND.JN.GE.2) GO TO 405
```

```
  786 CONTINUE
      IF(IN.EQ.(NV+1).AND.JN.GE.2) GO TO 402
C
      IF(JN.EQ.1) GO TO 406
      KM=KM-1
  406 VELOC=VELOC+GI*GRL(IN,JN)*(1./(ZSUR-Z(IN,KM))-1./(ZSUR-ZNT-1./(
     1DCONJG(Z(IN,KM))-DCONJG(ZNT)))+1./(ZSUR-ZNT))
  405 CONTINUE
  402 VEL1=VELOC/(1.-(BX**2)/((R**2)*(ZSUR**2)))
      VEL3=CDABS(VEL1)
C     ************  PRS IS CP  ***************
C        DFZ/DTME   IS   D(PHI)/DT
      PRS(ID,ITME)=-(VEL3**2)-2.*(DFZ(ID,ITME)-DFZ(ID,ITME-1))/(R*DTME)
      IA=IA+4
  404 CONTINUE
C
C     ************ CALCULATION OF THE STREAMLINES ***************
C     **************  PSI IS THE STREAM FUNCTION  ***********
C
C       DETERMINE PSI AT THE INITIAL POSITIONS OF THE STREAMLINES
C
  640 IF(IRP.GT.1) GO TO 637
      IF(ITME.LT.IPQ) GO TO 637
      IF(ITME.GT.IPQ) GO TO 637
      IIZ=300
      PINC=.1D0
      KD=3
C     DO 500 KD=1,5
      IF(KD.EQ.3) GO TO 500
      FZN=-(ZPSI(1,KD)-ZNT)*CDEXP(GI*ALF)-(CDEXP(-GI*ALF))/(ZPSI(1,KD)-
     1ZNT)+GI*GCL(ITME)*CDLOG(ZPSI(1,KD)-ZNT)
      DO 501 IN=1,NZ
      KM=ITME
      DO 501 JN=1,ITME
C
      DO 787 IVX=2,NV
      IF(IN.EQ.IVX.AND.JN.GE.2) GO TO 501
  787 CONTINUE
      IF(IN.EQ.(NV+1).AND.JN.GE.2) GO TO 502
C
      IF(JN.EQ.1) GO TO 503
      KM=KM-1
  503 FZN=FZN+GI*GRL(IN,JN)*(CDLOG(ZPSI(1,KD)-Z(IN,KM))-CDLOG(ZPSI(1,KD)
     1-ZNT-1./(DCONJG(Z(IN,KM))-DCONJG(ZNT)))+CDLOG(ZPSI(1,KD)-ZNT)-
     1CDLOG(-(DCONJG(Z(IN,KM))-DCONJG(ZNT))))
  501 CONTINUE
  502 PSI(KD)=GI*FZN
      WRITE(9,1005) KD,PSI(KD)
 1005 FORMAT(5XI5,F15.10)
  500 CONTINUE
C
C     ********** FIND X AND Y VALUES OF PSI  ***********
C
      KD=3
C     DO 504 KD=1,5
      DO 505 JD=1,30
      IF(KD.LT.3) GO TO 512
      IF(KD.EQ.3.AND.JD.EQ.1) GO TO 511
      IF(KD.EQ.3.AND.JD.GE.2) GO TO 512
C     IF(KD.GE.3) GO TO 512
C
C    *********  CALCULATE ZPSI FOR THE ZERO PSI LINE  ********
C
C 511 YPSI=-(XPSI-2.00D0)*DTAN(ALF)
  511 ZPSI(1,3)=XPSI+GI*(.1D0)
      IZ1=1
      DO 513 IZ=1,IIZ
```

```
  519 ZTSI=ZPSI(1,3)
      FZ2=-(ZTSI-ZNT)*CDEXP(GI*ALF)-(CDEXP(-GI*ALF))/(ZTSI-ZNT)+GI*
     1GCL(ITME)*CDLOG(ZTSI-ZNT)
      DO 514 IN=1,NZ
      KM=ITME
      DO 514 JN=1,ITME
C
      DO 788 IVX=2,NV
      IF(IN.EQ.IVX.AND.JN.GE.2) GO TO 514
  788 CONTINUE
      IF(IN.EQ.(NV+1).AND.JN.GE.2) GO TO 515
C
      IF(JN.EQ.1) GO TO 516
      KM=KM-1
  516 FZ2=FZ2+GI*GRL(IN,JN)*(CDLOG(ZTSI-Z(IN,KM))-CDLOG(ZTSI-ZNT-1./
     1(DCONJG(Z(IN,KM))-DCONJG(ZNT)))+CDLOG(ZTSI-ZNT)-CDLOG(-(DCONJG(
     1Z(IN,KM))-DCONJG(ZNT))))
  514 CONTINUE
  515 DFZ2=GI*FZ2
      IF(DABS(DFZ2).LE..000001D0) GO TO 517
      IF(DFZ2.LT.0.D00) GO TO 518
      IF(DFZ2.GT.0.D00) ZPSI(1,3)=ZTSI-GI*PINC
      IZ1=IZ1+1
      IF(IZ1.EQ.500) GO TO 517
      GO TO 519
  518 PINC=PINC/1.5D000
      IF(IZ.EQ.300) GO TO 517
      ZPSI(1,3)=ZTSI+GI*PINC
  513 CONTINUE
  517 ZPSI(1,3)=ZTSI
      PSI(3)=DFZ2
C
      WRITE(9,1114) IZ,PSI(3),ZPSI(1,3),PINC
 1114 FORMAT(2X,I5,2X,4F15.12)
C
C     **** THIS PART CALCULATES THE POSITION OF THE STREAMLINE PSI ****
C                  **** THIS IS THE PAC MAN SCHEME  *****
C
C
C       THIS IS CASE ONE
C
  512 ZPSI(JD+1,KD)=ZPSI(JD,KD)-DDR*(DCOS(THTA+DT4)-GI*DSIN(THTA+DT4))
      IZ1=1
      IVPSI=0
      DO 506 IV=1,500
  522 ZTSI=ZPSI(JD+1,KD)
      FZ1=-(ZTSI-ZNT)*CDEXP(GI*ALF)-(CDEXP(-GI*ALF))/(ZTSI-ZNT)+GI*GCL(
     1ITME)*CDLOG(ZTSI-ZNT)
      IVPSI=IVPSI+1
      DO 507 IN=1,NZ
      KM=ITME
      DO 507 JN=1,ITME
C
      DO 789 IVX=2,NV
      IF(IN.EQ.IVX.AND.JN.GE.2) GO TO 507
  789 CONTINUE
      IF(IN.EQ.(NV+1).AND.JN.GE.2) GO TO 508
C
      IF(JN.EQ.1) GO TO 509
      KM=KM-1
  509 FZ1=FZ1+GI*GRL(IN,JN)*(CDLOG(ZTSI-Z(IN,KM))-CDLOG(ZTSI-ZNT-1./(DCO
     1NJG(Z(IN,KM))-DCONJG(ZNT)))+CDLOG(ZTSI-ZNT)-CDLOG(-(DCONJG(Z(IN,KM
     1))-DCONJG(ZNT))))
  507 CONTINUE
  508 DFZ1=GI*FZ1
      DPSI=DABS(DFZ1)-DABS(PSI(KD))
      WRITE(9,1113) JD,DFZ1,PSI(KD),ZPSI(JD+1,KD),DT4
```

```
 1113 FORMAT(I2,4F13.9,1X,F6.4)
      IF(DABS(DPSI).LE.0.0005D0) GO TO 530
      IF(DFZ1.LT.PSI(KD).AND.IVPSI.EQ.1) GO TO 721
      IF(DFZ1.LT.PSI(KD)) GO TO 521
      IF(DFZ1.GT.PSI(KD)) DT4=DT4-DT3
C     IF(IZ1.EQ.150) DT4=DT4*1.5D0
      ZPSI(JD+1,KD)=ZPSI(JD,KD)-DDR*(DCOS(THTA+DT4)-GI*DSIN(THTA+DT4))
      IZ1=IZ1+1
      IF(IZ1.EQ.500) GO TO 531
      GO TO 522
  521 DT3=DT3/1.3D00
C     IF(IV.EQ.150) DT3=DT4*1.7D00
      DT4=DT4+DT3
      IF(IV.EQ.500) GO TO 531
      ZPSI(JD+1,KD)=ZPSI(JD,KD)-DDR*(DCOS(THTA+DT4)-GI*DSIN(THTA+DT4))
  506 CONTINUE
C
C         THIS IS CASE TWO
C
  721 DT4=DT4+DT3
      ZPSI(JD+1,KD)=ZPSI(JD,KD)-DDR*(DCOS(THTA+DT4)-GI*DSIN(THTA+DT4))
      IZ1=1
      DO 726 IV=1,500
  722 ZTSI=ZPSI(JD+1,KD)
      FZ1=-(ZTSI-ZNT)*CDEXP(GI*ALF)-(CDEXP(-GI*ALF))/(ZTSI-ZNT)+GI*GCL(
     1ITME)*CDLOG(ZTSI-ZNT)
      DO 717 IN=1,NZ
      KM=ITME
      DO 717 JN=1,ITME
      DO 719 IVX=2,NV
      IF(IN.EQ.IVX.AND.JN.GE.2) GO TO 717
  719 CONTINUE
      IF(IN.EQ.(NV+1).AND.JN.GE.2) GO TO 728
      IF(JN.EQ.1) GO TO 729
      KM=KM-1
  729 FZ1=FZ1+GI*GRL(IN,JN)*(CDLOG(ZTSI-Z(IN,KM))-CDLOG(ZTSI-ZNT-1./(DCO
     1NJG(Z(IN,KM))-DCONJG(ZNT)))+CDLOG(ZTSI-ZNT)-CDLOG(-(DCONJG(Z(IN,KM
     1))-DCONJG(ZNT))))
  717 CONTINUE
  728 DFZ1=GI*FZ1
      DPSI=DABS(DFZ1)-DABS(PSI(KD))
      WRITE(9,3007) JD,DFZ1,PSI(KD),ZPSI(JD+1,KD),DT4
 3007 FORMAT(I2,4F13.9,1X,F6.4)
      IF(DABS(DPSI).LE.0.0005D0) GO TO 530
      IF(DFZ1.GT.PSI(KD)) GO TO 712
      IF(DFZ1.LT.PSI(KD)) DT4=DT4+DT3
      ZPSI(JD+1,KD)=ZPSI(JD,KD)-DDR*(DCOS(THTA+DT4)-GI*DSIN(THTA+DT4))
      IZ1=IZ1+1
      IF(IZ1.EQ.500) GO TO 531
      GO TO 722
  712 DT3=DT3/1.3D0
      DT4=DT4-DT3
      IF(IV.EQ.500) GO TO 531
      ZPSI(JD+1,KD)=ZPSI(JD,KD)-DDR*(DCOS(THTA+DT4)-GI*DSIN(THTA+DT4))
  726 CONTINUE
C
C       THIS IS THE END OF CASES ONE AND TWO
C
  530 ZPSI(JD+1,KD)=ZTSI
      XPSI1=ZPSI(JD,KD)
      XPSI2=ZPSI(JD+1,KD)
      YPSI1=-GI*ZPSI(JD,KD)
      YPSI2=-GI*ZPSI(JD+1,KD)
C     WRITE(9,1113) JD,DFZ1,PSI(KD),ZPSI(JD+1,KD),DT4,JD2
C1113 FORMAT(I3,1X,5F12.9,I3)
C     WRITE(9,1119) XPSI1,YPSI1,XPSI2,YPSI2
C1119 FORMAT(2X,4F13.9)
```

```
      IF(KD.LT.3.OR.KD.GT.3) GO TO 634
C     IF((JD+1).GT.JD2) GO TO 634
      IF(DABS(XPSI2).LE.DABS(XSTG1)) GO TO 542
  634 XDSI=DABS(XPSI1)-DABS(XPSI2)
      IF(DABS(XDSI).LE..0001D0) GO TO 520
      YDSI=YPSI2-YPSI1
      XDSI=XPSI1-XPSI2
      THTA=DATAN(YDSI/XDSI)
C     WRITE(9,1115) THTA
C1115 FORMAT(5X,F15.10)
      GO TO 523
  520 THTA=90.D0*PI/180.D0
  523 DT4=8.D0*PI/180.D0
      DT3=2.D0*PI/180.D0
      GO TO 505
  542 ZPSI(JD+1,KD)=X(360,1)+GI*(0.D0)
      THTA=0.D0
      JD2=JD+1
      DT4=8.D0*PI/180.D0
      DT3=2.D0*PI/180.D0
  505 CONTINUE
C 504 CONTINUE
      GO TO 633
  531 WRITE(4,1111)
 1111 FORMAT(5X,'THE PAC MAN SCHEME DID NOT CONVERGE')
      WRITE(4,1112) KD,JD,IV,IZ1
 1112 FORMAT(2X,'IT STOPPED AT',3X,I4,2X,I4,2X,I4,2X,I4)
C
C    *****  NOW TRANSFORM ZPSI(JD,KD) TO THE ZETTA PLANE  *****
C
C 633 DO 635 KD=1,5
  633 KD=3
      DO 635 JD=1,30
      ZZETA=ZPSI(JD,KD)+(BX**2)/ZPSI(JD,KD)
      ZEPSI(JD,KD)=ZZETA
C     WRITE(9,1116) ZEPSI(JD,KD)
C1116 FORMAT(5X,2F13.9)
  635 CONTINUE
C
C    ************* CONSTRUCTION OF THE AXES OF THE AIRFOIL **************
C    ********** THIS CALL PLOT STMNT DEFINES A NEW ORIGIN  ************
C
  637 IF(ITME.LT.IPQ) GO TO 390
      IF(ITME.GT.IPQ) GO TO 390
      CALL PLOT(DP,DDP,-3)
      CALL  NEWPEN(2)
      CALL VPISYM(-1.,3.75,.13,35HTHE ANGLE OF ATTACK IS      DEGREES,0.
     1,35)
      CALL NUMBER(2.33,3.75,.13,ALFA,0.,1)
  315 CALL NUMBER(-.7,-3.1,.1,SSTP,0.,0)
      IF(ITME.GT.2) GO TO 316
      CALL VPISYM(-.54,-2.95,.07,2HND,0.,2)
      IF(ITME.EQ.2) GO TO 317
  316 CALL VPISYM(-.48,-2.95,.07,2HTH,0.,2)
  317 CALL VPISYM(-.25,-3.1,.1,9HTIME STEP,0.,9)
      CALL SYMBOL(-.5,-3.29,.1,68,0.,-1)
      CALL VPISYM(-.40,-3.29,.1,4HT IS,0.,4)
      CALL NUMBER(.14,-3.29,.1,DTME,0.,2)
      C=SCALE*(-1.0)
      E=SCALE
      CALL NEWPEN(2)
C
C************  CONSTRUCTION OF AXES IN THE ZETA PLANE **********
C
      AJ=SCALE*XJMIN
      BJ=SCALE*XJMAX*1.1
      CJ=2.0*C
```

```
      CCJ=CJ*1.08
C     CALL PLOT(CJ,-.1,3)
C     CALL PLOT(CJ,0.,2)
C
C*************  CONSTRUCT THE AIRFOIL  **************
C
      BGJ=BJ/1.1
      CALL PLOT(BGJ,0.,3)
      CALL NEWPEN(4)
C     XV=X(270,2)*SCALE
C     YV=Y(270,2)*SCALE
C     CALL PLOT(XV,YV,3)
      DO 7 K=1,N
      HJ=X(K,2)*SCALE
      HHJ=Y(K,2)*SCALE
      CALL PLOT(HJ,HHJ,2)
    7 CONTINUE
C
C     ********** THIS IF STMNT. PLOTS THE N0012 IF EY=0. ************
C     ****  (NOT NECESSARY SINCE THE FIT HAS BEEN COMPLETED)  ****
C
      IF(EY.EQ.0.0) GO TO 201
C
C**********************  CONSTRUCT THE NACA 0012  *********************
C
C                     XXJ IS THE AIRFOIL CHORD LENGTH
C
C*************************************************************************
C
      XXJ=(XJMAX-XJMIN)
      CALL PLOT(BGJ,0.,3)
      CALL NEWPEN(2)
      DO 27 MA=1,38
      XXN=(XN(MA)*XXJ+XJMAX)*SCALE
      YYN=YN(MA)*SCALE*XXJ
      CALL PLOT(XXN,YYN,2)
   27 CONTINUE
C
C *******    PLOT THE VORTICES AROUND THE AIRFOIL    ************
C
C    THE SHEDDING VORTICES DOWNSTREAM WILL BE PLOTTED FIRST
C    AND THE APPROACHING VORTEX STREET WILL BE PLOTTED SECOND
C
C*************************************************************************
C
C 201 IF(IRP.GT.1) GO TO 227
C     IF(ITME.EQ.IPQ) GO TO 314
  201 XXP=XP(1,1)*SCALE
      YYP=YP(1,1)*SCALE
      IF(IPP.EQ.1) GO TO 314
      CALL PLOT(XXP,YYP,3)
      DO 306 JL=1,ITME
      XXP=XP(1,JL)*SCALE
      YYP=YP(1,JL)*SCALE
      CALL PLOT(XXP,YYP,2)
      CALL SYMBOL(XXP,YYP,.05,11,0.,-1)
C
      XD2=XXP+XW(45)
      YD2=YYP+YW(45)
      CALL PLOT(XXP,YYP,3)
      DO 791 IW=45,315
      XD2=XXP+XW(IW)
      YD2=YYP+YW(IW)
      CALL PLOT(XD2,YD2,2)
  791 CONTINUE
C
      GRRL(1,JL)=GRL(1,JL)
```

```
      IF(GRRL(1,JL).GT.0.00) GO TO 792
C
      CALL SYMBOL(XD2,YD2,.10,2,45.,-1)
      GO TO 306
  792 XD2=XXP+XW(45)
      YD2=YYP+YW(45)
      CALL SYMBOL(XD2,YD2,.10,2,315.,-1)
  306 CONTINUE
  314 XXF=XP(2,1)*SCALE
      YYF=YP(2,1)*SCALE
      CALL PLOT(XXF,YYF,3)
      DO 309 JL=1,ITME
      XXF=XP(2,JL)*SCALE
      YYF=YP(2,JL)*SCALE
      CALL PLOT(XXF,YYF,2)
  309 CONTINUE
      XF1=XP(2,ITME)*SCALE
      YF1=YP(2,ITME)*SCALE
      CALL SYMBOL(XF1,YF1,.1,60,0.,-1)
C
      RW=.25
      CALL ARROW(XW,YW,RW)
C
      WRITE(9,796) DTME,TAUME
  796 FORMAT(2X,F10.6,2X,F10.6)
      DO 790 IVX=3,NZ
      XXD=XP(IVX,1)*SCALE
      YYD=YP(IVX,1)*SCALE
      CALL PLOT(XXD,YYD,3)
      DO 310 JL=1,ITME
      XXD=XP(IVX,JL)*SCALE
      YYD=YP(IVX,JL)*SCALE
      CALL PLOT(XXD,YYD,2)
  310 CONTINUE
      XD1=XP(IVX,ITME)*SCALE
      YD1=YP(IVX,ITME)*SCALE
      CALL SYMBOL(XD1,YD1,.08,11,0.,-1)
      IF(IVX.LT.12) GO TO 793
      IF(IVX.GT.12) GO TO 793
      DO 794 IGJ=1,ITME
      XD1=XP(IVX,IGJ)*SCALE
      YD1=YP(IVX,IGJ)*SCALE
      XD11=((2.*SCALE-XD1)/CHORD)*100.00
      YD11=(YD1/CHORD)*100.00
C
C       CALCULATE THE PHASE POSITION OF THE VORTEX
C
      PHME=360.00*IGJ/TAUME
      IF(PHME.GT.360.00) PHME=PHME-360.00
      WRITE(9,795) IGJ,XD11,YD11,PHME
  795 FORMAT(2X,I5,2X,F10.6,2X,F10.6,2X,F10.6)
  794 CONTINUE
      CALL VPISYM(-2.8,-3.5,.13,46HTHE X AND Y POSITION OF THE ELEVENTH
     1VORTEX IS,0.,46)
      CALL NUMBER(-1.25,-3.75,.13,XD11,0.,2)
      CALL NUMBER(.1,-3.75,.13,YD11,0.,2)
      CALL VPISYM(1.3,-3.75,.13,13HPERCENT CHORD,0.,13)
C
C      PLOT THE ARROW VECTOR INDICATING THE SENSE OF THE VORTICES
C
  793 XD2=XD1+XW(45)
      YD2=YD1+YW(45)
      CALL PLOT(XD2,YD2,3)
      DO 797 IW=45,315
      XD2=XD1+XW(IW)
      YD2=YD1+YW(IW)
      CALL PLOT(XD2,YD2,2)
```

```
  797 CONTINUE
C
      IF(GRLF(IVX).LT.0.00) GO TO 798
C
      CALL SYMBOL(XD2,YD2,.15,2,45.,-1)
      GO TO 790
  798 XD2=XD1+XW(45)
      YD2=YD1+YW(45)
      CALL SYMBOL(XD2,YD2,.15,2,315.,-1)
  790 CONTINUE
      IF(IPP.GT.1) GO TO 393
C
C         PLOT THE DIAMOND SHAPE MEASURING CONTOUR
C
      YDIA=0.00
      XDIA=-2.10*SCALE
      YDIA1=0.6125*SCALE
      XDIA1=XDIA-0.075*SCALE
      YDIA2=0.05*SCALE
      XDIA2=XDIA1-.24*SCALE
      YDIA3=-(0.575*SCALE)
      XDIA3=XDIA2+0.075*SCALE
      CALL PLOT(XDIA,YDIA,3)
      CALL PLOT(XDIA1,YDIA1,2)
      CALL PLOT(XDIA2,YDIA2,2)
      CALL PLOT(XDIA3,YDIA3,2)
      CALL PLOT(XDIA,YDIA,2)
C
      IF(IPP.GT.1) GO TO 393
C
C
C    ******   THIS IS THE GRID FOR THE WAKE VELOCITY *******
C    ***  (REDEFINE NEW VARIABLES IN TERMS OF REAL NUMBERS)  ***
C
      DO 445 IBJ=1,NGD
      DO 445 IBB=1,NGB
      ZZGPX(IBB,IBJ)=ZEGP(IBB,IBJ)
      ZZGPY(IBB,IBJ)=-GI*ZEGP(IBB,IBJ)
  445 CONTINUE
C
C   ***  PLOT THE GRID POINTS  ****
C
      DO 446 IBJ=1,NGD
      DO 446 IBB=1,NGB
      ZGPTX=ZZGPX(IBB,IBJ)*SCALE
      ZGPTY=ZZGPY(IBB,IBJ)*SCALE
      CALL PLOT(ZGPTX,ZGPTY,3)
      CALL SYMBOL(ZGPTX,ZGPTY,.05,3,0.,-1)
      WVELX=WVEL(IBB,IBJ)*0.15
      WVELY=GI*WVEL(IBB,IBJ)*0.15
      DWVLX=ZGPTX+WVELX
      DWVLY=ZGPTY+WVELY
      CALL PLOT(DWVLX,DWVLY,2)
      CALL SYMBOL(DWVLX,DWVLY,.10,110,180.,-1)
  446 CONTINUE
C
C      ******  PLOT THE STREAMLINES  *******
C
  393 IF(IRP.GT.1) GO TO 390
      IF(ITME.LT.IPQ.OR.ITME.GT.IPQ) GO TO 390
      KD=3
C     DO 561 KD=1,5
      XXS=ZEPSI(1,KD)*SCALE
      YYS=-GI*ZEPSI(1,KD)*SCALE
      CALL PLOT(XXS,YYS,3)
      DO 561 JD=1,30
      XXS=ZEPSI(JD,KD)*SCALE
```

```
      YYS=-GI*ZEPSI(JD,KD)*SCALE
      IF(KD.LT.3.OR.KD.GT.3) GO TO 562
      IF(JD.EQ.JD2) CALL PLOT(XXS,YYS,3)
  562 CALL PLOT(XXS,YYS,2)
  561 CONTINUE
  390 IF(ITME.EQ.(IPQ-1)) DP=20.
      IF(ITME.EQ.(IPQ-1)) DDP=5.
      ITME=ITME+1
      SSTP=SSTP+1.
      IF(ITME.LT.ISTP) GO TO 395
  470 IF(SQP.NE.1) GO TO 391
C
C********** PLOT THE PRESSURE DISTRIBUTION  ******
C
      SCALE=1.00
      CALL PLOT(12.,0.,-3)
C
C  *****  PLOT THE COORDINATE AXES FOR THE PRESSURE PROFILES ***
C
      XPC1=X(1,2)*SCALE*1.2
      XPC2=X(360,2)*SCALE*1.2
      CALL PLOT(XPC2,0.,3)
      CALL PLOT(XPC1,0.,2)
      CALL PLOT(0.,-.2,3)
      CALL VPISYM(0.,-.2,.13,3HX/C,0.,3)
      YPC1=2.5
      YPC2=-1.0
      CALL PLOT(0.,YPC2,3)
      CALL PLOT(0.,YPC2,2)
      YP1=-1.92
      YPC=-2.00
      DO 427 IQ=1,2
      IF(IQ.EQ.1) ITME=2
      IF(IQ.EQ.1) TT=2.00
      IF(IQ.EQ.2) ITME=IPQ
      IF(IQ.EQ.2) TT=IPQ*1.00
C     IF(IQ.EQ.3) ITME=20
C     IF(IQ.EQ.3) TT=20.00
C     IF(IQ.EQ.4) ITME=30
C     IF(IQ.EQ.4) TT=30.00
      NGG=IQ
      CALL VPISYM(-.3,YP1,.15,NGG,0.,-1)
      CALL NUMBER(0.0,YPC,.10,TT,0.,0)
      IF(IQ.GT.1) GO TO 601
      CALL VPISYM(.2,YPC,.05,2HND,0.,2)
      IF(IQ.EQ.1) GO TO 602
  601 CALL VPISYM(.2,YPC,.05,2HTH,0.,2)
  602 CALL VPISYM(.6,YPC,.10,9HTIME STEP,0.,9)
      ZSX=(X(1,2)+GI*Y(1,2))*SCALE
      CALL PLOT(ZSX,0.,3)
      IA=4
      DO 425 ID=1,180
      IID=181-ID
      ZSS=X(IA,2)+GI*Y(IA,2)
      ZSX=ZSS*SCALE
      CS=-1.
      PRES=CS*PRS(IID,ITME)*SCALE
      WRITE(9,7771) ID,IID,PRES
 7771 FORMAT(3X,I6,3X,I6,2X,2F13.7)
      CALL PLOT(ZSX,PRES,2)
C     CALL VPISYM(ZSX,PRES,.09,NGG,0.,-1)
  433 IA=IA+4
  425 CONTINUE
      YPC=YPC-.25
      YP1=YP1-.25
  427 CONTINUE
  391 CALL PLOT(0.,0.,999)
```

```
      WRITE(4,110)
  110 FORMAT(10X,'DO YOU WANT TO RUN THE PROGRAM AGAIN? 1=YES')
      READ(8,*) NTA
      IF(NTA.EQ.1) GO TO 1000
      GO TO 571
  571 STOP
      END
C
C
C     ******************************************************
C
C                     SUBROUTINE CIRCLE
C
C                    SOLVES FOR X AND Y
C
C     ******************************************************
C
      SUBROUTINE CIRCLE(X,Y,N,EX,EY,R)
      DOUBLE PRECISION X,Y,R,THT
      DIMENSION X(720,2), Y(720,2)
C
      TH=0.00
      DO 1 I=1,N
      TH=TH+.5
      THT=TH*3.141593/180.0
      X(I,1)=EX+R*DCOS(THT)
      Y(I,1)=EY+R*DSIN(THT)
    1 CONTINUE
      RETURN
      END
C
C
C     ******************************************************
C
C                  SUBROUTINE  JWKSK
C
C            SOLVES FOR X AND Y IN THE ZETA PLANE
C
C     ******************************************************
C
      SUBROUTINE JWKSK(X,Y,N,BX,XSTG1,YSTG1,XSTG2,YSTG2)
      DOUBLE PRECISION X,Y,XSTG1,YSTG1,XSTG2,YSTG2
      DIMENSION X(720,2), Y(720,2)
      COMPLEX*16 ZETTA,ZI,GI,ZSTG,ZSG
      DO 2 I=1,N
      GI=DCMPLX(0.D0,1.D0)
      ZI=DCMPLX(X(I,1),Y(I,1))
      ZETTA=ZI+(BX**2)/ZI
      Y(I,2)=(-GI)*ZETTA
      X(I,2)=ZETTA
    2 CONTINUE
      ZSTG=DCMPLX(XSTG1,YSTG1)
      ZSG=ZSTG+(BX**2)/ZSTG
      XSTG2=ZSG
      YSTG2=(-GI)*ZSG
      RETURN
      END
C
C
C*************************************************************
C                  SUBROUTINE NACA
C
C       READS IN COORDINATES OF THE NACA 0012
C
C*************************************************************
C
      SUBROUTINE NACA(XN,YN)
```

```
      DIMENSION XN(38), YN(38)
      REWIND 7
      READ(7,77) (XN(I), YN(I), I=1,38)
      DO 28 I=1,38
   28 XN(I)=-1.0*XN(I)
   77 FORMAT(2F10.5)
      RETURN
      END
C
C
C            THIS IS SUBROUTINE ARROW
C         THIS ROUTINE GENERATES A CIRCLE USED
C       TO PLOT A VECTOR ARROW AROUND THE VORTICES
C
C
      SUBROUTINE ARROW(XW,YW,RW)
      DIMENSION XW(360),YW(360)
C
      THW=0.00
      DO 3 I=1,360
      THW=THW+1.0
      THWT=THW*3.141593/180.0
      XW(I)=RW*COS(THWT)
      YW(I)=RW*SIN(THWT)
    3 CONTINUE
      RETURN
      END
```

The vita has been removed from the scanned document